Flow control in dual-bell nozzles : optimisation of operating mode transition using radial secondary fluidic injection

Brian Legros

To cite this version:

Brian Legros. Flow control in dual-bell nozzles : optimisation of operating mode transition using radial secondary fluidic injection. Mechanical engineering [physics.class-ph]. Université d'Orléans, 2024. English. NNT : 2024ORLE1008 . tel-04588641

HAL Id: tel-04588641
https://theses.hal.science/tel-04588641
Submitted on 27 May 2024

UNIVERSITÉ D’ORLÉANS

ÉCOLE DOCTORALE EMSTU
Institut ICARE, CNRS Orléans | Laboratoire PRISME, Orléans

THÈSE présentée par :

Brian LEGROS

soutenue le : **16 avril 2024**

pour obtenir le grade de : **Docteur de l’Université d’Orléans**

Discipline/ Spécialité : Génie Mécanique

Flow control in dual-bell nozzles: optimisation of operating mode transition using radial secondary fluidic injection

THÈSE dirigée par :

M KOURTA Azeddine	Professeur, Université d'Orléans
M LEGER Luc	Maître de Conférences, Université d’Orléans

RAPPORTEURS :

M HADJADJ Abdellah	Professeur, INSA Rouen Normandie
M ROBINET Jean-Christophe	Professeur, ENSAM Paris

JURY :

M BLANCHARD Simon	Docteur, CNES
M HADJADJ Abdellah	Professeur, INSA Rouen Normandie
M KOURTA Azeddine	Professeur, Université d'Orléans (PRISME)
M LEGER Luc	Maître de Conférences, Université d'Orléans (ICARE)
M ROBINET Jean-Christophe	Professeur, ENSAM Paris
M SELLAM Mohamed	Maître de Conférences, Université Paris-Saclay Evry
Mme SOCHET Isabelle	Professeure, INSA CVL, Présidente de jury

Ask, Believe, and Receive . . .

Acknowledgements

I would like to express my sincere gratitude to Professors Abdellah Hadjadj and Jean-Christophe Robinet for their manuscript reviews and insightful discussions during my defense. I also thank Dr. Simon Blanchard, Dr. Mohamed Sellam, and Professor Isabelle Sochet for their valuable contributions to the jury discussions.

I am grateful to the Labex CAPRYSSES framework for funding this thesis and to the two laboratories that hosted my research: the ICARE institute and the PRISME laboratory.

I am deeply thankful to my thesis directors, Dr. Luc Léger and Professor Azeddine Kourta. Working with you has been a pleasure, and I look forward to our future collaborations. A special shout-out to you, Luc! Learning the experimental part by your side was delightful, even when I had to contort myself to fit into the wind tunnel.

Thank you, Nicolas Gouillon, for always being available to assist with every experiment.

I am indebted to Professor Amer Chpoun and Dr. Mohamed Sellam, colleagues at the University of Paris-Saclay Evry, for their significant contributions to this project.

I would like to extend my appreciation to all my colleagues at ICARE and PRISME. I was fortunate to make many friends in both laboratories, making it incredibly hard to mention everyone. Nevertheless, at ICARE, I would like to thank Zahraa, Jean-Noël, Ahlem, Antoine, Melissa, and Bakr for making the PhD adventure more enjoyable with your daily company and encouragement. A special thanks to Etienne Michaux, with whom I have been leading the Aladdin startup project, and to Dr. Stéphane Mazouffre, who has supported us and Aladdin since day one.

At PRISME, I want to thank the PhD students of the Doctorarium and the aerodynamics researchers for their advice. Ahmed, Ernesto, Mathieu, Léo, Mylène, Gaétan, Willy, Marin, Enzo, Roshan, Wassim, Khaled: thank you for always making me feel welcome

and for providing invaluable insights into my research. A heartfelt thanks to our IT wizard, Xavier Michau, and our beloved secretary, Sylvie Plessard.

I am truly grateful to my life partner, Anči, who has been my rock through the good and difficult times of this PhD.

Lastly, I dedicate this work to my family: to my mother, Reinette, who has always been the key figure in my life; to my sisters, Kelly, Karen, Sarah, and Lydia, who have shown unwavering support at every step; and to Thierry, for never failing me in times of need.

The final words are dedicated to those I did not mention. Cheers, everyone! I truly appreciate your solicitude and company, which I hold in high regard.

Thank you...

Brian Legros
May 2024

Abstract

A dual-bell nozzle (DBN) is an altitude adaptive nozzle concept which consists of a conventional nozzle convergent section and a double successive divergent profile. The double divergent section is responsible for the two working modes in a DBN: low-altitude and high-altitude modes, which enhances the overall rocket performance across the flight trajectory. Despite its advantages, the DBN has drawbacks, including early transition between low-altitude and high-altitude modes, leading to sub-optimal performance. Additionally, three-dimensional separation during mode changes allows the generation of side forces. A hysteresis phenomenon causes a difference in nozzle pressure ratios (NPR) during transition and retransition, potentially resulting in buffeting effects under high ambient pressure fluctuations. Nevertheless, the DBN stands among the best candidates for the next generation of launchers as it would provide a substantial payload gain and high reliability due to the absence of moving parts. Therefore, the present thesis tackles the problems specific to the DBN by studying the effect of active flow control on a subscale DBN's performances using annular, radial secondary injection. The study begins with an experimental investigation of the natural transition within a DBN, delving into the analysis of intricate flow structures within its exhaust flow across a broad spectrum of NPR. Then, two DBNs with secondary injection slots are manufactured, one with an injection slot positioned 8mm downstream of the inflexion point and the other with the slot positioned 16mm downstream. The results clearly demonstrate the discernible influence of the secondary injection slot position on the natural transition of the DBN, with a notably pronounced effect during the retransition phases when positioned further downstream. Utilising secondary injection in the DBN was identified as a significant factor in delaying the transition NPR and reducing side forces during shifts in operating modes. These observations were even more accentuated when the secondary injection was performed farther downstream or when the secondary injectant gas exhibited different properties. The series of experimental and numerical test campaigns have permitted to demonstrate the significant influence of secondary injection on the DBN's behaviour and the possibility of dramatically changing its natural behaviour to alleviate its scientific obstacles. The study unveils the optimisation potential of DBNs using the secondary jet flow control method, even for small secondary-to-primary mass flow rate ratios.

Résumé

Une tuyère à double galbe (DBN) est un concept de tuyère adaptative qui se compose d'une section convergente conventionnelle et d'un divergent à double profil. La section divergente double est responsable des deux modes de fonctionnement dans une DBN : les modes basse altitude et haute altitude, améliorant ainsi les performances globales de la fusée sur toute la trajectoire de vol. Cependant, la DBN présente des inconvénients, notamment une transition précoce entre les modes basse et haute altitude, entraînant des performances sous-optimales. De plus, la décollement de la couche limite pendant les changements de régime entraîne la génération de charges latérales. Enfin, un phénomène d'hystérésis entre les taux de détente (NPR) de transition et de retransition est susceptible de générer un effet de "buffeting" sous des fluctuations élevées de la pression ambiante. Toutefois, la DBN figure parmi les meilleurs candidats pour la prochaine génération de lanceurs car elle permettrait de générer un gain substantiel de charge utile avec une fiabilité élevée en raison de l'absence de pièces mobiles. Par conséquent, la thèse actuelle aborde les problèmes spécifiques à la DBN en étudiant l'effet du contrôle actif d'écoulement sur les performances d'une DBN à échelle réduite en utilisant une injection secondaire annulaire radiale. L'étude débute par une exploration expérimentale de la transition naturelle dans une DBN et analyse les structures d'écoulement de sa sortie sur un large spectre de NPR. Ensuite, deux DBNs avec des fentes d'injection secondaire sont fabriquées, l'une avec une fente à 8 mm en aval du point d'inflexion et l'autre à 16 mm en aval. Les résultats mettent en évidence l'influence de la position de la fente d'injection secondaire sur la transition naturelle de la DBN, particulièrement prononcée pendant les phases de retransition avec une fente plus en aval. L'injection secondaire est identifiée comme un facteur clé pour retarder le NPR de transition et réduire les charges latérales lors des changements de régime, effet accentué en cas d'injection plus en aval ou de gaz secondaire aux propriétés différentes. Les résultats de cette étude démontrent l'influence significative de l'injection secondaire sur le comportement de la DBN, offrant ainsi la possibilité de modifier radicalement son comportement naturel pour surmonter les obstacles scientifiques. L'étude met en lumière le potentiel d'optimisation des DBNs grâce à l'utilisation d'un jet secondaire, même avec des faibles rapports de débit d'injection.

Table of contents

List of figures

List of tables

Nomenclature

Roman Symbols

A	surface area
a	speed of sound
a_1	$k\omega - SST$ turbulence model's structure parameter
C_f	skin friction coefficient
C_{fx}	thrust coefficient
c_p	specific heat at constant pressure
c_v	specific heat at constant volume
d_i	injection slot width
e	specific total energy
F_x	thrust
I_{sp}	specific impulse
k	specific turbulent kinetic energy
l'	inflexion region width
M	Mach number
p	pressure
$\dot{q}_j$	heat flux vector
r	ideal gas constant for air

r_{th}	throat radius
T	temperature
t	time
p	velocity vector
V	one dimensional flow velocity
x	axial or Cartesian coordinate

Greek Symbols

α	inflexion angle
δ_{ij}	Kronecker delta
ε	turbulent dissipation rate, nozzle area ratio
γ	specific heat ratio
λ	thermal conductivity
μ	dynamic viscosity
μ_t	turbulent viscosity
ν	kinematic viscosity
ω	specific dissipation rate
ϕ	flow variable
$\overline{\phi}$	average part of a flow variable
$\varphi_{\dot{m}}$	secondary mass flow rate ratio
ϕ'	fluctuating part of a flow variable
ϕ''	Favre fluctuating part of a flow variable
$\tilde{\phi}$	Favre mean of a flow variable
$\mathscr{Q}_i$	total heat flux vector
ρ	fluid density

τ_{ij}	stress tensor
τ_{ij}^{*}	total shear stress tensor
τ_w	wall shear stress

Superscripts

$*$	condition at the nozzle throat

Subscripts

0	stagnation flow condition
b	condition at the base nozzle exit
e	condition at the extension nozzle exit
i	unit vector in x ,y, z direction for i=1, 2, 3
j	unit vector in x, y, z direction for j=1, 2, 3

Other Symbols

$\dot{m}$	mass flow rate
y^{+}	non-dimensional wall distance

Acronyms / Abbreviations

CFD	computational fluid dynamics
CP	constant wall pressure
DBN	dual-bell nozzle
FSS	free shock separation
HASC	high-altitude simulation chamber
HASC	high-altitude simulation chamber
LEO	low earth orbit
MOC	method of characteristics
MUSCL	monotone upstream-centered cchemes for conservation laws

NP	negative pressure gradient
NPR	nozzle pressure ratio
$NPR_{retrans}$	retransition nozzle pressure ratio
NPR_{trans}	transition nozzle pressure ratio
PP	positive pressure gradient
$RANS$	Reynolds-Averaged Navier-Stokes
RSS	restricted shock separation
RST	Reynolds stress tensor
SA	Spalart Allmaras
SPR	secondary pressure ratio
SST	shear stress transport or $k\omega - SST$
$SWBLI$	shock wave boundary layer interaction
TIC	truncated ideal contoured
TOC	thrust optimised contoured
TOP	thrust optimised parabola

General introduction

Rocket nozzle optimisation

The space launch industry is experiencing unprecedented growth and competition, driven by the increasing demand for satellite deployments, and space exploration missions. The global space launch market is witnessing a surge in activity, with both established space agencies and private companies vying for a share of the growing demand for satellite launches and space exploration missions. A Euroconsult report [4] predicts a launch revenue increase by 23%, with 111 billion USD over the next decade, as opposed to 72 billion over the last decade. In this rapidly evolving environment, companies are seeking ways to gain a competitive edge through innovations in rocket technology. Conventional rocket nozzles, while reliable, face limitations in adapting to the varying atmospheric conditions during the launcher's ascent. The challenge resides in optimizing the nozzle for both sea-level and high-altitude conditions while mitigating the risk of lateral forces at low altitudes caused by extreme overexpanded flow within the nozzle. This limitation results in suboptimal nozzle performances, reduced payload capacity, and increased launch costs. Advanced rocket nozzles play a pivotal role in overcoming these challenges by offering altitude adaptive capabilities, thrust vector control, and overall performance enhancement.

Numerous nozzles with altitude-adaptive capabilities were investigated in the past, and a selection of these will be briefly introduced in the following chapter. However, amid the array of adaptive nozzle concepts, two solutions have accumulated substantial interest in recent years: the dual-bell nozzle (DBN) and the aerospike nozzle. Both of these nozzles exhibit superior performance at both low and high altitudes when compared to a conventional rocket nozzle. The aerospike achieves continuous flow adaptation by maintaining contact between the exhaust flow and the ambient air, whereas the DBN, characterised by two successive bell nozzle profiles, likely provides two operational modes: a low-altitude mode and a high-altitude mode. In the context of this thesis, the focus will be solely on investigating the DBN. The versatility inherent in the design of DBNs, allowing for seamless adjustment between two distinct bell profiles, facilitates optimisation for two different altitude regimes. This concept not only yields an overall gain in specific impulse along the flight trajectory but also presents the opportunity for thrust vector control. The latter aspect contributes significantly to enhanced rockets' manoeuvrability, making the DBN a compelling subject for in-depth exploration within the scope of this study.

Nevertheless, the utilisation of the DBN during a launcher's ascent presents three critical challenges: the early transition from the low-altitude mode to the high-altitude mode, the generation of substantial side-loads during the transition process, and a stability issue that could trigger buffeting between the two operating modes, amplifying the risk of dangerous side-loads. Existing studies in the open literature have shed light on the influence of DBN geometry and the operating environment on its behaviour during both the ascent and descent phases, details of which will be discussed in the subsequent chapter. Recent investigations employing active flow control have demonstrated the potential to mitigate these scientific obstacles. These studies revealed a delayed transition during the ascent phase and a reduction in the magnitude of side forces, thus showcasing the promise of active flow control in addressing these challenges.

Context of the study

The potential payload gain achievable with the DBN could lead to a significant enhancement in competitiveness for both companies and state agencies. The present thesis is conducted within the framework of the Labex CAPRYSSES, whose objective is to foster interactions among its expertise areas—chemical kinetics, fluid dynamics, and plasma—to gain a better understanding of their coupling in energy production, propulsion, chemical explosions, and flow control, with the ultimate goal of improving combustion efficiency and aerodynamic performance.

The optimisation of the dual-bell nozzle aligns seamlessly with this framework, and its optimisation through transverse secondary injection in its extension section has yielded promising results, leading to the filing of patents worldwide.

The purpose of this thesis is to showcase the optimisation potential of DBNs by comprehensively exploring the impact of secondary injection on its behaviour in altitude-varying conditions. Building upon a previous study on thrust vector control in a conventional rocket nozzle [3], the current research aims to highlight the optimisation potential of DBNs' performance while ensuring that the secondary to primary mass flow rate ratio remains below 5%.

This study primarily focuses on experimental investigations conducted in the EDITH depressurised wind tunnel at the ICARE Institute of CNRS. To complement these experiments, a preliminary numerical approach is undertaken using steady-state Reynolds-Averaged Navier-

Stokes calculations on the CaSciModOT cluster (Calcul Scientifique et Modélisation Orléans Tours). The comparison between experimental results and numerical simulations aims to advance our understanding of the flow characteristics in DBNs.

Document organisation

The first chapter gives an overview of the studies related to rocket nozzles. The basic working principles of rocket nozzles are exposed, and the focus on the dual-bell nozzle increases as the reader progresses through the chapter. The key features of DBNs are discussed and the motivations for this thesis are presented.

The second chapter describes the experimental and numerical setup at our disposal for the test campaigns. The experimental setup section describes the EDITH wind tunnel facility, and the different means of measurement employed to analyse the test specimens. The numerical setup employed for the simulation campaigns is given.

The third chapter experimentally analyses the behaviour of the smooth DBN, which is not mounted with an injection slot; it is a conventional DBN. The experimental results are used to improve the turbulence model capability to predict flow separation location in the DBN.

Chapter four discusses the effect of the presence of an annular secondary injection slot without operating secondary injection. The study is realised for two distinct injection slot positions: 8 mm and 16 mm downstream of the inflexion point.

Chapter five presents a parametrical investigation of the DBN operating with a secondary injection of air 8 mm downstream of the inflexion point.

The sixth chapter extends the analysis realised in chapter five by performing two test campaigns, the first to study the influence of the secondary injection position in the extension section and the second for the effect of another injectant gas, helium.

A general conclusion is then given which summarises the key findings of this thesis. Perspectives for future work and potential improvements to the experimental and numerical setup are given.

Chapter 1

Literature review

1.1 Historical context

The aerospace industry has been a continuous march of human ingenuity and ambition. Characterised by the exclusive dominion of government space agencies in the past, it has now given way to a new era marked by unprecedented collaboration, technological innovation, and a commercial frenzy for space. Grasping this transformation is crucial to understanding the challenges and opportunities that define the current landscape. In its early years, the aerospace industry was characterised by ambitious visions driven by the space race between international superpowers. The race to conquer the cosmos was triggered in 1957 by the Soviet Union after the successful launch of the first artificial satellite. The United States later emerged as a central player by accomplishing monumental achievements such as the Apollo moon landing in 1969. In that era, government-driven initiatives shaped the aerospace landscape, with space exploration serving as a geopolitical battleground. The scale and complexity of space missions meant that space access was exclusively reserved for government entities with substantial resources. The idea of commercial entities playing a significant role in space pursuits seemed distant, if not improbable.

The turning point came with the gradual decrease of Cold War tensions and the subsequent recognition of private companies to play a significant role in the future of space exploration. The Commercial Space Launch Act of 1984 was a US act that encouraged the development of a commercial space industry, which fostered international cooperation and played a major role in setting a regulatory framework adopted by many other countries. As governments increasingly looked to outsource certain space activities, private companies filled the gap with significantly more agility, a quality often lacking in traditional governmental programs. This shift radically altered the dynamics of the aerospace industry, resulting in democratising space access.

The miniaturisation of electronic components has propelled the rise of CubeSats and SmallSats, opening the path for universities, research institutions, and startups to engage in space activities. This surge in small satellite deployments marked the beginning of a new era where the aerospace industry must adapt rapidly to accommodate the changing landscape. The demand for frequent, cost-effective launches has become the new norm, prompting the need for propulsion systems that can effectively respond to a broad spectrum of mission profiles. Unfortunately, the performances of current rocket nozzles are limited as they fail to adjust to altitude changes during the rocket's ascent through the atmosphere. The threat of substantial side-loads at lower altitudes compels private companies and state agencies to reduce their nozzle expansion ratio, consequently restricting the nozzle's effectiveness at higher altitudes. Numerous studies have explored alternative nozzle concepts with the aim of enhancing the efficiency of rocket nozzles. These concepts will be detailed in a subsequent section. Within the scope of this thesis, the focus is on the examination and optimisation of a subscale dual-bell nozzle to achieve improved performance.

1.2 Conventional Bell Nozzle Limitations

In the contemporary landscape, the imperative for companies and state agencies lies in the reduction of operational costs and the optimisation of launcher efficiency to curtail the overall expense of accessing space. The escalating competition within the aerospace industry has instigated a concerted effort among well-established companies to diminish their service fees. Enhancing a rocket's global efficiency can be achieved through the optimisation of three key parameters: aerodynamics, combustion performance, and nozzle performance. While the aerodynamics of rockets is a well-explored domain, focusing on this aspect yields limited additional gains. Similarly, achieving a substantial increase in combustion cycle efficiency proves challenging, given that current rocket engines are operating close to their theoretical limits. As a result, the rocket nozzle emerges as the most promising area for reducing launch costs, with losses in performance ranging from 0 to 15% due to non-optimized nozzle flow in a conventional rocket nozzle [2]. Rocket nozzles, integral components of launchers, have garnered increasing attention from researchers in recent decades. Today's launchers such as Ariane 5, employ parallel staging, necessitating the ignition of the first-stage engine before liftoff for safety reasons [5]. This arrangement, however, subjects the main stage engine to off-design operating conditions, leading to notable efficiency losses. To unravel the origins of losses incurred during off-design operations, let us derive the equation for nozzle thrust.

1.2.1 Background

A propulsive nozzle functions by converting enthalpy to kinetic energy. In a steady, continuous, inviscid, monodimensional flow without chemical reactions or heat conduction, the Hugoniot theorem (refer to Eq. 1.1) reveals that for subsonic flow $\left(V^2/a^2\right) < 1$, an increase in speed is achieved by decreasing the cross-sectional area, while for supersonic flow $\left(V^2/a^2\right) > 1$, an increase in the cross-sectional area leads to enhanced speed. Consequently, to transition from subsonic to supersonic flow, the cross-sectional area must pass through a minimum value, known as the "throat." The propulsive nozzle is thus composed of a convergent section, facilitating the acceleration of the flow from a subsonic condition to a sonic condition at the throat. Following the throat, there is a divergent section designed to accelerate the flow from a sonic condition to supersonic conditions at the nozzle exit.

$$\frac{dV}{V}\left(1-\frac{V^2}{a^2}\right)+\frac{dA}{A}=0 \tag{1.1}$$

Here, V, A, and a represent the flow velocity, cross-sectional area, and speed of sound, respectively. In an isentropic flow, explicit expressions for flow properties in terms of stagnation conditions can be derived. The static temperature, pressure, and density are written as:

$$\frac{T_0}{T}=\left(1+\frac{\gamma-1}{2}M^2\right) \tag{1.2}$$

$$\frac{P_0}{P}=\left(1+\frac{\gamma-1}{2}M^2\right)^{\frac{\gamma}{\gamma-1}} \tag{1.3}$$

$$\frac{\rho_0}{\rho}=\left(1+\frac{\gamma-1}{2}M^2\right)^{\frac{1}{\gamma-1}} \tag{1.4}$$

M is the Mach number defined as $M = V/a$ and the subscript 0 refers to the stagnation conditions (flow brought at rest isentropically). Using the previous relations and the mass flow rate conservation, we may derive the law of the sections:

$$\frac{A}{A^*}=\left(\frac{2}{\gamma+1}\right)^{\frac{\gamma+1}{2(\gamma-1)}}\frac{1}{M}\left(1+\frac{\gamma-1}{2}M^2\right)^{\frac{\gamma+1}{2(\gamma-1)}} \tag{1.5}$$

Where the superscript '*' refers to the critical conditions at the throat. This relation shows that the local Mach number is only a function of cross-section area ratio $\frac{A}{A^*}$.

1.2.2 Thrust equation and limitations

In a propulsive nozzle, we demonstrate that the thrust F_x can be expressed as:

$$F_x = \dot{m}V_e + (P_e - P_a)A_e \tag{1.6}$$

Where $\dot{m}$, V_e, P_e, P_a and A_e are, respectively, the exhaust gas mass flow rate, the nozzle exit flow velocity, the exit static pressure, the ambient pressure, and the exit area. Deriving Eq. 1.6 with respect to P_e, we demonstrate that the thrust equation reaches a maximum when $P_e = P_a$. In this scenario, the nozzle is considered 'adapted.' However, as the launcher ascends into the atmosphere, the ambient pressure decreases whereas the exit pressure remains constant. These changes in ambient pressure give rise to three distinct operating conditions.

When $P_e < P_a$, the nozzle is considered overexpanded, and the exhaust jet pressure must increase to adjust to the ambient pressure. This adaptation occurs through a shock at the nozzle exit, decreasing the nozzle performance.

In the case of $P_e = P_a$, the adapted exhaust jet exits the nozzle as a cylindrical jet, separated from the ambient air by a slip line. In these conditions, the nozzle operates at its maximal performance.

If $P_e > P_a$, the nozzle flow is underexpanded, and the exhaust jet pressure must decrease to adapt to the ambient conditions. In this configuration, the flow expands at the nozzle lip through a centred expansion fan, radially deviating the flow away from the nozzle axis. The radial flow component does not contribute to the effective thrust, resulting in additional losses. The three configurations are illustrated in Fig. 1.1. Excessive overexpansion poses a potential threat, leading to boundary layer separation within the rocket nozzle. Asymmetric separation introduces significant side-loads, posing a risk to nozzle integrity and potentially resulting in destruction. To mitigate boundary layer separation at lower altitudes, current launchers adopt a reduced nozzle expansion ratio. However, this compromise significantly limits performance at higher altitudes, where important flow expansion is essential for optimal efficiency.

A higher area ratio ε (where $\varepsilon = A_e/A^*$) promises superior vacuum performance but comes at the expense of poor sea-level efficiency, characterised by highly overexpanded flow and internal separation inducing side-loads. Conversely, a lower area ratio offers improved sea-level performance with reduced side-load risks, but at the cost of greatly underexpanded flow at higher altitudes. This longstanding challenge persists, and despite the conventional nozzle's continued use due to its high reliability, extensive efforts have been invested in

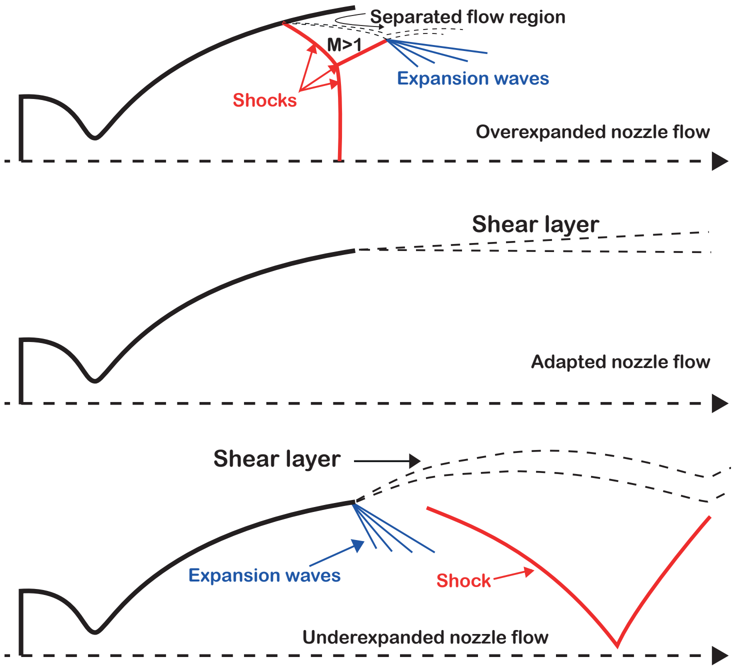

Fig. 1.1 Conventional nozzle operating modes.

researching nozzles with altitude-adaptive capabilities. These endeavours aim to enhance the overall performance of space launchers by addressing the inherent trade-offs in traditional nozzle designs.

1.2.3 Nozzle contour design

Rocket nozzles' divergent profiles can be contoured in various configurations based on the intended objectives. One straightforward design is the conical contour, featuring a conical divergent section [6–9]. This design is particularly suitable for boosters with modest expansion ratios or small thrusters due to its manufacturing simplicity. A commonly accepted compromise for this nozzle type involves a 15° half angle.

An ideal nozzle contour can be designed using the method of characteristics (MOC), resulting in a uniform exit flow. The flow expansion occurs without the formation of internal shocks, necessitating a substantial extension length to attain the designed Mach number. The ideal nozzle is typically utilised in wind tunnels to attain a uniform flow, where the weight of the nozzle is of no significant concern. However, for rocket applications, the impracticality of this concept arises due to the substantial weight associated with the long nozzle. Since the aft part of the nozzle makes only a moderate contribution to thrust, the ideal nozzle is truncated [10, 11]. This truncation leads to a substantial reduction in weight without significantly compromising nozzle thrust. In this scenario, the nozzle is referred to as a truncated ideal contoured nozzle (TIC).

An alternative approach involves determining the exit area and nozzle profile to optimise thrust, referred to as the thrust-optimized contoured nozzle (TOC) or Rao-type nozzle [12, 13]. This contour shares similarities with the TIC but incorporates a higher initial flow expansion and a strong overturning downstream. The significant overturning induces the formation of an internal shock in the divergent section. Despite the similarities, variations in flow structures lead to significant differences in flow separation phenomena in overexpanded conditions.

Rao later introduced a parabolic-geometry approximation to the TOC nozzle [14]. This design, known as the thrust-optimized parabolic nozzle (TOP), produces the nozzle contour using the nozzle throat radius, the nozzle wall angle at the end of the expansion region, the nozzle length, the nozzle exit radius, and the nozzle wall exit angle. This method accurately approximates the TOC nozzle with minimal performance loss. However, the altered flow field in the thrust-optimized parabolic nozzle results in higher exit wall pressure, which proves beneficial in preventing flow separation, especially at sea level.

1.2.4 Side-loads in rocket nozzles

The limitations of conventional rocket nozzles to adapt to altitude changes during the launcher's ascent into the atmosphere force launch operators to reduce the nozzle expansion ratio, preventing boundary layer separation in sea-level conditions. However, flow separation may occur briefly during engine startup on the launch pad. Although considerable efforts have been invested in analysing side-loads in rocket nozzles, a comprehensive understanding and modelling of this phenomenon are still lacking. The investigation of side-loads in rocket nozzles has attracted significant interest [15–19]. Several parameters influence the generation of side forces in rocket nozzles, including an asymmetric separation line, Reynolds number, aeroelastic coupling, external flow instabilities, pressure fluctuations near the separation line, and the transition from free shock separation (FSS) to restricted shock separation (RSS) [1, 20, 21]. Free shock separation, occurring in any type of overexpanded nozzle, involves boundary layer separation inside the nozzle without reattachment downstream of the separation point. On the other hand, RSS occurs in contoured nozzles with internal shocks, where the boundary layer separates from the nozzle wall and reattaches downstream, forming a closed separation bubble. Both separation types induce significant side-loads, yet the mechanisms driving them differ. Pressure fluctuations enhance side-load generation in ideal nozzles, while the transition between FFS and RSS (and vice versa) in contoured nozzles plays a crucial role. Recent studies have delved into the resonant dynamics of a TIC nozzle flow, highlighting that lateral forces were predominantly influenced by tonal jet oscillations

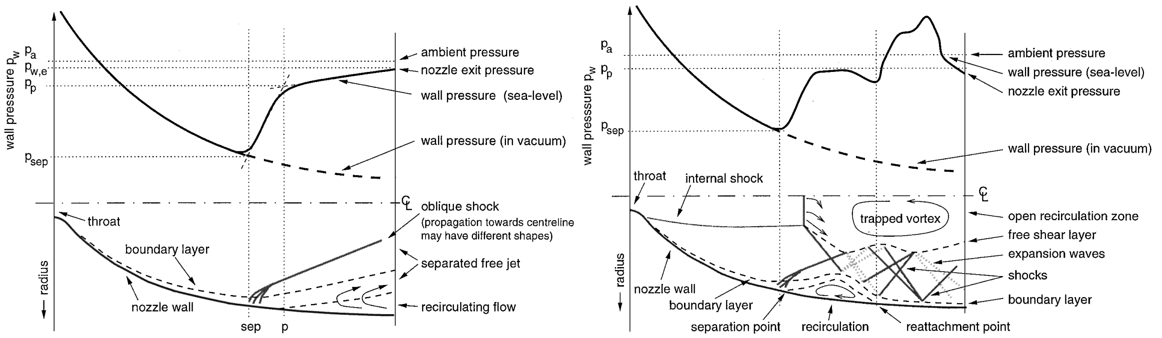

(a) Flow features during FSS.

(b) Flow features during RSS.

Fig. 1.2 Free shock separation (left) and Restricted shock separation (right) sketches from [1].

[22, 23]. The findings indicated that 20% of the side-loads could be attributed to resonant waves, with the remaining 80% attributed to the separation shock movement, itself induced by the resonance.

1.3 Nozzles with altitude adaptive capability

The current section outlines several nozzle concepts with altitude-adaptive capabilities that have been explored in the past and, in some cases, are still subjects of ongoing investigations. Fig. 1.3 shows some of the concepts.

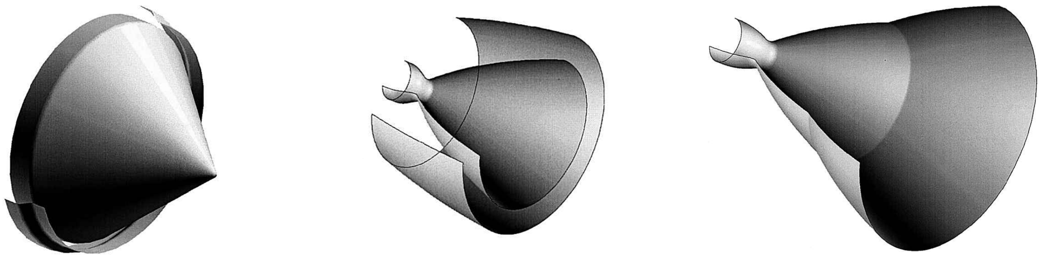

(a) Aerospike

(b) Extendible

(c) Dual-bell

Fig. 1.3 Altitude adaptive nozzle concepts [2].

1.3.1 Aerospike (or Plug) nozzles

Plug nozzles theoretically provide continuous altitude adaption during the launcher's ascent into the atmosphere [24–27]. In contrast to traditional bell nozzles, the plug nozzle is characterised by a central body along which the flow expands, with the outer part of the exhaust jet directly interacting with the ambient air. When operating below the designed NPR, the flow expands along the central body, forming a series of compression and expansion cells that enable the exhaust jet to adapt to the surrounding environment. At or above the design NPR, the pressure along the body wall remains constant, and the exhaust jet expands in a manner similar to a conventional bell nozzle. Various designs are possible for the feeding pressure chamber and nozzle geometry. For instance, the pressure chamber may be toroidal or consist of a cluster of circular or rectangular bell nozzles. The central body design may also range from conical to more intricate configurations, as discussed in [28]. Due to its considerable weight, the plug nozzle is often truncated before its exit. However, this truncation introduces an aspiration effect near the truncation location, potentially impacting performance negatively, as noted in [29, 30]. This underscores the necessity for a careful tradeoff in considering the implementation of the plug nozzle concept.

1.3.2 Pintle nozzles

The pintle nozzle concept has emerged as a response to traditional rocket nozzles' inherent lack of throttling capabilities. This innovative concept incorporates a conventional bell nozzle with the addition of a pintle placed within. A mechanical device facilitates the movement of the pintle in the streamwise direction, thereby altering the nozzle throat area [31]. This dynamic adjustment of the pintle position provides the nozzle with throttling capabilities, enhancing flexibility for various mission requirements. Despite its advantages, the pintle nozzle concept raises valid concerns in several areas. Issues such as system complexity and reliability, the introduction of additional weight, and the effective cooling of the pintle pose challenges that need careful consideration in the implementation of this nozzle design.

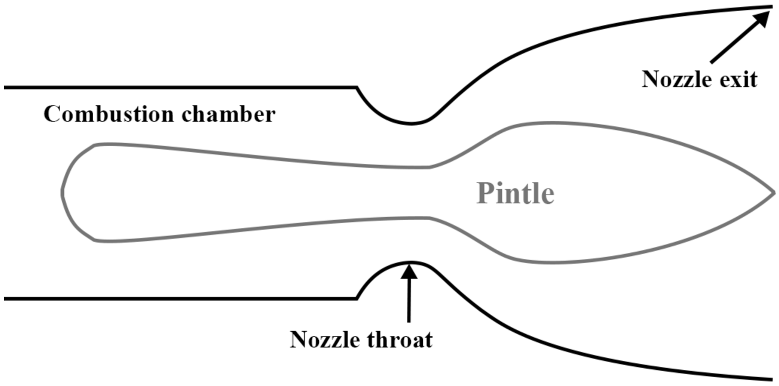

Fig. 1.4 Pintle nozzle.

1.3.3 Dual-throat nozzles

Dual-throat nozzles are made of an inner conventional bell nozzle enclosed within another conventional bell nozzle, each equipped with its own settling chamber to generate distinct flow stagnation conditions [32, 2]. This nozzle design offers dual operating modes: low-altitude and high-altitude modes. During the low-altitude mode, both nozzles operate in parallel. Here, the larger throat radius contributes to a moderate expansion ratio. Conversely, the outer thrust chamber is shut down in the high-altitude mode. This causes the inner flow to expand and attach to the outer nozzle wall, leading to a significantly larger expansion ratio and better vacuum performance.

1.3.4 Dual-expander nozzles

The dual-expander nozzle shares similarities with the dual-throat nozzle, offering two operating modes. It consists of a conventional bell nozzle surrounded by an annular thrust chamber [33, 34]. At low altitudes, the two nozzles operate and share the same exit area, resulting in a modest flow expansion. At high altitudes, the inner thrust chamber is shut down. The external nozzle flow expands fully, resulting in improved vacuum performance. However, significant heat fluxes and pressure oscillations in the inner nozzle may emerge during the high-altitude mode, which could be treated with bleed gas injection [35].

1.3.5 Extendible nozzles

The extendible nozzle concept features a large expansion ratio nozzle divided into two parts [36–39]. At low altitudes, the extension profile is retracted, directing exhaust gas through the first section only for a moderate expansion ratio near sea level. As the rocket

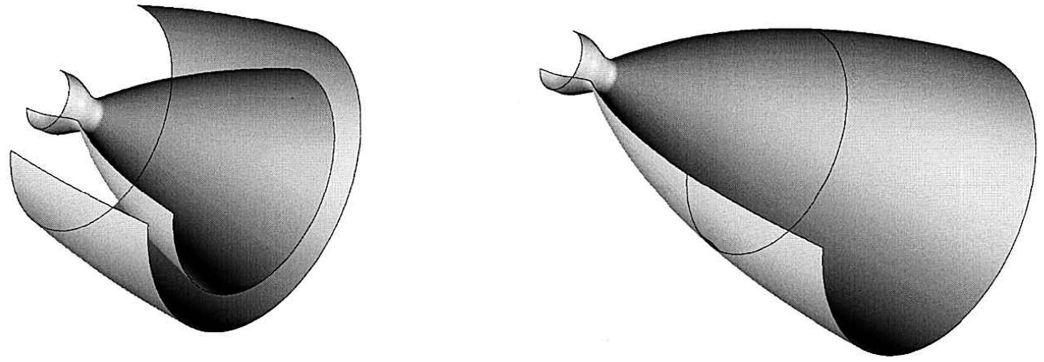

(a) Retracted (b) Deployed

Fig. 1.5 Extendible nozzle in retracted and deployed position [2].

ascends, a mechanical device merges the first profile with the extension profile, enabling expansion through the whole nozzle for improved vacuum performance. Despite providing good and predictable performance, challenges include increased engine mass and reduced reliability due to the mechanical deployment device. Additionally, issues like the cooling of the extension and nozzle vibrations are associated with this concept.

1.3.6 Nozzles with transverse secondary injection

Transverse secondary injection can induce flow separation at specific locations within the nozzle. In the passive secondary injection technique, the nozzle features hole openings to the ambience. At low altitudes, these openings are exposed to the atmosphere, and the higher ambient pressure prompts a flow inside the nozzle, leading to boundary layer separation, a reduced expansion ratio, and consequently improved sea-level performance. As the rocket ascends to higher altitudes, the openings are sealed, allowing the nozzle to fully expand and enhancing vacuum performance. This technique demonstrates performance gains at low NPRs. In contrast, active flow control demands a significant secondary mass flow rate to generate substantial flow separation. This entails incorporating a higher-pressure reservoir on the rocket, making this concept not conceivable for real flight conditions [40–45].

1.3.7 Nozzles with temporary inserts

The concept of nozzles with temporary inserts also offers altitude-adaptive capabilities without the high-altitude losses associated with fixed inserts (see the following section). These inserts may take the form of either ablative or ejectible materials. Ablative methods raise concerns about ablation control and the uncertainty of maintaining symmetrical flow separation. In the ejectible case, the insert may be a nozzle placed inside a larger expansion ratio nozzle. During sea-level mode, exhaust gas flows through the insert nozzle. At the transition point, a mechanical device ejects the insert, allowing the exhaust gas to flow through the larger expansion ratio nozzle. Concerns arise regarding the safety of the ejecting mechanical device, which may generate internal shocks and side loads, or the ejected insert may collide with the larger nozzle. Nevertheless, the feasibility of this concept has been demonstrated in the past [46, 47].

1.3.8 Nozzles with fixed inserts

To achieve a moderate expansion ratio at low altitudes and a large expansion ratio at high altitudes, a trip ring is incorporated into a conventional rocket nozzle. At lower altitudes, the trip ring induces separation of the boundary layer from the nozzle wall, resulting in a moderate expansion ratio [48, 49]. As the rocket ascends into the atmosphere, the ambient pressure decreases, leading to the flow reattachment to the nozzle wall and enabling complete nozzle flow expansion. While large inserts facilitate controlled flow separation in sea-level conditions, they come at the expense of performance loss in vacuum conditions. This concept shares similarities with the DBN concept but is less reliable in terms of transition prediction and more sensitive to high temperatures.

1.3.9 Dual-bell nozzles

The DBN concept comprises a converging/diverging nozzle design. The divergent section is composed of two bell nozzles featuring distinct expansion ratios. The initial bell profile, known as the base nozzle, incorporates a small expansion ratio ε_b to yield better performance at low altitudes while limiting the risk of side loads. The second profile, referred to as the extension nozzle, features a larger expansion ratio $\varepsilon_e > \varepsilon_b$ for better performance in vacuum conditions [50]. The two bell profiles forming the divergent section are linked together through an inflexion point. In sea-level mode, the flow undergoes controlled, symmetric separation from the nozzle wall at the inflexion point, mitigating the risks of lateral forces. As the launcher progresses through the atmosphere, ascending to higher altitudes, the ambient pressure decreases. At a defined point during the ascent, the flow reattaches to the extension wall, causing the separation location to shift at the nozzle exit, providing a larger nozzle expansion ratio. This adjustment enhances vacuum performance at elevated altitudes. The concept is free from cooling issues, doesn't demand any complex mechanical systems, and emerges from a well-established technological configuration (conventional nozzle), positioning it as one of the prime candidates for the next generation of rocket nozzles.

1.4 Dual-bell nozzle: an overview

1.4.1 The origins of the dual-bell nozzle

The dual-bell nozzle concept was initially introduced by Swan [51] in his investigation of step nozzles. Swan's research revealed that integrating a two-step nozzle led to a performance enhancement exceeding 7%. Crucially, his findings indicated that employing more than two steps did not yield a significant increase in performance. This was due to the additional mass introduced by the extra extensions, which outweighed the gains achieved by the nozzle. Two decades later, the DBN concept was patented by Rocketdyne [52], but as of the writing of this thesis, the patent has expired, and the technology is no longer under Rocketdyne's exclusive ownership.

Even though Swan initially highlighted the potential payload gain using step nozzles in the mid-50s and Foster and Cowles [53] acknowledged the concept shortly after, it wasn't until 1993 that the first experimental results using cold flow on DBN were published by Horn and Fisher [50]. In their report, Horn and Fisher documented a substantial 12.1% increase in payload gain to low earth orbit (LEO). The proven ability of dual-bell nozzles to reduce the cost of space access drew increasing global interest, with research in Europe [54–58], Asia [59–61], and Russia [47, 62].

As research on DBN progressed, sophisticated optimisation codes emerged to quantify the financial benefits of this concept [5, 63]. In 2016, numerical studies conducted by Stark et al. at the German Aerospace Center on the main stage of the Ariane 5 launcher, equipped with a Vulcain 2 engine featuring a dual-bell nozzle, showed a payload mass gain into geostationary transfer orbit of 490 kg [5]. More recently, an analysis performed by Ferrero [63] under similar conditions indicated a payload gain of 1.5 metric tons, achieved through an optimised radial secondary injection to control flow separation during the ascent.

Despite the apparent promise and feasibility of implementing DBNs, three primary challenges must be meticulously addressed to make the DBN a viable concept:

- Early transition nozzle pressure ratio (NPR_{trans})
- Side-loads generation
- Nozzle stability

Where the nozzle pressure ratio (NPR) is defined as the ratio between the feeding total pressure P_0 and the ambient pressure P_a.

These issues shall be described in more detail as one progresses through this thesis, aiming to provide a comprehensive understanding of the challenges associated with implementing the dual-bell nozzle concept.

1.4.2 The two operating modes

The DBN consists of a converging/diverging nozzle, featuring a divergent section composed of two successive nozzle profiles with different expansion ratios. Its geometry is illustrated in Fig. 1.6. This distinctive geometrical characteristic enables it to operate in two modes: a low-altitude mode, also known as sea-level mode, and a high-altitude mode. During sea-level mode, the flow is overexpanded and the high ambient pressure compresses the exhaust jet column. In this configuration, the boundary layer separates from the nozzle wall at the inflexion point, providing a controlled and symmetric flow separation. Because the

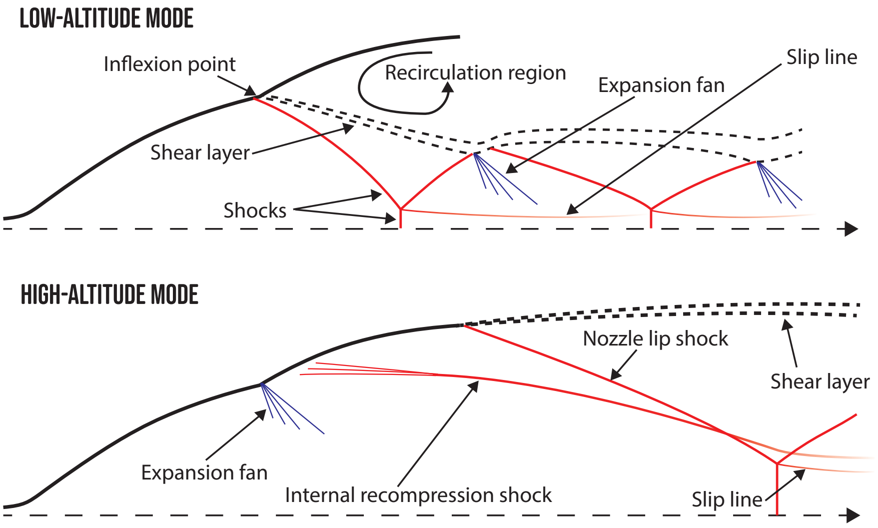

Fig. 1.6 Operating modes in a dual-bell nozzle mounted with a constant pressure extension.

separation occurs at the base nozzle exit, the behaviour of the DBN is comparable to that of a conventional nozzle with an expansion ratio ε_b. The fixed position of the separation front at the inflexion point plays a crucial role in reducing the risk of side-loads.
As the launcher ascends into the atmosphere, the ambient pressure decreases and the flow will eventually reattach the extension nozzle wall. During this process, known as transition, the flow expands through an expansion fan at the inflexion point and the separation front moves from the inflexion point to the nozzle exit. The increased expansion and the larger exit area naturally yield better performance at high altitudes. In the high-altitude mode, the behaviour of the DBN is comparable to that of a conventional nozzle with a high expansion ratio ε_e.
The transition from the low-altitude mode to the high-altitude mode is commonly referred to as **transition**, and inversely, the switch from the high-altitude mode to the low-altitude mode is called **retransition**. The behaviour of the DBN significantly varies depending on the contour design. In the following section, we will explore design considerations crucial for achieving the desired behaviour of the DBN.

1.4.3 Design considerations

The contour design of the DBN is of critical importance for its behaviour. The base nozzle and the extension nozzle may be designed independently, giving a wide range of DBN flow considerations. To simplify the DBN flow, the base profile is often designed as an ideal contour. The expansion ratio is chosen for obtaining an overexpanded nozzle at sea-level. The ideal contour profile has the advantage of not inducing internal shock waves in the flow as is the case for optimised contours. At the base nozzle exit lies an inflexion point. The greater the inflexion angle α, the higher the transition NPR. The extension section design plays the most important part in the DBN behaviour [64, 65]. Three options are available for the extension design. The streamwise wall pressure either decreases, remains constant, or increases. In the literature, these three configurations are referred to as negative pressure gradient (NP), constant wall pressure (CP), and positive wall pressure gradient (PP) extensions. Starting from the low-altitude mode, an increase in NPR brings the DBN to the transition process. The separation in a rocket nozzle is determined by the ratio $P_{sep}/P_a = f(M)$. At any given position in the nozzle, there exists a separation nozzle pressure ratio NPR_{sep} for which the boundary layer separates from the wall. NPR_{sep} is expressed as:

$$NPR_{sep} = \frac{P_0}{P_{a,trans}} \tag{1.7}$$

Which is also written:

$$NPR_{sep} = \frac{P_0}{P_w} \cdot \frac{P_{sep}}{P_a} \tag{1.8}$$

And becomes after using the Stark separation criterion [21]:

$$NPR_{sep} = \frac{P_0}{P_w} \cdot \frac{1}{M_{sep}} \tag{1.9}$$

The streamwise pressure distribution and Mach number are constant in a CP extension profile. Consequently, when the ambient pressure decreases and the transition begins, if the NPR_{sep} is reached at the entrance of the extension profile, it is also reached throughout the extension section. In this configuration, the separation front suddenly moves from the inflexion point to the nozzle exit, providing a fast transition from low-altitude to high-altitude mode.

In the PP extension configuration, the separation criterion first intersects with the wall pressure profile at the extension exit. However, the actual transition takes place only when the separation criterion is satisfied at the inflexion region. Once this condition is met, and as it has already been fulfilled downstream of the extension entrance, there is a sudden movement of the separation front from the inflexion point to the nozzle exit, resulting in an abrupt transition.

In the NP extension profile, the separation front remains at the inflexion point until the separation criterion is satisfied at the entrance of the extension section, at which point the separation front moves in the extension section. A continuous (no sudden) movement of the separation front throughout the nozzle driven by the negative pressure gradient nature of the extension section is observed as in conventional bell nozzles. The substantial risk of high side-loads resulting from this progressive movement makes this option impractical and unsuitable for DBNs [66].

1.4.4 Natural transition in dual-bell nozzles

The simplicity of the DBN concept, which offers two altitude functioning modes without the need for any moving parts, represents a significant advancement that has the potential to reduce the cost of access to space for companies. However, despite its promise, several challenges must be addressed before considering the integration of DBN on rocket launchers. The natural transition in DBNs is characterised by two stages: the sneak transition and the 'main' transition. The sneak transition involves the movement of the separation front from the inflexion point to the location of minimum wall pressure. Subsequently, the main transition is the movement of the separation front from the minimum wall pressure location to the nozzle exit [67]. In both phases, a swift transition is crucial to mitigate the risk of unsteady, asymmetrical flow separation within the nozzle and to prevent hazardous lateral forces. The extensive test campaign at DLR to analyse flow separation characteristics in a dual-bell nozzle [67] led the authors to suggest a rapid increase in feeding total pressure variation ($\delta P_0/\delta t$) to minimise the risk of side loads during the transition. This recommendation is based on experimental results indicating that an increase in feeding total pressure variation leads to a decrease in the amplitude of pressure fluctuations associated with the separated shock near the wall inflexion point.

One of the key issues with the DBN is the early transition, characterised by the transition occurring before the optimum transition point, which results in significant losses (refer to Fig. 1.7). The additional mass associated with the presence of an extension section needs to be compensated by optimal DBN performance during rocket launches. This necessitates finding solutions to delay the natural early transition and to ensure efficient operation.

As mentioned in the previous section, the natural transition varies depending on the geometry of the extension profile. With a NP extension profile, the separation location depended on the nozzle pressure ratio and was well predicted by flow separation criteria such as Schmucker's criterion [68–70]. No sudden transition from the inflexion point to the nozzle exit was observed, as the separation location progressively shifted towards the extension. Consequently, the uncontrolled yet stable separation front, coupled with the unsteadiness of the shock wave boundary layer interaction (SWBLI), may give rise to significant side-loads [50, 58, 68, 66].

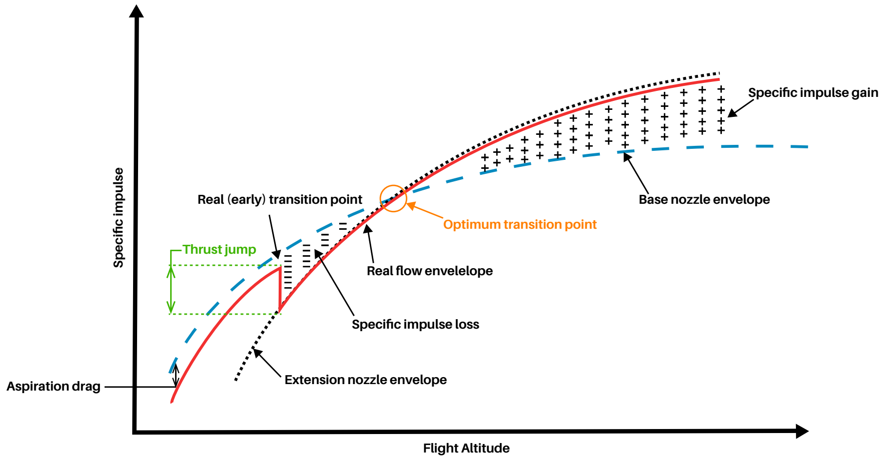

Fig. 1.7 Drawing of the specific impulse as a function of flight altitude for conventional bell nozzle and the DBN.

With PP and CP extension profiles, experimental [58] and numerical [71] observations revealed a sudden transition. As the NPR increases from the low altitude mode, the separation continuously advances through the base nozzle until it freezes at the inflexion point. When the NPR_{trans} is reached, the separation rapidly jumps to the nozzle exit. The separation point's rapid movement limits the risk of lateral forces, which may be detrimental to the rocket integrity during the operating mode changes [50, 72, 58, 68, 73–75].

PP extension profiles provide a higher NPR_{trans} whose values depend on the type of pressure gradient inside the extension. Numerical simulations were carried out in [64] to investigate three extension configurations: 1) a PP extension with a linearly increasing wall pressure, 2) a PP extension with a parabolically increasing wall pressure, and 3) a CP extension. The study showed a higher NPR_{trans} for the parabolically increasing wall pressure gradient configuration compared to the linearly increasing one, with the CP exhibiting the lowest NPR_{trans}. The study also demonstrated that the pressure profile along the extension could suffer from oscillations depending on the interpolation used to design the CP extension. The PP profiles also showed a shorter main transition time than the CP profile, suggesting a lower risk of side forces. However, the CP configuration exhibited a higher gain in thrust coefficient compared to the other PP extension types. The extension length also plays an important role on DBN's behaviour. Reducing the extension length decreases the lever arm, consequently lowering the magnitude of side-loads. However, this reduction in extension length comes at a cost—it diminishes the stability of the DBN, leading to a smaller hysteresis [1] and an increase in the total duration of transition. This, in turn, elevates the potential risk for side-loads, as noted in [74].

---

[1] The hysteresis is defined as $100 \cdot (NPR_{trans} - NPR_{retrans})/NPR_{trans}$

Given the launcher's ascent, which induces relatively high-pressure fluctuations — approaching 20% of the ambient pressure — stability concerns persist for the DBN concept. In a comprehensive study conducted in 2014 [76], the impact of ambient pressure fluctuations on transition behaviour was investigated. The study revealed the presence of a flip-flop phenomenon beyond a certain magnitude of ambient pressure fluctuation. This flip-flop corresponds to an unsteady movement of the separation front between the inflexion point and the nozzle exit, significantly heightening the risk of lateral forces as transition and re-transition nozzle pressure ratios are approached. Other experimental and numerical analyses have delved into the influence of ambient pressure fluctuations on DBN modes. These investigations uncovered characteristic frequencies at which the separation location would shift from the inflexion point to the nozzle exit, triggering early transition. Furthermore, hazardous vibrations could originate from radial acoustic resonance in the separated flow [77, 78].

The transition and retransition processes in DBNs are influenced by numerous parameters, still under investigation. These parameters include the Reynolds number, testing environment, nozzle geometry, ambient pressure fluctuations, and temperature [79–81, 75, 82, 83].

Testing environment [67, 84] and boundary layer condition (laminar or turbulent) [85] were identified as key parameters capable of changing the features of transition and re-transition processes in DBNs. Both of these parameters are related to the Reynolds number in the flow which will be discussed in the next section.

1.4.5 Reynolds number influence on dual-bell nozzle transition

Numerous studies in the literature have been conducted under sea-level conditions ($P_a = 1$ bar), with variations in the nozzle pressure ratio achieved by adjusting the feeding total pressure [86]. During a real flight test, the feeding total pressure is constant, and the ambient pressure varies. When the ambient pressure is held constant, the change in NPR requires adjusting the stagnation pressure P_0. Yet, any change in stagnation pressure affects the fluid flow parameters, inducing a different flow in the nozzle. An experimental investigation [87] addressed the effects of the Reynolds number on the DBN's behaviour. Tests were conducted under ambient conditions and within a high-altitude simulation chamber (HASC). In the former configuration, ambient pressure remains constant, and the NPR varies by adjusting stagnation pressure, consequently altering the Reynolds number during the experiment. In the HASC, stagnation pressure remains constant, while ambient pressure is changed. Various tests utilising different stagnation pressures in the HASC showed that reducing the Reynolds number results in an increased NPR_{trans}. A lower Reynolds number induces a thicker boundary layer, resulting in a larger inflexion region width l' and a less steep negative pressure gradient. The width of the inflexion region is defined by the length measured from the inflexion point to the minimum pressure location in the inflexion region [64]. The larger inflexion region width at low Reynolds numbers also comes with a boundary layer located in the inflexion region for a longer period of time, favouring the increase of NPR_{trans} [81, 87, 88]. The dependence of transition behaviour on Reynolds number was also supported in other studies [89, 90, 85].

1.4.6 Flow control in dual-bell nozzles

Flow control in rocket nozzles has been extensively studied for various purposes, such as preventing flow separation in over-expanded nozzles at low altitudes, thrust vector control, and side-loads reduction [91, 3, 45, 92, 93]. For DBNs, researchers have primarily explored flow control through the injection of a secondary flow in the vicinity of the inflexion point. Two main methods have been employed: secondary injection parallel to the mainstream, commonly used for film cooling and secondary injection in the perpendicular direction of the mainstream flow. However, the film cooling technique has shown limited impact on addressing the three major challenges faced by DBNs: early transition, side-loads, and stability. A 2009 study observed the potential to lower wall temperatures but at the expense of enduring lateral forces [94]. Numerical simulations indicated a decrease in transition NPR with varying mixture ratios and secondary injection mass flow rates [95]. Conversely, the transition NPR increased with operating film cooling in [96]. The latter study also reported a reduction in thrust jump during transition phases and lower side-loads.

Annular, radial fluidic secondary injection has been the subject of past investigations. Tomita et al. (2009) conducted a cold flow test on a DBN equipped with a PP extension operating with secondary injection at the inflexion point [97]. The experiment revealed that secondary injection decreased the transition NPR, thereby increasing the gap toward the optimum transition point.

The latest experimental test campaigns, conducted at the ICARE Institute of CNRS on a DBN equipped with a CP extension, demonstrated a notable and positive impact of secondary injection on a subscale DBN's behaviour when the injection was positioned downstream of the inflexion point (in the extension section) [82, 98]. In this case, the transition NPR was increased, and side-loads were reduced during changes in operating modes. The positive effect of secondary injection was distinctly observed, even for relatively modest secondary-to-primary mass flow rates (less than 1%). The experiments also indicated the influence of secondary injection on the DBN's stability with a modified hysteresis [99].

These preliminary studies demonstrated the possibility of improving DBN performance by employing annular, radial secondary injection downstream of the inflexion point. However, optimisation of the control method, considering factors such as secondary injection pressure, injection location, or injectant gas, is still lacking. The present thesis aims to provide a more thorough investigation of this control method by exploring the influence of the aforementioned factors on the behaviour of a subscale DBN.

Chapter 2

Experimental and numerical setup

2.1 Experimental setup

2.1.1 Subscale test nozzles

Three subscale dual-bell nozzles were manufactured to perform the investigations presented in this thesis:

- A "smooth" DBN (conventional DBN without a secondary injection slot)
- A DBN with a secondary injection slot located 8 mm downstream of the inflexion point
- A DBN with a secondary injection slot located 16 mm downstream of the inflexion point.

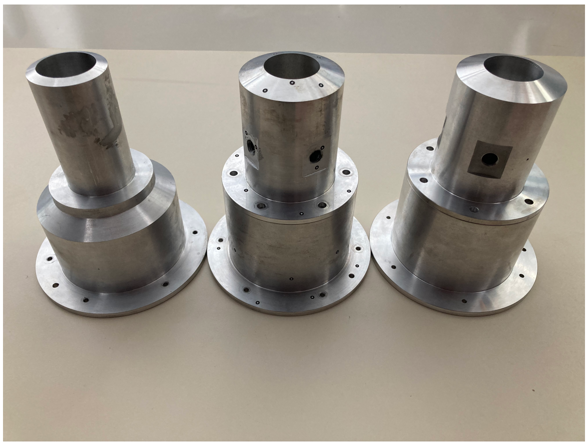

Fig. 2.1 Subscale DBN models: Smooth, injection 8 mm, and injection 16 mm (from left to right)

The nozzles were designed using the inverse method of characteristics. In this method, the base profile coordinates are obtained by finding the point on a characteristic line which satisfies, on a fictional wall, the same mass flow rate as at the nozzle throat. This iterative process yielded an error of $4.1 \cdot 10^{-3}\%$. Another MOC-based code generated the extension profile downstream of the Prandtl-Meyer expansion issued by the 8 deg inflexion angle.

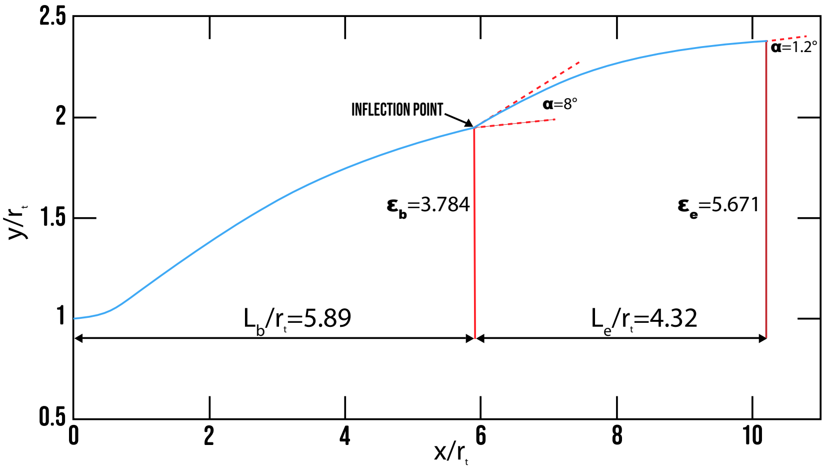

Fig. 2.2 DBN divergent profile with geometrical details.

Excluding the presence of the secondary injection slot, the three profiles are identical. The base nozzle was designed as an ideal contour for an exit Mach number of three and was truncated at a wall Mach number M_b of 2.76. The extension nozzle was built as a constant pressure extension profile for an exit Mach number M_e of 3.17 after the expansion at the inflexion point.

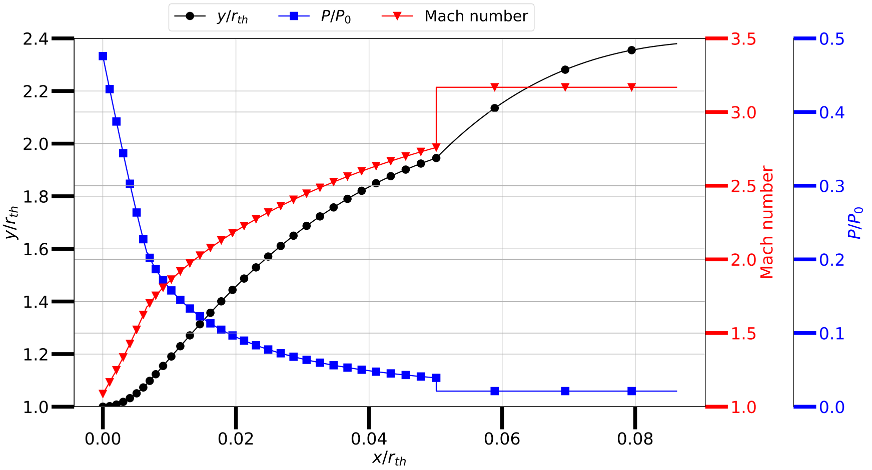

Fig. 2.3 DBN divergent profile with theoretical wall pressure and Mach number distribution.

The transition NPR estimated from the Stark criterion [100] amounted to 14.89. Figures 2.2 and 2.3 present the geometrical details of the DBN, along with the theoretical Mach number and normalised wall pressure distribution. When active flow control is performed, a secondary flow is radially injected into the DBN's extension section through an annular slot. In this thesis, two secondary injectant gases are experimented: air and helium. This active flow control technique directly affects the DBN's behaviour during the transition and retransition phases. Manufacturing the DBN in two parts allowed for the presence of the 0.2 mm width secondary injection slot. The secondary injection slot was positioned 8 mm (or $0.94 \cdot r_{th}$) downstream of the inflexion point in the first nozzle (DBNi8), and 16 mm (or $1.88 \cdot r_{th}$) in the second one (DBNi16).

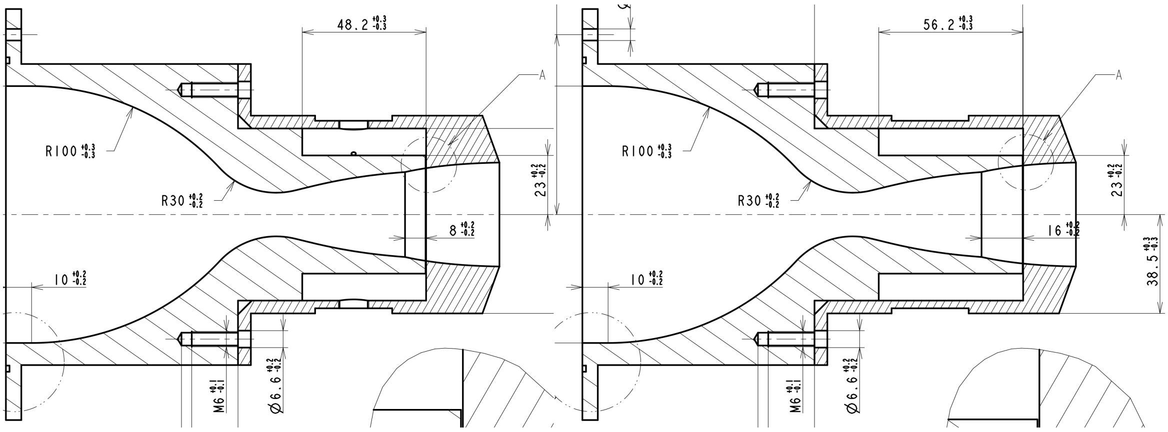

Fig. 2.4 Cross-section view of the DBNi8 (left) and the DBNi16 (right).

This technique also allowed for the presence of a settling chamber to set the stagnation conditions of the secondary jet. The secondary injection settling chamber is referred to as the **cavity** throughout this thesis and it is visible on the DBNi8 and DBNi16 cross-section views in Fig. 2.4. The complete cross-section views are available in Appendix B. The cavity and the annular secondary injection slot presence provided an axisymmetric, homogeneous secondary injection. The DBNs' parameters are summarised in Table 2.1.

Table 2.1 DBN parameters

Parameter	Value
Throat radius	$r_{th} = 0.0085$ m
Base nozzle geometry	Length: $l_b/r_{th} = 5.89$
	Expansion ratio: $\varepsilon_b = 3.78$
Extension nozzle geometry	Length: $l_e/r_{th} = 4.32$
	Expansion ratio: $\varepsilon_e = 5.67$
Inflection angle	$\alpha = 8$ deg
Injection slot	Width: $d_i/r_{th} = 0.024$
	Location: $\{0.94; 1.88\} \cdot r_{th}$ downstream inflexion
Design NPR_{trans} (Stark's criterion)	$NPR_{trans} = 14.89$

2.1.2 Test facility

The experimental test campaigns were conducted at the FAST (Facilities for Aerothermodynamics and Supersonic Technologies) platform of the ICARE Institute of CNRS. The experiments were performed in the EDITH wind tunnel, a former continuous-operation Mach 5 wind tunnel to study supersonic and hypersonic flows. EDITH has since been adapted into a blow-down wind tunnel offering nozzle test measurements in a depressurised environment.

(a) Pumping group. (b) EDITH wind tunnel facility.

After being dried and cleaned by a Bauer Mini Verticus3 compressor, the ambient air is compressed to 30,000 kPa and supplied to the main valve and the pressure regulator via an 8 mm diameter pipeline. The pressure regulator adjusts the pressure to 600 kPa, and a manual valve downstream regulates the mainstream stagnation pressure to 350 kPa before being injected through six 10 mm radially distributed pipes. Then, the air travels through the dual-bell nozzle and exits in the depressurised wind tunnel test section. The pressure inside the test section is controlled by a butterfly-type valve upstream of an overall 345 kW MPR pumping group in the wind tunnel diffuser.

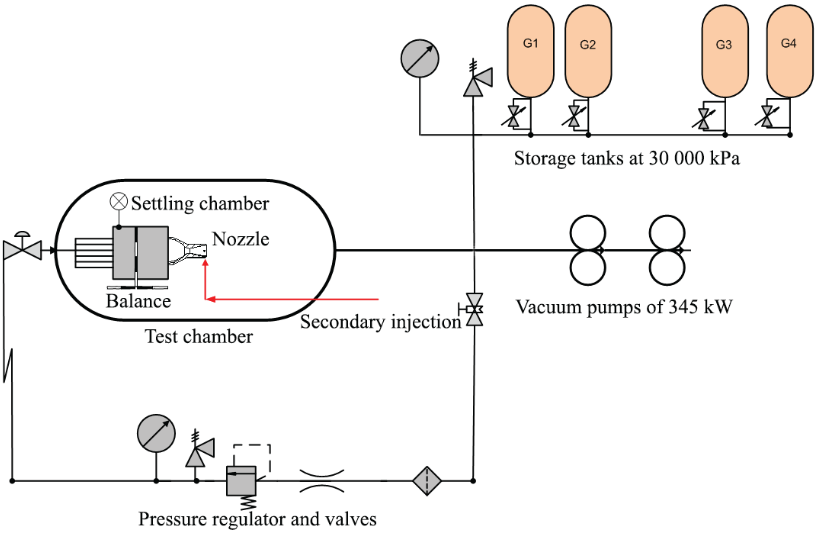

Fig. 2.6 EDITH wind tunnel operation scheme [3].

During the experiments, the mainstream feeding total pressure is kept constant. In contrast, the ambient pressure in the wind tunnel test section is repetitively increased and decreased between NPR $\approx$ 11.67 and NPR $\approx$ 50 to trigger the transition and retransition phases. For experiments involving active flow control with transverse secondary injection, the cavity is fed from a secondary pressure line connected to the 600 kPa laboratory compressed air reservoir or compressed helium bottles. Before entering the cavity, the secondary feeding pressure is regulated, and the flow is split into four secondary injection pipes connected symmetrically to the cavity's outer wall. Table 2.2 summarises the information relative to the experimental setup.

Table 2.2 Experimental environment parameters

Experimental environment	Value
Reservoir	Pressure: $P_{reservoir}$ = 30,000 kPa
	Volume: $V_{reservoir}$ = 320 l
Settling chamber	Pressure: P_0 = 350 kPa
Wind tunnel test section	Height: H_{WT} = 1200 mm
	Length: L_{WT} = 1700 mm
Pumping group	Power: P_{pumps} = 345 kW
Secondary feeding line	Pressure: P_i = 600 kPa

2.1.3 Qualitative flow analysis

In such challenging experimental conditions, where very few non-intrusive measurements can be made, observing the flow features in the nozzle exhaust plume provides critical information on the DBN working modes. Therefore, a monochromatic z-type schlieren imaging technique was set up to visualise the jet structure. The schlieren technique is based on the change in refraction index in a translucent homogeneous medium. In this technique, a parallel beam of light crosses the subject (in this case, the nozzle exhaust jet) and is then focused on a sharp edge using lenses or mirrors. A density change in the subject induces a change in the refraction index and a deviation of the parallel beam of light above or below the sharp edge. The deviated light creates brighter or darker zones on the final image, indicating where the density change occurred. In the present thesis, the Lamp GHD light source issues the light beam. The beam goes through a horizontal slit and is reflected by the 300 mm diameter parabolic mirror used to collimate the light. The parallel beam crosses the wind tunnel through treated glass windows before being decollimated on the opposite side by a second identical parabolic mirror. For feasibility reasons, the beam of light issued by the second parabolic mirror is reflected onto a planar mirror, after which the beam is cut by a sharp razor edge located at the focal point. Then, the beam crosses a collecting lens to project the image directly onto the Canon EOS60D sensor, recording images at 50Hz.

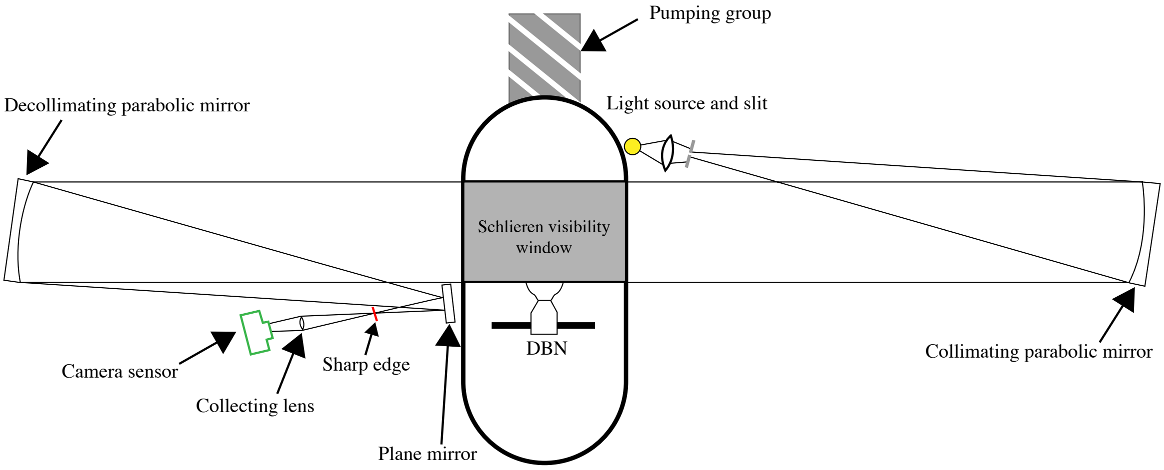

Fig. 2.7 Schlieren imaging setup.

Because the recorded video is not synchronised with the quantitative measurement techniques (see section below), an in-house Python program re-synchronises the schlieren images to the quantitative measurements during post-processing. The re-synchronisation does not allow for the exact matching of the data but provides a fairly good agreement regarding the DBN's working mode and the associated measured parameters.

2.1.4 Quantitative flow analysis

In addition to the flow features obtained from the schlieren system, several quantitative measurements were made during the experiments. The measurement tools used during the experiments depended on the test specimen under investigation (smooth DBN, DBNi8, or DBNi16). Nonetheless, they can be categorised into: 1) Stagnation condition measurements, 2) Wall pressure measurements, and 3) Force measurements.

Stagnation conditions measurements

In every configuration studied, the stagnation pressure and temperature of the DBN mainstream flow were measured using an Omega 100 to 700 kPa range pressure transducer and a type-K thermocouple. When a nozzle with a secondary injection slot was operated (with or without secondary injection), the stagnation pressure (or static pressure if no injection) inside the cavity was measured using a Kulite XCQ-062 pressure transducers with a range of 0–100 kPa. For secondary injection pressures above 88 kPa, the pressure transducer inside the cavity was replaced by a Kulite XCQ-093 with a 0–350 kPa range. The ambient pressure in the wind tunnel test section was measured using a Kulite XCQ-062 pressure transducer with a 0–100 kPa range. For all pressure measurements, a LabView program was used to convert the voltage measurements into pressure values and to record the data at 1000 Hz.

Wall pressure measurements

The wall pressure distribution was only measured in the smooth DBN configuration. A series of 6 Kulites XCQ-062 fast pressure transducers with a range of 0–100 kPa was positioned in the DBN divergent section. The sensors' location ranges from $0.27 \cdot r_{th}$ upstream of the inflexion point to $3.44 \cdot r_{th}$ downstream of the inflexion point (corresponding to $\approx 80\%$ of the extension length). Table 2.3 summarises the sensors' location and Fig. 2.8 shows their position in the DBN.

Table 2.3 Pressure sensors' location (from the nozzle throat and the inflexion point) and position of the sensors in terms of percentage of the extension length.

Sensor	1	2	3	4	5	6
x_p/r_{th} (from throat)	5.63	6.10	6.69	7.57	8.45	9.33
x_p/r_{th} (from inflexion)	-0.27	0.20	0.79	1.68	2.56	3.44
x_p/l_e (from inflexion) [%]	-6.16	4.73	18.35	38.77	59.20	79.62

To minimise the impact of sensors on the nozzle flow, two different hole sizes were employed for the pressure sensors. The initial larger hole (1.7 mm in diameter) facilitates the insertion of the pressure transducer through the outer nozzle wall. Then, the hole size is reduced to 0.5 mm in diameter to extend to the inner nozzle wall, ensuring minimal intrusion while measuring wall pressure. The Kulites were fixed using silicon to ensure good impermeability. The pressure signals are amplified via an amplifier to the computer. For feasibility reasons, such measurements could not be performed in the DBNs containing an injection slot. In such case, the Kulites would have to cross the external cavity wall, the cavity volume, and the DBN wall which would have resulted in their destruction during retrieval.

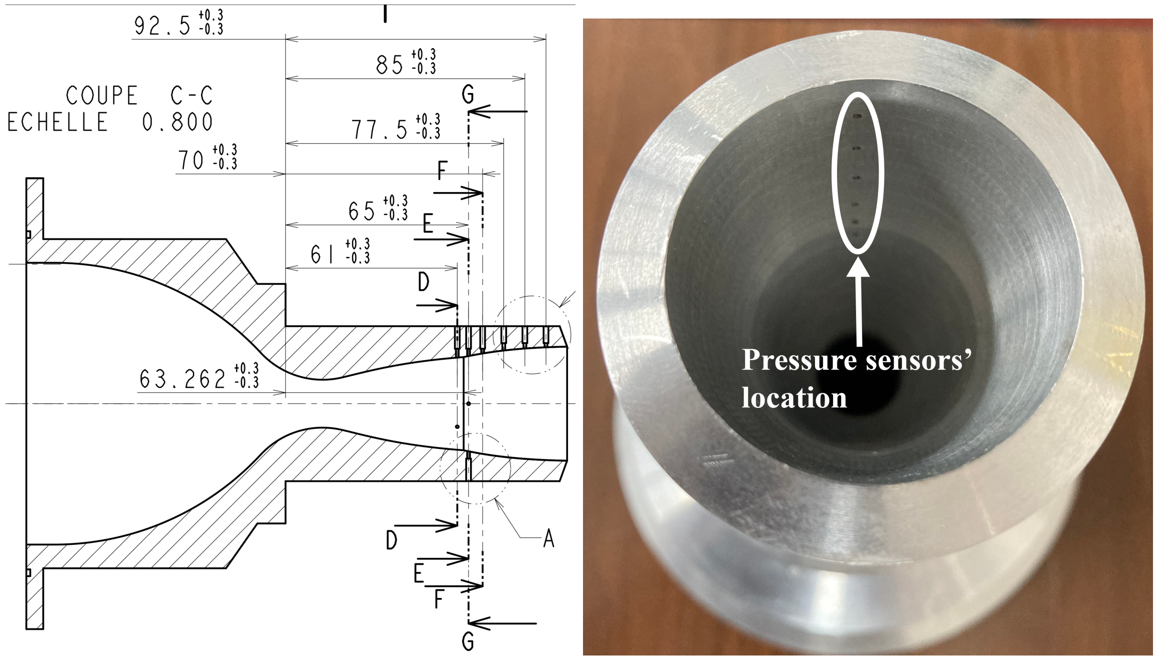

Fig. 2.8 Pressure sensors location in the smooth DBN.

Force balance

The dual-bell nozzle is mounted on a force balance designed by the authors in [3]. The force balance allows free movement along the (x,y,z) orthogonal axis through frictionless Bosh-Rexroth slide bearings. It measures the thrust and lateral forces using four HBM S2 strain-gauge force transducers, providing high-accuracy measurement with an accuracy class of 0.05. The transducers' signals are amplified to a 0-10 V range by an HBM RM4220 amplifier before being acquired by the SCXI-1140 cards at 1000 Hz. Two transducers of a nominal range of 0-200 N located on both sides of the force balance were used to measure the vertical force component; one 0-200 N range transducer measured the nozzle thrust; and a 0-20 N transducer measured the lateral forces. Previous studies for the validation of the force balance measurements showed a 0.24 N standard deviation for the force measurements on the longitudinal axis, 0.06 N on the vertical axis and 0.17 N on the lateral axis. The force measurements were recorded by the LabView program at a frequency of 1000 Hz along with the other parameters mentioned in the previous subsections.

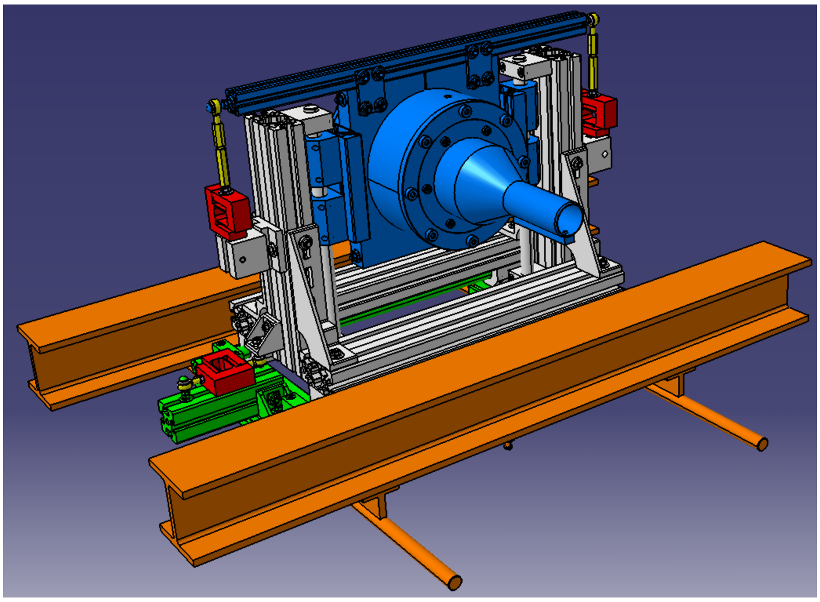

Fig. 2.9 Numerical view of the force balance.

2.2 Numerical setup

2.2.1 Geometry and computational domain

Smooth nozzle configuration

The study focuses on the supersonic flow inside a dual-bell nozzle. The nozzle convergent was considered in the simulations to allow for a fully developed boundary layer profile in the divergent section. A two-dimensional axisymmetric model was assumed. It is worth mentioning that the flow features involved in dual-bell nozzles are highly three-dimensional. However, the 2D steady approach represents an easy, cost-effective option before performing more challenging numerical work. The full computational domain (dual-bell nozzle + wind tunnel) was generated using the design modeller of the commercial software ANSYS Workbench 2022 R2, and it is displayed in Figure 2.10.

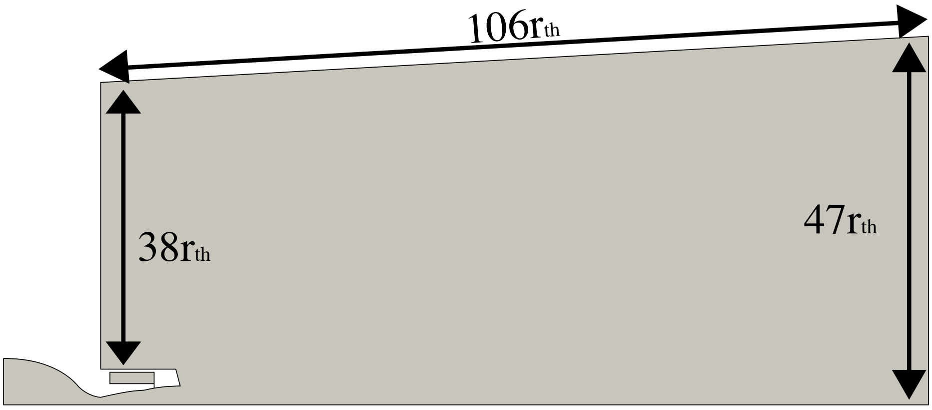

Fig. 2.10 DBN numerical computational domain.

The origin of the coordinate system was placed at the nozzle throat, on the symmetry axis. The convergent inlet was set as a 350 kPa pressure inlet with a stagnation temperature of 290 K and a turbulence intensity of 5%. The EDITH wind tunnel boundaries were considered as pressure outlets of fixed values, which ranged between 30 kPa to 7 kPa (NPR = 11.67 to 50). A static temperature of 290 K and a turbulence intensity of 5% were assumed at the wind tunnel boundaries. Non-slip conditions were applied on the DBN internal and external walls.

Injection nozzle configuration

Only two DBNs were studied numerically: the smooth DBN and the DBNi8. To take into account the presence of the cavity and the injection slot, the initial smooth DBN geometry was modified. The cavity's presence, as in the experimental DBN, induced a thicker nozzle lip and therefore a change of the computational domain in the vicinity of the outer nozzle wall. The difference between the smooth DBN and DBNi8 is shown in Fig. 2.11.

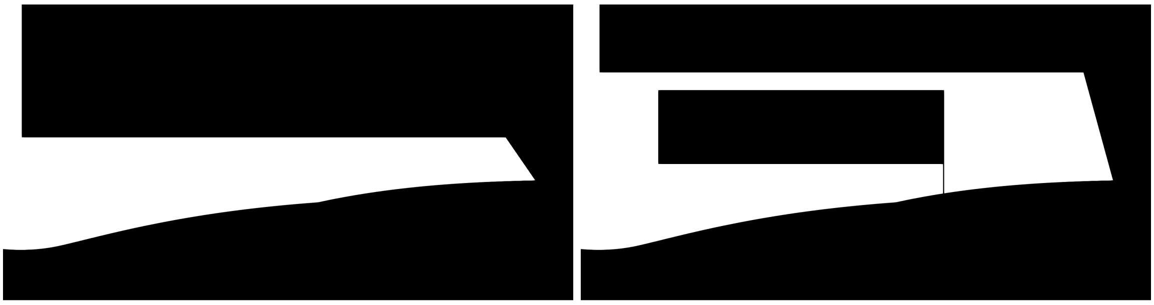

(a) Smooth DBN computational domain. (b) DBNi8 computational domain.

Fig. 2.11 Smooth DBN and DBNi8 computational domains.

2.2.2 Grid description

A structured mesh type composed of 1,544,300 hexahedral cells was adopted for the present study and the mesh was generated with the commercial software ANSYS MESHING. The final mesh used in the smooth DBN study (grid D) was obtained following a mesh sensitivity analysis. Table 2.4 summarises the different grid sizes which range from roughly 250,000 to 1,800,000. The results from the mesh sensitivity analysis are given in Appendix A.

Table 2.4 Mesh sizes information

Grid	A	B	C	D	E
Number of cells	250770	498200	1005950	1544300	1835300

The large volume cells were located in the bulk flow area, close to the nozzle symmetry axis before gradually refining towards the nozzle wall to resolve the boundary layer.
Generating the meshes with a first cell height of $2.3 \cdot^{-6}$ m at the nozzle wall outlet resulted in y^+ values near unity along the wall. The streamwise y^+ distribution and the boundary layer profiles according to different similarity transformations [101, 102] at x/r_{th} = 5.36 (in the base nozzle) and NPR = 50 are displayed in Fig. 2.13. The grid was kept relatively fine downstream of the nozzle exit to capture the shear layer of the exhaust jet. The cells' size was set to increase towards the wind tunnel boundaries progressively.

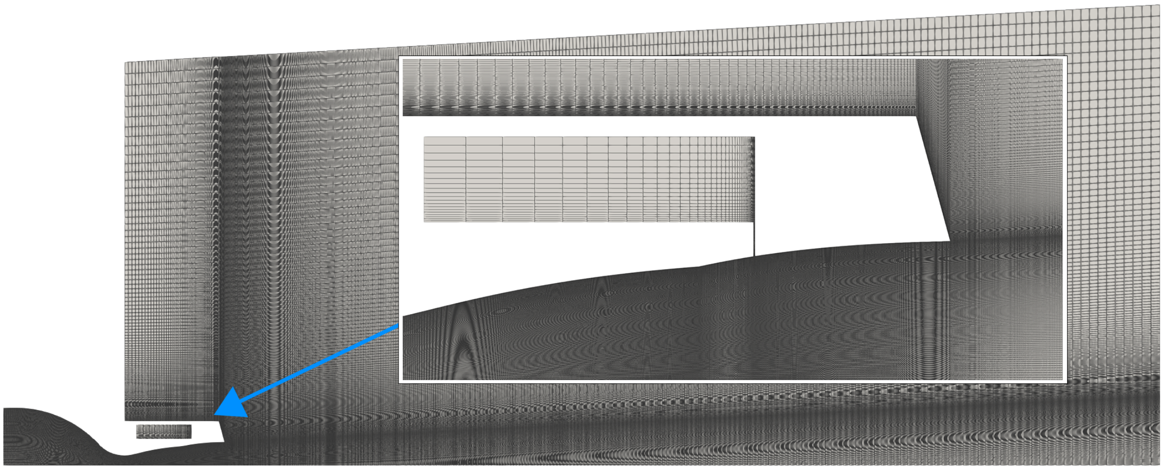

Fig. 2.12 Numerical grid for DBNi8.

For the numerical study of the secondary injection effect on the DBN behaviour, another structured mesh composed of 1597206 cells was computed. Thirty cells were added in the streamwise direction within the 0.2 mm width injection slot and the nozzle bulk flow area. The cell number in the radial direction of the DBNi8 core flow was unchanged.

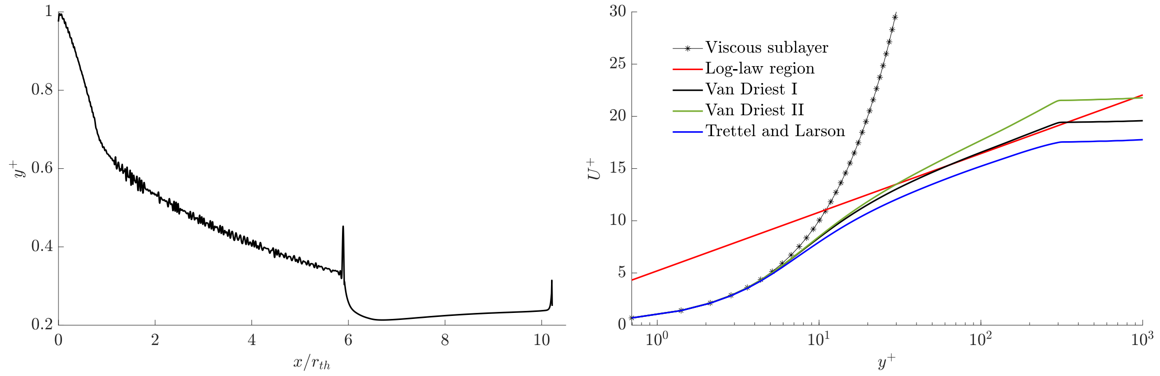

(a) Streamwise y^+ distribution from the throat.

(b) Boundary layer profiles.

Fig. 2.13 Streamwise y^+ distribution and boundary layer profiles for different scaling transformations at x/r_{th} = 5.36. Grid D, NPR = 50.

2.2.3 Governing equations

Let ρ be the fluid density, u_i the three velocity components (u_1, u_2, u_3) in the Cartesian coordinate directions (x_1, x_2, x_3), p the static pressure, and e the total energy (internal + kinetic) per unit mass. The governing Navier-Stokes equations for a compressible, viscous flow of an ideal gas in their conservative differential form are

- Continuity:

$$\frac{\partial \rho}{\partial t} + (\rho u_i)_{,i} = 0 \tag{2.1}$$

- Momentum:

$$\frac{\partial \rho u_i}{\partial t} + (\rho u_i u_j + p\delta_{ij} - \tau_{ij})_{,j} = 0 \tag{2.2}$$

Where for a Stokes-Newtonian fluid, the stress tensor τ_{ij} is written as:

$$\tau_{ij} = 2\mu S_{ij}$$

and where S_{ij} is expressed as:

$$S_{ij} = \frac{1}{2}(u_{i,j} + u_{j,i}) - \frac{1}{3}u_{k,k}\delta_{ij}$$

- Energy:

$$\frac{\partial \rho e}{\partial t} + [(\rho e + p)u_j + \dot{q}_j - u_i\tau_{ij}]_{,j} = 0 \tag{2.3}$$

Here, e is defined as

$$e = c_v T + \frac{1}{2}u_i u_i \tag{2.4}$$

with c_v the specific heat at constant volume. The specific heat ratio $\gamma = c_p/c_v$ is assumed to be constant ($\gamma = 1.4$), where c_p is the specific heat at constant pressure.
The heat flux vector $\dot{q}_j$ is

$$\dot{q}_j = -\lambda T_{,j} \tag{2.5}$$

- Ideal gas:

$$p = \rho r T \tag{2.6}$$

The above conservation laws already describe turbulence in the flow. However, for general purposes, directly solving the equations for all turbulence and time scales (DNS) is an unrealistic option due to the extensive computer speed and storage required. Even though DNS remains important to obtain deep insight into the physics of the flow, such a method is mostly restricted to relatively low Reynolds number flows. More affordable methods based on averaging or filtering approaches such as RANS, DDES, and LES have been developed in past and provide a large panel of choices that fits the CFD user needs. Given the numerous configurations studied experimentally in this thesis, the averaging approach was chosen to obtain numerical results in a short amount of time to be compared to the experiments.

2.2.4 Ensemble-averaging approach

In the standard ensemble-averaging (or Reynolds-averaging) approach, all flow variables are decomposed into a mean and fluctuating part. Let ϕ be any flow variable, we write

$$\phi = \overline{\phi}(x_i,t) + \phi'(x_i,t) \tag{2.7}$$

where the mean part becomes in a stationary turbulent flow:

$$\overline{\phi}(x_i) = \lim_{T\to\infty} \frac{1}{T} \int_0^T \phi(x_i,t)dt$$

and the Reynolds-averaged value of the fluctuating part is zero:

$$\overline{\phi'}(x_i) = \lim_{T\to\infty} \frac{1}{T} \int_0^T \left[\phi(x_i,t) - \overline{\phi(x_i)}\right] dt = \overline{\phi}(x_i) - \overline{\phi}(x_i) = 0$$

Since all flow variables have a mean and a fluctuating component, the ensemble average can be applied to the three conservation equations and the state equation. The resultant set of equations gives rise to uncomputable terms for compressible flows, requiring another mathematical formalism to simplify the equations: the Favre (density-weighted) averaging approach. The Favre average of a flow variable is defined as

$$\tilde{\phi} = \frac{\overline{\rho\phi}}{\overline{\rho}}$$

The new decomposition of the flow variable ϕ, except for the density and pressure (which remains Reynolds averaged), is given by

$$\phi = \widetilde{\phi} + \phi''$$

where $\widetilde{\phi}$ and ϕ'' are the Favre mean and Favre fluctuating parts, respectively. Applying the Favre average to the continuity and momentum equations gives

- Continuity:

$$\frac{\partial\overline{\rho}}{\partial t} + (\overline{\rho}\tilde{u}_i)_{,i} = 0 \tag{2.8}$$

- Momentum:

$$\frac{\partial\overline{\rho}\tilde{u}_i}{\partial t} + (\overline{\rho}\tilde{u}_i\tilde{u}_j + \overline{p}\delta_{ij} + \overline{\rho u_i'' u_j''} - \overline{\tau}_{ij})_{,j} = 0 \tag{2.9}$$

The term $-\overline{\rho u_i'' u_j''}$ is called the Reynolds Stress Tensor (RST). Similarly to the molecular viscous stress tensor which represents the momentum transfer inside the fluid due to the

Brownian motion of particles, the RST represents the momentum transfer in the averaged velocity field due to the turbulent motion. The specification of this term is necessary to close the set of governing equations and will be discussed later. The ensemble-averaged molecular viscous stress tensor $\overline{\tau}_{ij}$ is usually approximated by

$$\overline{\tau}_{ij} = \tilde{\mu}(\tilde{u}_{i,j} + \tilde{u}_{j,i}) - \frac{2}{3}\tilde{\mu}\tilde{u}_{k,k}\delta_{ij} \tag{2.10}$$

where the molecular viscosity $\tilde{\mu}$ is taken as a function of the temperature.

- Energy:

The Favre averaged energy equation can be written

$$\frac{\partial \overline{\rho}\tilde{e}}{\partial t} + [(\overline{\rho}\tilde{e} + \overline{p})\tilde{u}_j + \tilde{u}_i(\overline{\rho u_i'' u_j''} - \overline{\tau}_{ij}) + c_p\overline{\rho T'' u_j''} + \overline{q}_j + \frac{1}{2}\overline{\rho u_i'' u_i'' u_j''} - \overline{u_i'' \tau_{ij}}]_{,j} = 0 \tag{2.11}$$

where the last two terms are often considered negligible, resulting in:

$$\frac{\partial \overline{\rho}\tilde{e}}{\partial t} + [(\overline{\rho}\tilde{e} + \overline{p})\tilde{u}_j + \tilde{u}_i(\overline{\rho u_i'' u_j''} - \overline{\tau}_{ij}) + c_p\overline{\rho T'' u_j''} + \overline{q}_j]_{,j} = 0 \tag{2.12}$$

Defining the total shear stress tensor τ_{ij}^* and the total heat flux vector $\mathscr{Q}_i$ as

$$\tau_{ij}^* = \overline{\rho u_i'' u_j''} - \overline{\tau}_{ij} \tag{2.13}$$

and

$$\mathscr{Q}_i = c_p\overline{\rho T'' u_j''} + \overline{q}_j \tag{2.14}$$

the Favre averaged Navier-Stokes equations can be written:

$$\begin{gathered}
\frac{\partial \overline{\rho}}{\partial t} + (\overline{\rho}\tilde{u}_i)_{,i} = 0 \\
\frac{\partial \overline{\rho}\tilde{u}_i}{\partial t} + (\overline{\rho}\tilde{u}_i\tilde{u}_j + \overline{p}\delta_{ij} + \overline{\rho u_i'' u_j''} - \overline{\tau}_{ij})_{,j} = 0 \\
\frac{\partial \overline{\rho}\tilde{e}}{\partial t} + [(\overline{\rho}\tilde{e} + \overline{p})\tilde{u}_j + \tilde{u}_i\mathscr{T}_{ij} + \mathscr{Q}_i]_{,j} = 0 \\
\overline{p} = \overline{\rho}r\tilde{T}
\end{gathered} \tag{2.15}$$

2.2.5 Computational method

Two-dimensional axisymmetric, steady-state RANS calculations are carried out using the finite volume commercial code ANSYS FLUENT 2022R2. Ideal gas is assumed and the

Sutherland's law is applied to consider the influence of temperature on the dynamic viscosity. Fluent uses a finite volume method approach, where the integral form of the governing equations of continuity, momentum, energy and turbulence are solved using a density-based solver. Here, the continuity, momentum and energy equations are coupled together and solved simultaneously. The equations are linearised in an implicit form and the unknown variables are solved in all cells simultaneously. Turbulence equations are also linearised and solved implicitly, but they are solved after the coupled set and sequentially from one another. Even though the flow variables values are stored at the cell centre, the values are also needed at the face centre to compute the convection terms, hence the need for a spatial discretisation scheme. For density based solver, two choices are possible for the continuity, momentum and energy equations :

1. Upwind (1st and 2nd order)
2. Third order MUSCL

MUSCL does not contain a flux limiter which can undershoot and overshoot in the case of flows containing shock waves. Therefore, the 2nd order upwind spatial discretisation scheme was chosen for this case. For the additional scalar transport equations, another scheme was available: QUICK. However, QUICK is only applicable in structured and hexahedral meshes, which might have been a problem should other types of meshes be used in the present thesis. The computation of gradients is required for the second-order upwind scheme, for evaluating the secondary diffusion terms, and the velocity derivatives. By default, the least squares cell-based gradient method is used because of its much superior accuracy compared to the cell-based method, and because it is far less computationally expensive than the node-base method. To prevent oscillations in the solutions in the zones containing discontinuities (such as shock waves), the non-differentiable standard limiter is used. This limiter uses the minimum modulus function (Minmod) and a cell-to-face limiting method, in which the limited value of the reconstruction gradient is determined at the cell face centre.

2.2.6 Turbulence modelling

Turbulent flows contain a continuous, large spectrum of eddy scales. The large-scale eddies, whose length scale is comparable to the flow scale, transport most of the energy and are responsible for the enhanced diffusivity and shear stress in the flow. They migrate in the flow and, as turbulence decays, they transfer their turbulent kinetic energy to the smaller-scale eddies that they carry. Eventually, the smaller scales dissipate and are converted into heat through the effect of viscosity. The large-scale proneness to migrate and last through the flow significantly far downstream of the turbulence source involves accounting for the time history of turbulence. Unlike laminar flows, the diffusivity and the shear stress cannot be uniquely inferred from the local flow properties. Cost-effective methods that consider the time history of turbulence have emerged to model the Reynolds stress tensor. The two turbulence models presented in this thesis, namely the $k\omega - SST$ and the Spalart Allmaras, are based on the Boussinesq hypothesis. This hypothesis transposes the laminar shear stress formulation (where the shear stress is expressed as local flow properties) to the turbulent flow by introducing a turbulent viscosity coefficient:

$$-\overline{\rho u_i'' u_j''} = \tilde{\mu}_t(\tilde{u}_{i,j} + \tilde{u}_{j,i}) - \frac{2}{3}(\overline{\rho}\tilde{k} + \tilde{\mu}_t \tilde{u}_{k,k})\delta_{ij} \tag{2.16}$$

The calculation of the turbulent viscosity is necessary to infer the RST. The approximation method to compute the later is given for each turbulence model in the below.

SST model

The $k\omega$-SST turbulence model, a pivotal advancement in computational fluid dynamics, was developed to overcome the limitations of traditional turbulence models when simulating complex flows in engineering applications. Introduced as a hybrid model, it integrates the strengths of the k-ω and k-ε models, aiming to provide a more accurate and versatile prediction of turbulent flows. Its formulation is particularly well-suited for regions with strong adverse pressure gradients and separated flows, making it an invaluable tool for simulating a wide spectrum of aerodynamic phenomena. It became a preferred choice in numerous disciplines, including aerospace, automotive engineering, and industrial processes. Unlike most eddy-viscosity models, the $k\omega - SST$ accounts for the important effect of the transport of turbulent shear stress by redefining the eddy viscosity.
In the $k\omega - SST$ turbulence model, the turbulent viscosity is computed as:

$$\mu_t = \frac{\rho k}{\omega} \frac{1}{\max\left[1, \frac{SF_2}{a_1 \omega}\right]} \tag{2.17}$$

where S is the strain rate magnitude, F_2 a blending function, and a_1 the structure parameter. The structure parameter limits the turbulent shear stress and the coefficient F_2 constraints this limitation inside the boundary layer using:

$$F_2 = \tanh\left(\max\left[2\frac{\sqrt{k}}{0.09\omega y}, \frac{500\mu}{\rho y^2 \omega}\right]^2\right) \tag{2.18}$$

where y corresponds to the distance from the wall. $F_2 = 1$ for boundary layer flow and $F_2 = 0$ for free sheer flows.

The value of μ_t is derived from the resolution of scalar transport equations for k and ω, formulated in ANSYS FLUENT as:

$$\frac{\partial}{\partial t}(\rho k) + \frac{\partial}{\partial x_i}(\rho k u_i) = \frac{\partial}{\partial x_j}\left(\Gamma_k \frac{\partial k}{\partial x_j}\right) + \widetilde{G}_k - Y_k + S_k \tag{2.19}$$

and

$$\frac{\partial}{\partial t}(\rho \omega) + \frac{\partial}{\partial x_i}(\rho \omega u_i) = \frac{\partial}{\partial x_j}\left(\Gamma_\omega \frac{\partial \omega}{\partial x_j}\right) + G_\omega - Y_\omega + D_\omega + S_\omega \tag{2.20}$$

where Γ_k and Γ_ω are the effective diffusivity of k and ω. $\widetilde{G}_k$ and $\widetilde{G}_\omega$ are the terms corresponding to the production of k and ω. The terms Y_k and Y_ω correspond to the dissipation of k and ω. S_k and S_ω are source terms.

The transformation of the k-ε equations into k-ω equations gives rise to the cross-diffusion term D_ω. The turbulence model incorporates the 2003 Menter formulation [103] which can be expressed as:

$$\frac{\partial(\rho k)}{\partial t} + \frac{\partial(\rho U_i k)}{\partial x_i} = \widetilde{P}_k - \beta^* \rho k \omega + \frac{\partial}{\partial x_i}\left[(\mu + \sigma_k \mu_t)\frac{\partial k}{\partial x_i}\right]$$

$$\frac{\partial(\rho \omega)}{\partial t} + \frac{\partial(\rho U_i \omega)}{\partial x_i} = \alpha \rho S^2 - \beta \rho \omega^2 + \frac{\partial}{\partial x_i}\left[(\mu + \sigma_\omega \mu_t)\frac{\partial \omega}{\partial x_i}\right] + 2(1 - F_1)\rho \sigma_{w2}\frac{1}{\omega}\frac{\partial k}{\partial x_i}\frac{\partial \omega}{\partial x_i}$$

The blending function F_1 is defined by:

$$F_1 = \tanh\left\{\left\{\min\left[\max\left(\frac{\sqrt{k}}{\beta^* \omega y}, \frac{500 v}{y^2 \omega}\right), \frac{4 \rho \sigma_{\omega 2} k}{CD_{k\omega} y^2}\right]\right\}^4\right\}$$

with $CD_{kw} = \max\left(2\rho\sigma_{\omega 2}\frac{1}{\omega}\frac{\partial k}{\partial x_i}\frac{\partial \omega}{\partial x_i}, 10^{-10}\right)$. F_1 is equal to one in boundary layer flows (($k - \omega$ model) and to 0 in the free shear flow (k - ε model). The turbulent kinetic energy production limiter is written in [103] as:

$$P_k = \mu_t \frac{\partial U_i}{\partial x_j}\left(\frac{\partial U_i}{\partial x_j} + \frac{\partial U_j}{\partial x_i}\right)$$

with

$$\widetilde{P}_k = \min\left(P_k, 10 \cdot \beta^* \rho k \omega\right)$$

The model constants can be found in the work of Menter et al. [103]. The turbulent viscosity is then substituted into the momentum equation, closing the Navier-Stokes set of equations.

Spalart Allmaras model

The Spalart-Allmaras turbulence model was introduced as a computationally efficient alternative for predicting turbulent flows, providing a simplified one-equation approach [104]. Designed to address the limitations of more complex turbulence models, it is particularly suited for attached boundary layers. Widely adopted in aerospace engineering, where precise predictions of turbulent flows are crucial, the Spalart-Allmaras model strikes a balance between accuracy and computational efficiency, making it a practical choice for simulating turbulent flows in various engineering applications.

The additional scalar transport equation is solved for the modelled kinematic viscosity $\widetilde{\nu}$ to compute the turbulent viscosity. The transport equation for $\widetilde{\nu}$ is written:

$$\frac{\partial}{\partial t}(\rho\widetilde{\nu})+\frac{\partial}{\partial x_i}(\rho\tilde{\nu}u_i)=G_\nu+\frac{1}{\sigma_{\tilde{\nu}}}\left[\frac{\partial}{\partial x_j}\left\{(\mu+\rho\tilde{\nu})\frac{\partial\widetilde{\nu}}{\partial x_j}\right\}+C_{b2}\rho\left(\frac{\partial\widetilde{\nu}}{\partial x_j}\right)^2\right]-Y_\nu \tag{2.21}$$

Where G_ν and Y_ν represent the production of turbulent viscosity and the destruction of turbulent viscosity occurring in the near-wall region, respectively. $\sigma_{\widetilde{\nu}}$ and C_{b2} are the constants and ν is the molecular kinematic viscosity.

After solving the transport equation for $\widetilde{\nu}$, the turbulent viscosity is inferred by multiplying $\widetilde{\nu}$ to the function f_{v1} defined as:

$$\mu_t=\rho\widetilde{\nu}f_{v1} \tag{2.22}$$

Where

$$f_{v1}=\frac{\chi^3}{\chi^3+C_{v1}^3} \tag{2.23}$$

And

$$\chi=\frac{\widetilde{\nu}}{\nu} \tag{2.24}$$

The turbulent viscosity is then substituted into the momentum equation, thereby completing the closure of the system of equations. For more in-depth information on the turbulence model, refer to [104].

Chapter 3

Dual-bell nozzle natural behaviour

3.1 Introduction

This chapter delves into the inherent behaviour of the smooth DBN under changing altitude conditions. It begins with a preliminary section exposing the experimental procedure. The second section discusses the behaviour of the DBN experimentally. The experimental analysis investigates the exhaust flow topology during the low-altitude mode and the high-altitude mode using the experimental schlieren images. This section further presents a quantitative exploration of key DBN parameters, including the transition NPR and retransition NPR, while also delving into side forces generated during operational mode shifts, thrust jumps, and the hysteresis phenomenon.

The third section undertakes a numerical exploration of the smooth DBN, employing 2D steady RANS simulation and the $k\omega - SST$ turbulence model. The ensuing numerical data is then juxtaposed with experimental findings.

Subsequently, the fourth section retains its focus on numerical simulations but employs the Spalart-Allmaras turbulence model, with results being compared not only to experimental data but also to the $k\omega - SST$ turbulence model.

In the fifth section, experimental results are leveraged to calibrate the $k\omega - SST$ turbulence model, enhancing its predictive capacity for separation locations. This calibration involves investigating the influence of the turbulence model structure coefficient, utilising experimental schlieren images, wall pressure measurements, and thrust data to identify the most fitting coefficient.

The chapter concludes by summarising its pivotal findings and revealing the selected turbulence model for subsequent simulation test campaigns.

3.2 Preliminary section

This test campaign examines the smooth DBN's natural behaviour under altitude-varying conditions. The test specimen was mounted on the force balance, in the wind tunnel test section. A feeding total pressure of 350 kPa was applied and the ambient pressure was repetitively decreased and increased to trigger the transitions and the retransitions in the DBN. The thrust, normalised side forces, NPR, and streamwise wall pressure distribution were measured. The normalised side-loads have been defined as the ratio between the side force magnitude and the thrust to present the side forces as a percentage of the thrust. Fig. 3.1 shows the specific impulse, side forces, and NPR during a conventional test run. The specific impulse (I_{sp}) is calculated using Eq. 3.1:

$$I_{sp} = \frac{F_x}{\dot{m} \cdot g_0} \tag{3.1}$$

where F_x, $\dot{m}$, and g_0 are respectively the thrust, mainstream mass flow rate, and standard gravity. The nozzle pressure ratio is calculated as $NPR = P_0/P_a$, where P_0 and P_a are, respectively, the feeding total pressure and the ambient pressure in the wind tunnel test section.

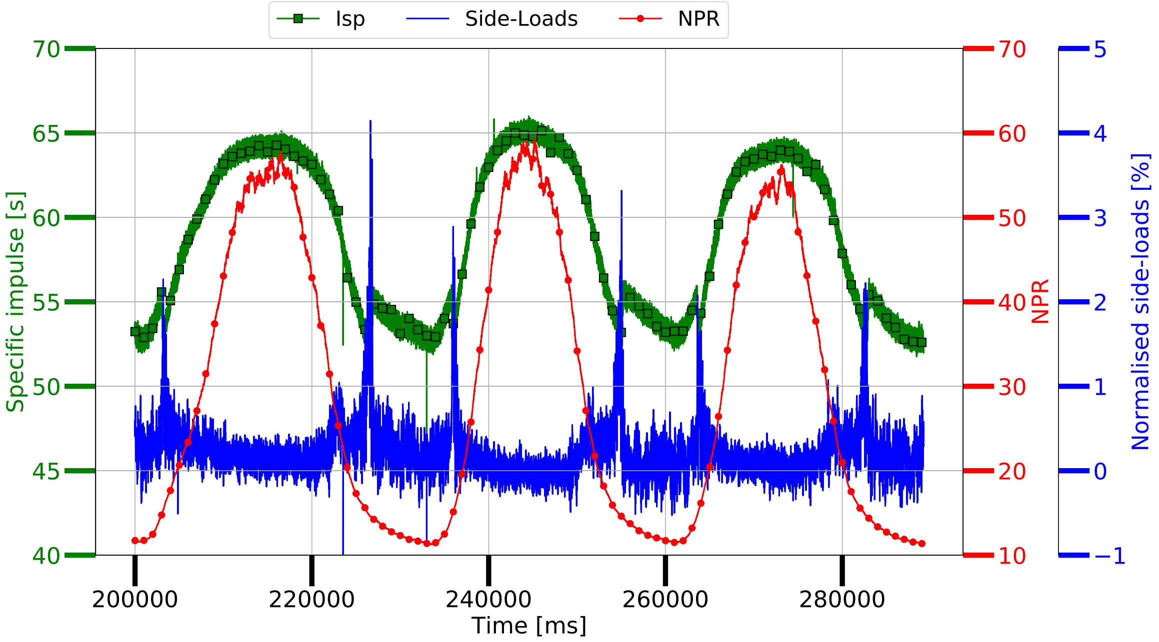

Fig. 3.1 Specific impulse, NPR, and side-loads as a function of time in the smooth DBN

Fig. 3.1 indicates that the present test specimen exhibits the key characteristics of a DBN equipped with a CP extension, namely the sudden jump in specific impulse during the transition from the low-altitude mode to the high-altitude mode (and vice-versa) and the generation of side forces during these operating mode switches. Before diving into the quantitative analysis of the smooth DBN, the flow characteristics of the test specimen are presented in the next section.

3.3 Experimental investigation

3.3.1 Qualitative analysis

The dual-bell nozzle is well known for its altitude adaptive capability and its concept simplicity, providing two distinct operating modes: low-altitude and high-altitude. Fig. 3.2 shows experimental schlieren images of the smooth DBN operating in the low-altitude mode (NPR = 14) and in the high-altitude mode (NPR = 30). The numerical results presented in a subsequent section give an indication of the flow topology inside the DBN's extension section and the different shock/expansion configurations are inferred qualitatively.

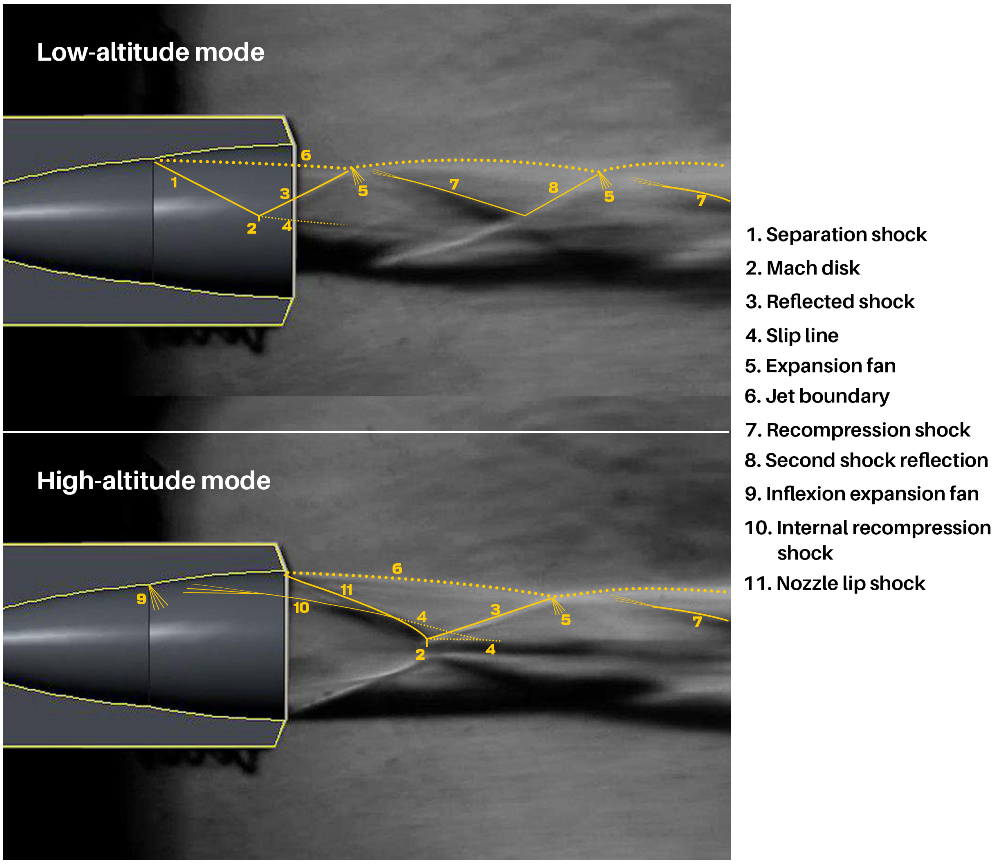

Fig. 3.2 Experimental schlieren of the smooth DBN operating in the low-altitude mode (NPR = 14; top picture) and the high-altitude mode (NPR = 30; bottom picture).

In the low-altitude mode, the high ambient pressure compresses the jet column. The upcoming flow faces an adverse pressure gradient, which causes the upstream boundary layer to thicken and separate from the nozzle wall at the inflexion point. The flow separation induces the formation of an oblique separation shock wave (1). The presence of slip lines (4) at the nozzle exit suggests that the separation shock interacts with a Mach disk (2) in the vicinity of the nozzle symmetry axis. The separation shock is reflected (3) at the triple point and is turned into an expansion fan (5) upon contact with the jet boundary (6). Further downstream, a series of compression waves coalesce to form another shock (7), which will be reflected at the nozzle symmetry axis (8), and so on. This series of compression and expansion cells continues downstream until the exhaust jet adapts to the ambience. It is worth highlighting that in the low-altitude mode, the presence of the inflexion point and the constant pressure nature of the extension section contribute to maintaining the flow separation at a fixed location, therefore limiting the generation of side forces in the nozzle.

In the high-altitude mode, the flow expands at the inflexion point through an expansion fan (9) and remains attached to the extension section wall. The constant pressure nature of the extension section induces the formation of compression waves which coalesce to form an internal recompression shock (10). At the nozzle exit, the high ambient pressure compresses the jet column and an oblique shock wave (11) emerges from the nozzle wall and interacts with the recompression shock. At NPR = 30, the ambient pressure remains relatively high, and a Mach disk (2) exists, which interacts with the oblique shock wave (11) and the reflected shock (3) at the triple point. The reflected shock is turned into an expansion fan (5) at contact with the exhaust plume boundary, and the conventional series of compression/expansion cells adapt the exhaust plume to the ambience downstream.

During an ascent phase, the switch from the low-altitude mode to the high-altitude mode is called the **transition**. Conversely, the switch from the high-altitude mode to the low-altitude mode during the descent phase is referred to as the **retransition**. In the present case, the constant pressure extension of the DBN induces abrupt transitions and retransitions. The evolution of the flow topology during an ascent and a descent phase is given in Fig. 3.3 and Fig. 3.4.

These figures illustrate that the flow topologies are similar during both the transition and the retransition phases for a given NPR. The increase in NPR causes the exhaust jet flow to expand during the ascent phase, while the decrease in NPR compresses the jet column, displacing the separation front towards the DBN's inflexion point. In the low-altitude mode (NPR $\approx$ 14) for both configurations, the DBN's wall conceals an oblique shock wave that interacts with the Mach disk. The presence of slip lines near the nozzle exit, close to the nozzle symmetry axis, strongly implies the existence of a Mach disk within the DBN.

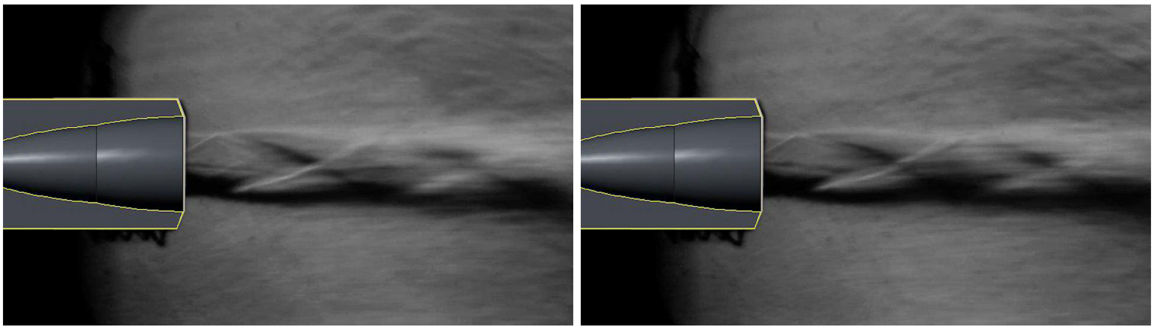

(a) NPR = 14.03 (b) NPR = 14.00

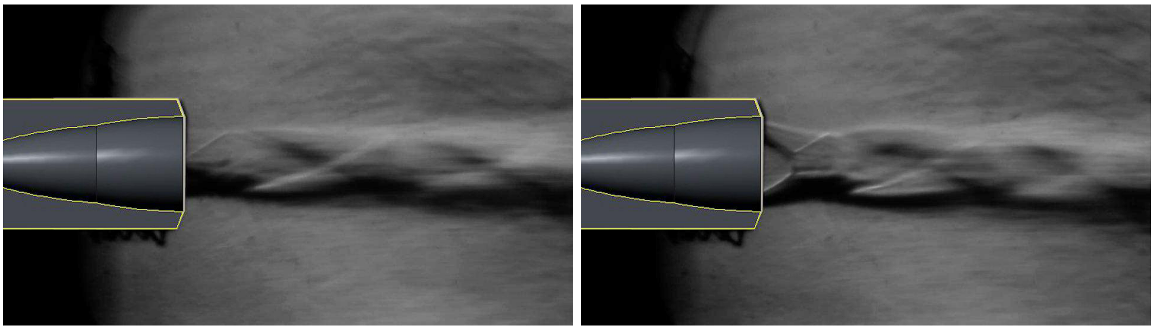

(c) NPR = 14.51 (d) NPR = 14.50

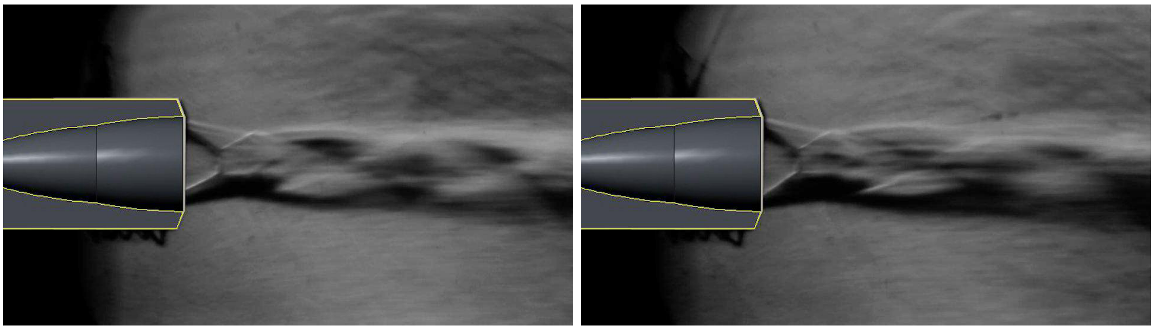

(e) NPR = 14.80 (f) NPR = 14.82

Fig. 3.3 Experimental schlieren during a transition phase (left) and a retransition phase (right) in the smooth DBN. Part I

At NPR $\approx$ 14.5, the DBN operates in the low-altitude mode during the ascent phase and the high-altitude mode during the descent phase. This difference is justified by the existence of a hysteresis effect inherent to DBNs, where transition NPRs are higher than retransition NPRs. In this case, an NPR value of 14.5 is not large enough to observe a transition to high-altitude mode during the ascent, while it is high enough to observe the high-altitude mode before the retransition occurs during the descent phase. A larger gap between NPR_{trans} and $NPR_{retrans}$ minimises the risk of flip-flop during the operating mode changes. The flow features at NPR $\approx$ 14.5 remain similar to those at NPR $\approx$ 14 during the ascent phase. In the descent phase, the operation in high-altitude mode results in an oblique shock wave that intersects

with a Mach disk and a reflected shock at a triple point. The reflected shock is turned into an expansion fan upon contact with the exhaust jet boundary and is succeeded by a series of compression and expansion cells that adapt the exhaust jet to the ambient conditions.
At NPR $\approx$ 14.80, the transition occurred during the ascent phase. At this NPR, flow topologies during ascent and descent are identical, featuring an oblique shock wave at the nozzle exit interacting with a Mach disk and a reflected shock, followed by compression and expansion cells to adapt the exhaust jet to the ambient conditions.

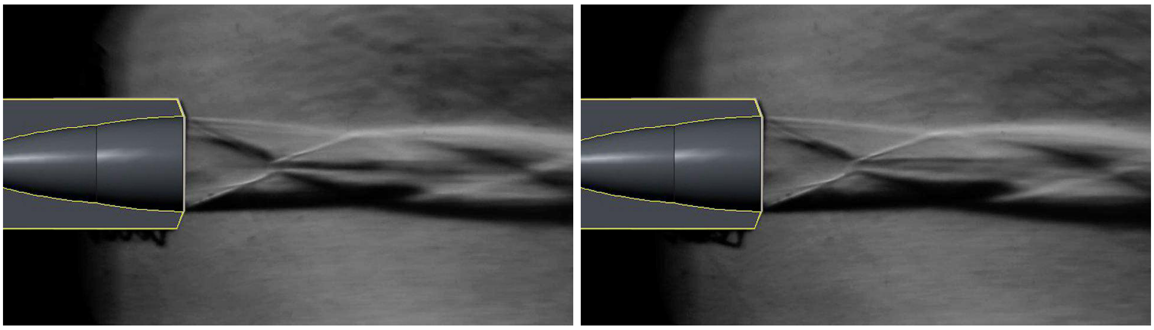

(a) NPR = 29.94

(b) NPR = 29.97

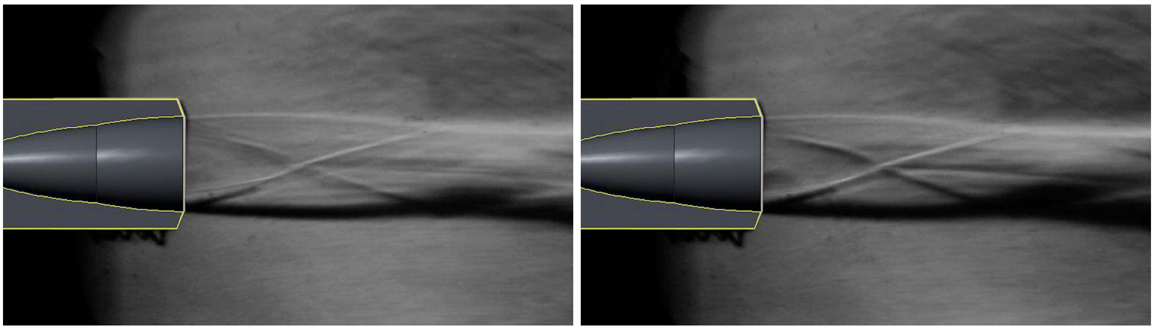

(c) NPR = 50.01

(d) NPR = 50.05

Fig. 3.4 Experimental schlieren during a transition phase (left) and a retransition phase (right) in the smooth DBN. Part II.

The flow features at NPR $\approx$ 30 prominently display the aforementioned oblique and reflected shocks, along with the Mach disk. An internal recompression shock is noticeable, highlighting the constant pressure nature of the extension section. The lower ambient pressure reduces the angle of the oblique shock and the height of the Mach disk.
Near NPR = 50, both ascent and descent flow topologies are the same. The most significant feature at this NPR is the internal recompression shock and its reflection further downstream. It is noteworthy to highlight that the flip-flop phenomenon often observed during the retransition process had been documented in the current DBN in the past. Nevertheless, experiments conducted after introducing holes for pressure sensors in the DBN did not reveal any indication of flip-flop. This observation suggests that instabilities in the DBN's flow may be notably

influenced by the presence of surface discontinuities, emphasising the potential impact of any intrusive measurement technique on the overall flow dynamics.

3.3.2 Quantitative analysis

The transition phase

In a conventional test run, approximately seven transition and retransition phases were observed. In this thesis, each test run is meticulously conducted twice, resulting in an average of 14 transition and retransition phases. The measured values of NPR_{trans}, $NPR_{retrans}$, thrust, and side-loads during the switch in operating modes are then averaged, and standard deviations are subsequently calculated.

In the smooth DBN and below NPR = 14, the nozzle functions in the low-altitude mode. The overexpanded flow separates at the inflexion point and a separation shock is formed. If the NPR increases, the DBN's specific impulse rises until a sudden drop occurs at NPR = 14.85 (see Fig. 3.1 and Fig. 3.5b). At this NPR, the separation front suddenly moves from the inflexion point to the nozzle exit. This process, called transition, indicates that the DBN switched from the low-altitude mode to the high-altitude mode. During the transition, the sudden jump in thrust amounted to 3.8% of the nozzle thrust.

Fig. 3.5b displays the specific impulse as a function of NPR during an ascent phase. Plotting these variables during an ascent or descent phase allows one to clearly identify the transition NPR and the magnitude of the jump in specific impulse (or thrust) during the abrupt change in operating modes.

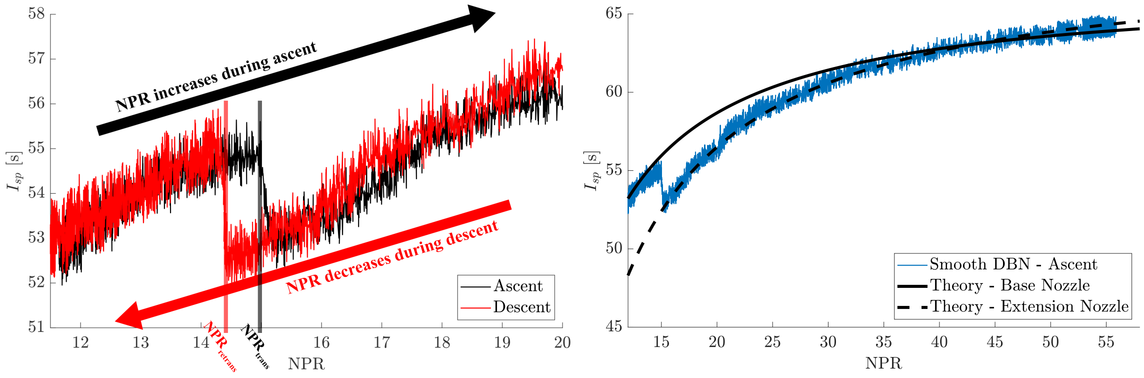

(a) Detection method of NPR_{trans} and $NPR_{retrans}$. (b) Specific impulse trajectory.

Fig. 3.5 Detection method of NPR_{trans} and $NPR_{retrans}$ (left) and specific impulse as a function of NPR (right) during an ascent phase in the smooth DBN

The experimental data in Fig. 3.5b is directly obtained from the force balance measurements. In contrast, the base (resp. extension) theoretical curve is deduced by substituting the base (resp. extension) nozzle exit area into the thrust equation. Additionally, the evolution of pressure with respect to altitude is incorporated into the ambient pressure variable in this equation. The specific impulse is then inferred. Fig. 3.5b shows that the experimental measurements are in good agreement with the theory. The NPR associated with a sudden jump in specific impulse during ascent phases is identified and termed as the transition NPR (NPR_{trans}). Similarly, the NPR corresponding to a sudden jump in specific impulse during descent phases is reported and referred to as the retransition NPR $(NPR_{retrans})$. These operating mode changes are distinctly identifiable during the ascent and descent phases, as illustrated in Fig. 3.5a. However, for the sake of simplicity, the explanation of the fundamental working concepts of the DBN will primarily focus on the ascent phases, given their similarity to the descent phases. Any notable differences in behaviour between the two phases will be explicitly mentioned and thoroughly explained when necessary.

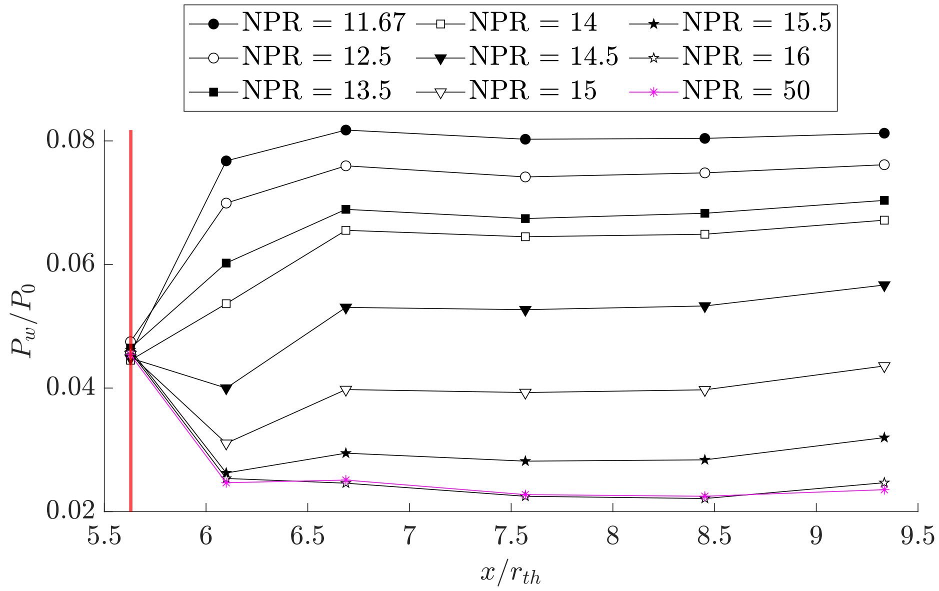

Fig. 3.6 Instantaneous streamwise wall pressure distribution. The red line indicates the inflexion point.

It is worth highlighting that the transition does not occur at the optimum transition point, the intersection between the two theoretical curves, but rather earlier (see Fig. 3.5b). Nonetheless, the experimentally measured NPR_{trans} of 14.85 is relatively close to the predictions of the Stark criterion [100] applied to the smooth DBN with a NPR_{trans} of 14.89 (see Section 2.1). Fig. 3.6 shows the evolution of the streamwise (instantaneous) wall pressure distribution during a transition phase. At NPR = 11.67, it shows that the DBN operates in the low-altitude mode and the flow separates near the inflexion point, between x/r_{th} = 5.63 and x/r_{th} = 6.10. Downstream of the inflexion point, the wall pressure inside the separation bubble rapidly increases and reaches a constant value, lower than the ambient pressure.

From NPR = 11.67 to NPR = 14, the decline in ambient pressure causes the separation bubble size to reduce and the wall pressure in the separated flow region to decrease.

From NPR = 14.5 to NPR = 15, the wall pressure decreases from x/r_{th} = 5.63 to x/r_{th} = 6.10 and increases from x/r_{th} = 6.10 to the nozzle exit. This pressure distribution pattern suggests that the separation front moves downstream of the inflexion point, in the inflexion region. This phenomenon is called the sneak transition. The increase in NPR reduces the adverse pressure gradient strength and the separation front moves in the inflexion region. The flow expands through the inflexion region and the wall pressure decreases locally. The rise in wall pressure downstream is caused by the separation shock and the relatively high pressure in the recirculation bubble downstream of the separation front.

Between NPR = 15 and NPR = 15.5, the complete transition occurs and the flow fully attaches to the extension section wall. The frequency of data acquisition was not sufficient to track the movement of the separation front in the DBN's extension section.

Furthermore, during the transition phase, the separation front and shock movement in the extension section does not occur symmetrically, causing an uneven wall pressure distribution and consequently side-loads. The average normalised side-loads measured during the transition phase reached 2.4% of the nozzle thrust. The normalised side-loads are presented in blue in Fig. 3.1.

The retransition phase

Starting from the highest nozzle pressure values, the DBN operates in the high-altitude mode. In the high-altitude mode, the flow expands at the inflexion point through an expansion fan and separates at the nozzle exit. When the NPR decreases, Fig. 3.1 shows that the DBN's specific impulse declines until a sudden increase occurs at NPR = 14.53. At this NPR, the separation front suddenly moves from the nozzle exit to the inflexion point. This process, called retransition, indicates that the DBN switched from the high-altitude mode to the low-altitude mode. During the retransition, the sudden jump in thrust amounted to 4.2% of the nozzle thrust. Fig. 3.7a shows the evolution of the streamwise wall pressure distribution during a retransition phase. At NPR = 50, it shows that the DBN functions in the high-altitude mode. The flow is attached to the extension section wall and the flow separates at the nozzle exit. The constant pressure nature of the extension section justifies the flat streamwise wall pressure distribution. At NPR = 15, the higher ambient pressure compresses the jet column and the separation front is pushed upstream of the nozzle exit. The boundary layer separates from the extension wall between x/r_{th} = 8.45 and x/r_{th} = 9.33 and a separation shock is formed. The presence of the shock and the recirculation region downstream of the separation front induces a sharp rise in pressure for the furthest pressure sensor. Between NPR = 15 and NPR = 14.6, the sudden retransition occurs and the flow fully separates from the extension section wall. Then, until NPR = 14.4, the increasing ambient pressure pushes the separation front from the end of the inflexion region to the inflexion point. The recirculation bubble size downstream of the separation front increases and the wall pressure in the extension rises. The presence of the separation shock in the vicinity of the inflexion region is responsible for the sharp rise in wall pressure between x/r_{th} = 6.10 and x/r_{th} = 6.69. A further increase in NPR causes the wall pressure in the separated flow region to increase and the separation point moves back to the inflexion point.

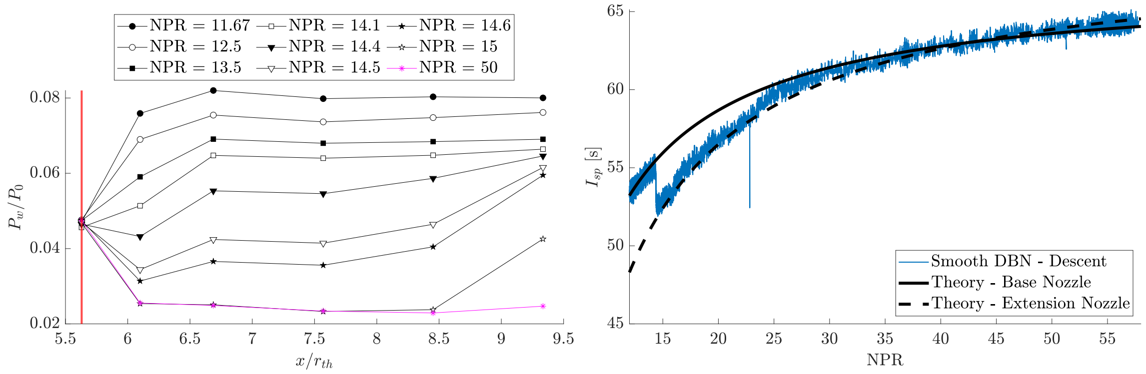

(a) Instantaneous wall pressure distribution. The red line indicates the inflexion point.

(b) Experimental and theoretical specific impulse trajectory.

Fig. 3.7 Instantaneous streamwise wall pressure distribution (left) and specific impulse as a function of NPR (right) during a descent phase in the smooth DBN

Fig. 3.8 shows the wall pressure measured by the Kulite sensor at $x/r_{th} = 7.57$ as a function of time during a transition/retransition cycle. The black curve shows the pressure measured during the ascent phase, and the red curve shows the pressure measured during the descent phase. In the ascent phase, the flow is initially detached from the extension section wall and the sensor measures the high pressure in the separated flow region. When the transition occurs, the pressure suddenly decreases to reach the value imposed by the constant pressure extension when the DBN operates in the high-altitude mode. The transition occurs without flip-flop, a high-amplitude and unsteady displacement of the separation point. During the retransition phase, the flow is initially attached to the extension wall and the pressure sensor measures the constant pressure of the extension section. The increase in NPR eventually triggers the retransition process and the boundary layer separation point suddenly moves from the nozzle exit to the inflexion point. The presence of a recirculating flow region downstream

of the separation front induces an increase in wall pressure.
The uneven azimuthal wall pressure distribution during the retransition phase is, as during the transition phase, the cause of side-loads generation. The normalised-side loads are displayed in blue in Fig. 3.1. In the smooth DBN, the average normalised side-loads measured during the retransition phase reached 3.4% of the nozzle thrust.

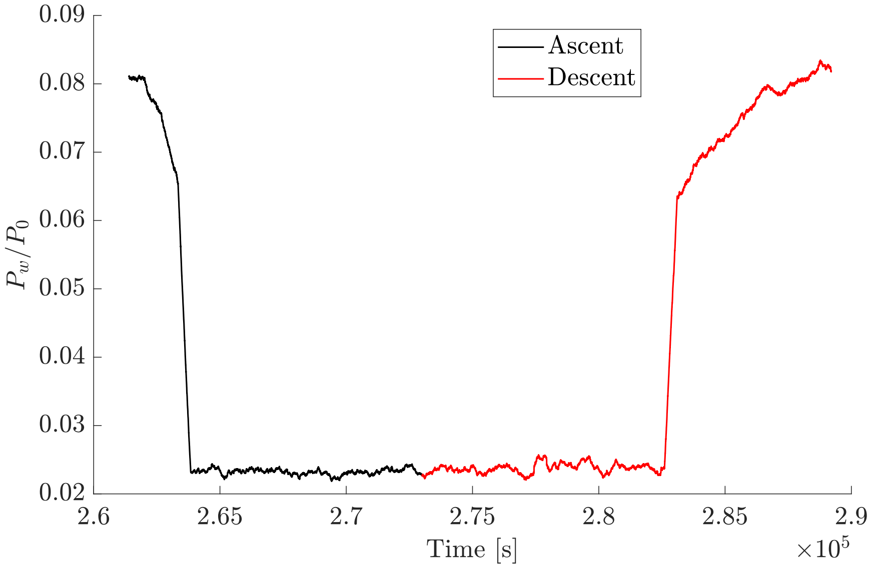

Fig. 3.8 Wall pressure measurements at $x/r_{th} = 7.57$ as a function of time during a transition phase and a retransition phase..

The hysteresis effect

The hysteresis effect is the difference between the transition and retransition NPR. The formula to calculate the hysteresis is given in Eq. 3.2.

$$H = 100 \cdot \frac{NPR_{trans} - NPR_{retrans}}{NPR_{trans}} \tag{3.2}$$

The hysteresis can be seen as a potential indicator of stability. A DBN with a large hysteresis is less likely to flipflop when operated in an environment with large amplitude ambient pressure fluctuations. Conversely, a DBN with a small hysteresis is expected to flip-flop in such conditions, which would generate uncontrolled side-loads and impact the nozzle integrity. Fig. 3.9 shows the specific impulse of the smooth DBN as a function of NPR during an ascent and a descent phase. It distinctly highlights the hysteresis effect in the DBN. The hysteresis measured experimentally for the smooth DBN configuration amounted to 2.1%, a rather small value given the pressure fluctuation during a rocket launch can reach 20% of the ambient pressure.

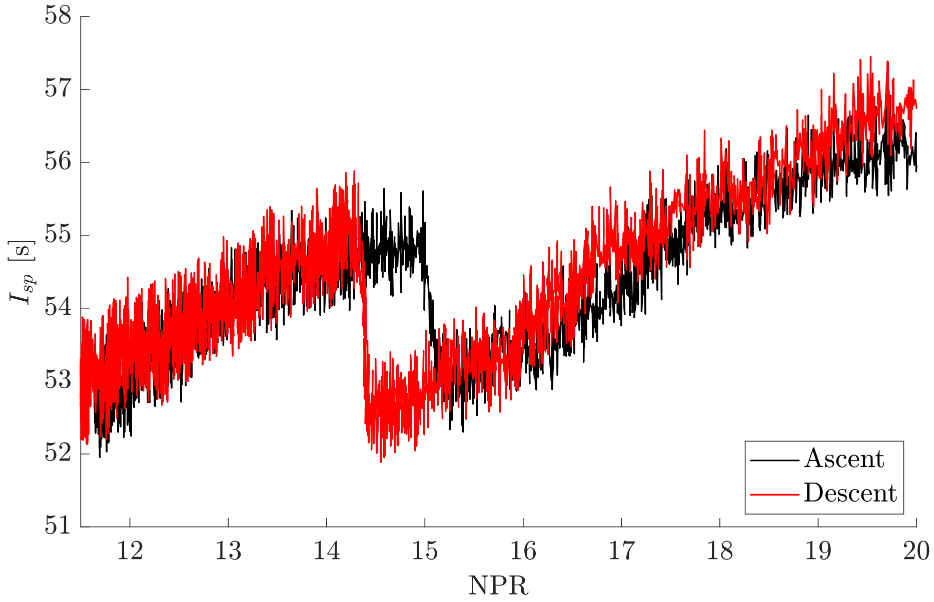

Fig. 3.9 Hysteresis for the smooth DBN configuration

3.3.3 Conclusions

This section provided the experimental results for the smooth DBN. The two operating modes of the DBN, specifically the low-altitude mode and the high-altitude mode, were illustrated using experimental schlieren images. The flow topology for both operational modes was comprehensively detailed, providing insights into the evolution of shock structures during both ascent and descent phases. Through experimental observation, the abrupt transition and retransition processes inherent in DBN equipped with a constant pressure extension were identified. Notably, the internal recompression shock, characteristic of such DBNs, was observed. The NPRs marking the transition of the DBN to the high-altitude mode and its subsequent return to the low-altitude mode were determined to be 14.85 and 14.53, respectively. The nozzle thrust and the evolution of the streamwise wall pressure distribution were analysed during the transition and retransition phases. The experimental results demonstrated a strong agreement with theoretical predictions. The existence of a hysteresis effect between the transition and retransition phases was confirmed and its quantification revealed a modest value of 2.1%. In previous experiments conducted with the same test specimen, a flip-flop phenomenon was identified, contrasting with its absence in the current test campaign. This difference was attributed to the introduction of pressure sensor holes in the extension section, creating discontinuities at the wall surface. This observation highlights the importance of the surface state in influencing the flow dynamics within the DBN.

The next section investigates the $k\omega - SST$ turbulence model capability to predict the DBN flow at various nozzle pressure ratios.

3.4 Standard SST turbulence model

The intrinsic mechanisms governing the DBN transition (resp. retransition) involve small and large time scales, posing a significant challenge in capturing the complete flow dynamics throughout the entire transition (resp. retransition) process. Following the numerous configurations studied during the experimental test campaign, it was decided to focus only on the 2D steady modelling approach at different NPR. In the following sections, we investigate the flow within the smooth DBN for NPR values ranging from 11.67 to 50. These NPR values correspond to the low-altitude, high-altitude, and intermediate operational modes of the DBN. The study utilises the $k\omega$-SST turbulence model, and the simulations are conducted using the ANSYS FLUENT 2022R2 commercial code. Subsequent sections delve into both qualitative and quantitative analyses of the DBN flow. The qualitative assessment involves a comparison of numerical schlieren results with experimental data. Following that, the quantitative analysis compares the streamwise wall pressure distribution and thrust between the simulations and the experimental results.

3.4.1 Qualitative analysis

The DBN operating modes in simulations

Fig. 3.10 shows the DBN mach number contour at different NPRs. At NPR = 11.67, the DBN operates in the low-altitude mode. The jet column is compressed due to the high ambient pressure, causing the boundary layer to separate from the wall, $0.18 \cdot r_{th}$ upstream of the inflexion point. The large recirculating flow region deviates the flow and an oblique shock emerges at the separation onset, which interacts with a Mach disk close to the nozzle symmetry axis. A series of compression and expansion cells continues further downstream to adapt the exhaust jet to the ambient pressure. A significant recirculation bubble exits downstream of the separation point. The ambient flow is accelerated inside the nozzle, inducing a wall pressure smaller than the ambience. The recirculating flow, along with the lower wall pressure on the extension wall, induces a thrust loss of less than 3% called aspiration drag [2]. Two trapped vortices are visible in the separation bubble: one core vortex in the separated flow area, the other close to the wall at the nozzle exit.

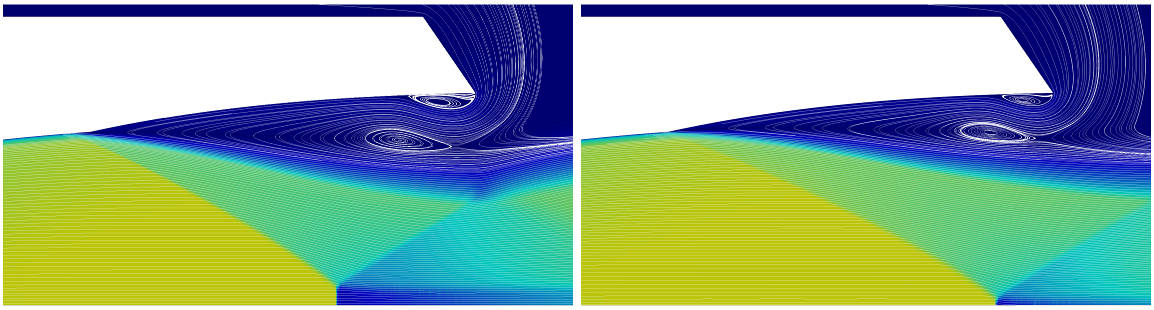

(a) NPR = 11.67

(b) NPR = 14

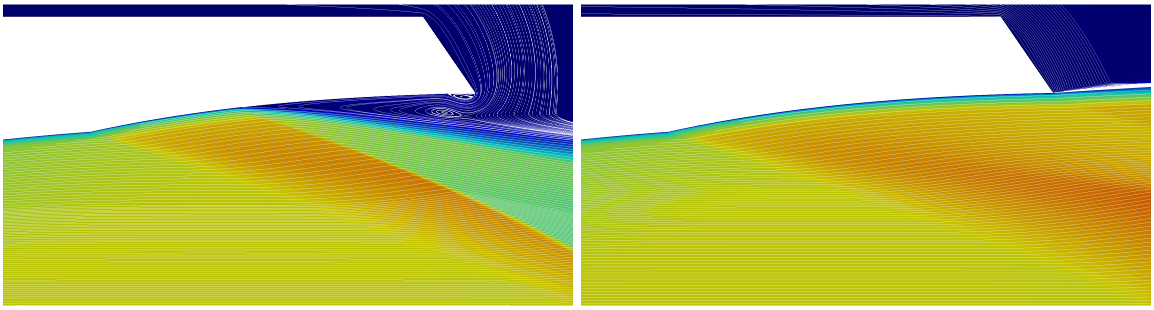

(c) NPR = 17.5

(d) NPR = 50

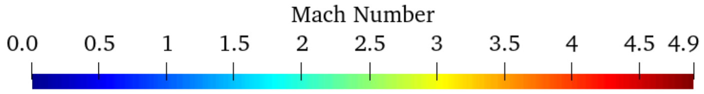

Fig. 3.10 Mach number contour and streamlines at several NPR.

At NPR = 14 (Fig. 3.10b), the DBN still operates in the low-altitude mode. The decrease in ambient pressure causes the reduction of the recirculation bubble size. The two trapped vortices remain visible, though their size distinctively decreased. The lower wall static pressure in the extension section causes the displacement of the boundary layer separation, which occurs in the inflexion region, $0.005 \cdot r_{th}$ downstream of the inflexion point. The shock topology is relatively unchanged when compared to the NPR = 11.67 case. Here, the Mach disk size is reduced due to the lower ambient pressure, but the series of compression and expansion cells in flow are fairly similar.

At NPR = 17.5, the transition from the low-altitude mode to the high-altitude mode started to occur. The decrease in ambient pressure reduces the separation bubble size and the adverse pressure gradient downstream of the separation point. This causes the boundary layer to separate at $x_{sep}/r_{th} = 7.55$, $1.66 \cdot r_{th}$ downstream of the inflexion point. At this NPR, the flow expands at the inflexion point through an expansion fan and remains attached to a portion of the extension wall. The flow expansion causes the Mach number to increase in the extension section before the oblique separation shock slows down the jet. The higher jet speed, caused by the presence of the inflexion point, is slowed down by a normal shock in the vicinity of the nozzle symmetry axis (see Fig. 3.11). The Mach disk interacts with the separation shock and the reflected shock at the triple point. A series of compression and expansion cells follow downstream to adapt the exhaust jet to the ambient pressure in the wind tunnel test section. It is worth highlighting that this flow state, where the separation is located in the extension section, only exists for a short period of time experimentally. Indeed, the extension section is designed as a CP extension, causing a rapid transition between the low-altitude mode and the high-altitude mode in the experiments. The steady-state simulations do not account for the flow dynamics, causing the solutions to converge to these intermediate states.

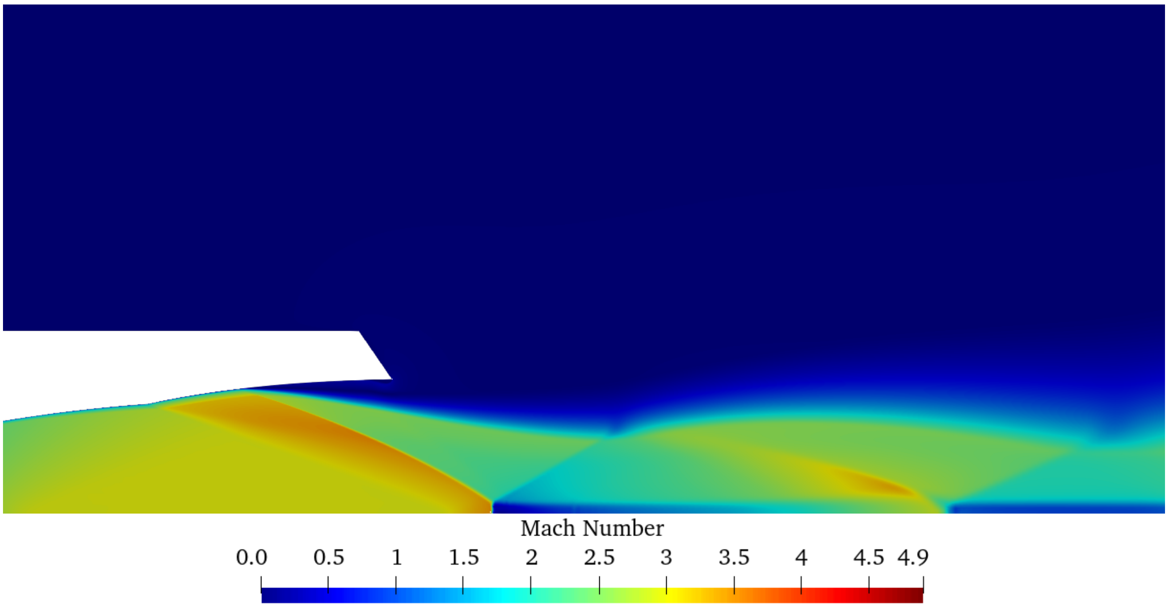

Fig. 3.11 Mach number contour in the smooth DBN at NPR = 17.5.

Fig. 3.12 shows the DBN operating in the high-altitude mode, at NPR = 50. At this NPR, the low ambient pressure causes the flow to expand at the inflexion point and to remain attached to the entire extension section. The boundary layer separates at the nozzle exit, at x_{sep}/r_{th} = 10.22. No recirculation bubble exists in the DBN's core flow. In these conditions, no oblique shock is formed at the nozzle exit or inside the DBN. However, an internal recompression shock emerges in extension, which is a distinctive feature of DBN mounted with a CP extension. This internal recompression shock interacts with a Mach disk downstream, near the nozzle symmetry axis (see Fig. 3.12). A series of compression and expansion cells follow, adapting the exhaust flow to the ambient pressure.

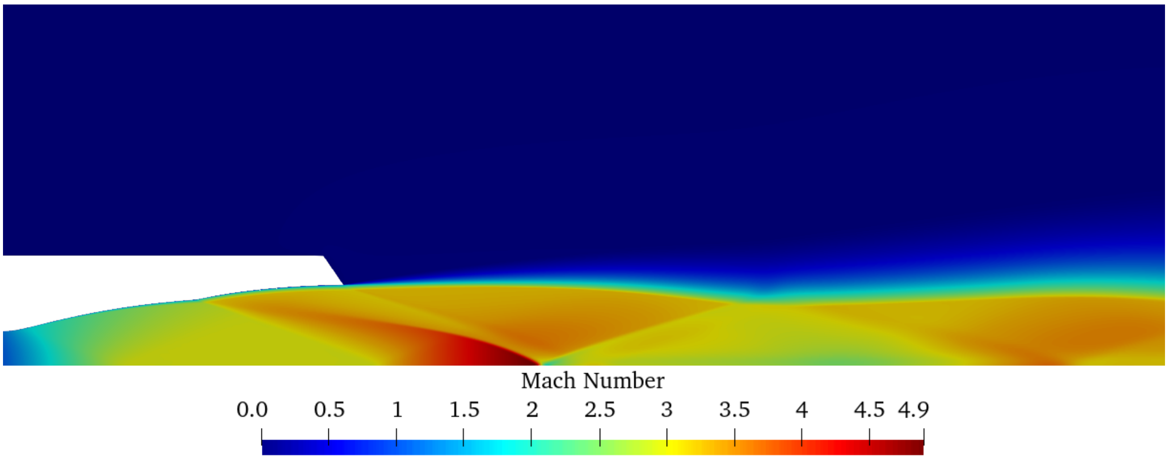

Fig. 3.12 Mach number contour in the smooth DBN at NPR = 50.

Fig. 3.13 shows the normalised density and pressure contours in the smooth DBN for the operating modes discussed above.

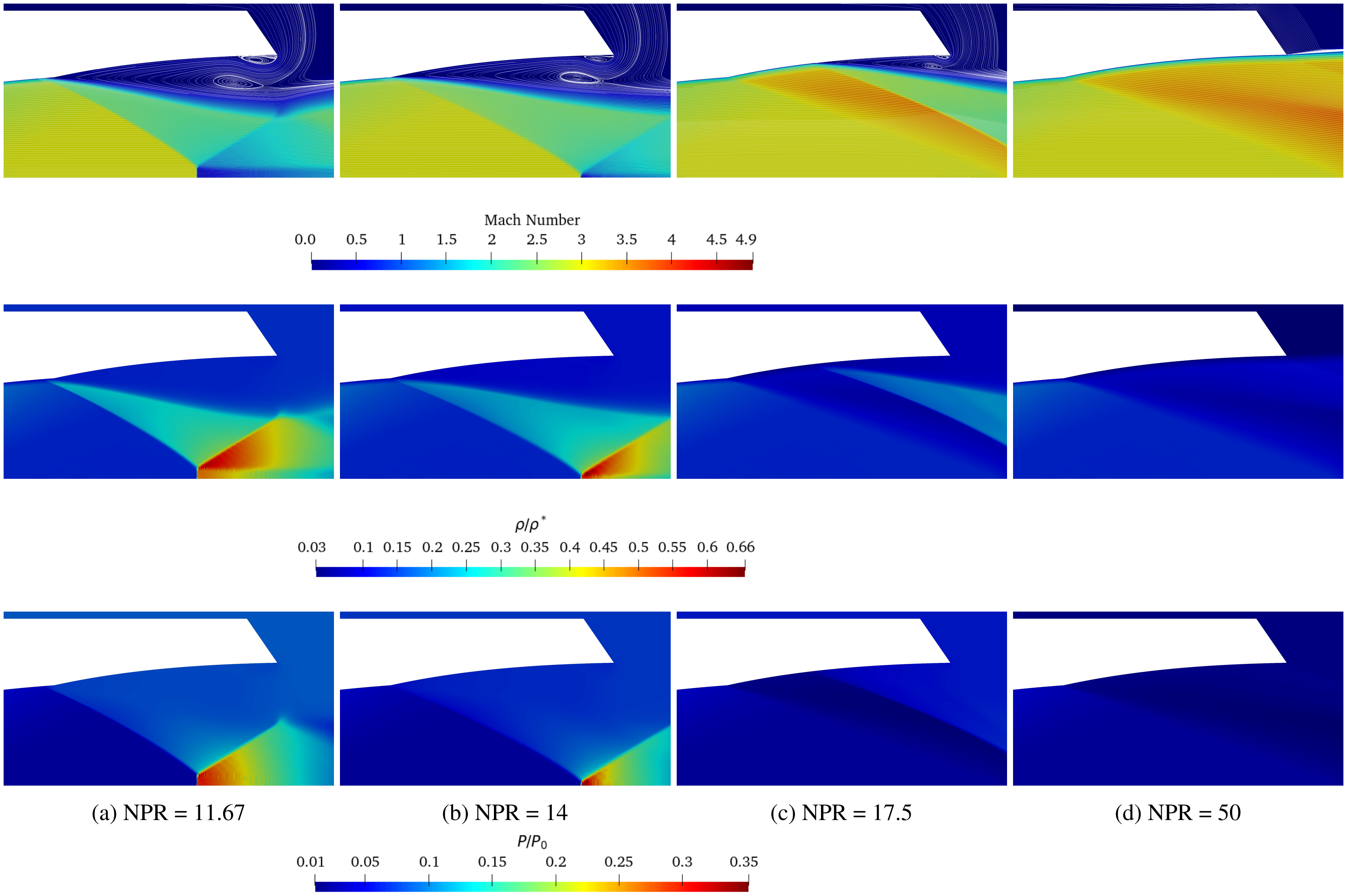

(a) NPR = 11.67 (b) NPR = 14 (c) NPR = 17.5 (d) NPR = 50

Fig. 3.13 Mach number (top), density (middle) and pressure (bottom) contours at several NPR (from left to right)

Experimental and numerical schlieren

This section discusses and compares the flow topology obtained from the experiments and the simulations. In experiments conducted within the EDITH wind tunnel, the schlieren technique proved valuable not only for post-processing analysis of flow topology but also for real-time visualisation of the DBN operational mode on the live screen. Fig. 3.14 to Fig. 3.18 displays the experimental and the numerical schlieren images for several NPRs. The upper half of each figure corresponds to the experimental schlieren, whereas the lower half corresponds to the numerical schlieren. The numerical schlieren S was obtained using Eq. 3.3.

$$S = e^{-15 \cdot G} \tag{3.3}$$

Where G is defined as:

$$G = \frac{||\overrightarrow{grad}\rho|| - ||\overrightarrow{grad}\rho||_{min}}{||\overrightarrow{grad}\rho||_{max} - ||\overrightarrow{grad}\rho||_{min}} \tag{3.4}$$

Fig. 3.14 shows the experimental and numerical schlieren images at NPR = 11.67. Here, the DBN functions in the low-altitude mode and the flow topology agrees well with the experiment. The advantage of the simulation is that it offers insights into flow features that are not experimentally accessible, particularly those occurring within the nozzle.

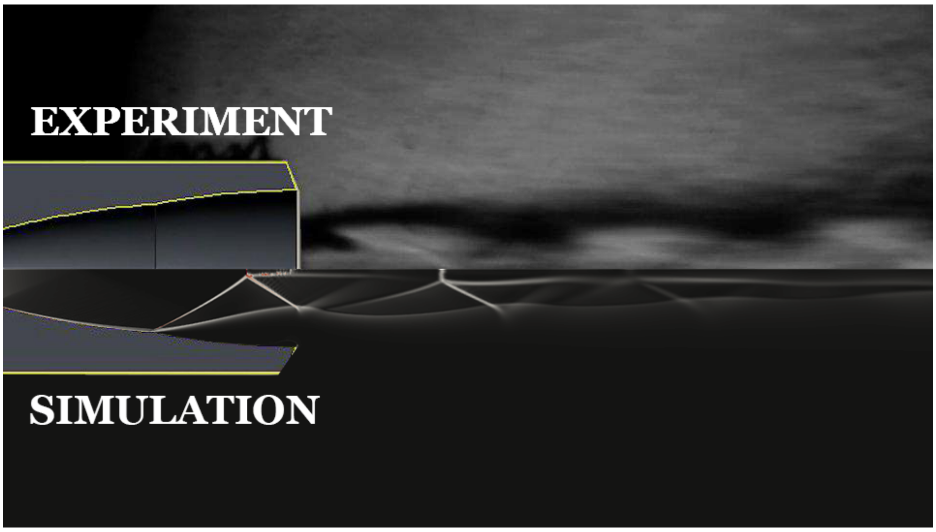

Fig. 3.14 Experimental and numerical schlieren at NPR = 11.67.

The good agreement between the two images suggests that a separation shock exists at the inflexion point (concealed behind the nozzle wall) in the experiment. Further downstream, the separation shock intersects with a Mach disk and a reflected shock at a triple point. The reflected shock then intersects with the jet boundary and is turned into an expansion fan.

Further downstream, a series of compression waves coalesce to form a recompression shock, intersecting with another Mach disk near the nozzle symmetry axis. The intersection of the second Mach disk with the nozzle symmetry axis is predicted slightly upstream by the simulations compared to the experiments. The slip line predicted by the simulation, located downstream of the second Mach disk, agrees well with the one observed experimentally. Moreover, a light line is visible after the nozzle exit in the experiment. The position of this line is relatively symmetric to the slip line downstream of the first Mach disk predicted by the simulation. This indicates the presence of a Mach disk inside the DBN extension section in the experiment. The series of compression and expansion cells generated by the shock structures continues downstream to adapt the exhaust flow to the ambience. One may notice that the exhaust plume is significantly bigger in the experiment than in the simulation. This behaviour may be induced by the low diffusivity of the numerical model.

Fig. 3.15 shows the experimental and numerical schlieren images at NPR = 14. The experiment and the simulation are again in good agreement. At this NPR, the DBN remains in the low-altitude mode and the flow separates at the inflexion point. The flow topology closely resembles that of NPR = 11.67, with the distinction that the lower NPR causes the intersection of shocks with the nozzle symmetry axis to shift further downstream. The several shocks intersection with the symmetry axis are also well predicted by the simulation. The presence of symmetric slip lines between the experiment and the simulation confirms the existence of a Mach disk inside the DBN when operated in these conditions. One may notice the absence of the second Mach disk in the exhaust plume, which emanates from the lower ambient pressure, decreasing the core flow compression.

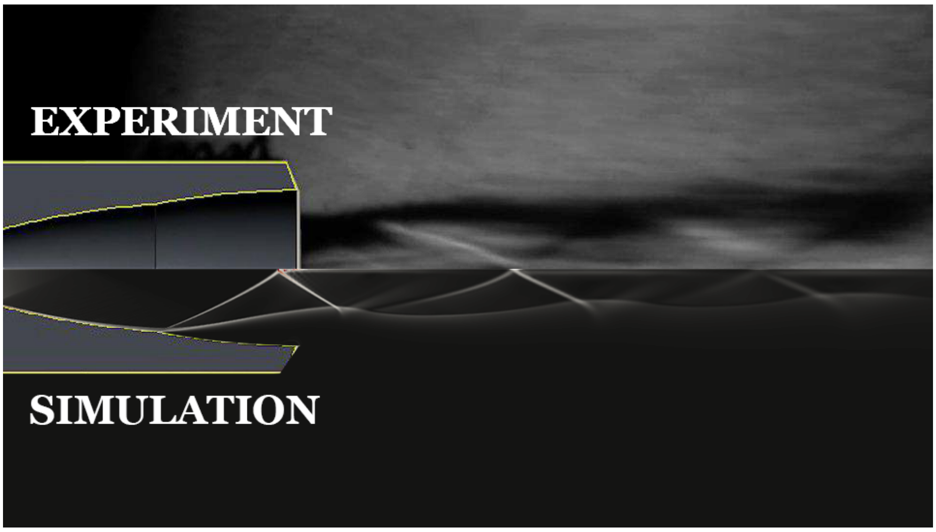

Fig. 3.15 Experimental and numerical schlieren at NPR = 14.

The numerical and experimental schlieren images for NPR = 17.5 are displayed in Fig. 3.16, Here, the transition has taken place experimentally and the flow is attached in the extension profile. However, the simulation under-predicts the separation location and the flow separates in the extension section. The underprediction of the separation location in the $k\omega - SST$ turbulence model is caused by the limitation of the shear stress in the boundary layer [105, 106]. Unlike the last two previous NPR configurations, the flow is accelerated at the inflexion point through an expansion fan. The separation location predicted by the simulation occurs in the extension profile instead of at the nozzle exit. The resulting shock topology is displaced upstream of the experimental findings. As the flow did not fully expand compared to the experiment, a smaller Mach disk is observed on the numerical schlieren. Moreover, the fully attached flow observed experimentally gives rise to a recompression shock in the extension section which does not exist in the simulation.

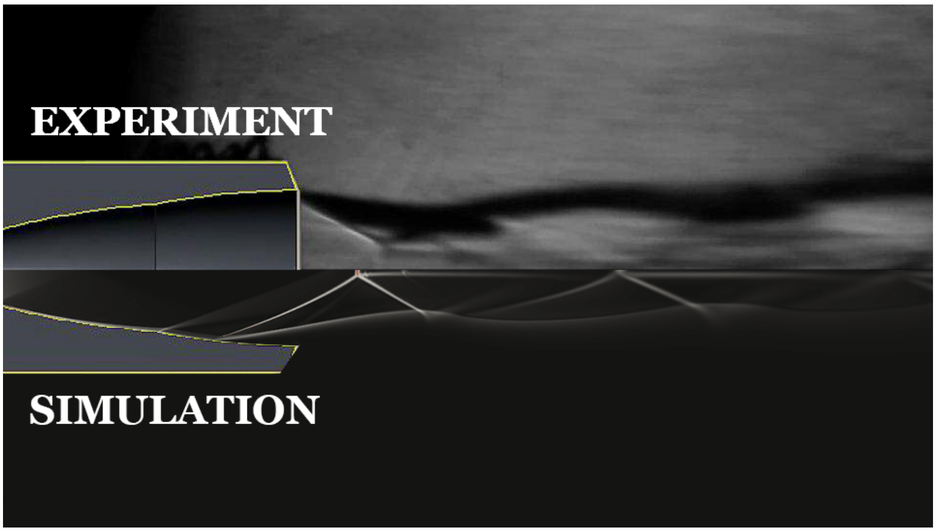

Fig. 3.16 Experimental and numerical schlieren at NPR = 17.5.

At NPR = 23.33, both numerical and experimental schlieren in Fig. 3.17 indicate that the DBN transitioned to the high-altitude mode and the flow separates at the nozzle exit. The flow expands at the inflexion point and fully attaches the extension profile. The constant pressure nature of the extension section gives rise to an internal recompression shock which is well captured by the simulation. The high ambient pressure (relative to the jet pressure) compresses the exhaust jet and an oblique shock wave emerges at the nozzle exit. The oblique shock interacts with a Mach disk and a reflected shock near the nozzle symmetry axis. These primary flow features, including the slip line, correspond remarkably well with the experimental observations. The series of compression and expansion cells present downstream in the simulation do not fully agree with the experimental image. The exhaust plume thickness predicted by the simulation is here again smaller than the jet in the experiments, perhaps due to the low model diffusivity.

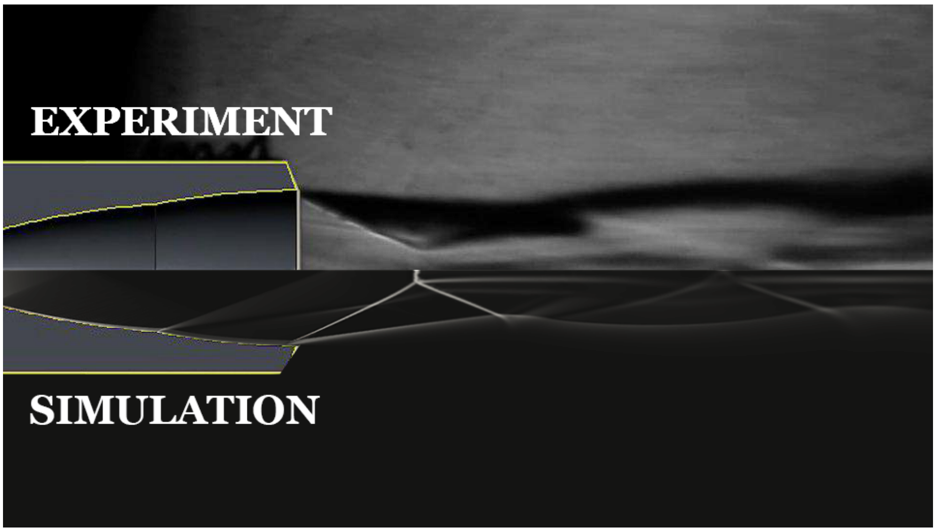

Fig. 3.17 Experimental and numerical schlieren at NPR = 23.33.

Fig. 3.18 shows the experimental and numerical schlieren at NPR = 50. Both show the DBN operating in the high-altitude mode and the simulation agrees with the experiment. The most significant feature of the flow topology is the internal recompression shock and its reflections. An oblique weak shock wave is observed at the nozzle exit in both cases, however, the strength of the shock obtained numerically diminishes fairly rapidly downstream compared to the one observed experimentally. At this NPR, the flow features obtained numerically closely mirror the experiment's and the thickness of the jets' plume is nearly identical between the numerical simulation and the experimental results.

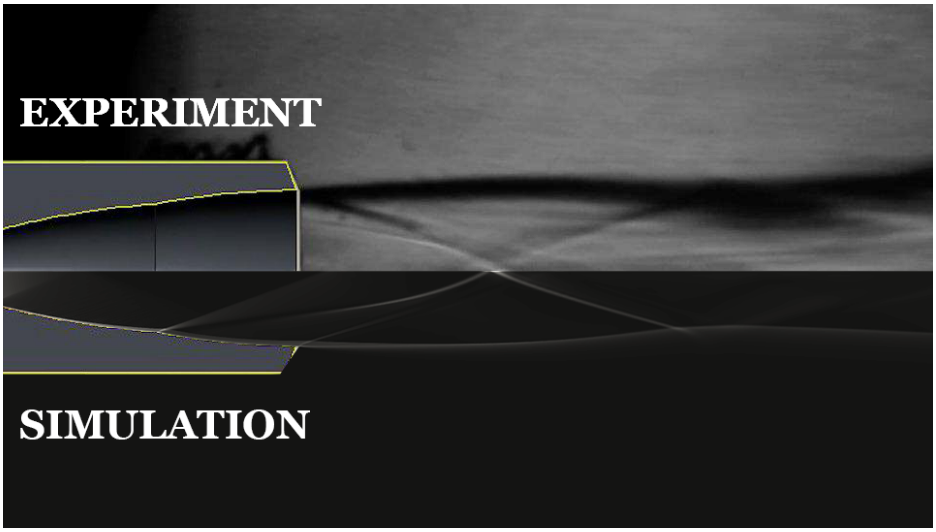

Fig. 3.18 Experimental and numerical schlieren at NPR = 50.

3.4.2 Quantitative analysis

Wall pressure distribution and separation location

Fig. 3.19 to Fig. 3.23 show the experimental and numerical wall pressure distribution for several NPRs. The experimental wall pressure data was averaged using five transitions and five retransitions. Standard deviations are also computed. They also show the numerical wall shear stress distribution. The wall pressure and the streamwise direction axis are respectively normalised by the nozzle feeding total pressure P_0 and the nozzle throat radius r_{th}. The skin friction coefficient was computed with the following relation:

$$C_f = \frac{\tau_w}{\rho^* u^{*2}}, \tag{3.5}$$

where τ_w, ρ^* and u^* are respectively the axial wall shear stress, the density and velocity at the nozzle throat obtained from the isentropic relations.

At NPR = 11.67, both the experiments and the simulations predict the separation location upstream of the inflexion point (see Fig. 3.19). The analysis of the skin friction coefficient indicates that the boundary layer separation occurs at x_{sep}/r_{th} = 5.71, that being $0.18 \cdot r_{th}$ upstream of the inflexion point. After the separation point, a recirculating flow region forms in the extension part and the pressure rapidly increases. The numerical pressure recovery downstream of the separation location is in good agreement with the experiments, which indicates a reasonably well-captured separation bubble size and length. The larger discrepancies from x/r_{th} = 6.10 and x/r_{th} = 8.45 may emanate from the wrong prediction of the jet spreading rate.

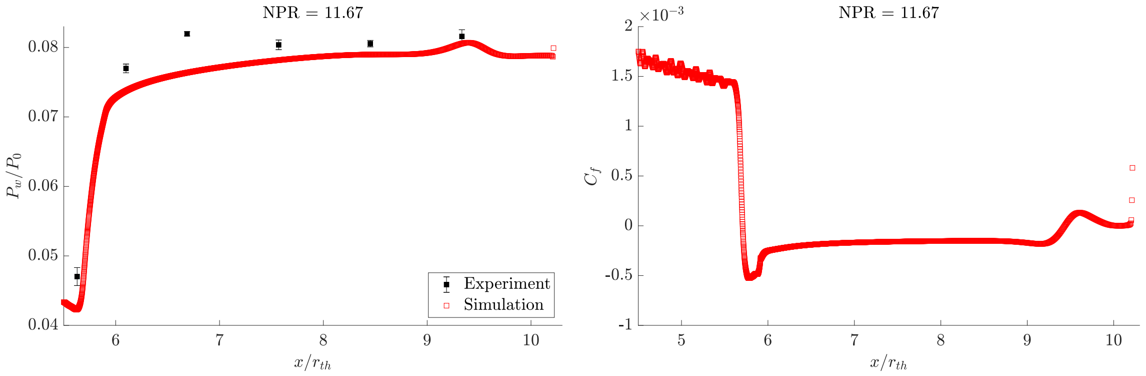

(a) Wall pressure (NPR = 11.67)

(b) Skin friction coefficient (NPR = 11.67)

Fig. 3.19 Streamwise wall pressure and axial skin friction coefficient distribution at NPR=11.67.

Fig. 3.20a shows the DBN wall pressure distribution at NPR = 14. Here, the DBN still operates in the low-altitude mode. Fig. 3.20a and Fig. 3.20b show that the flow separates at the inflexion point, at $x_{sep}/r_{th} = 5.90$. The limited number of pressure sensors in the DBN does not allow to precisely state whether the separation line is ahead, within, or after the inflexion region. Nonetheless, the pressure recovery predicted by the simulation is in good agreement with the experimental data. At $x/r_{th} = 6.69$, the simulation and the experiment show a larger difference in the wall pressure value. The experiment shows a fairly constant wall pressure distribution in the extension part, whereas the simulation indicates an increasing wall pressure. This difference may be caused by the smaller jet spreading rate and/or the wrong recirculation bubble size, which induces a smaller wall pressure in the simulation.

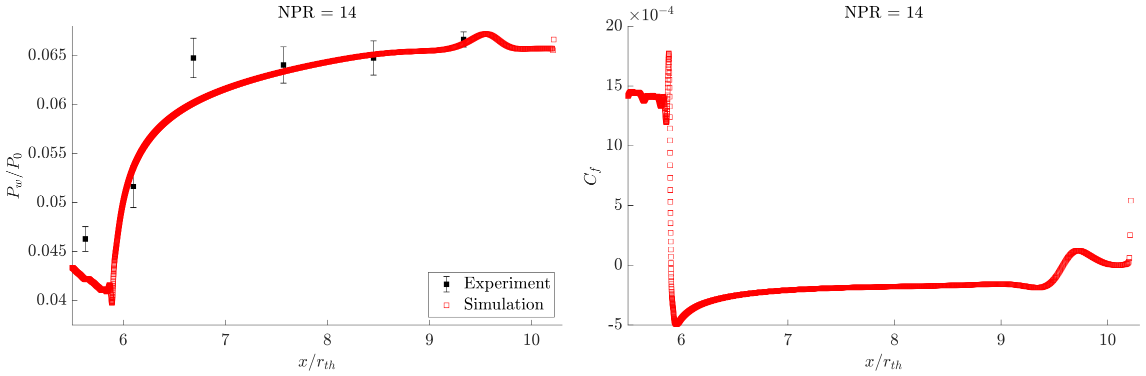

(a) Wall pressure (NPR = 14)

(b) Skin friction coefficient (NPR = 14)

Fig. 3.20 Streamwise wall pressure and axial skin friction coefficient distribution at NPR=14.

Fig. 3.21a shows the wall pressure distribution and wall shear stress in the DBN at NPR = 17.5. The simulation shows that the flow expands at the inflexion point which causes the pressure to decrease. Then the adverse pressure gradient caused by the high ambient pressure causes the boundary layer to separate inside the extension section profile, at $x_{sep}/r_{th} = 7.55$. The flow separation is followed by a sudden rise in wall pressure, caused by the presence of a separation bubble and a separation shock. Meanwhile, the experimental data indicate that the DBN has transitioned from the low-altitude mode to the high-altitude mode. The fully attached flow in the experiment is justified by the rather constant pressure value in the extension section. The $k\omega - SST$ turbulence model's failure to predict the separation location is caused by the inexact values of Reynolds shear stress in the eddy-viscosity hypothesis. The calibration of the turbulence model for a better prediction of the separation location is discussed in a subsequent section.

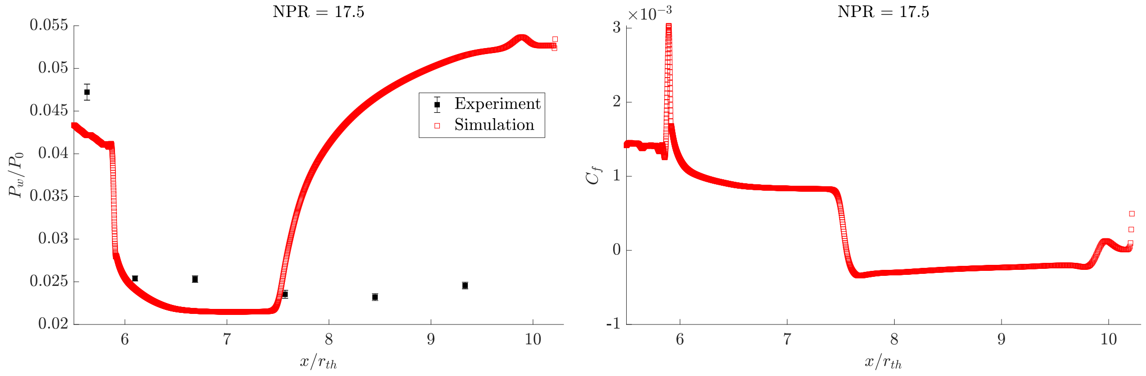

(a) Wall pressure (NPR = 17.5)

(b) Skin friction coefficient (NPR = 17.5)

Fig. 3.21 Streamwise wall pressure and axial skin friction coefficient distribution at NPR=17.5.

At NPR = 23.33 (see Fig. 3.22), the experimental data reveals that the DBN operates in the high-altitude mode. The wall pressure distribution obtained numerically is in good agreement with the experimental values. The flow expands at the inflexion and the pressure decreases. The constant pressure nature of the extension profiles justifies the flat pressure distribution in this section. Further downstream, at $x_{sep}/r_{th} = 9.78$, the boundary layer separates under the adverse pressure gradient induced by the higher ambient pressure. Nonetheless, the lack of pressure sensors at the nozzle exit does not allow us to state whether the flow has separated upstream of the nozzle exit, or if the flow is attached to the entire extension section.

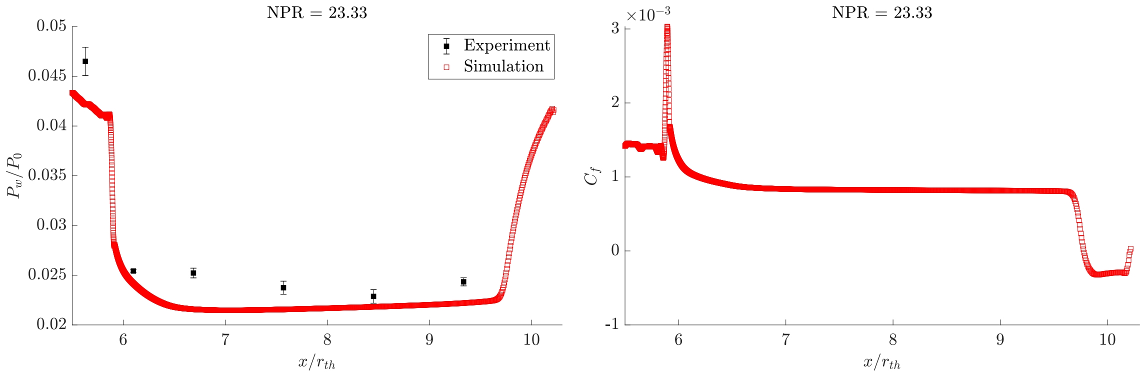

(a) Wall pressure (NPR = 23.33) (b) Skin friction coefficient (NPR = 23.33)

Fig. 3.22 Streamwise wall pressure and axial skin friction coefficient distribution at NPR=23.33.

Finally, Fig. 3.23 shows the wall pressure distribution and shear stress in the DBN at NPR = 50. At this NPR, the DBN operates in the high-altitude and the boundary layer separates at the nozzle exit. The numerical wall pressure distribution agrees well with the experiment. In both cases, the flow is attached to the base and the extension profile. The axial skin friction coefficient, displayed in Fig. 3.23b, confirms that flow separation does not occur in the DBN extension profile. Here again, the geometrical constraints did not permit the presence of a pressure sensor in the vicinity of the nozzle exit to verify the wall pressure drop obtained numerically at the nozzle exit. Nevertheless, it is safe to say that low ambient pressure in the wind tunnel test section causes the exhaust jet to be underexpanded. As a consequence, an expansion fan emerges from the nozzle exit, inducing a sharp drop in pressure.

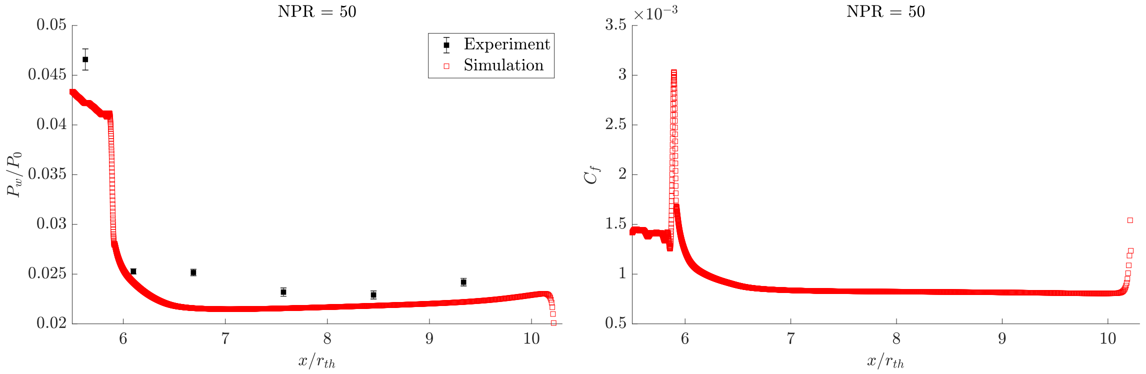

(a) Wall pressure (NPR = 50) (b) Skin friction coefficient (NPR = 50)

Fig. 3.23 Streamwise wall pressure and axial skin friction coefficient distribution at NPR=50.

Fig. 3.24 displays the separation location predicted by the $k\omega - SST$ turbulence model as a function of NPR. It shows that the separation location increases with the NPR, indicating that the steady RANS simulation cannot predict the sudden transition from the low-altitude mode to the high-altitude mode. However, the simulations provide insights into the flow inside the DBN during the different operating modes, which are in good agreement with the experimental data. The last part of this section will discuss the thrust measured experimentally and numerically.

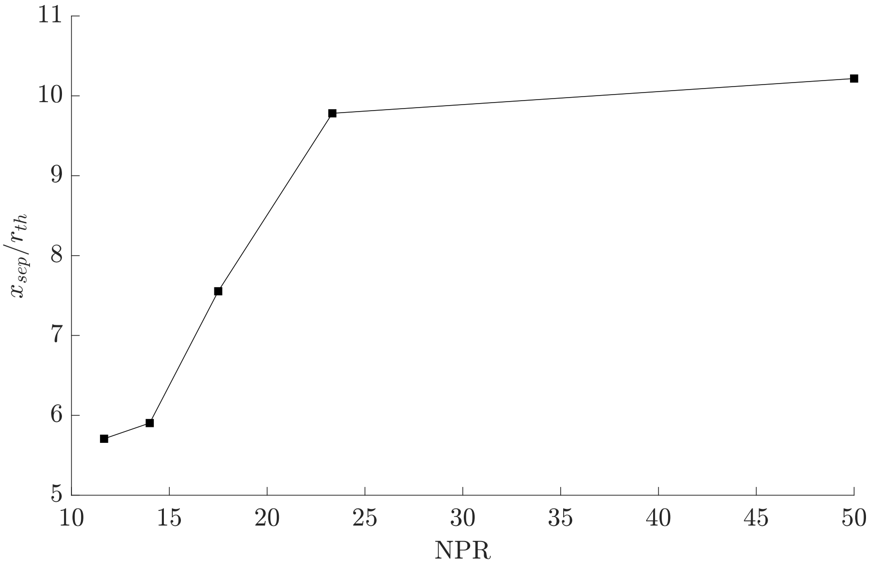

Fig. 3.24 Separation point location as a function of NPR.

Numerical thrust validation

The total force acting on the nozzle is given by:

$$F = \iint_{S_{wall}+S_{inlet}} (p - p_a)\overrightarrow{n}\,\overrightarrow{dS}, \tag{3.6}$$

where $\overrightarrow{n}$ is the nozzle wall normal vector.

Projecting the previous equation on the x-axis, the force generated by the fluid on the nozzle is computed as:

$$F = -\iint_{S_{inlet}} (p - p_a) r(x_0)\, dr d\theta - \iint_{S_{wall}} (p - p_a) r(x)\, dr d\theta \tag{3.7}$$

where x_0 represents the nozzle inlet abscissa.

In axisymmetric simulations, the flow variables are independent of θ. Assuming a constant pressure at the nozzle inlet and after further simplification, the expression becomes:

$$F = -\pi R_{inlet}^2 \cdot (P_0 - P_a) - 2\pi \int_{l_{wall}} (p - p_a) r(x) \frac{dr(x)}{dx} dx \tag{3.8}$$

The thrust generated by the nozzle in a 2D axisymmetric simulation finally becomes:

$$F_x = \pi R_{inlet}^2 \cdot (P_0 - P_a) + 2\pi \int_{l_{wall}} (p - p_a) r(x) \frac{dr(x)}{dx} dx \tag{3.9}$$

The local nozzle radius gradient in Equation. 3.9 is calculated using a second-order, centred scheme:

$$\left.\frac{dr}{dx}\right|_i = \frac{r_{i+1} - r_{i-1}}{x_{i+1} - x_{i-1}} + \mathscr{O}(\Delta x^2) \tag{3.10}$$

Calculating the thrust using the above equation we plot the thrust as a function of NPR in Fig. 3.25a. The thrust coefficient, visible in Fig. 3.25b is computed using the nozzle thrust, pressure and cross-section area as $C_{fx} = F_x/(P^* A^*)$, where the star superscript indicates the values at the nozzle throat. The experimental values in Fig. 3.25 have been averaged using nearly fourteen data points obtained from the transition and retransition phases. The error bars represent the standard deviation.

For NPR < 15, the DBN operates in the low-altitude mode. The flow is attached to the base nozzle and separates in the vicinity of the inflexion point. As a result, the DBN performance curve aligns with the conventional, theoretical performance of the base nozzle. A slight difference is noticeable between the thrust measured during the transition phases and the retransition phases. This gap emanates from multiple factors, namely the feeding total temperature and pressure changes during the experiment, instabilities in the flow, etc...

For NPR > 15, the flow reattaches in the extension profile and the DBN operates in the high-altitude mode. In this case, the DBN aligns with the performances of a conventional nozzle with the same expansion ratio as the DBN extension section. Fig. 3.25 reveals two main characteristics of DBNs: the early transition and the need to delay the transition phase to achieve better performances.

Fig. 3.26 shows the relative difference between the experimental and numerical thrust as a function of NPR, where the difference is calculated as:

$$\left.\varepsilon_{F_x}\right|_{trans/retrans} = \frac{F_{x trans/retrans} - F_{xCFD}}{F_{x trans/retrans}} \tag{3.11}$$

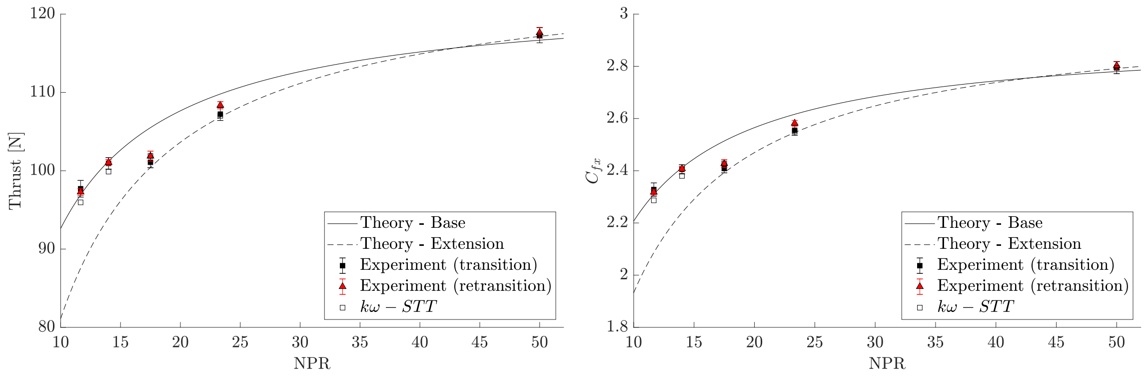

(a) Thrust as a function of NPR (b) Thrust coefficient as a function of NPR

Fig. 3.25 Performance curves for the theory, the experiments, and the simulations.

It shows that the numerical thrust agrees with the experimental measurements. In the NPR range investigated, the relative difference between the experimental and numerical thrust was less than 2% when calculated during the transition phases, and less than 1.5% when calculated during the retransition phases.

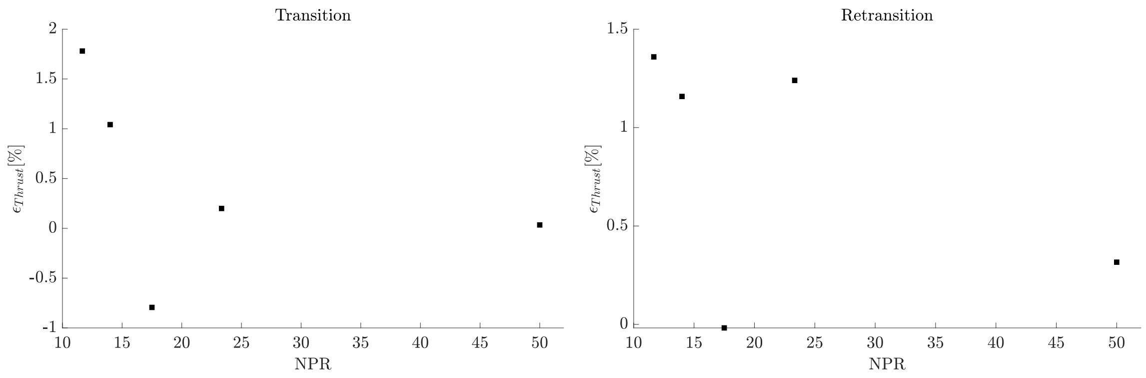

(a) Relative difference during transition phases (b) Relative difference during retransition phases

Fig. 3.26 Relative difference in thrust between experiments and simulations during transition and retransition phases

3.4.3 Conclusions

This section discussed the numerical simulations performed with the standard $k\omega - SST$ turbulence model. The flow field, the wall pressure distribution and the dual-bell nozzle performance were analysed and compared to the experimental data. The experimental and numerical schlieren images were generally in good agreement during the different operating conditions, which allowed for identifying the flow features inside the DBN. The discrepancies between the numerical and experimental schlieren, especially at NPR = 17.5 were attributed to the underprediction of the separation location by the turbulence model. The wall pressure computed numerically agreed with the experiment on most NPR investigated, except NPR = 17.5 where the separation was underpredicted. The issue of eddy-viscosity turbulence models to predict flow separation in supersonic flow with shock wave boundary layer interaction was brought to light.

The next section investigates the differences between the flow predicted by the Spalart-Allmaras turbulence model and the $k\omega - SST$ turbulence model.

3.5 Spalart-Allmaras turbulence model

The choice of turbulence modelling is critical for correctly predicting the key variables in a flow. Simulations were performed to study the flow in DBNs and the Spalart-Allmaras (SA) turbulence model was often considered to accurately reproduce the key features of DBNs' flows. As a result, the SA turbulence model appeared as a serious candidate to perform the numerous simulations in the thesis. This section qualitatively and quantitatively compares the results obtained with the SA turbulence model to those of the $k\omega - SST$ (SST) turbulence model.

3.5.1 Qualitative analysis

Fig. 3.27 shows the Mach number contours and the normalised density contours at different NPRs. On each sub-figure, the upper half corresponds to the contours obtained with the SST model and the lower half corresponds to those obtained with the SA model. The contours indicate that the SA model is able to compute the DBN flow in the low-altitude mode and the high-altitude mode with a reasonable level of relevance. From NPR = 11.67 to NPR = 17.5, Fig. 3.27 indicates that the boundary layer separation in the SA simulations always occurs downstream of the location predicted by the SST model. At NPR = 11.67, the flow separation occurs $0.18 \cdot r_{th}$ upstream of the inflexion point for the SST model, whereas $0.03 \cdot r_{th}$ downstream of the inflexion point for the SA model, corresponding to a relative difference of 3.7%. Fig. 3.28a shows the experimental and numerical schlieren at NPR = 11.67. As in the SST model, a separation shock forms downstream of the separation point and interacts with a small Mach disk at a triple point. The shock reflected from the triple point interacts with the jet plume further downstream and is turned into an expansion fan. Then, a series of compression waves coalesce to form another shock.

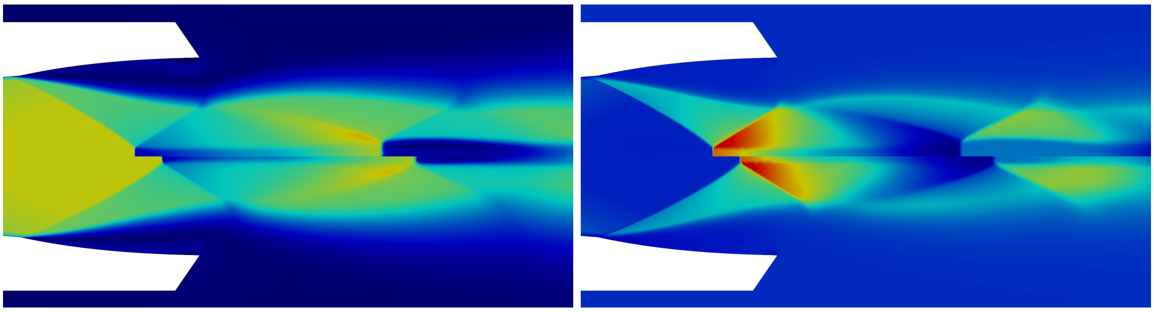

(a) Mach number contour (NPR = 11.67) (b) Density contour (NPR = 11.67)

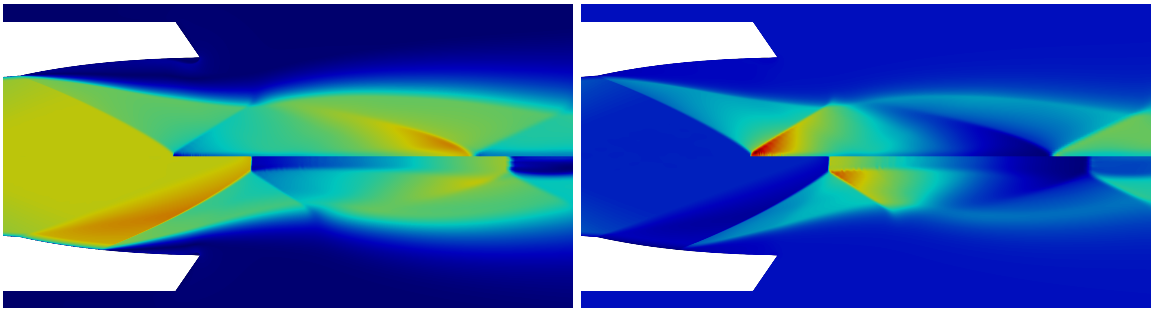

(c) Mach number contour (NPR = 14) (d) Density contour (NPR = 14)

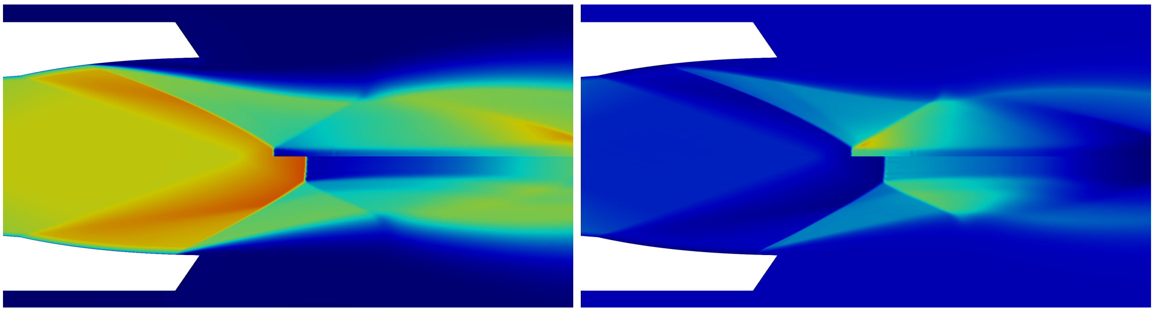

(e) Mach number contour (NPR = 17.5) (f) Density contour (NPR = 17.5)

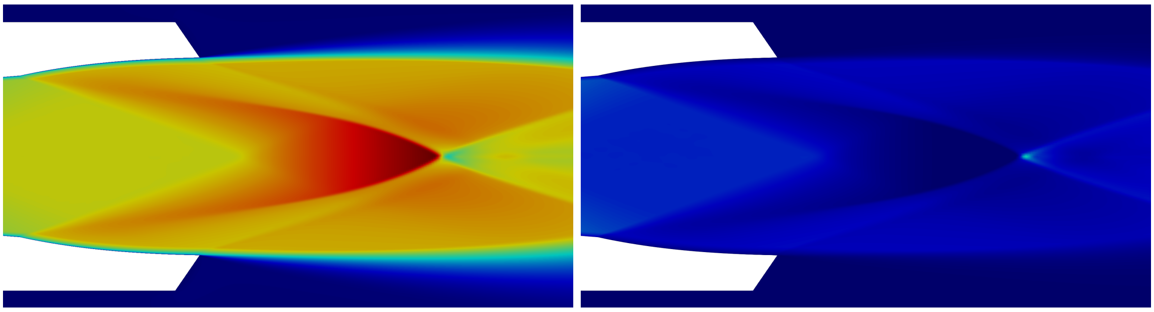

(g) Mach number contour (NPR = 50) (h) Density contour (NPR = 50)

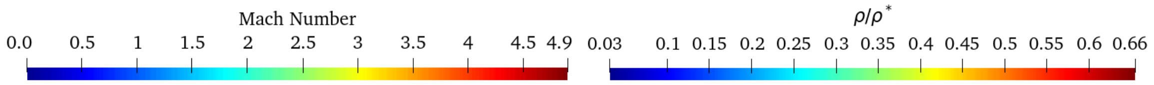

Fig. 3.27 Mach number and density contours at several NPR for $k\omega - SST$ (upper half of the nozzle contour) and Spalart-Allmaras (lower half of the nozzle contour).

The latter’s intersection with the nozzle symmetry axis occurs further downstream in the simulation, indicating the SA model overpredicts the separation location.
The misprediction of the separation location is even more striking at NPR = 14. In these conditions, the transition from the low-altitude mode to the high-altitude mode has begun for the SA simulation, in which the boundary layer separates at $x_{sep}/r_{th} = 7.87$, $1.98 \cdot r_{th}$ downstream of the inflexion point. The overprediction of the separation is confirmed by the experimental schlieren in Fig. 3.28b, which reveals that the DBN operates in the low-altitude mode at NPR = 14. Conversely, the simulations performed with the SST turbulence model resulted in better separation predictions than the SA model for NPR = 11.67 and NPR = 14.

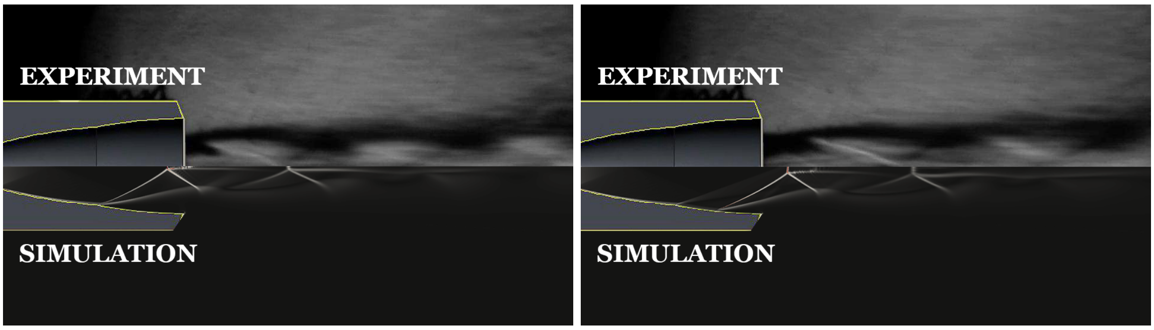

(a) NPR = 11.67 (b) NPR = 14

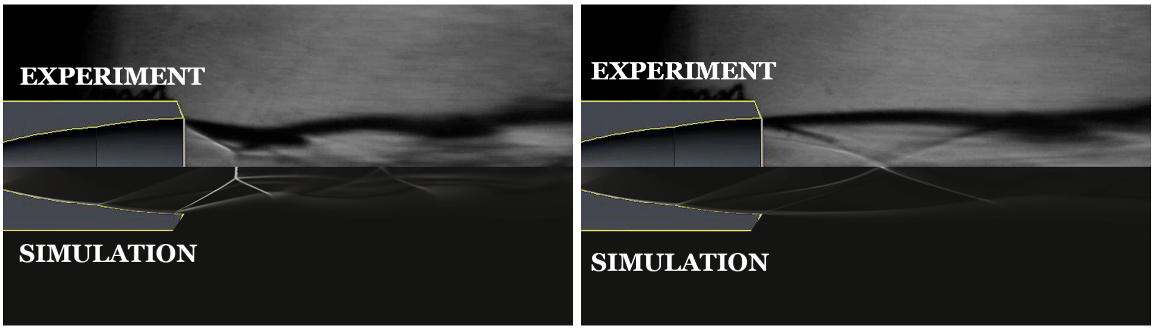

(c) NPR = 17.5 (d) NPR = 50

Fig. 3.28 Experimental and numerical (Spalart-Allmaras) schlieren imaging for several NPR.

At NPR = 17.5, Fig. 3.27e indicates that the DBN has almost fully transitioned to the high-altitude mode for the SA model, whereas the SST model predicts the separation in the extension section, at $x_{sep}/r_{th} = 7.55$. At this NPR, the experimental schlieren in Fig. 3.28c reveals that the boundary layer separation is predicted more accurately by the SA model than the SST’s. The oblique shock, the Mach disk and slip line, the internal recompression shock, and the series of compression and expansion cells are well captured by the SA simulation. The simulation performed with the $k\omega - SST$ turbulence model underpredicts the separation point, situated inside the extension profile, whereas the transition has occurred in the experiment.

At NPR = 50, in Fig. 3.27 and Fig. 3.28, the simulations (both SST and SA) are in good agreement with the experimental flow topology. No significant difference was noticed regarding the Mach number or density contour either. The analysis of the turbulent viscosity ratio (μ_t/μ) in the low-altitude mode and the high-altitude mode in Fig. 3.29 reveals that the SA turbulence model is notably more diffusive.

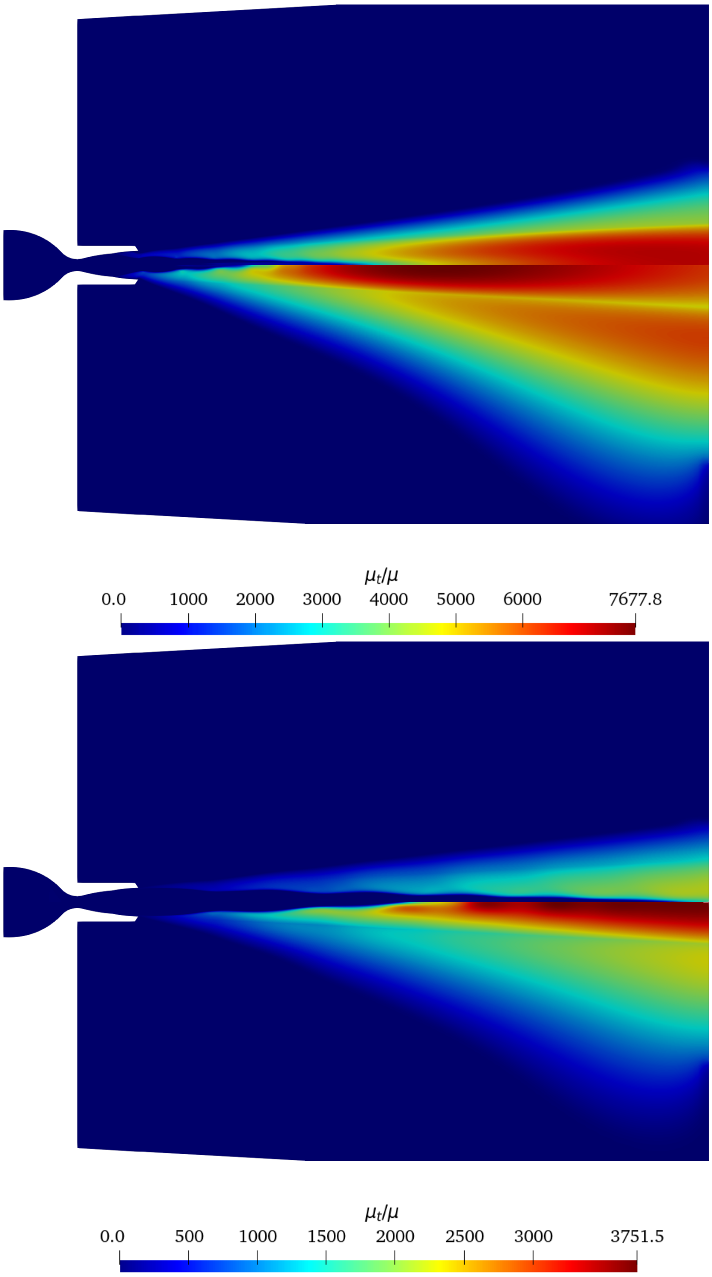

Fig. 3.29 Turbulent viscosity ratio for $k\omega - SST$ (upper half of the nozzle contour) and Spalart-Allmaras (lower half of the nozzle contour) at NPR = 11.67 (top) and NPR = 50 (bottom).

3.5.2 Quantitative analysis

Wall pressure distribution and separation location

Fig. 3.30 displays the streamwise wall pressure distribution of the SST and SA model for NPR = 11.67 to NPR = 50. Fig. 3.30a and Fig. 3.30b confirm the qualitative analysis performed in Section 3.5.1, which indicated the overprediction of the separation point by the SA model at NPR = 11.67 and NPR = 14. The wall pressure distribution comparison between the simulations and the experiments at these NPRs shows that the SA model overpredicts the separation onset. In the low-altitude mode (NPR = $\{11.67; 14\}$), the SST model agrees well with the experimental data. The predictions for the pressure plateau and separation point are fairly close to the experimental results. Meanwhile, the SA model overpredicts the separation point and underpredicts the pressure plateau values. The inflexion point plays a key role in the discrepancy between the SST and the SA model. The overprediction of the separation point by the SA model causes the flow to expand in the inflexion region. The smaller recirculation bubble causes the recirculating flow speed to increase, inducing a lower wall static pressure.

At NPR = 17.5, the SA turbulence model outperforms the SST model (see Fig. 3.30c). The experimental wall pressure distribution suggests that the DBN has transitioned to the high-altitude mode. The pressure distribution was well captured by the SA model, which shows a constant pressure distribution in the extension section. The SST turbulence model underpredicts the separation location and the flow separates from the nozzle in the extension section, at x_{sep}/r_{th} = 7.55. The wall pressure increase predicted by the SA model in the vicinity of the nozzle exit is caused by the flow separation. Unfortunately, the lack of pressure sensors in this area does not allow one to state whether the flow separates upstream of the nozzle exit.

For NPR equal to or larger than 23.33, the SA and SST models yielded similar streamwise wall pressure distributions. Both turbulence models predicted a constant pressure in the extension profile which was in good agreement with the experimental wall pressure measurements. For NPR = 23.33, the SA model predicted the separation near the nozzle exit, at 98.8% of the extension section length, whereas the SST model separates upstream of the nozzle exit, at 95.8% of the extension length. The presence of the separation bubble and separation shock downstream induces the sudden rise in wall pressure, as visible in Fig. 3.30d.

Fig. 3.30f shows the flow separation location as a function of the NPR for the two turbulence models. It reveals that the separation location predicted by the two models differs significantly when the DBN operates in the vicinity of the transition NPR. The difference in separation location resulted in major differences in flow topology and wall pressure distribution, even for a separation displacement of 1.5% at NPR = 11.67.

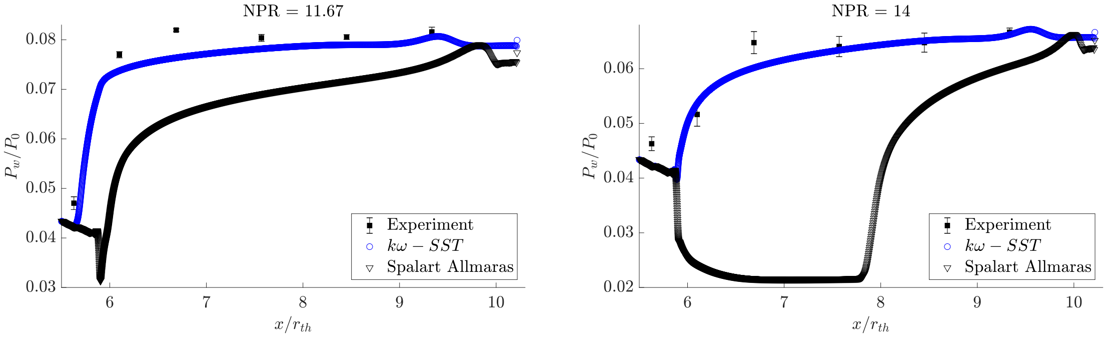

(a) Wall pressure (NPR=11.67) (b) Skin friction coefficient (NPR=14)

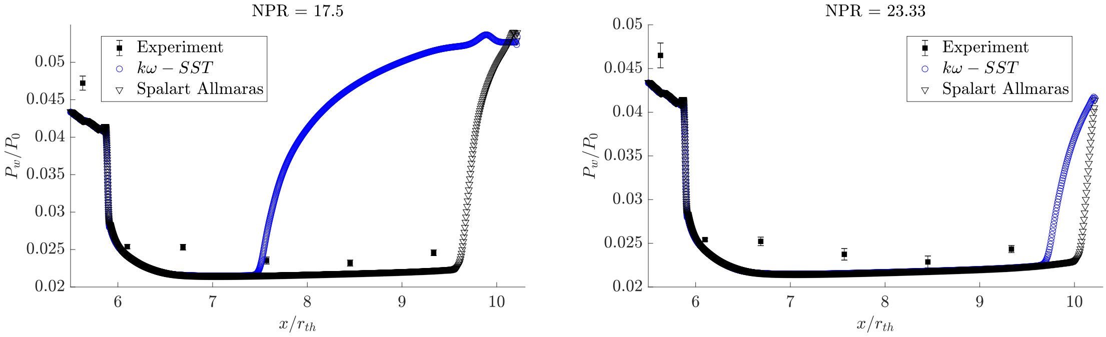

(c) Wall pressure (NPR=17.5) (d) Skin friction coefficient (NPR=23.33)

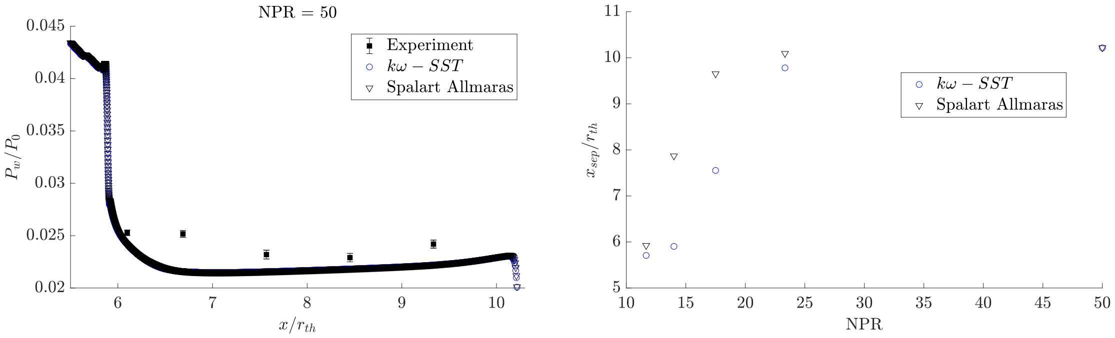

(e) Wall pressure (NPR=50) (f) Separation point location.

Fig. 3.30 Streamwise wall pressure distribution and separation location as function of NPR.

Numerical thrust validation

The thrust is computed for each NPR under investigation using Eq. 3.9 and displayed in Fig. 3.31. The thrust values obtained in both models are in good agreement with the experimental data. The separation location misprediction by the SA model when the DBN operates in the low-altitude mode (NPR < 14.89) induces lower thrust values compared to the experiments.

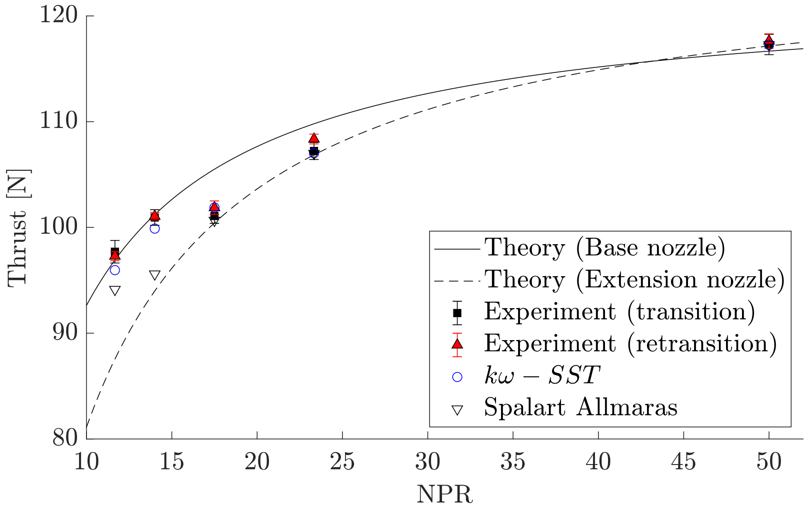

Fig. 3.31 Experimental and numerical thrust for the standard SST model and the Spalart-Allmaras model as a function of NPR.

Fig. 3.32 shows the relative error in thrust between the numerical simulations and the experiment. It shows that the thrust computed with the SST model remains within 2% of the experimental data for all of the NPRs investigated. The differences between the SST model and the SA model are marginals for NPRs > 23.33. Below this NPR, the gap between the two widens. In the simulations performed with the SA turbulence model, the relative difference in thrust between the simulations and the experiments reached 5.3% and 5.4% during the transition and retransition phases, respectively.

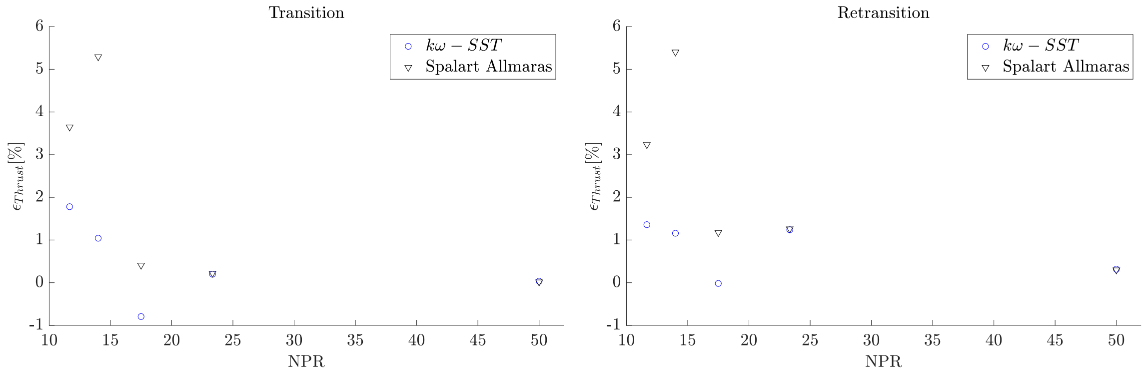

(a) Relative difference during ransition phases (b) Relative difference during retransition phases

Fig. 3.32 Relative difference in thrust between experiments and simulations during transition and retransition phases

3.5.3 Conclusions

The analysis performed above suggests that the prediction of separation location should be improved for both turbulence models. To improve the simulations, one should overpredict the separation location at NPR = 17.5 using the SST model, or under-predict the separation location at NPR = 11.67 and NPR = 14 using the SA model. Nevertheless, the $k\omega - SST$ turbulence flow predictions were generally in better agreement with the experiments than the Spalart-Allmaras model whether the attention was focused on the flow topology, the wall pressure distribution, or the thrust. Consequently, the $k\omega - SST$ turbulence model is chosen to perform the numerical simulations in this thesis. The next section discusses the calibration of an important parameter in the turbulence model to improve its flow separation prediction capability.

3.6 Turbulence model calibration

3.6.1 Introduction to the shear stress limiter

The $k\omega - SST$ turbulence model presented a fairly good agreement with the experimental data (see Section 3.4), whether the focus was made on the flow topology, the streamwise wall pressure distribution or the thrust. It was only at NPR = 17.5 that the SST model significantly mispredicted the separation location. At this NPR, the SST model predicted the boundary layer separation inside the extension section of the DBN, whereas the transition had fully occurred experimentally. The prediction of the separation location is significantly influenced by a parameter within the turbulence model known as the structure parameter, which constrains the wall shear stress in the boundary layer. This section examines the effect of the turbulence model's structure parameter, denoted as a_1, on the separation point location in the smooth DBN.

In the $k\omega - SST$ turbulence model, the turbulent viscosity is computed as

$$\mu_t = \frac{\rho k}{\omega} \frac{1}{\max\left[\frac{1}{\alpha^*}, \frac{SF_2}{a_1 \omega}\right]} \tag{3.12}$$

with $\alpha^* = 1$ in the high-Reynolds-number formulation of $k\omega$ model, resulting in

$$\mu_t = \frac{\rho k}{\omega} \frac{1}{\max\left[\frac{SF_2}{a_1 \omega}\right]} \tag{3.13}$$

where S is the strain rate magnitude, a_1 the structure parameter, and F_2 the blending function. The structure parameter, therefore appears to be of critical importance in the behaviour of the SST model. Here, the structure parameter a_1 is employed to restrain the turbulent shear stress within a certain fraction of the turbulent kinetic energy in the inner section of the boundary layer. This parameter, whose value was set to 0.31 in the standard SST model, is calibrated to yield fairly reliable results in various canonical flows containing mild adverse pressure gradients. However, for high-speed flows with SWBLI, an adjustment to the coefficient becomes necessary to enhance the accuracy of the flow separation prediction.

The influence of the structure parameter a_1 on diverse flows, including those at high Mach numbers with SWBLI, was explored in [105]. The investigation demonstrated that a structure parameter value of 0.355 effectively predicted the separation size and turbulent statistics in the experiment. Further simulations using the $k\omega$-SST turbulence model were conducted in [106]. This study affirmed that achieving accurate predictions of the separation location and pressure recovery in RANS simulations necessitated the precise capture of the jet spreading rate. This was facilitated by increasing the structure parameter to a value of 0.35 and adjusting the diffusion coefficients of k and ω.

In the present work, the influence of the structure parameter in the smooth DBN is investigated for several NPRs. The simulations were initially performed with a structure parameter $a_1 = 0.31$ (standard SST). Then, three other values of a_1 were investigated: 0.33, 0.355, and 0.39. The study compares the simulations to the experiments for a DBN operating in the low-altitude mode and the high-altitude mode.

Fig. 3.33 shows the y^+ streamwise distribution in the high-altitude mode on the left and the wall boundary layer profile on the right for the standard and modified structure parameters. Both figures indicate that the boundary layer remains properly resolved and behaves conventionally. The impact of the structure parameter on the main flow topology will be discussed in a subsequent quantitative section.

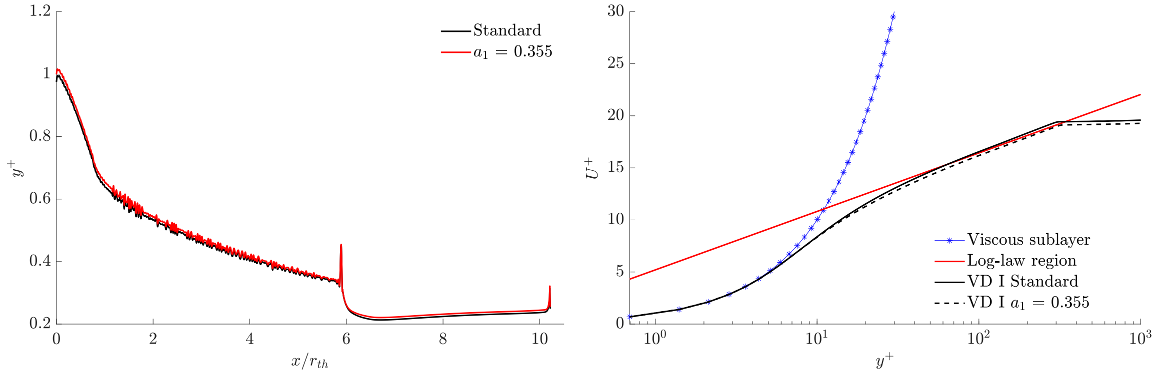

(a) Streamwise y^+ distribution from the throat.

(b) Boundary layer profiles.

Fig. 3.33 Streamwise y^+ distribution and boundary layer profiles for different two structure coefficients at x/r_{th} = 5.36 and NPR = 50.

3.6.2 Qualitative analysis

Fig. 3.34 shows the Mach number and density contours in the smooth DBN operating at different NPRs. For each figure, the upper half of the nozzle contour shows the results obtained with the standard SST model ($a_1 = 0.31$), and the lower half corresponds to a modified SST model with structure parameter $a_1 = 0.355$. The set of figures exposes the effect of the structure parameter on the separation location and the flow topology.

The standard structure coefficient naturally causes the model to underpredict the separation location. Increasing its value increases the turbulent shear stress in the boundary layer, causing the separation front to move downstream. The separation location displacement induced by the change in structure parameter is minor for NPR = 11.67 and NPR = 14.

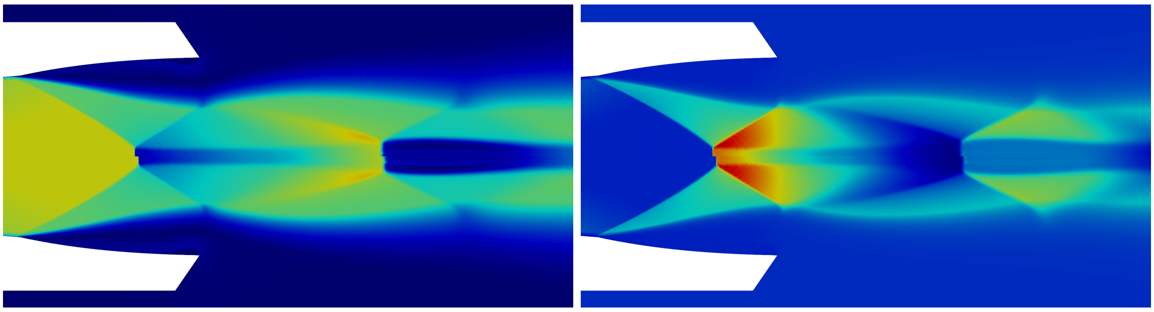

(a) Mach number contour (NPR = 11.67) (b) Density contour (NPR = 11.67)

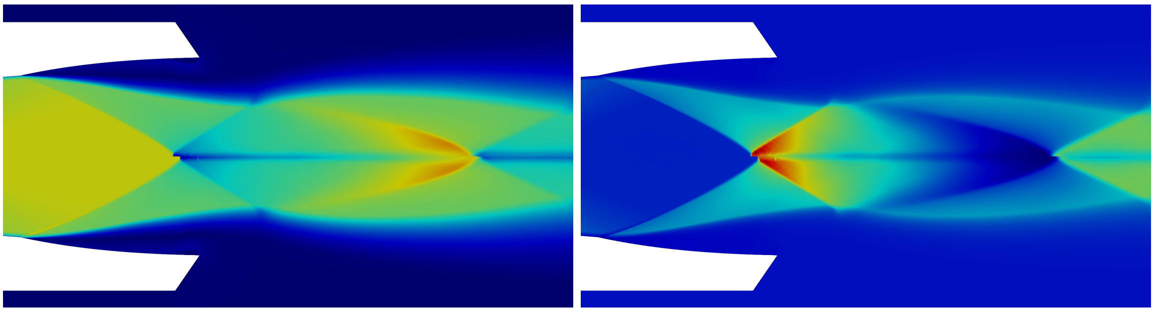

(c) Mach number contour (NPR = 14) (d) Density contour (NPR = 14)

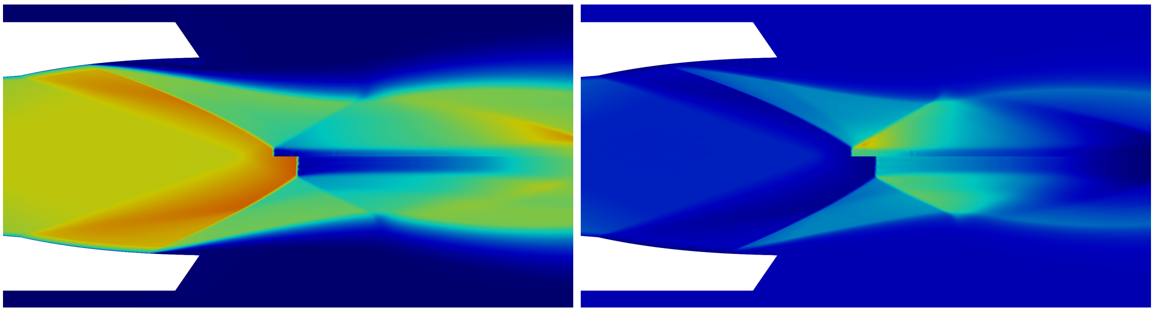

(e) Mach number contour (NPR = 17.5) (f) Density contour (NPR = 17.5)

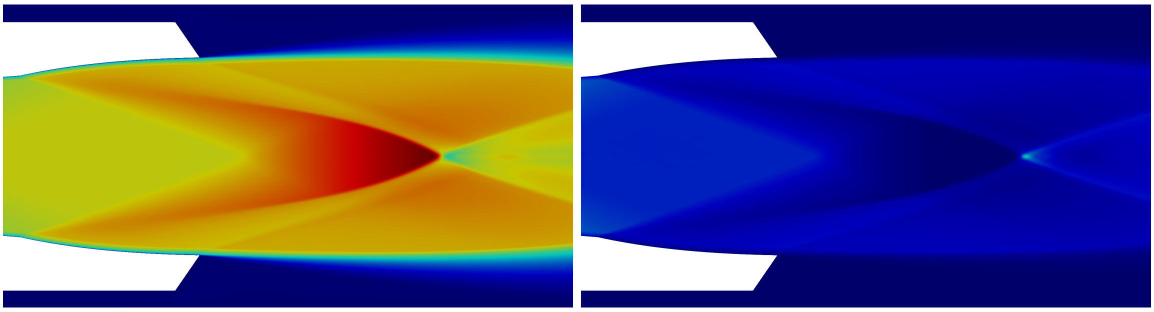

(g) Mach number contour (NPR = 50) (h) Density contour (NPR = 50)

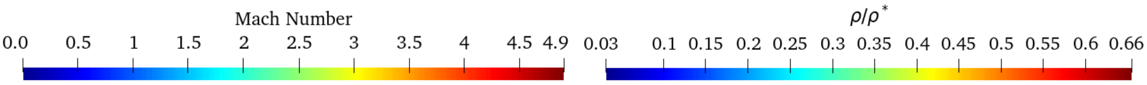

Fig. 3.34 Mach number and density contours at several NPR for $a_1 = 0.31$ (upper half of the nozzle contour) and $a_1 = 0.355$ (lower half of the nozzle contour).

For the latter two and a structure coefficient of 0.355, the separation locations were located at x_{sep}/r_{th} = 5.83 and x_{sep}/r_{th} = 5.98 respectively, compared to the standard coefficient. These changes in separation location correspond to an increase of 2.1% and 1.4% respectively. The small change in the separation position for the latter NPRs is favourable for the present study as the simulations agreed with the experiments when the DBN operates in these conditions. The schlieren images in Fig. 3.35a and Fig. 3.35b show that the flow topology prediction by the modified SST model agrees well with the experimental schlieren.

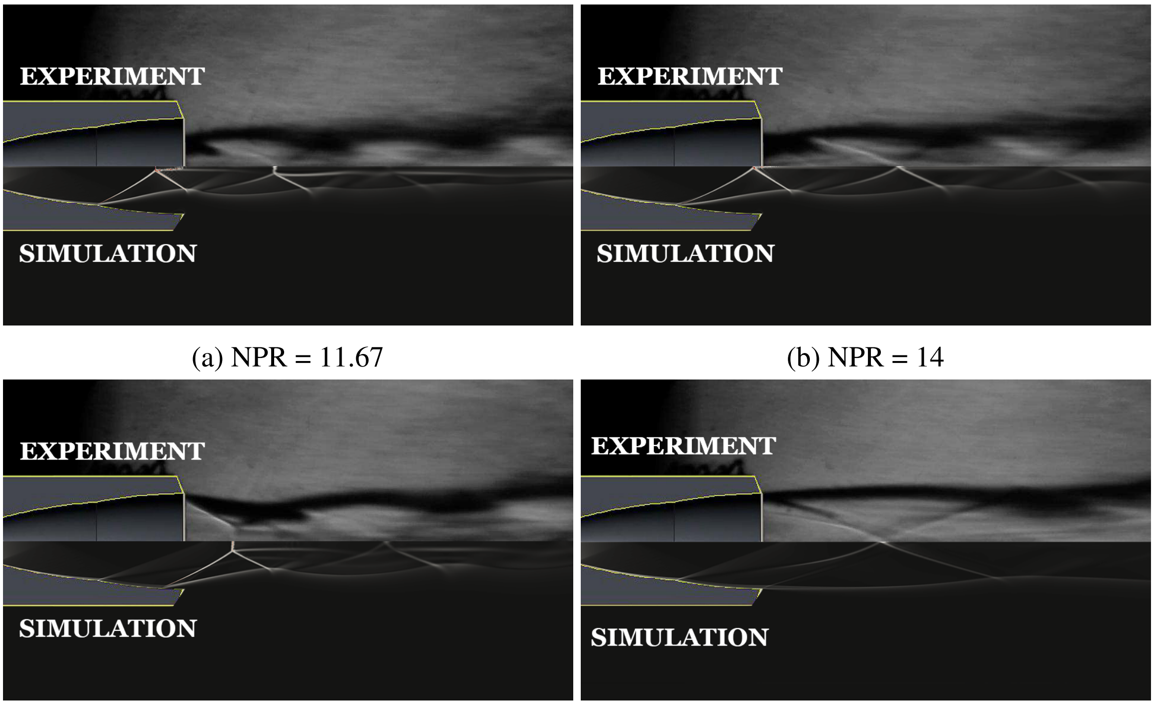

(a) NPR = 11.67

(b) NPR = 14

(c) NPR = 17.5

(d) NPR = 50

Fig. 3.35 Experimental and numerical schlieren imaging using $a_1 = 0.355$ for several NPR.

The standard SST model underpredicts the separation point at NPR = 17.5, inducing a mismatch in flow topology compared to the experiment. By increasing the structure parameter to 0.355, the separation location displacement was greater than for the lower NPRs. In this case, the separation front moved from x_{sep}/r_{th} = 7.55 to x_{sep}/r_{th} = 9.05, an increase of 19.9%. This significant increase aligns with the intent of improving the turbulence model's capability of predicting the separation position. The further separation location yields a better agreement in flow topology when compared to the experiments. The numerical and experimental schlieren given in Fig. 3.35c reveal that the oblique shock wave, the Mach disk, the slip line, and the series of compression/expansion obtained for $a_1 = 0.355$ agree fairly well.

At NPR = 50, Fig 3.34g shows the DBN in the high-altitude mode. The standard SST and the modified SST yielded identical results and both exhibited excellent agreement with the experimental data. The schlieren images in Fig. 3.35d show the perfect prediction of the internal recompression shock topology with the modified SST model when the DBN operates in the high-altitude mode.

3.6.3 Quantitative analysis

Wall pressure distribution and separation location

Fig. 3.36a to Fig. 3.36e show the streamwise wall pressure distribution for the different structure parameters at several NPR. The figures reveal the influence of the structure parameter on the flow separation location, which is pushed downstream as the parameter increases. The separation location difference between $a_1 = 0.355$ and $a_1 = 0.39$ is marginal in all figures. This observation suggests that above $a_1 = 0.355$, the structure parameter does not significantly affect the separation location.

At NPR = 11.67, Fig. 3.36a shows that the furthest separation point displacement was reached for $a_1 = 0.39$ with $x_{sep}/r_{th} = 5.84$, $0.05 \cdot r_{th}$ upstream of the inflexion point. The latter corresponds to a displacement of 2.3% compared to the standard SST mode, indicating the low influence of the structure parameter when the DBN operates at this NPR. In this case, the limited influence of the structure parameter prevented the expansion of the flow through the inflexion region and the displacement of the shock system downstream, as observed when using the Spalart-Allmaras turbulence model. The overprediction of the separation point in the SA model led to mild flow expansion through the inflexion and noticeable differences between the experimental and numerical schlieren.

At NPR = 14, the boundary layer separates at the inflexion point in the standard SST simulation. Increasing the structure parameters to 0.33, 0.355 and 0.39 moves the flow separation abscissa downstream by 0.7%, 1.4%, and 1.5%, respectively. This increase of a_1 pushed the boundary layer up to $0.1 \cdot r_{th}$ downstream of the inflexion point, causing the flow to expand in the inflexion region. Compared to the standard SST model, the separation location difference for $a_1 = 0.355$ and $a_1 = 0.39$ modestly displace the jet's shock topology downstream, which improves the agreement between the numerical and the experimental observations (see Fig. 3.35b). The separation displacement obtained with the change in structure parameter yielded better flow topology than the SA turbulence model. In the latter, the separation point was situated at $x_{sep}/r_{th} = 7.87$, nearly 32% further than with the modified SST model with $a_1 = 0.355$, resulting in large differences in flow topology when compared to the experiments.

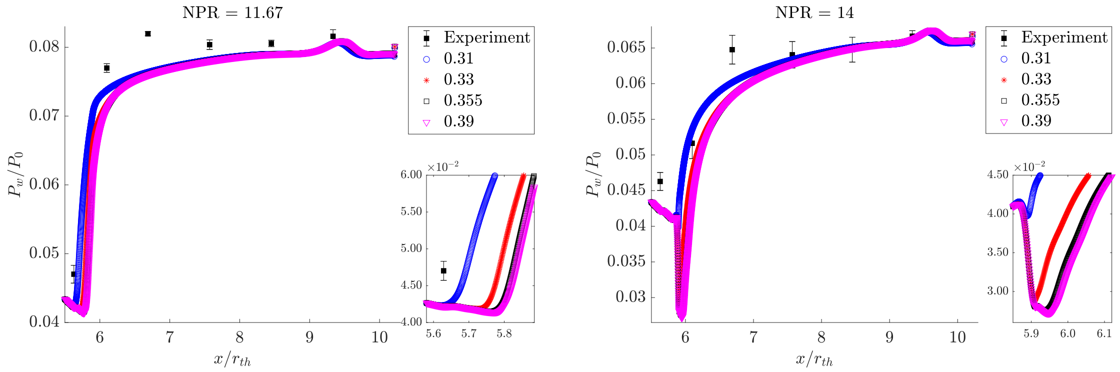

(a) Wall pressure (NPR = 11.67)

(b) Wall pressure (NPR = 14)

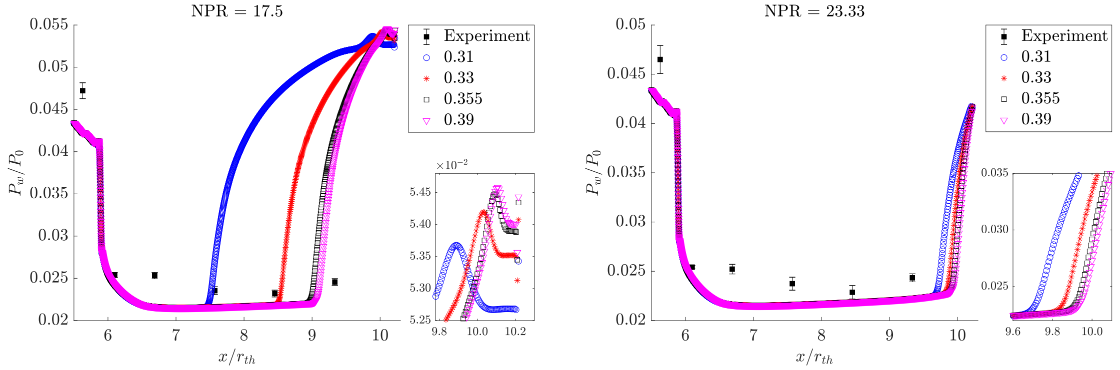

(c) Wall pressure (NPR = 17.5)

(d) Wall pressure (NPR = 23.33)

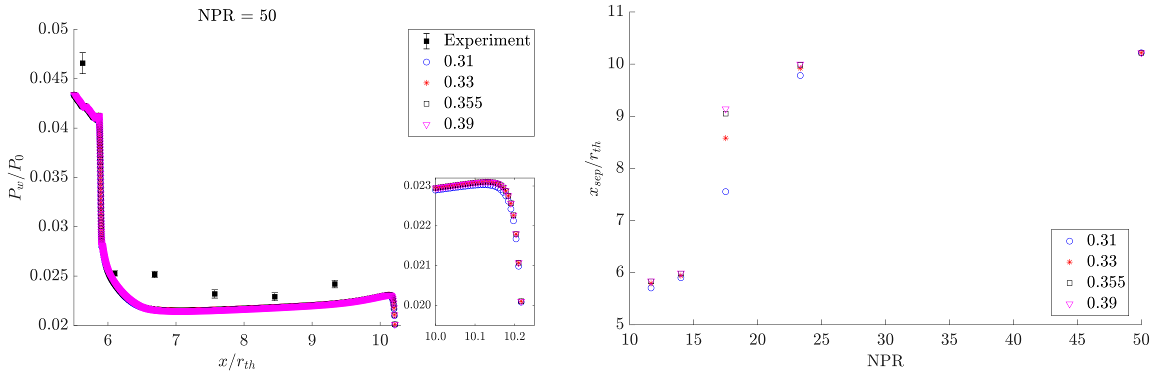

(e) Wall pressure (NPR = 50)

(f) Separation point location.

Fig. 3.36 Streamwise wall pressure distribution as a function of NPR for different structure coefficients.

Fig. 3.36c shows the wall pressure distribution at NPR =17.5 for the different structure parameters. The separation point displacement limitation was again identified, with a 1% relative difference in separation point between the two highest structure parameters. Furthermore, Fig. 3.36c indicates that the separation front could not be fully pushed at the nozzle exit, even for the highest structure parameter. For a_1 = 0.355, the separation front position increased by 19.9% compared to the standard SST model. The numerical schlieren for a_1 = 0.355, given in Fig. 3.37, distinctly shows the improvement in predicting the flow topology when the structure parameter is adapted to the flow under investigation. It reveals that a_1 = 0.355 (value suggested in the literature) and a_1 = 0.39 give separation positions that best correspond to the experimental flow topology.

The effect of the structure parameter on the separation location becomes less visible at NPR = 23.33 (see Fig. 3.36d). The increase in the structure parameter resulted in a separation position increase of 2.2% at most for a_1 = 0.39.

At NPR = 50, Fig. 3.36e shows that the curves fall onto one another and the boundary layer separates at the nozzle exit. It also indicates that the structure parameter does not affect the wall pressure distribution in the attached supersonic flow. Fig. 3.36f summarises the effect of the structure parameter on the separation position for the range of NPR investigated.

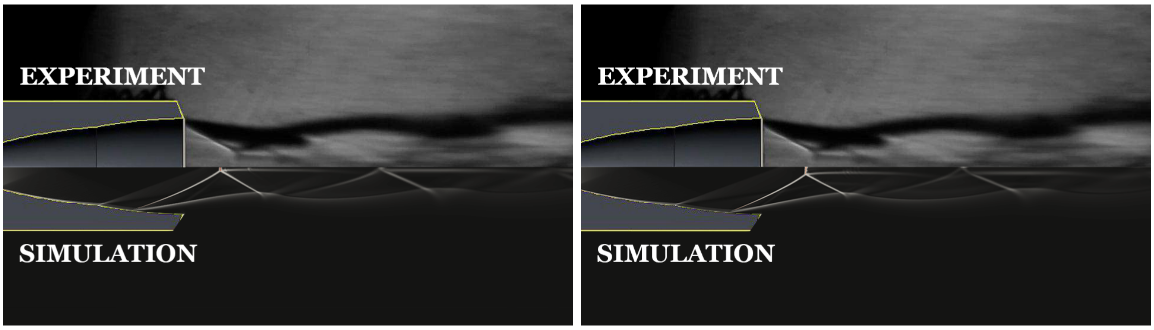

(a) $a_1 = 0.31$ (Standard SST model) (b) $a_1 = 0.33$

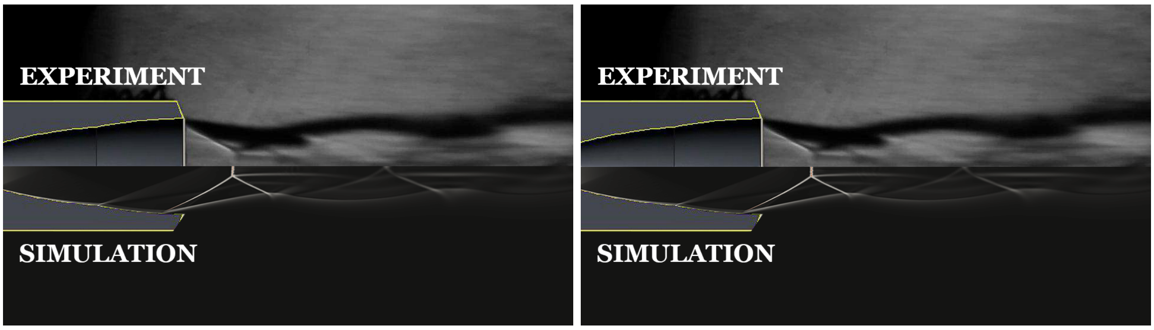

(c) $a_1 = 0.355$ (d) $a_1 = 0.39$

Fig. 3.37 Experimental and numerical schlieren images at NPR = 17.5 for several structure parameters.

Numerical thrust validation

The thrust was calculated at each NPR and for all structure parameters investigated. Fig. 3.38 shows the thrust coefficient as a function of NPR for different values of a_1. The thrust calculated in the Spalart-Allmaras simulations is added to the figure. It shows that the structure parameter had a limited impact on the thrust coefficient. The significant change in the DBN flow topology, particularly for NPR = 17.5 did not result in a substantial shift in thrust compared to the standard $k\omega - SST$ turbulence model.

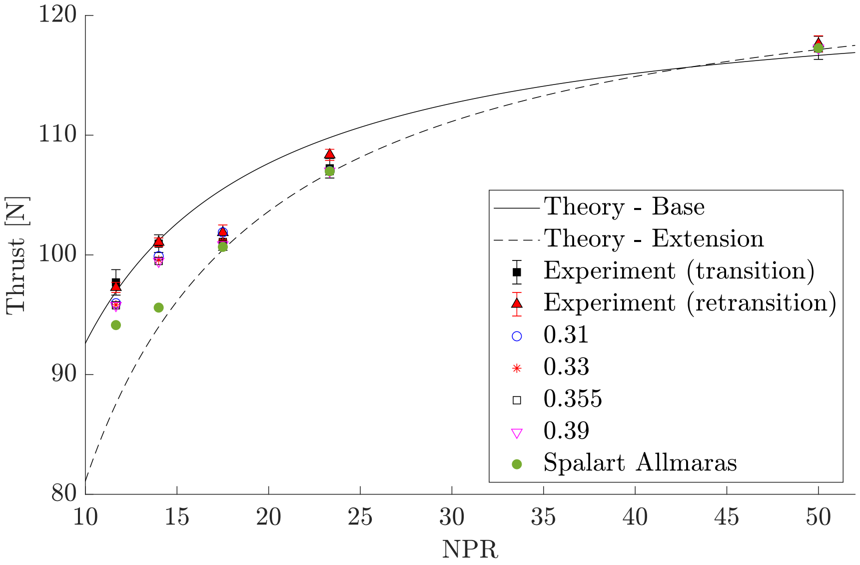

Fig. 3.38 Experimental and numerical thrust as a function of NPR for different structure coefficients.

Fig. 3.39 shows the relative error in thrust between the numerical simulations and the experiment. It shows that the numerically computed thrust remains within 2% of the experimental data for all SST model configurations. The differences between the standard and modified SST models are marginals, within 1 percentage point. The thrust predicted by the Spalart-Allmaras turbulence model presented larger discrepancies compared to the experiments, especially when the DBN operates in the low-altitude mode.

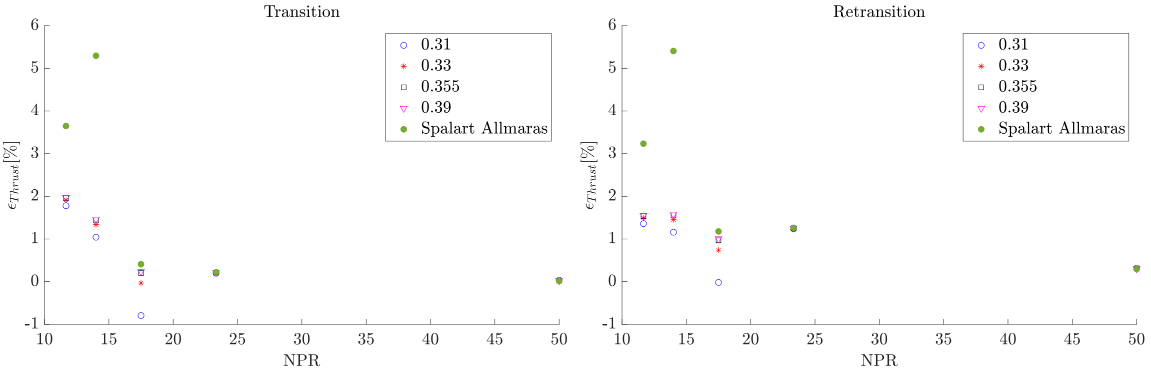

(a) Relative difference during transition phases (b) Relative difference during retransition phases

Fig. 3.39 Relative difference in thrust between experiments and simulations during transition and retransition phases

3.6.4 Conclusions

The previous section discussed the influence of the $k\omega - SST$ turbulence model structure parameter a_1 on the flow in the smooth DBN. This parameter controls the turbulent shear stress in the boundary layer and significantly affects the separation location prediction.
Increasing the structure parameter resulted in distinctive displacements of the separation point further downstream for the range of NPR under investigation. The largest separation displacement was observed at NPR = 17.5, where the standard SST model notably under-predicted the separation location. At this NPR, a structure parameter a_1 of 0.355 and 0.39 induced an increase in separation location by 19.9% and 21.1% respectively. In the meantime, a structure coefficient of 0.33 displaced by 13.6% the separation location. These observations indicated that the influence of the structure parameter was limited. Nonetheless, the boundary layer separation location displacement caused by the increase in structure coefficient yielded a remarkable improvement of the flow topology agreement between the numerical and the experimental schlieren images, particularly at NPR = 17.5. The improved flow topology prediction was achieved without adversely affecting the numerically calculated thrust. The results were compared to those of the Spalart-Allmaras turbulence model, which revealed larger discrepancies than the SST model configurations.
Considering the mild difference between the results obtained from $a_1 = 0.355$ and $a_1 = 0.39$, and the suggested structure parameter value in the open literature, a structure parameter of 0.355 was chosen for the next numerical simulation campaigns.

3.7 Conclusions

This chapter investigated the natural behaviour of the smooth DBN under altitude-varying conditions. The two operating modes of the DBN, specifically the low-altitude mode and the high-altitude mode, were illustrated using experimental schlieren images. The flow topology for both operational modes was comprehensively detailed, providing insights into the evolution of shock structures during both ascent and descent phases. Through experimental observation, the abrupt transition and retransition processes inherent in DBN equipped with a constant pressure extension were identified. Notably, the internal recompression shock, characteristic of such DBNs, was observed. The NPRs marking the transition of the DBN to the high-altitude mode and its subsequent return to the low-altitude mode were determined to be 14.85% and 14.53%, respectively. The nozzle thrust and the evolution of the streamwise wall pressure distribution were analysed during the transition and retransition phases. The experimental results demonstrated a strong agreement with theoretical predictions. The existence of a hysteresis effect between the transition and retransition phases was confirmed and its quantification revealed a modest value of 2.1%. In previous experiments conducted with the same test specimen, a flip-flop phenomenon was identified, contrasting with its absence in the current test campaign. This difference was attributed to the introduction of pressure sensor holes in the extension section, creating discontinuities at the wall surface. This observation highlights the importance of the surface state in influencing the flow dynamics within the DBN.

Following this experimental analysis, the second section dealt with the numerical modelisation of the DBN flow at several NPRs using a steady RANS approach and the standard $k\omega - SST$ turbulence model. The flow topology, the wall pressure distribution and the dual-bell nozzle performance were investigated and compared to the experimental data. The experimental and numerical schlieren images were generally in good agreement during the different operating conditions, except at NPR = 17.5. At this NPR, significant discrepancies in the flow topology emerged between the simulation and the experiment. These differences were attributed to the underprediction of the separation location by the turbulence model. The problem of eddy-viscosity turbulence models in accurately predicting flow separation in supersonic flow with shock wave boundary layer interaction was emphasised. This underscored the necessity to tailor the turbulence model to the specificities of the flow inside DBNs.

The third section investigated the differences between the flow predicted by the $k\omega - SST$ turbulence model and the Spalart-Allmaras turbulence model. Both turbulence models well predicted the DBN flow in the high-altitude mode. In the low-altitude mode, the Spalart-Allmaras turbulence model significantly overpredicted the separation location, whereas the

$k\omega - SST$ was in better agreement with the experimental data. The performance of the Spalart-Allmaras turbulence mode regarding the prediction of the wall pressure distribution and the thrust measurements in the low-altitude mode were found to be inferior to that of the $k\omega - SST$'s. Consequently, the $k\omega - SST$ turbulence model was adopted to perform the numerical simulations in this thesis, but the optimisation of its performances needed to be addressed.

The final section focused on enhancing the separation prediction capabilities of the $k\omega - SST$ turbulence model. Specifically, the turbulence model structure parameter was adjusted to minimize disparities in flow topology between simulations and experimental observations. Increasing the structure parameter increased the turbulent shear stress in the boundary layer, which resulted in distinctive displacements of the separation point further downstream at NPRs where separation was initially underpredicted. The largest separation displacement was observed at NPR = 17.5, where the standard SST model notably mispredicted the separation location. At this NPR and compared to the standard $k\omega - SST$, a structure parameter a_1 of 0.355 and 0.39 induced an increase in separation location by 19.9% and 21.1%, respectively. The influence of the structure coefficient was found to be limited, with no substantial differences noted between $a_1 = 0.355$ and $a_1 = 0.39$ within the NPR range under investigation. Nevertheless, the increase in structure coefficient yielded a remarkable improvement of the flow topology agreement between the numerical and the experimental schlieren images, particularly at NPR = 17.5. The improved flow topology prediction was achieved without adversely affecting the numerically calculated thrust. Considering the marginal difference between the results obtained from $a_1 = 0.355$ and $a_1 = 0.39$, and considering the suggested structure parameter value in the existing literature, a structure parameter of 0.355 was selected for the next numerical simulation campaigns.

Chapter 4

Injection slot presence and cavity influence study

4.1 Introduction

To operate secondary injection in a DBN as an active flow control technique, the presence of a secondary injection slot and a settling chamber, here called **cavity**, is necessary to set the stagnation conditions of the secondary jet. This chapter assesses the impact of the secondary injection slot's presence and location on the DBN's behaviour. It also investigates the influence of the cavity's volume on the nozzle. The chapter starts by briefly reminding the method used to generate the secondary injection slot and the cavity. Then, the chapter focuses on the influence of the cavity's volume on the DBNi8 test specimen, a dual-bell nozzle whose secondary injection slot is located 8 mm downstream of the inflexion point. The presence of the secondary injection slot and the influence of the cavity's volume are assessed by analysing the DBN's key parameters: the transition and retransition NPR, the side forces generated, and the thrust jump. The results are then opposed to those of the smooth DBN configuration.

The last section of the chapter discusses the impact of the secondary injection slot location and its cavity's volume on the DBN's behaviour under altitude-varying conditions. To do so, a DBN equipped with a secondary injection slot located 16 mm downstream of the inflexion point (DBNi16) was designed and tested. The results are opposed to those obtained with the DBNi8 test specimen and the smooth DBN to expose the effects of the secondary injection slot location and the cavity's volume on the DBN.

4.2 Preliminary section

The secondary injection is made possible by the presence of an annular injection slot inside the DBN extension profile and an external cavity to set the stagnation conditions for the secondary jet. However, the potential effect of the injection slot and cavity presence on the DBN's behaviour has yet to be investigated and reported in the open literature. The present chapter aims to provide insight into the secondary injection slot and cavity volume effect on the DBN's behaviour during the transition and the retransition phases. To do so, several cavity volumes are tested on two subscale DBNs: the DBNi8 and the DBNi16, where the secondary injection slot is located 8 mm and 16 mm downstream of the inflexion point, respectively. Three cavity volumes are tested for the DBNi8 test specimen, and two for the DBNi16. Three methods were used to change the cavity's volume for the DBNi8: 1) Inserting a hollow cylinder inside the cavity to reduce its volume and sealing the cavity with plugs, 2) Sealing the cavity with plugs but without an internal cylinder to have an intermediate volume, and 3) Removing the plugs and connect the cavity to the secondary injection pipes to have a larger volume. The aforementioned configurations will be referred to as 1) Filled cavity, 2) Empty cavity, and 3) Empty cavity connected to injection pipes. Only the second and third method was used in the DBNi16 test specimen. The different cavity volumes are summarised in Table 4.1 and the results are compared to the ones obtained using the smooth DBN, which serves as a baseline. The different configurations can be visualised in Fig. 4.1.

Table 4.1 DBNi8 and DBNi16 cavity volumes

Configuration	Filled cavity [cm^3]	Empty cavity [cm^3]	Cavity with pipes [cm^3]
DBNi8	30.1	89.8	558.8
DBNi16	-	104.7	573.7

The experimental test environment is the same as described in Chapter 2, and the same way the experiments of Chapter 3 were performed, for each configuration listed above, the tests were carried out to provide an average of fourteen transition and retransition phases per configuration, and to allow the calculation of the standard deviation. Because the presence of the secondary injection slot did not result in any change in the flow topology compared to the smooth DBN, the schlieren images during the ascent and descent phases are not discussed in this chapter. The acquisition rate was set to 1000 Hz and the feeding total pressure, the ambient pressure, the pressure inside the cavity, the thrust and the side forces were measured. The following section analyses the influence of the cavity's presence on the DBN's behaviour.

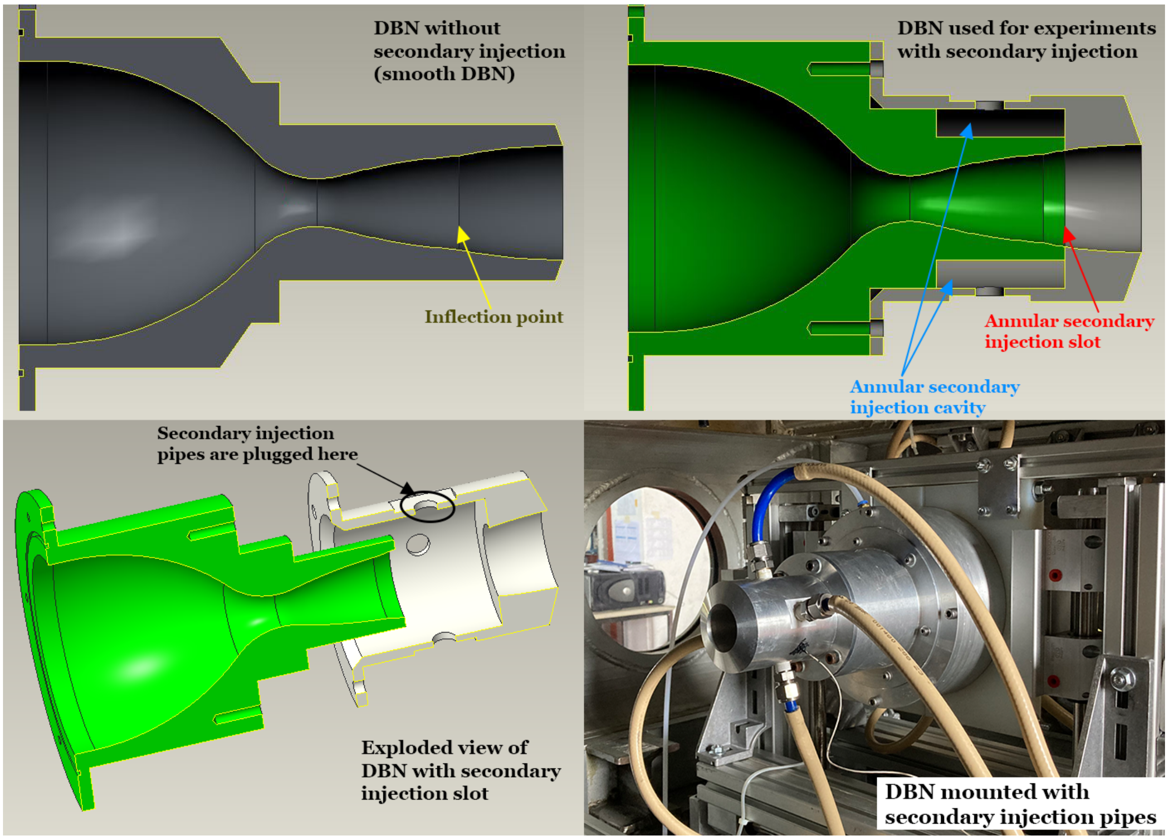

Fig. 4.1 Smooth DBN versus DBN designed with a secondary injection slot

4.3 Cavity influence in the DBNi8 test specimen

4.3.1 Experimental procedure

Fig. 4.2 shows, for the DBNi8 test specimen, the evolution of the specific impulse, NPR and normalised side-loads during a typical test-run in the wind tunnel for the empty cavity connected to the injection pipes but without an operating secondary injection. The normalised side-loads are obtained by dividing the lateral forces by the thrust to analyse the side force peaks as a percentage of the thrust.

Below NPR = 15, the dual-bell nozzle operates in the low-altitude mode and the flow separates from the nozzle flow wall at the inflexion point. As the NPR is increased from its lowest values (see Fig. 4.2), the specific impulse produced by the nozzle increases until a sudden decline occurs at NPR=15.92 as represented by the green curve in Fig. 4.2. At this NPR, the transition takes place and the separation front moves from the inflexion point to the nozzle exit, switching the DBN from the low-altitude mode to the high-altitude mode and inducing side forces and a jump in specific impulse.

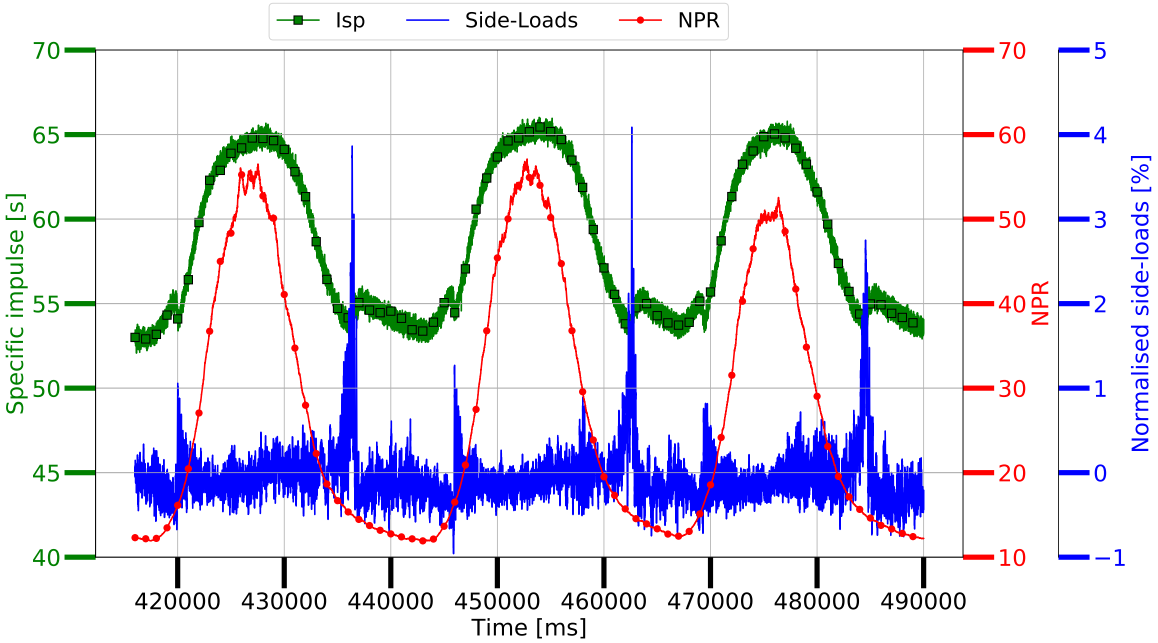

Fig. 4.2 Specific impulse, NPR, and side-loads as a function of time: DBNi8

Starting from the high-altitude mode, as the NPR decreases, the specific impulse decreases until NPR=14.82. If the NPR continues to decrease, a sudden jump in specific impulse is observed at NPR=14.81, which occurs due to the retransition from the high-altitude mode to the low-altitude mode. During the retransition, the separation front moves back from the nozzle exit to the inflexion point. Similarly to the transition phase, the movement of the separation front generates lateral forces, which are higher during retransition than during the transition phase, as depicted in Fig. 4.2. After conducting the experiments for the four different scenarios (smooth nozzle, filled cavity, empty cavity, and empty cavity connected to the injection pipes nozzles), several parameters were examined to assess the impact of the cavity's presence in the DBN during transitions and retransitions. These parameters included

- Transition and retransition NPR
- Maximum magnitude of side-loads
- Magnitude of thrust jump (as illustrated in Fig. 1.7)

4.3.2 Quantitative analysis

Fig. 4.3 shows NPR_{trans} and $NPR_{retrans}$ for the smooth DBN and DBNi8 for three different cavity configurations. It shows that the cavity's volume does not significantly impact the

$NPR_{retrans}$ compared to the smooth nozzle. However, the presence of the cavity results in a slightly greater NPR_{trans} although the difference between the filled cavity and the empty cavity is not readily apparent. The filled cavity's minimal air pocket volume implies that the mere presence of the injection slot is sufficient to delay the transition. The injection slot appears to function as an obstacle that temporarily maintains the separation at a fixed location, causing a slightly greater NPR_{trans}.

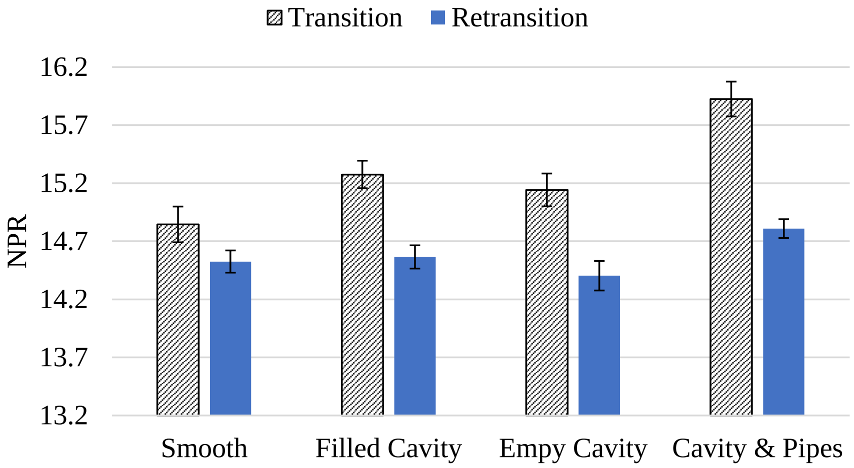

Fig. 4.3 Cavity influence: transition and retransition NPR for different configurations. Error bars show the standard deviation calculated for each configuration.

When the injection pipes were mounted on the cavity, a larger increase in NPR_{trans} became visible compared to all the other scenarios and the NPR_{trans} was increased by 7.3% compared to the smooth nozzle configuration. This result suggests that the air pocket volume inside the cavity plays a role in the DBN's transition behaviour. While the $NPR_{retrans}$ remains fairly unchanged between the smooth nozzle and the two smallest cavity volume configurations, the increase in NPR_{trans} leads to an increase in hysteresis from 2.1% for the smooth nozzle to 4.6% and 4.9% for the filled and empty cavity, respectively. In the cavity with pipes configuration, the $NPR_{retrans}$ experiences a slight increase but remains proportionally smaller than the increase in NPR_{trans}, resulting in a hysteresis of 7%. Therefore, the presence of an injection slot and the volume of air inside the cavity not only delay the transition NPR but also enhance the DBN's stability.

Similarly to the previous analysis on the retransition NPR, the influence of the cavity volume on side-loads generation during the retransition phases could not be readily identified in Fig. 4.4 which displays the normalised maximum lateral forces generated during the transition and retransition phases for each configuration. For the smooth, empty cavity, and cavity with pipes DBN configurations, Fig. 4.4 depicts similar side-load magnitudes during retransition. However, the presence of a cavity led to a decrease of over half in the lateral forces generated during transition for the two largest cavity volume configurations when compared to the smooth DBN. The most significant reduction was observed in the empty cavity case with a maximum decrease of 1.3 percentage points, reducing the lateral forces from 2.4% of the nozzle thrust in the smooth configuration to 1.1%. These side-loads reductions may result from the more symmetrical separation line induced by the injection slot downstream of the inflexion region. Even though the decrease in side-loads due to the injection slot and cavity is evident during the transition phase, the impact of the volume of air inside the cavity remains uncertain, particularly between the empty cavity and the cavity with pipes configurations.

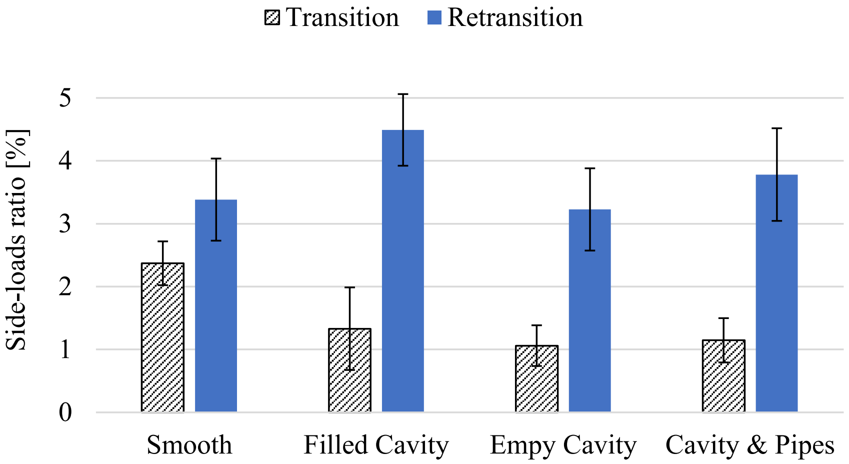

Fig. 4.4 Cavity influence: lateral forces generated during transition and retransition for different configurations. Error bars show the standard deviation calculated for each configuration.

In both the transition and the retransition phases, the movement of the separation front from the inflexion region to the nozzle exit (and vice versa) triggers a jump in specific impulse. These abrupt variations, caused by the sudden change in nozzle area ratio represent a serious risk for the rocket. Fig. 4.5 shows the normalized thrust jump generated during the transition and the retransition phases for the different configurations. The experiments unveiled a decrease in thrust jump during both phases when the cavity volume increases. During the ascent phase, the thrust jump was reduced by nearly half in the cavity with pipes case compared to the smooth nozzle, dropping from 3.8% of the nozzle thrust to 2.1%. The decrease in thrust jump during the descent phase was less substantial, decreasing by a fifth at most, going from 4.2% of the nozzle thrust to 3.4%. These findings indicate that the presence of an annular secondary injection slot distinctly impacts the DBN's behaviour during the ascent phase and that its effect on the thrust jump remains limited during the descent phase.

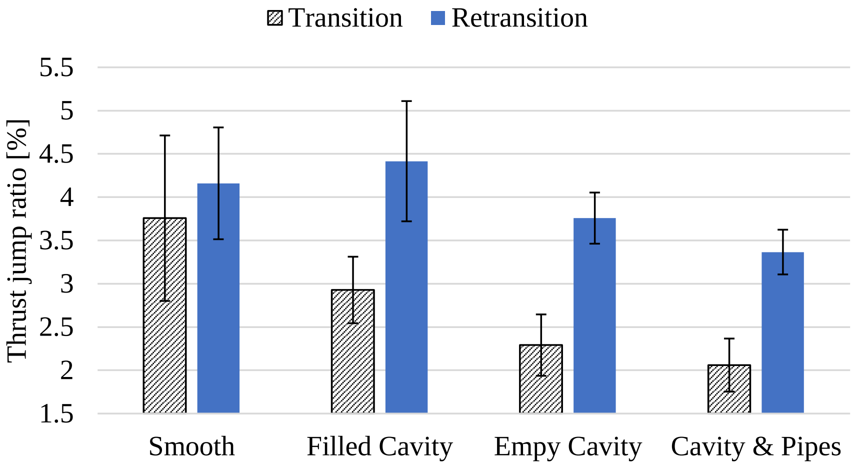

Fig. 4.5 Cavity influence: thrust jump during transition and retransition for different configurations. Error bars show the standard deviation calculated for each configuration.

4.3.3 Conclusions

The investigation of the DBNi8 test specimen without operating secondary injection indicated a clear influence of the injection slot and cavity's presence on DBN's behaviour. The study showed that the cavity's volume mostly affected the DBN's behaviour during the transition phase, where the transition NPR increased with an increase in the cavity volume. The maximum increase in transition NPR reached 7.3% when compared to the smooth DBN. The side-loads and thrust jump ratio were decreased with an increase in the cavity's volume during the ascent phase. The influence of the injection slot and cavity's volume on these parameters during the retransition phase was not readily observable, suggesting a limited impact on the DBN during the descent phase.

The following section investigates the effect of the secondary injection slot location on the DBN's behaviour.

4.4 Cavity influence in the DBNi16 test specimen

4.4.1 Experimental procedure

After assessing the cavity influence on the DBN's behaviour for the DBNi8 test specimen, the impact of the injection slot location is addressed. To do so, experiments were carried out with the DBNi16 test specimen to observe the effects of displacing the secondary injection slot further downstream, 16 mm ($1.88 \cdot r_{th}$) from the inflexion point. In the DBNi16 test specimen, due to the marginal volume difference between the filled and empty cavity configurations, only two cavity volumes were investigated: the empty cavity and the cavity with pipes configurations.

Fig. 4.6 shows, for the DBNi16 test specimen, the evolution of the specific impulse, NPR and normalised side-loads during a typical test-run of the wind tunnel for the empty cavity connected to the injection pipes but without an operating secondary injection.

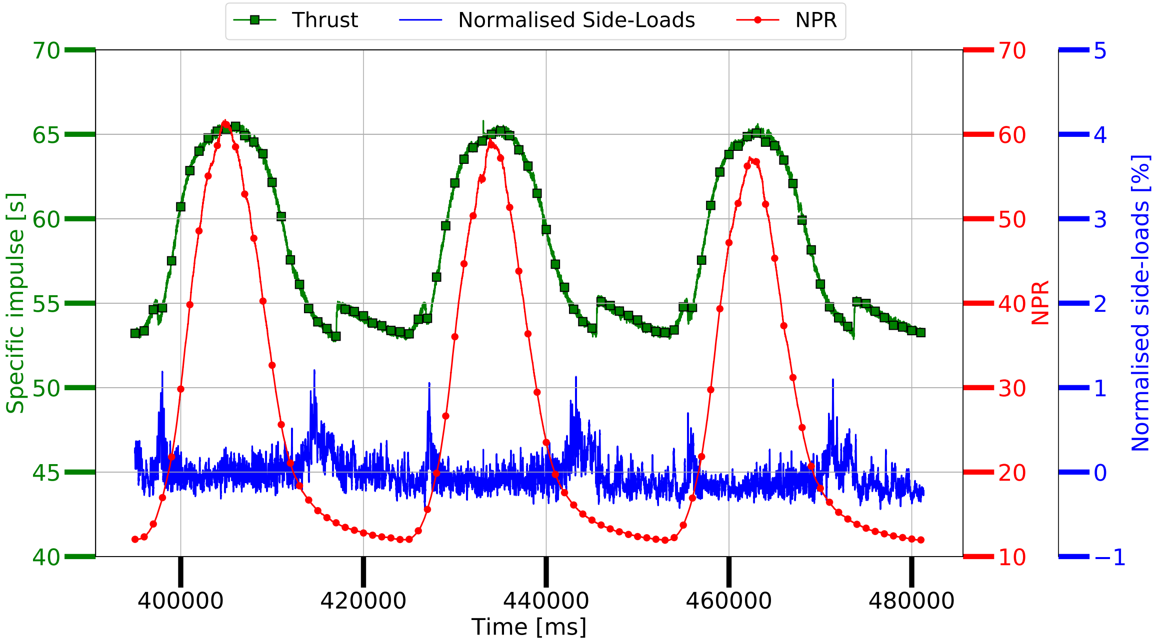

Fig. 4.6 Specific impulse, NPR, and side-loads as a function of time: Cavity

It shows that the dual-bell nozzle operates in the low-altitude mode below NPR = 14. As the NPR is increased from its lowest values, the specific impulse produced by the nozzle also increases until a sudden decline occurs at NPR=14.84, indicating the transition from the low-altitude mode to the high-altitude mode. Similarly to the smooth and the DBNi8 test specimens, this transition phase causes the shock system and the separation line, initially located in the inflexion region, to move to the nozzle exit, which induces lateral forces.

Starting from the high-altitude mode at NPR = 50, reducing the NPR causes the specific impulse to decrease until NPR = 13.99. If the NPR continues to decline, a sudden jump in specific impulse is observed at NPR = 13.98, which occurs during the retransition from the high-altitude mode to the low-altitude mode. During the retransition, the separation front moves back from the nozzle exit to the inflexion point. Similarly to the transition phase, the movement of the separation front generates lateral forces.

4.4.2 Quantitative analysis

Fig. 4.7 shows NPR_{trans} and $NPR_{retrans}$ for the smooth DBN, the three DBN cavity configurations of the DBNi8 test specimen, and the two cavity configurations of the DBNi16 test specimen, denoted by "16". The DBNi16 test specimen showed an opposite behaviour than the DBNi8. In the former case, the cavity's volume does not significantly impact the NPR_{trans} compared to the smooth nozzle, but it significantly affects the $NPR_{retrans}$.
Displacing the injection slot downstream revealed a marginal influence of the injection slot and cavity's presence during the transition phase as the NPR_{trans} decreased by 1.7% for the empty cavity configuration and 0.1% for the cavity with pipes case when compared to the smooth DBN. However, a more pronounced effect during the retransition phase was noted, where the $NPR_{retrans}$ declined by 5% and 3.7% compared to the smooth DBN for the two cavity cases respectively. All experimental data are given in a table at the end of this chapter.

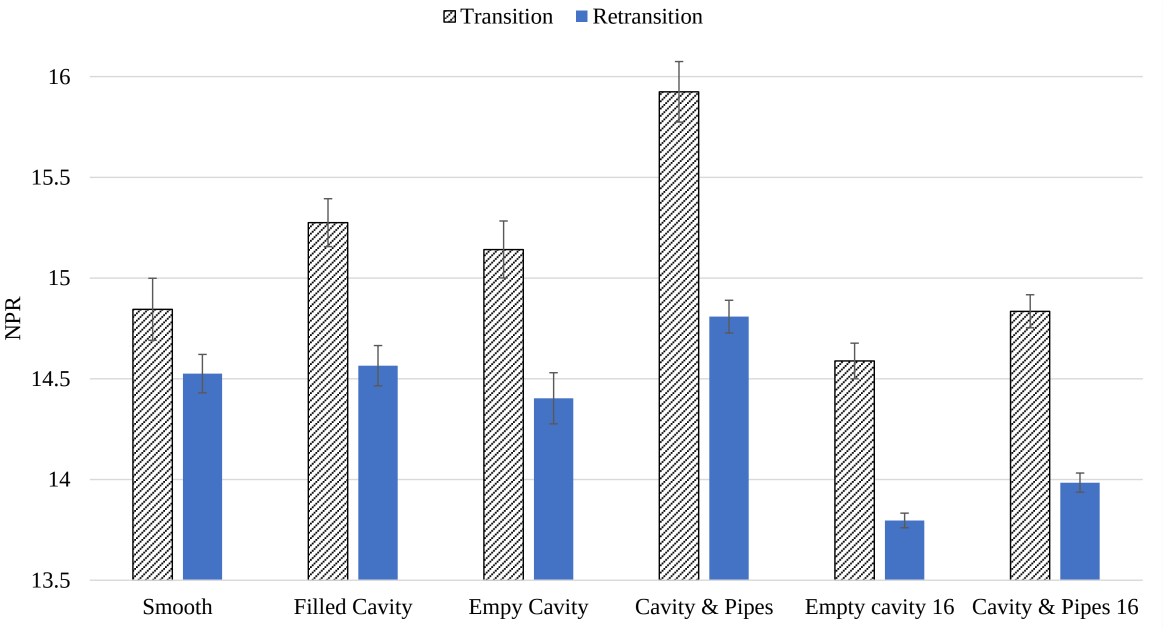

Fig. 4.7 Cavity influence: transition and retransition NPR for different configurations. Error bars show the standard deviation calculated for each configuration.

The 0.25 points difference in NPR_{trans} between the empty cavity and the cavity with pipes identified in the DBNi16 nozzle indicates that the larger cavity volume positively influences the transition process, but its effect remains limited. The 0.19 points difference in $NPR_{retrans}$ between the two cavity volumes in the DBNi16 configuration also shows the mild and limited impact of the cavity's volume during the retransition phases. Similar results were obtained when examining the influence of cavity volume on the transition and the retransition phases of the DBNi8 specimen. The test campaign demonstrates the significant influence of the secondary injection slot location on the DBN's behaviour. A secondary injection slot located near the inflexion point is favourable to delay the natural transition with limited effects on the retransition phase, while a secondary injection slot positioned further downstream delays the natural retransition with a limited effect on the transition phase. This may suggest that during the transition phase in the DBNi8 specimen, the secondary injection slot and the cavity presence are close enough to the inflexion point so that their influence is felt by the upstream boundary layer, inducing a delay in flow reattachment to the nozzle extension wall (higher NPR_{trans}). Conversely, the injection slot may be located too far downstream in the DBNi16 to influence the boundary layer reattachment in the extension section, resulting in a similar NPR_{trans} than the smooth DBN. However, the reasons for the significant decrease in $NPR_{retrans}$ in the DBNi16 test specimen is yet to be found, and further investigations are necessary.

Fig. 4.8 displays the normalised lateral forces generated during the transition and retransition phases for each configuration. Unlike the DBNi8 test specimen, where the influence of the injection slot presence and the cavity volume were not readily identified during the retransition phase, a substantial decrease in side-loads was observed in the DBNi16 test specimen during both the ascent and descent phases. The side-loads measurements even became a challenging task as they decreased to 1% of the nozzle thrust, a decrease of 2.4 percentage points when compared to the smooth DBN. However, a clear influence of the cavity volume was not readily identified. The two cavity volumes of the DBNi16 specimen also exhibited the clear influence of the secondary injection slot presence on the generation of side-loads during the transition phase, where the side forces decreased to 0.8% of the nozzle thrust. This corresponds to a decrease of 1.6 percentage points compared to the smooth DBN, as opposed to a maximum decrease of 1.3 percentage points for the DBNi8 configuration. The large decrease in side forces during the ascent and the descent phase in the DBNi16 (a decrease only observed during the ascent phase in the DBNi8) clearly indicates that the secondary injection slot position plays a key role in the DBN's natural behaviour. In low-altitude mode, the separation front is located at the inflexion point; the DBNi8 and DBNi16 injection slots are located at 22% and 44% of the extension length downstream of the inflexion point.

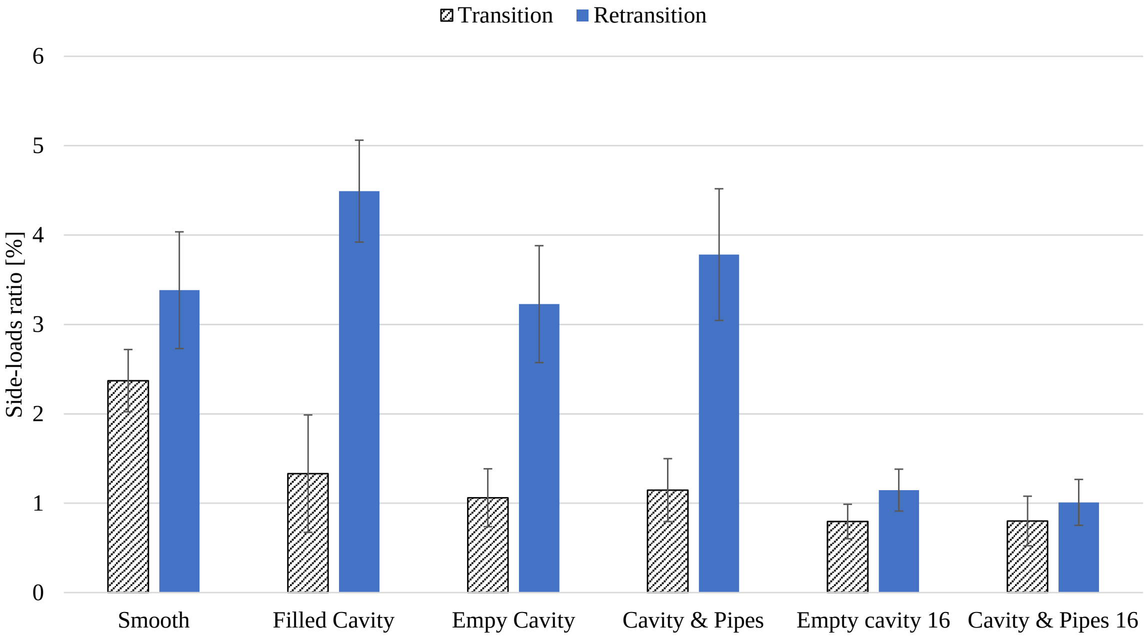

Fig. 4.8 Cavity influence: lateral forces generated during transition and retransition for different configurations. Error bars show the standard deviation calculated for each configuration.

The proximity of the DBNi8 injection slot to the separation front may re-symmetrise the flow and reduce the side forces during the transition. The DBNi16 injection is roughly in the middle of the extension section, but its presence may also cause the flow to re-symmetrise and decrease the side-forces during the retransition. However, in high-altitude mode, the separation front is located at the nozzle exit. Here, the DBNi8 and DBNi16 injection slots are located 78% and 56% of the extension length upstream of the nozzle exit. Because the DBNi16 injection slot is, also in this case, roughly in the middle of the extension section, its presence may re-symmetrise the separation line and decrease the side forces during the retransition. However, the presence of the DBNi8 injection slot may not be sufficient to re-symmetrise the separation line during the retransition phase, as it is located 78% upstream of the nozzle exit. Therefore, the location of the injection slot in the DBNi16, which is roughly in the middle of the extension section, may be favourable to the flow re-symmetrisation during both the transition and the retransition phases.

Fig. 4.9 shows the normalised thrust jump generated during the transition and the retransition phases for the different configurations. Similarly to the DBNi8 configuration, the experiments performed with the DBNi16 specimen unveiled a decrease in thrust jump with an increase in cavity volume during the transition phase. The thrust jump was decreased to a similar extent for both test specimens with a thrust jump ratio of 1.9% and 2.1% for the

DBNi16 and DBNi8 respectively. The former corresponds to a decrease of 1.9 percentage points compared to the smooth nozzle configuration, 0.2 percentage points more than for the DBNi8, suggesting the limited influence of the secondary injection slot location on the thrust jump ratio during the transition phase. During the retransition phase, the injection slot and the cavity volume in the DBNi16 configuration did not show any significant change in thrust jump ratio, as observed in the DBNi8 test specimen.

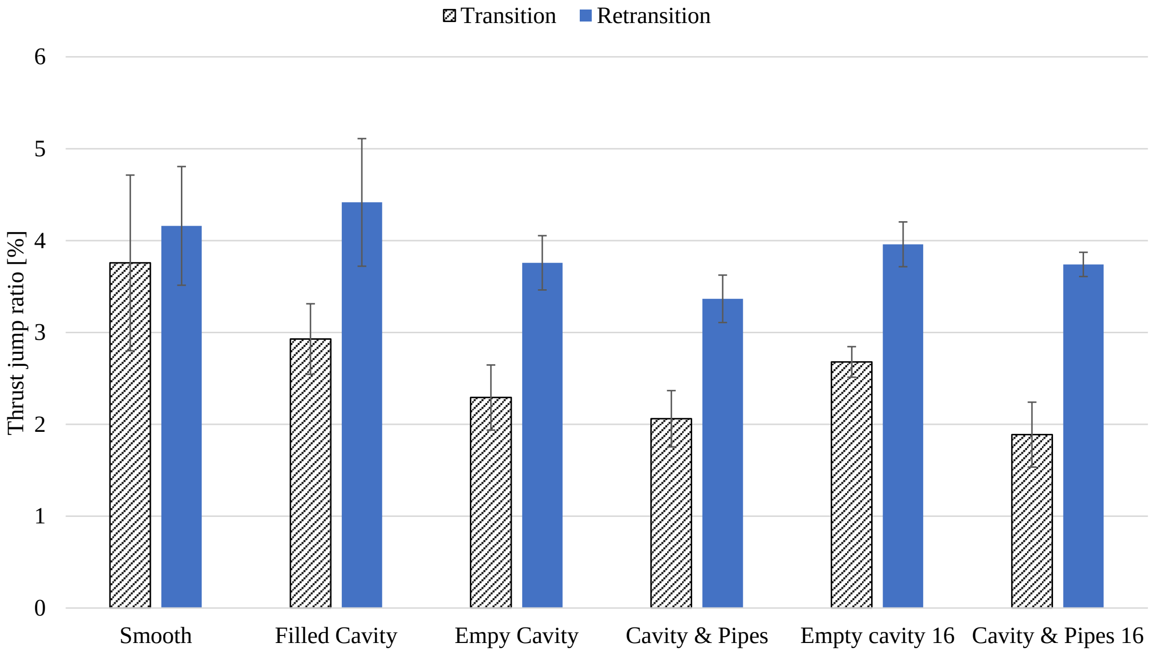

Fig. 4.9 Cavity influence: thrust jump during transition and retransition for different configurations. Error bars show the standard deviation calculated for each configuration.

4.4.3 Conclusions

The investigation of the DBNi16 test specimen without operating secondary injection showed the effects of the cavity's presence when positioned at a different location and the influence of its volume on the DBN's behaviour. The study uncovered a different behaviour than in the DBNi8 test specimen. Here, the cavity's presence mostly affected the DBN's behaviour during the retransition phase, where the retransition NPR decreased by over 5% compared to the smooth DBN. The side-loads were reduced significantly during both the ascent and descent phases. The thrust jump ratio was decreased to the same extent as in the DBNi8 configuration during the transition phase but was not significantly impacted during the retransition phases.

4.5 Conclusions

The potential use of annular secondary injection in a DBN as an active flow control technique to improve its performance necessitates the presence of a secondary injection slot and a settling chamber, called cavity, to set the stagnation conditions of the secondary jet. This chapter discusses the impact of the secondary injection slot's location and the influence of the cavity's volume on a subscale DBN. The analysis is divided into three sections.

First, the experimental procedure is described. The second section investigates the influence of the secondary injection slot presence and the cavity's volume on the DBNi8 test specimen, a dual-bell nozzle whose secondary injection is located 8 mm downstream of the inflexion point. The study revealed that the cavity's volume mainly impacted the DBN's behaviour during the transition phase, where the transition NPR increased with an increase in the cavity volume. The transition NPR rose by 7.3% at most when compared to the smooth DBN. At the same time, the side-loads and thrust jump ratio were reduced to 1.1% and 2.1% of the nozzle thrust, a decrease of 1.3 and 1.7 percentage points when compared to the smooth DBN. The influence of the cavity's volume on these parameters during the retransition phase was not readily observable, suggesting a limited impact on the DBN during the descent phase.

The chapter's last section explores the impact of the secondary injection slot location on the DBN's behaviour. A DBN equipped with a secondary injection slot located 16 mm downstream of the inflexion point (DBNi16) was studied. As opposed to the DBNi8 configuration, displacing the secondary injection slot downstream resulted in a limited effect during the transition process, with a decrease in transition NPR of 1.7% at most for the smallest cavity's volume when compared to the smooth DBN. In the DBNi16 test specimen, the presence of the injection slot decreased the retransition NPR by over 5%. The further secondary injection slot showed a decrease in side forces to less than 1% of the nozzle thrust during both, the ascent and the descent phases, as opposed to the DBNi8 case which showed a limited influence of the injection slot on side forces during the descents. The thrust jumps during the transition phase were reduced to the same extent for both DBNs but the effect of the injection slot remained limited during the retransition phase in both cases.

These experimental campaigns showed the clear impact of the secondary injection slot position in the DBN's extension section, especially regarding its stronger impact during the retransition phases should it be positioned further downstream. The nature of this phenomenon is presumed to be associated with the proximity of the injection slot to the inflexion point. This series of experiments further underscores the considerable sensitivity of the DBN's flow to the surface condition and the precise location of these surface discontinuities.

The next chapter will discuss the effect of active secondary injection on the DBNi8's behaviour.

Chapter 5

Secondary injection influence - 8mm

5.1 Introduction

This chapter presents the effects of radial secondary injection downstream of the inflexion point, in the extension section of a subscale DBN. Secondary injection in DBN has been studied in the past mostly by performing film cooling [95, 96, 94] and less often with transverse injection [98, 99] at the inflexion point or in the extension nozzle section. The open literature has shown the limited influence of film cooling on delaying the dual-bell nozzle transition NPR and on limiting the generation of side forces. However, radial secondary injection in the extension section of the DBN has yielded promising outcomes. This includes the ability to notably postpone the NPR of transition and reduce side-loads and thrust jump magnitude during the transition and the retransition phases [82]. This chapter extends the previous studies by performing an initial steady 2D axisymmetric numerical analysis using the commercial software FLUENT 2022 R2. The DBN examined in this study is the DBNi8, featuring the same wall profile as the smooth DBN but equipped with a secondary injection slot positioned 8 mm downstream of the inflexion point (refer to the configuration's details in Chapter 2).

This chapter first describes a conventional test run performed in the experimental campaign. A qualitative analysis of the flow topology is performed by observing the schlieren images, followed by a quantitative analysis containing experimental and numerical results. The key findings are then summarised in the conclusion section.

5.2 Preliminary section

The experimental test environment is the same as described in Chapter 2. The secondary injection was made possible by manufacturing the DBN in two parts, allowing the presence of a secondary injection slot and a cavity to set the secondary jet stagnation conditions. The injection system is displayed in Fig. 5.1. The secondary jet stagnation pressure is controlled by a valve located downstream of the main air pressure line. The flow issued by the pressure line is spread into the four different injection pipes and plugged symmetrically into the DBN outer wall. The secondary gas fills the cavity and generates the stagnation conditions of the secondary jet. The air inside the cavity is accelerated and ejected in the mainstream DBN flow through a 0.2 mm wide annular injection slot. Here, the secondary injection is positioned 8 mm downstream of the inflexion point. Several secondary injection pressures were considered for this study. The secondary pressure values P_i, the secondary pressure ratios (SPR = P_i/P_0), the theoretical secondary mass flow rates $\dot{m}_i$, and the secondary mass flow rate ratios ($\varphi_{\dot{m}} = \dot{m}_i/\dot{m}$) are restated in Table 5.1. Here, $\dot{m}$ corresponds to the mainstream mass flow rate of 187 g/s. It is worth pointing out the relatively small secondary mass flow rates used in this test campaign, which ranged between 1.1% and 6.2% of the mainstream mass flow rate.

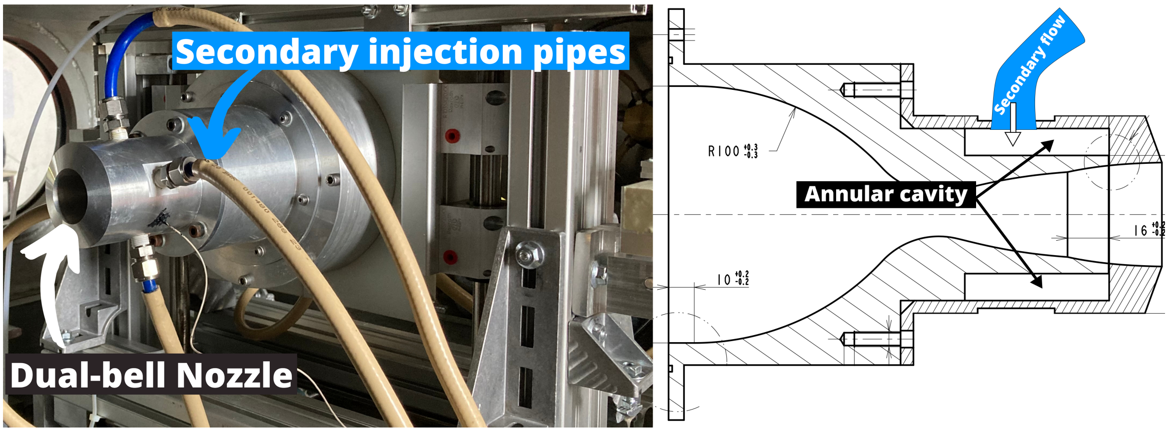

Fig. 5.1 Secondary injection influence test campaign: experimental setup.

For each configuration listed in Table 5.1, the experiments were carried out so as to provide an average of fourteen transitions and retransitions phases per configuration, and to allow the calculation of the standard deviation. The acquisition rate was set to 1000 Hz.

Table 5.1 Secondary injection pressure, pressure ratio, mass flow rate, and mass flow rate ratio used in test campaign

	P_i, kPa						
	37	51	69	88	126	163	217
SPR	0.11	0.15	0.2	0.25	0.36	0.47	0.62
$\dot{m}_i$, g/s	1.98	2.73	3.7	4.72	6.73	8.75	11.63
$\varphi_{\dot{m}}$	0.011	0.015	0.020	0.025	0.036	0.047	0.062

Fig. 5.2 shows the evolution of the NPR, specific impulse, side-loads ratio, and secondary pressure ratio during an ordinary experiment using $\varphi_{\dot{m}} = 0.015$ (SPR = 0.15). The specific impulse is determined by considering the primary and secondary mass flow rate, as per the following formula:

$$I_{sp} = \frac{F_x}{(\dot{m}+\dot{m}_i)\cdot g_0} \tag{5.1}$$

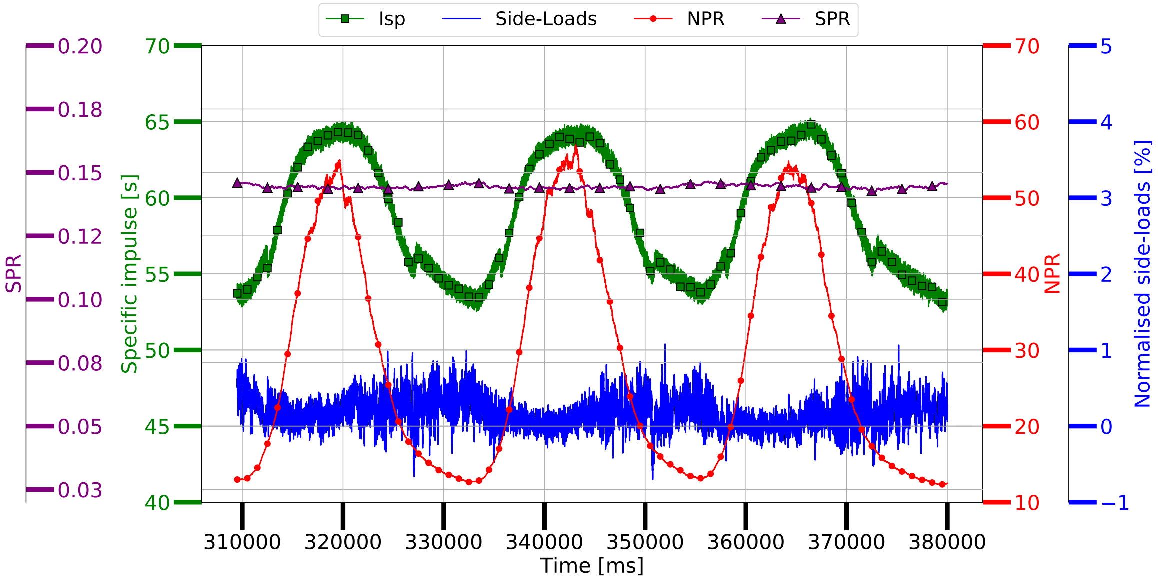

Fig. 5.2 Specific impulse, NPR, side-loads, and secondary pressure ratio as a function of time: DBNi8 operating with $\varphi_{\dot{m}} = 0.015$.

Starting from the lowest NPR values, the DBN operates in the low-altitude mode. When the NPR increases, the specific impulse increases until a sudden drop occurs at NPR = 17.77. At this NPR, the nozzle transitions from the low-altitude mode to the high-altitude mode. A further increase in NPR results in a rise in specific impulse. Unlike the smooth DBN and the cavity configurations studied in the previous chapter, the measurements do not show a sudden rise in lateral forces in this configuration. Explanations regarding this behaviour will be proposed in the subsequent sections. Starting from the highest NPR values, the DBN operates in the high-altitude mode. Decreasing the NPR induces a decrease in specific impulse until a sudden jump occurs at NPR = 16.86, where the retransition to the low-altitude mode occurs. A further decrease in NPR also results in a specific impulse decline. Similarly to the transition phase, no side force is measured in this configuration and further explanations are given in the next sections.

The hysteresis effect measured between the ascent and the descent phase is highlighted in Fig. 5.3, which shows the evolution of the specific impulse as a function of NPR during an ascent and a descent phase. As opposed to the hysteresis observed in the smooth DBN (refer to Fig. 3.9), Fig. 5.3 exhibits a less abrupt transition and retransition phase. These observations are further discussed in detail in a subsequent section.

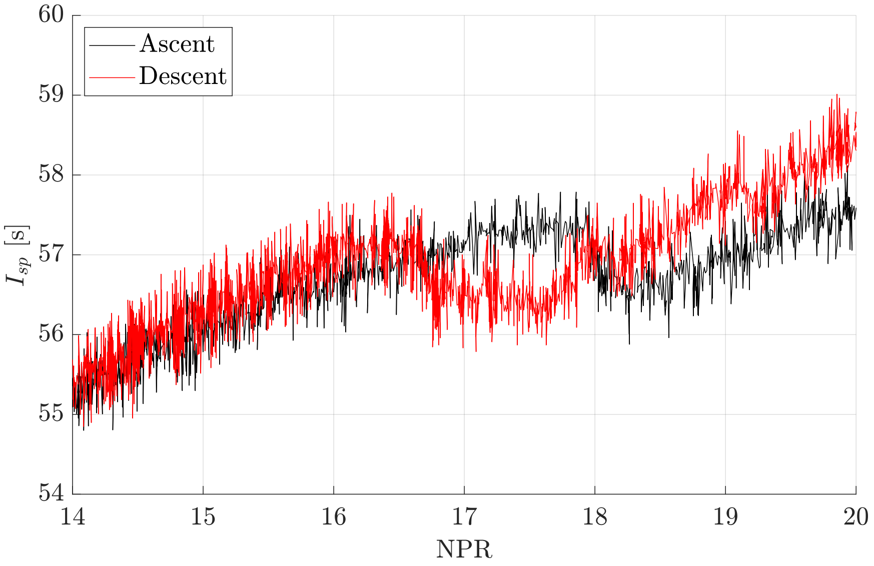

Fig. 5.3 Hysteresis phenomenon in DBNi8 operating with $\varphi_{\dot{m}} = 0.015$.

5.3 Qualitative analysis

5.3.1 Flow topology in the low-altitude mode

This section analyses the schlieren images of the DBNi8 test specimen operating in the low-altitude mode for four secondary mass flow rate ratios: $\varphi_{\dot{m}} = \{0.015; 0.020; 0.036; 0.062\}$. The numerical results presented later in Section 5.4 give an indication of the flow topology inside the DBN's extension section and the different shock configurations are inferred qualitatively. Fig. 5.4 shows the dual-bell nozzle flow topology at NPR = 17 for the different secondary mass flow rate ratios. The flow features are discussed for the transition phase only, given that their characteristics closely resemble those seen during a retransition phase, as already discussed in Chapter 3.

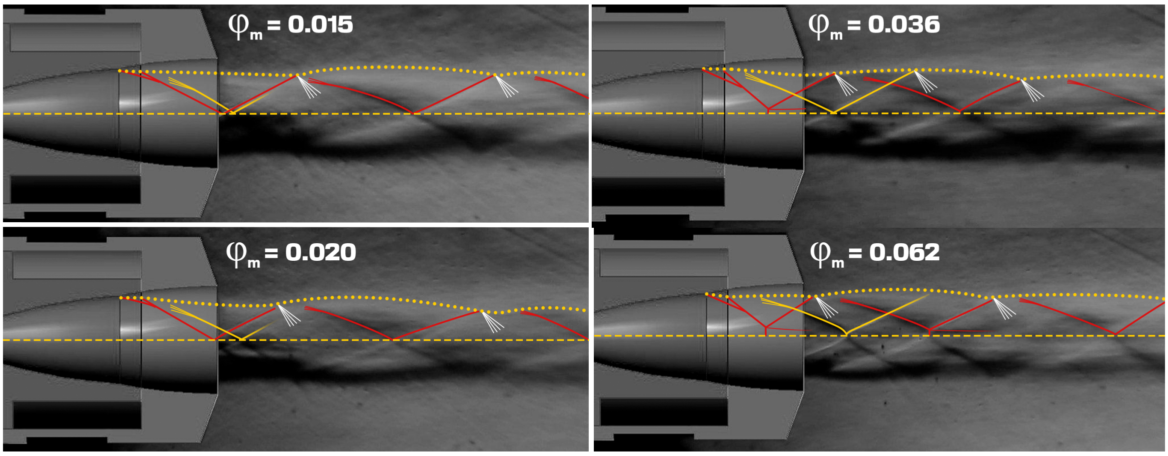

Fig. 5.4 Key flow features of DBNi8 when controlled by secondary injection at NPR = 17.

At NPR = 17, all configurations exhibit a DBN operating in the low-altitude mode, except for $\varphi_{\dot{m}} = 0.062$ where the transition from the low-altitude mode to the high-altitude mode started. In all cases, the flow at the inflexion point faces an adverse pressure gradient caused by the presence of the secondary jet and the high ambient pressure. Consequently, the upcoming boundary layer thickens and separates at the inflexion point, inducing the formation of a separation shock. Due to the presence of the secondary injection, a bow shock wave emerges in the vicinity of the secondary jet and coalesces with the separation shock, forming the well-known lambda shock structure. As the secondary mass flow rate ratio increases, the lambda shock angle relative to the nozzle wall increases. From an inviscid point of view, the lambda shock is reflected at the nozzle symmetry axis. For high-enough secondary mass flow rate ratios such as $\varphi_{\dot{m}} = 0.036$ or 0.062, the lambda shock reflection changes from a regular to singular, and interacts with a Mach disk near the nozzle symmetry axis. Even though the Mach disk is not visible through the nozzle wall, the presence of slip lines near the nozzle exit and the numerical results confirm the existence of the Mach reflection. Downstream of the lambda shock, a second shock emerges to compress the jet column. This shock will be called high ambient pressure (HAP) shock. This HAP shock structure becomes more identifiable for the higher-end range of secondary mass flow rate ratios, with a Mach disk existing for $\varphi_{\dot{m}} = 0.062$. The reflected lambda shock is then turned into an expansion fan at the contact with the exhaust plume boundary. Further downstream, a series of compression waves coalesce to form a shock, which will be reflected near the symmetry axis and will interact with the jet boundary, and so on. This process results in the conventional series of compression and expansion cells to adapt the exhaust flow to the ambience. Similarly, the HAP shock follows the same process as the lambda shock for the higher-and range of secondary mass flow rate ratios.

5.3.2 Flow topology in the high-altitude mode

This section analyses the schlieren images of the DBNi8 test specimen operating in the high-altitude mode for the four secondary mass flow rate ratios previously examined: $\varphi_{\dot{m}} = \{0.015; 0.020; 0.036; 0.062\}$. Fig. 5.5 shows the dual-bell nozzle flow features at NPR = 40 for the different secondary mass flow rate ratios. At such NPR, all configurations exhibit a DBN operating in the high-altitude mode. In this case, the flow expands at the inflexion point through an expansion fan not visible on the images (the DBN wall hides the internal flow). After expanding at the inflexion point, the flow encounters the secondary injection jet. The presence of the secondary injection induces a wall adverse pressure gradient, whose strength increases with the secondary mass flow rate ratio. The adverse pressure gradient causes the upcoming boundary layer to thicken and separate from the extension section wall.

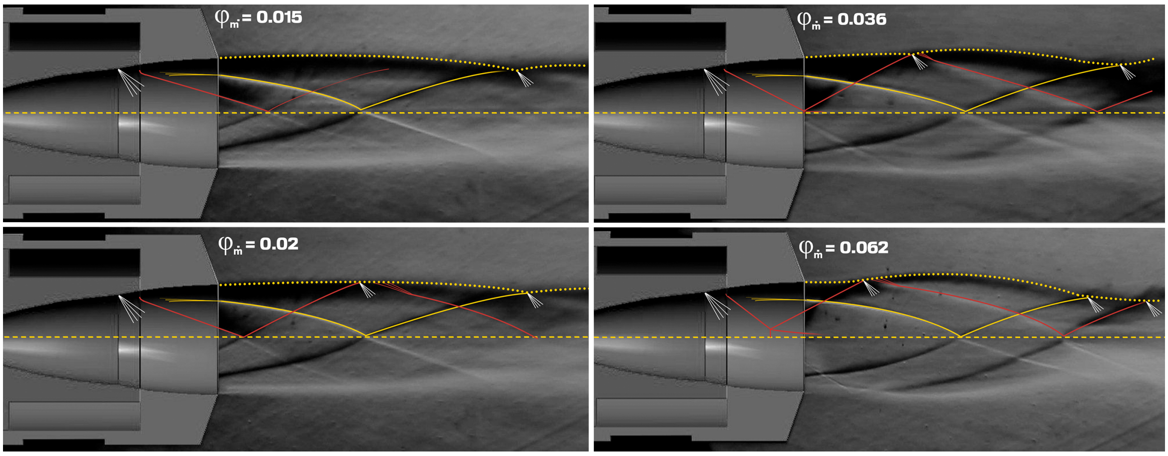

Fig. 5.5 Key flow features of DBNi8 when controlled by secondary injection at NPR = 40.

The flow deviation in the vicinity of the separation point causes a separation shock to form in the DBN core flow. Fig. 5.5 indicates that the angle of the separation shock increases with the secondary mass flow rate ratio. From an inviscid point of view, the separation shock is reflected on the nozzle symmetry axis towards the exhaust plume. For high secondary mass flow rate ratios as $\varphi_{\dot{m}} = 0.062$, singular Mach reflection even emerges near the symmetry axis.

The existence of a Mach disk in these conditions is confirmed by the presence of slip lines at the nozzle exit and by the numerical results presented in Section 5.4. After separating from the nozzle wall, the flow re-attaches downstream of the secondary injection slot. Due to the constant pressure nature of the extension section, a series of compression waves coalesce to form an internal recompression shock. This internal recompression shock interacts with the separation shock in the exhaust plume. When the separation shock and the recompression shock reflections interact with the exhaust plume boundary, they are turned into expansion fans which causes the flow to expand. Further downstream of these expansion fans, a series of compression waves coalesce to form other recompression shocks and so on, leading the conventional series of compression and expansion cells until the exhaust jet adapts to the ambience.

5.3.3 Flow topology during an ascent phase

This section compares the Schlieren images from the experiments and the numerical simulations during an ascent phase. As previously mentioned in Chapter 3, the flow topology remains comparable during both the ascent and descent phases. Consequently, this section exclusively addresses the flow topology during an ascent phase, with the understanding that the findings can be extrapolated to the descent phase. Two secondary mass flow rate ratios are chosen, $\varphi_{\dot{m}} = 0.020$ and $\varphi_{\dot{m}} = 0.062$, to analyse the flow topology at different NPR during an ascent phase.

Fig. 5.6 shows the flow topology at NPR = 17 for the DBN with a secondary mass flow rate ratio $\varphi_{\dot{m}} = 0.020$ (top) and $\varphi_{\dot{m}} = 0.062$ (bottom). On both images of the figure, the simulations predict a DBN in low-altitude mode with flow separation in the vicinity of the inflexion point: downstream the inflexion point for $\varphi_{\dot{m}} = 0.020$, and upstream the inflexion point for $\varphi_{\dot{m}} = 0.062$. The numerical simulations indicate that the secondary jet acts as an obstacle and the adverse pressure gradient caused by the injection triggers the upcoming boundary layer to separate, leading to the lambda shock structure. The lambda shock structure emerges from the coalescence of the separation shock and the bow shock in the vicinity of the secondary jet. Because this structure emanates from the presence of the secondary injection jet, it will be called the "SI" shock. Downstream of the SI shock, the high ambient pressure recompresses the jet column, and another is formed, which will be referred to as HAP shock (high ambient pressure). Both of these structures are visible in Fig. 5.6a, though less distinctly in the simulation. Following these shock structures, a series of compression and expansion cells commonly observed in supersonic overexpanded jets exist downstream. As the secondary mass flow rate ratio increases, the fluidic obstacle becomes more significant and it increases the shock angle relative to the nozzle wall.

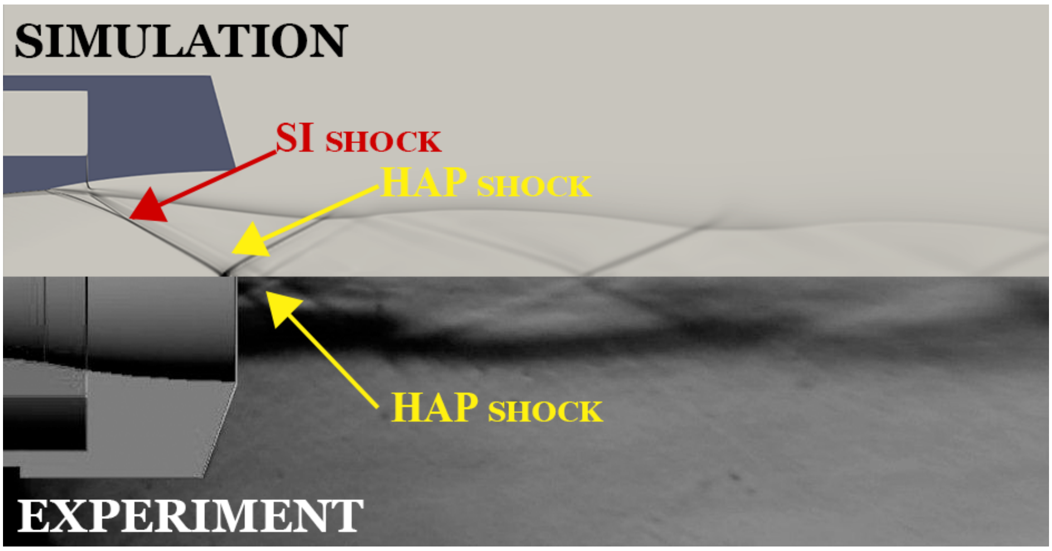

(a) NPR = 17 | $\varphi_{\dot{m}} = 0.020$

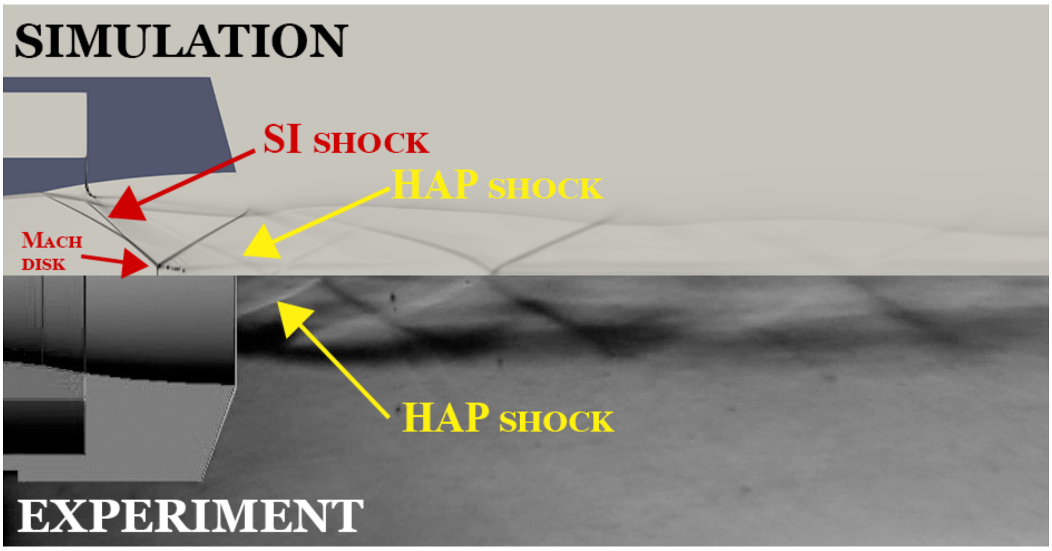

(b) NPR = 17 | $\varphi_{\dot{m}} = 0.062$

Fig. 5.6 Numerical and experimental Schlieren comparison at NPR = 17 for $\varphi_{\dot{m}} = 0.020$ (on top) and $\varphi_{\dot{m}} = 0.062$ (on bottom).

In Fig. 5.6b, the significant flow deviation induced by the high secondary mass flow rate increases the SI shock angle to the extent that the shock reflection becomes singular and a Mach disk emerges near the symmetry axis. At this NPR, the simulation and the experiment provide a fairly similar shock topology when $\varphi_{\dot{m}} = 0.020$. However, for $\varphi_{\dot{m}} = 0.062$, the DBN flow in the experimental case is transitioning from the low-to high-altitude mode, shifting the separation location downstream along with the shock structure topology. This observation, exclusively taking place at the higher-end range of secondary injection pressure operated, is due to the earlier transition observed in the experiments (see Section 5.4.1). In this case, the numerical simulation failed to predict the early transition, causing the discrepancy in the shock structure topology.

At NPR = 19 (see Fig. 5.7), the DBN has transitioned from the low-altitude mode to the high-altitude mode in the experiments. However, in both simulations, the separation location is underpredicted.

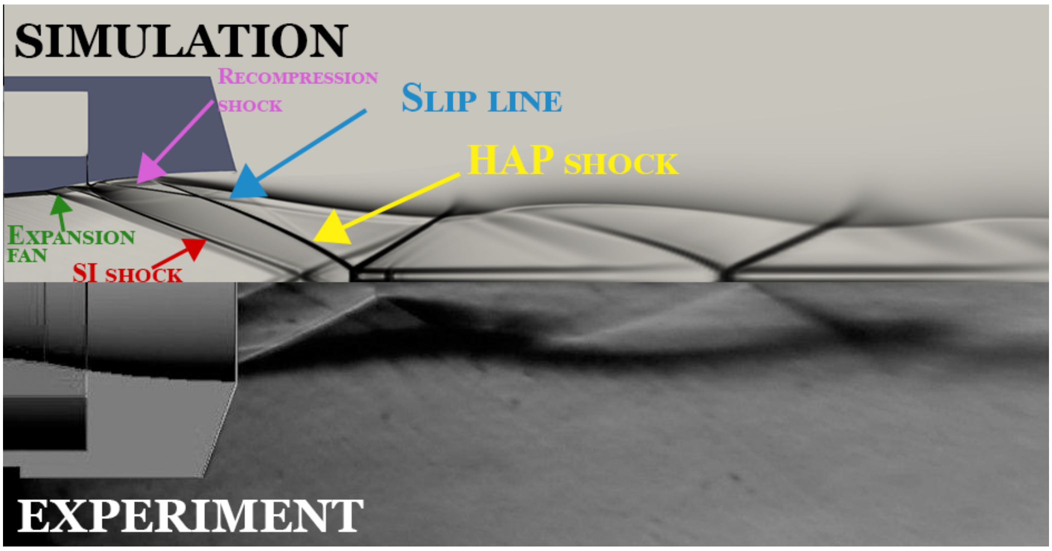

(a) NPR = 19 | $\varphi_{\dot{m}} = 0.020$

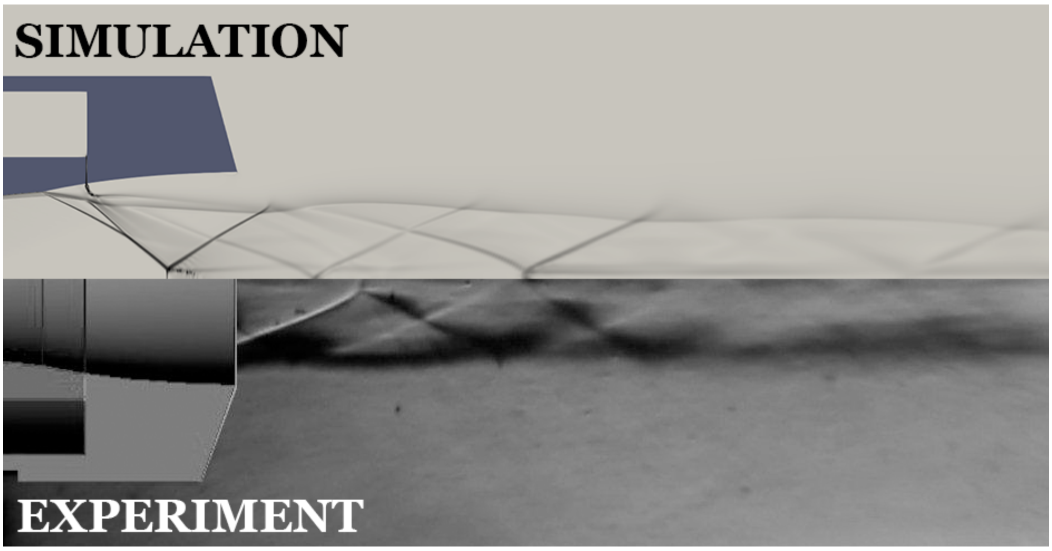

(b) NPR = 19 | $\varphi_{\dot{m}} = 0.062$

Fig. 5.7 Numerical and experimental Schlieren comparison at NPR = 19 for $\varphi_{\dot{m}} = 0.020$ (on top) and $\varphi_{\dot{m}} = 0.062$ (on bottom).

For $\varphi_{\dot{m}} = 0.020$, the flow expands through the inflexion region before the boundary layer separates upstream of the injection slot due to the presence of the injection. Then, the flow reattaches the extension section wall downstream of the injection slot location before it separates a second time in the extension section. For $\varphi_{\dot{m}}$ = 0.062, the separation is located at the inflexion point while the transition has almost fully already occurred in the experiment. The misprediction of the separation location by the simulations in both cases causes discrepancies in the flow topology when compared to the experiments. Both configurations display the SI shock. However, the reattachment of the boundary layer in the $\varphi_{\dot{m}}$ = 0.020 configuration and the constant pressure nature of the extension section gives rise to an internal recompression shock. The internal recompression shock interacts with the separation shock downstream and a slip line emerges from the interaction. Because the later separation shock is caused by the boundary layer separation induced by the high ambient pressure, this separation shock is also referred to as HAP (High Ambient Pressure) shock. The HAP shock interacts with a Mach disk and a reflected shock at a triple point near the symmetry axis. The flow topology obtained numerically contains all of the features observed experimentally but the wrong separation location prediction induces a difference in the shock cells positions. For $\varphi_{\dot{m}}$ = 0.062, the absence of internal recompression shock in the experiment suggests that the flow is not attached to the entirety of the extension wall. Nonetheless, the HAP shock is noticeable in the exhaust plume, in front of what appears to be one of the SI shock reflections. In this case, the absence of flow reattachment in the extension section in the simulation justifies the mismatch of the HAP shock position with the experiment. The difference in transition NPR values between simulations and experiments introduces certain discrepancies, yet the presence of key flow features demonstrates a reasonably good agreement between experimental observations and numerical simulations. This enables us to leverage numerical schlieren to elucidate the flow topology within the DBN and evaluate the impact of secondary injection on the flow topology.

At NPR = 30 (see Fig. 5.8), the transition to high-altitude mode has fully taken place experimentally and numerically. For both secondary injection pressures, the flow topology between the experiment and the simulation is in good agreement. For both secondary injection pressures, experimentally and numerically, the exhaust flow exhibits the presence of the SI shock, the recompression shock, and the HAP shock. The simulations indicate that the bigger secondary mass flow rate ratio ($\varphi_{\dot{m}}$ = 0.062) induces a larger SI shock angle. This SI shock interacts with a Mach disk near the symmetry axis and is reflected towards the exhaust plume boundary. The presence of the Mach disk is also confirmed experimentally as a slip line can be identified at the nozzle exit. The reflected SI shock is turned into an expansion fan at the contact with the plume boundary followed by the coalescence of compression waves to form another shock.

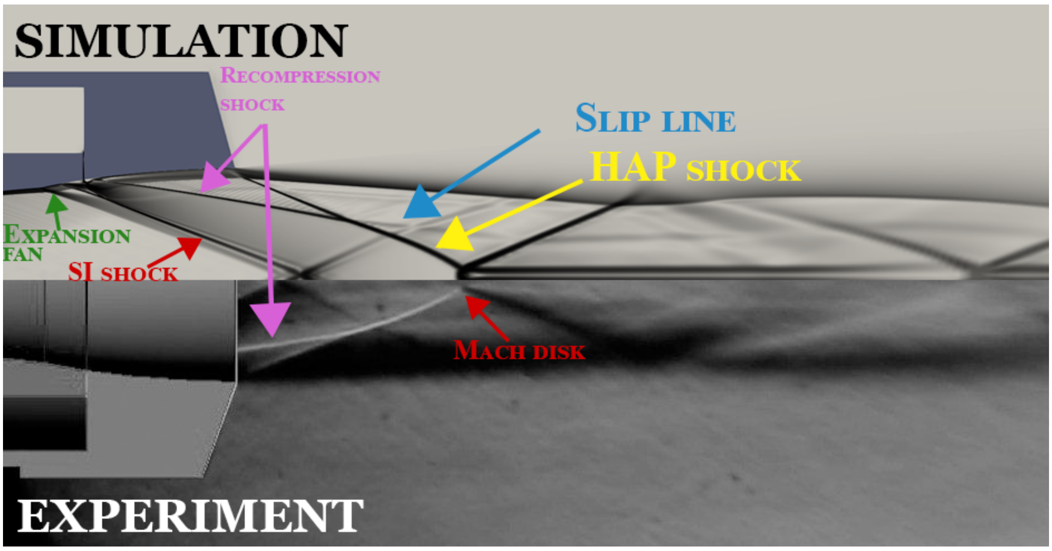

(a) NPR = 30 | $\varphi_{\dot{m}} = 0.020$

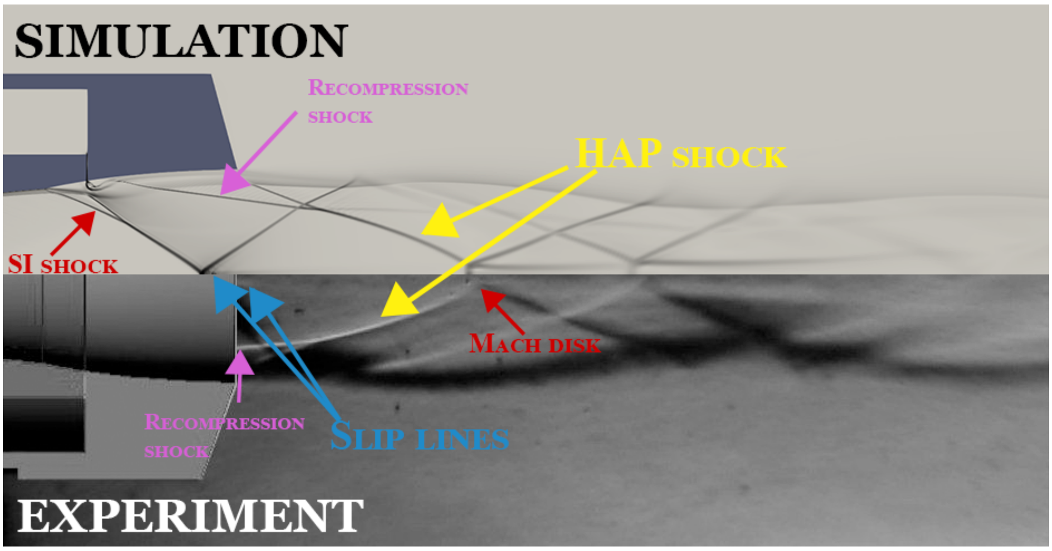

(b) NPR = 30 | $\varphi_{\dot{m}} = 0.062$

Fig. 5.8 Numerical and experimental Schlieren comparison at NPR = 30 for $\varphi_{\dot{m}} = 0.020$ (on top) and $\varphi_{\dot{m}} = 0.062$ (on bottom).

The latter is called secondary SI shock reflection in this thesis. When the DBN operates with $\varphi_{\dot{m}} = 0.062$, the secondary SI shock reflection topology agrees with the experiment, also displaying the Mach disk, the shock reflection, and the slip line. The series of compression and expansion cells continues downstream until the exhaust jet pressure adapts to the ambience. It is noteworthy that, during experiments conducted with secondary injection, akin to those in the smooth DBN, the flip-flop phenomenon was not observed. The presence of both the secondary injection slot and the secondary jet appears to influence the flow dynamics and may contribute to mitigating this unsteady and potentially hazardous phenomenon.

5.4 Quantitative flow analysis

5.4.1 Delay of transition and retransition NPR

Fig. 5.9 shows the evolution of the transition and the retransition NPR as a function of the secondary mass flow rate ratio. The greyed-out area indicates when the secondary injection is subsonic. The configuration associated with a mass flow rate ratio of 0 in Fig. 5.9, Fig. 5.16, and Fig. 5.17, corresponds to the case with the empty cavity connected with the injection pipes, but without operating secondary injection (see Section 4). The experiments performed with secondary injection in the extension profile confirm that the NPR_{trans} and $NPR_{retrans}$ are significantly influenced by the secondary injection jet (see Fig. 5.9).

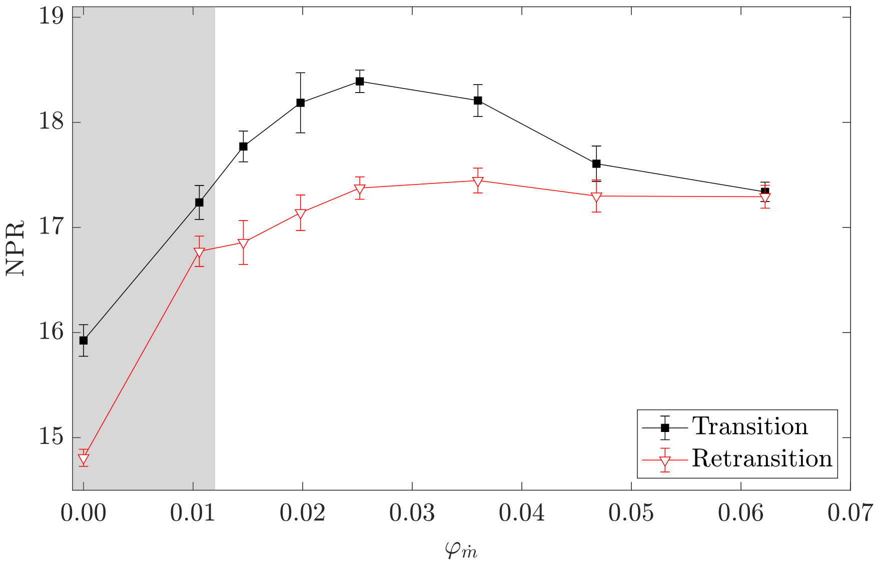

Fig. 5.9 Transition and retransition NPR versus secondary mass flow rate ratio. Greyout area defines when secondary injection is subsonic. Error bars show the standard deviation calculated for each configuration

From $\varphi_{\dot{m}} = 0.011$ to $\varphi_{\dot{m}} = 0.025$, the NPR_{trans} increased when the secondary mass flow rate ratio was increased. The NPR_{trans} rose between a minimum value of 8.2% up to a maximum value of 15.5% compared to the cavity with pipes case, where the transition NPR was 15.92. Similarly, from $\varphi_{\dot{m}} = 0.011$ to $\varphi_{\dot{m}} = 0.036$, the $NPR_{retrans}$ increased within a range of 13.3% to 17.8% with an increase in secondary mass flow rate ratio, bringing the $NPR_{retrans}$ from 14.81 for the cavity with pipes case, up to 17.45. The transition NPR and the retransition

NPR reached a maximum value of 18.39 and 17.45 respectively. The two maximums were reached for a different secondary mass flow rate ratio: $\varphi_{\dot{m}} = 0.025$ for the transition phases, and $\varphi_{\dot{m}} = 0.036$ for the retransition phases. Even though the steady RANS calculations do not give any information on the dynamics of the flow (whether the DBN is under a transition phase or a retransition phase), the numerical findings also confirm the delay in operating mode switch to higher NPRs. Fig. 5.10 and Fig. 5.11 shows the Mach number contours for four secondary injection pressures at several NPR. The figures indicate that the higher the secondary injection pressure, the higher the NPR at which the flow reattaches the second bell, indicating a full-flowing mode.

At NPR = 17, Fig. 5.10 and Fig. 5.11 reveal significantly growing recirculating flow region as the secondary injection pressure is increased. For $\varphi_{\dot{m}} = 0.011$, the secondary jet does not enter the DBN mainstream flow at sonic speed. The low momentum carried by the injection jet is not sufficient to act as a strong barrier to the upcoming flow, and the transition takes place at NPR = 17.5. Nevertheless, the larger the secondary mass flow rate, the higher the momentum in the vertical direction and the secondary flow expansion in the recirculation bubble, acting as a forward-facing step in the supersonic flow. The increase in secondary mass flow rate causes the fluidic obstacle to become more significant, and the size of the upstream and downstream separation bubble increases, preventing the flow from reattaching the extension section until the critical transition NPR is reached. Moreover, the upstream separation bubble size increases due to higher secondary injection pressure, causing the boundary layer separation to occur further upstream, in the vicinity of the inflexion point (see Fig. 5.12). Throughout this simulation campaign and depending on the NPR and the $\varphi_{\dot{m}}$, the separation onset might be located from $-0.15 \cdot r_{th}$ upstream the inflexion point to $0.63 \cdot r_{th}$.

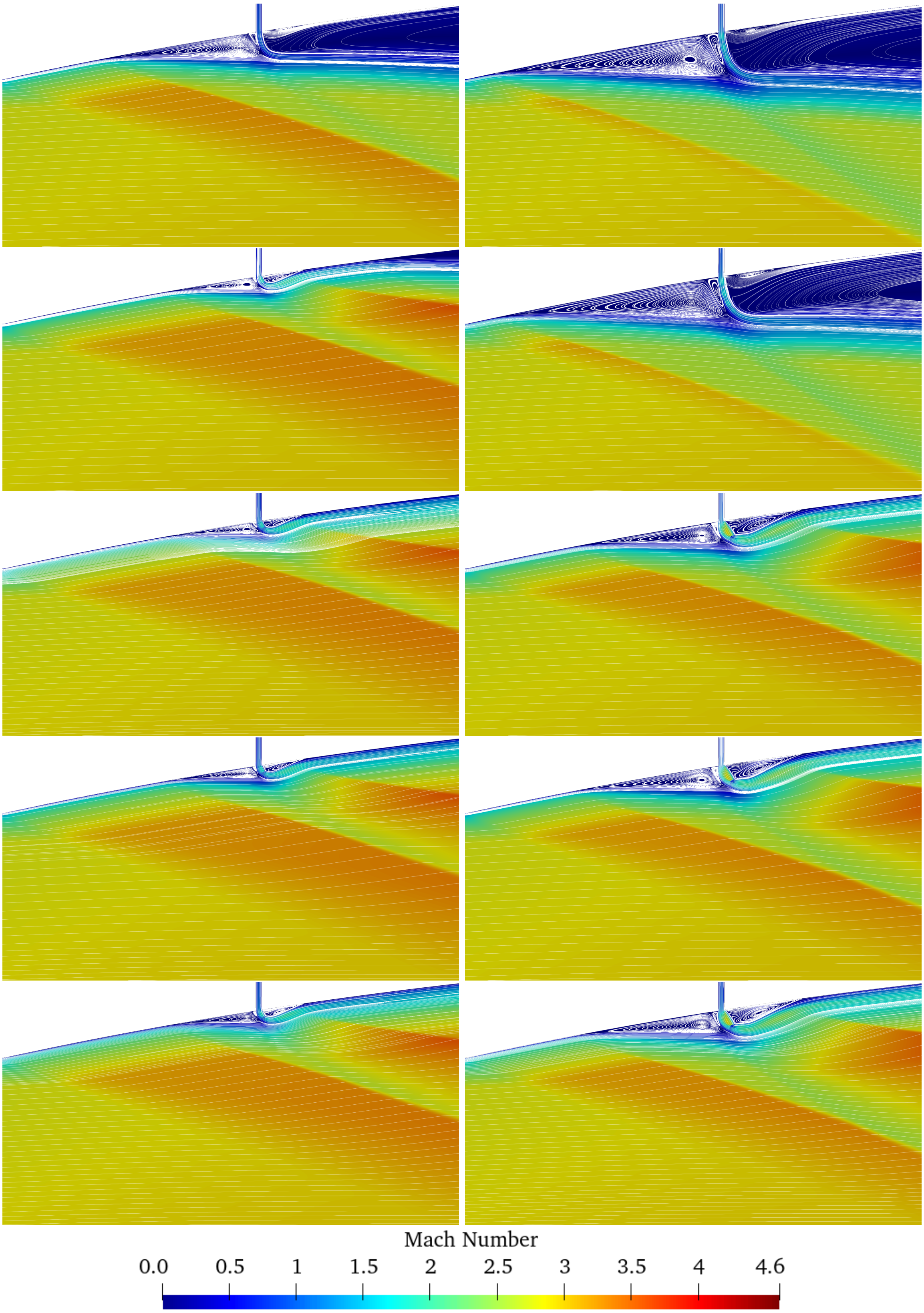

Fig. 5.10 Mach contours for $\varphi_{\dot{m}} = 0.011$ on the left and $\varphi_{\dot{m}} = 0.020$ on the right. NPR = $\{17, 17.5, 18.5, 19, 30\}$ from top to bottom.

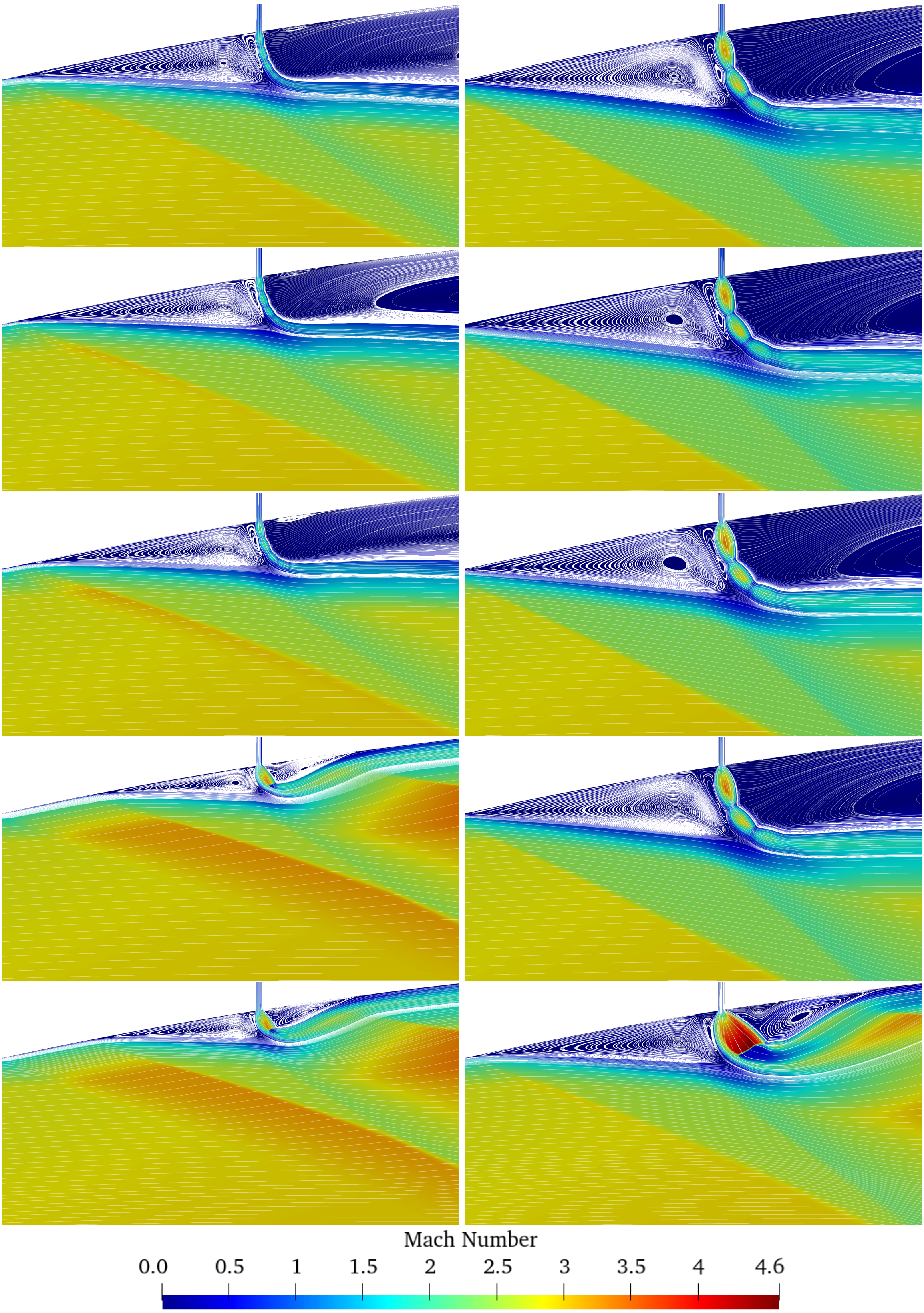

Fig. 5.11 Mach contours for $\varphi_{\dot{m}} = 0.025$ on the left and $\varphi_{\dot{m}} = 0.062$ on the right. NPR = {17, 17.5, 18.5, 19, 30} from top to bottom.

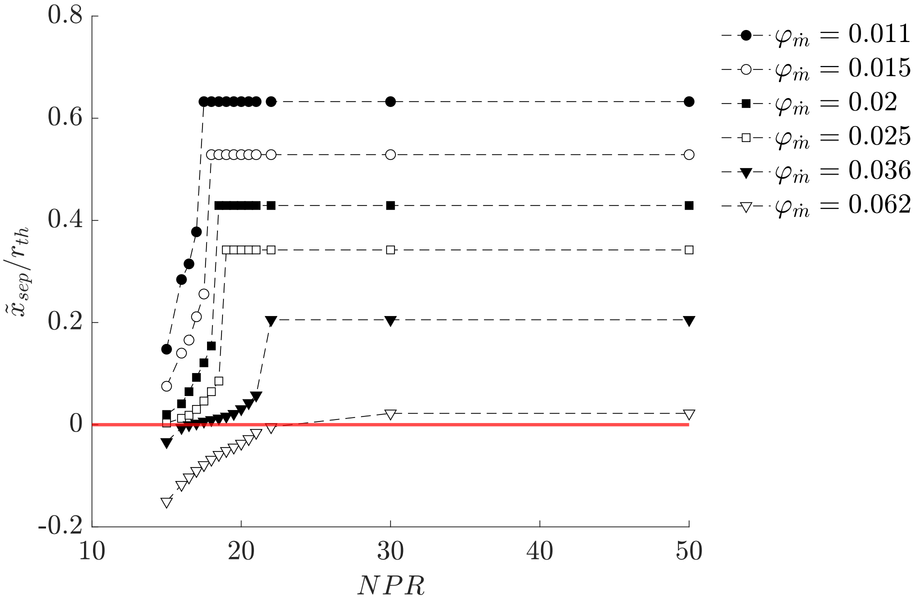

Fig. 5.12 Separation location position from the inflexion point vs NPR for all injection pressure. The red line indicates the position of the inflexion point.

Even though the flow dynamics have not been investigated, an explanation regarding the transition and retransition processes in a DBN with secondary injection may be possible through the analysis of the streamwise wall pressure distribution. At NPR = 17, Fig. 5.13 show that the higher the secondary mass flow rate ratio, the bigger the upstream recirculation bubble and the more upstream the boundary layer separation occurs. Moreover, as the downstream recirculation bubble grows with the secondary mass flow rate ratio, the wall pressure downstream the injection slot also increases, causing more unfavourable conditions for reattachment and transition of the DBN to full-flowing mode. These observations remain valid when the NPR is increased until the transition to high-altitude mode takes place and the flow reattaches the extension section.

Inversely, starting from the streamwise wall pressure distribution in high-altitude mode (NPR = 50), Fig. 5.13 displays several clues to justify the DBN behaviour during retransition. At NPR = 50, the wall pressure downstream the injection slot decreases when the secondary injection pressure increases and the boundary layer reattachment point is pushed downstream. In these conditions, and should the NPR decrease, the shock system located outside the DBN will be pushed inside, triggering boundary layer separation. As the reattachment point for high secondary mass flow rate ratios is located further downstream, the boundary layer of the highest secondary injection cases should sense the shock system presence first, inducing earlier retransitions and consequently higher $NPR_{retrans}$.

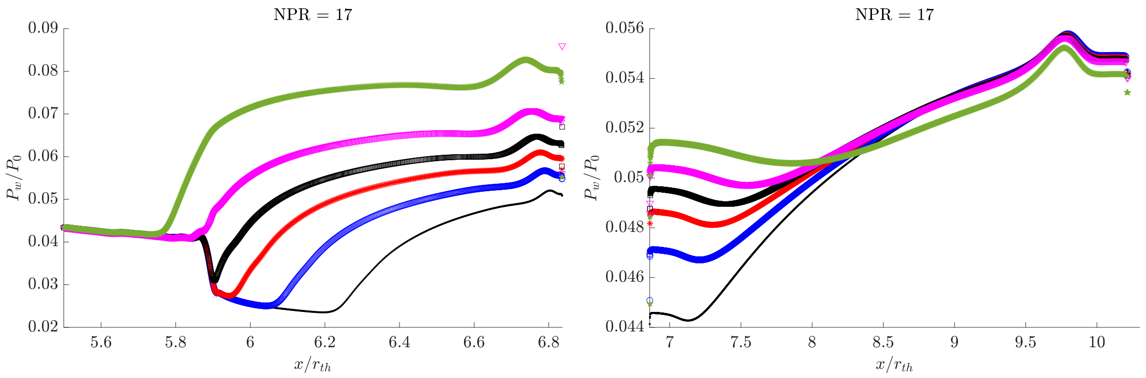

(a) Upstream the injection slot (NPR = 17) (b) Downstream the injection slot (NPR = 17)

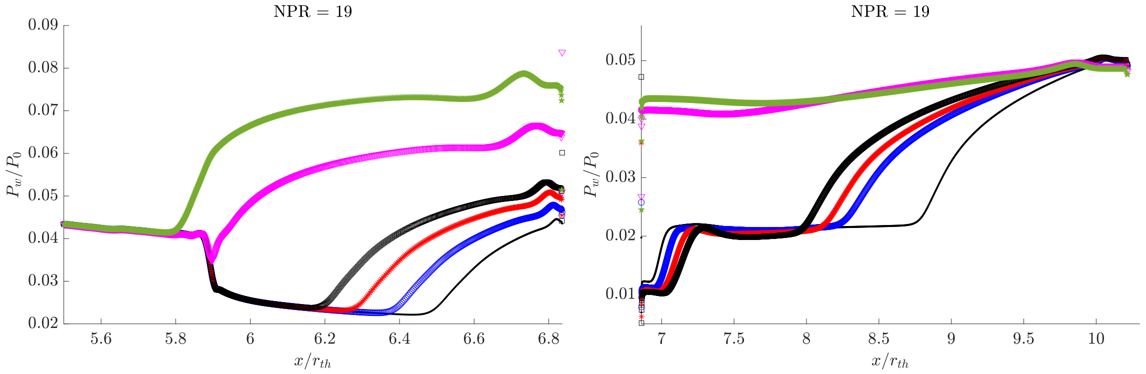

(c) Upstream the injection slot (NPR = 19) (d) Downstream the injection slot (NPR = 19)

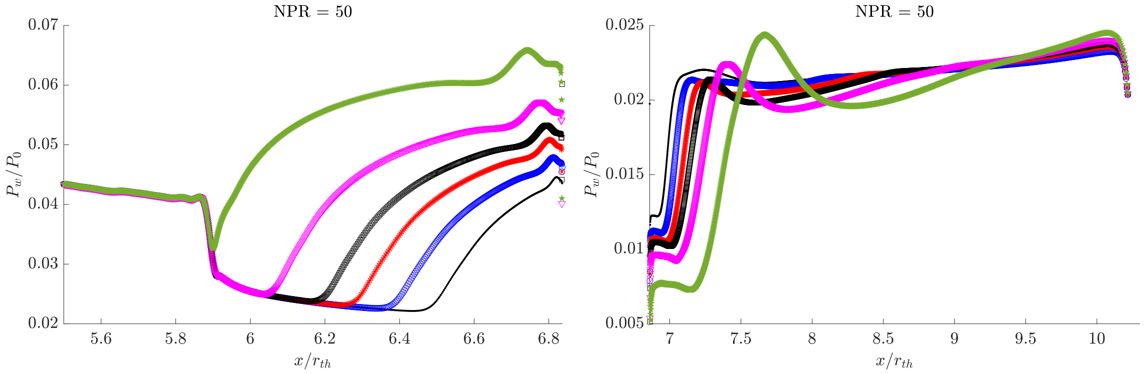

(e) Upstream the injection slot (NPR = 50) (f) Downstream the injection slot (NPR = 50)

· $\varphi_{\dot{m}} = 0.011$ ○ $\varphi_{\dot{m}} = 0.015$ ∗ $\varphi_{\dot{m}} = 0.02$ □ $\varphi_{\dot{m}} = 0.025$ ▽ $\varphi_{\dot{m}} = 0.036$ ★ $\varphi_{\dot{m}} = 0.062$

Fig. 5.13 Streamwise wall pressure at different NPRs upstream the secondary injection slot (left) and downstream the secondary injection slot (right).

From the maximum values of NPR_{trans} and $NPR_{retrans}$, an increase in secondary mass flow rate ratio induced a decrease in both parameters. In the highest mass flow rate ratio case ($\varphi_{\dot{m}}$ = 0.062), the decrease in NPR_{trans} and $NPR_{retrans}$ compared to their maximum values reached 5.7% and 0.9% respectively. Fig. 5.9 clearly shows that there exists a limit in delaying the transitions phases, as there is a point from which an increase in secondary mass flow rate ratio causes a decrease in NPR_{trans} and $NPR_{retrans}$. Using important secondary mass flow rate ratios might change the physics involved in the flow. For the highest secondary injection pressures, the numerical simulations revealed a change in the trend of the separation location curve as a function of NPR (see Fig. 5.12). Indeed, for $\varphi_{\dot{m}} = 0.036$, the separation point moves by $0.03 \cdot r_{th}$ upstream the inflexion point, changing locally the curve trend with a curve inflexion at low NPRs. For $\varphi_{\dot{m}} = 0.062$, the change in curve trend is even more pronounced with a separation point up to $0.15 \cdot r_{th}$ upstream the inflexion point. The change in curve trend may result from the size of the upstream separation bubble, where, if the separation takes place ahead of the inflexion point, the upstream separation bubble behaves as a fluid obstacle upon which the mainstream flow slides. Because the height of the upstream vortex exceeds the inflexion point height (relative to the nozzle wall), we believe that the separation front does not interact with the geometry (inflexion point) and causes a decline in the separation control effectiveness.

Furthermore, it is important to keep in mind that having the highest transition and retransition NPR does not mean better performance. If the secondary mass flow rate is important, the transition NPR is high (with the abovementioned limits), but the specific impulse decreases as it considers the secondary mass flow rate at the denominator.

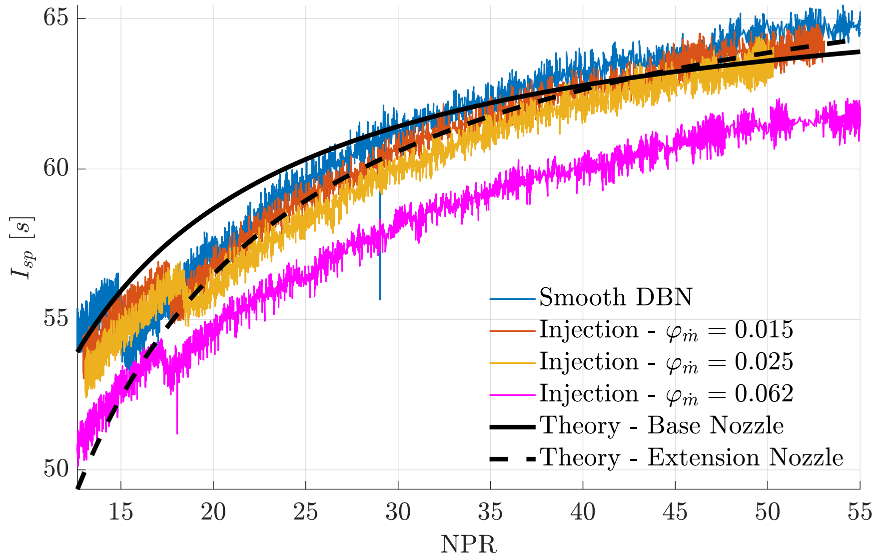

Fig. 5.14 I_{sp} versus NPR for the smooth DBN and different secondary injection configurations. The theoretical performances of the base profile and the extension profile are represented by the black curves.

Fig. 5.14 shows the specific impulse as a function of NPR during an ascent phase for the smooth DBN and the DBNi8 operating with $\varphi_{\dot{m}} = \{0.015; 0.025; 0.062\}$, and for theoretical conventional nozzles with the same expansion ratio as the base nozzle and the extension nozzle. It shows that the secondary jet does not contribute positively to the thrust and reduces the overall performance of the nozzle when the secondary mass flow rate increases. Fig. 5.14 reveals the importance of carefully managing the trade-off between achieving the desired delay in both NPR_{trans} and $NPR_{retrans}$ while considering the reduction in specific impulse when operating the secondary injection.

5.4.2 Impact on the hysteresis

The hysteresis effect is of critical importance for the stability of a DBN as a small hysteresis may lead to uncontrolled operating mode change, called flip-flop behaviour. Fig. 5.15 shows the hysteresis as a function of secondary mass flow ratio $\varphi_{\dot{m}}$. It shows that the secondary injection mass flow rate ratio distinctively affects the stability of the nozzle. In Fig. 5.15, the hysteresis was the largest for the cavity without injection, reaching 7%, then decreased to 2.7% for $\varphi_{\dot{m}} = 0.011$. At this secondary mass flow rate ratio, the secondary jet is not sonic and may harm the DBN's stability. For $\varphi_{\dot{m}} > 0.011$, the hysteresis increases with the secondary mass flow rate ratio to hit a maximum of 5.7% for $\varphi_{\dot{m}} = 0.020$. A further increase in the secondary mass flow rate ratio induced a decrease in stability as the hysteresis became smaller, dropping to 0.3% for the highest mass flow rate ratio.

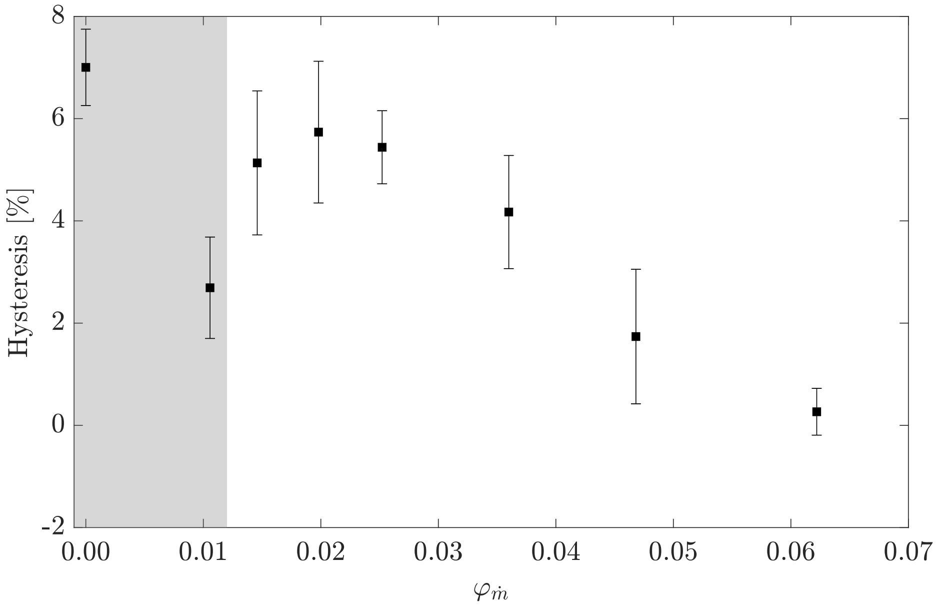

Fig. 5.15 Hysteresis versus secondary mass flow rate ratio.

From Fig. 5.9 and 5.15, one notices that the NPR_{trans} was delayed by 14.2% for $\varphi_{\dot{m}} = 0.020$ when compared to cavity with pipes case, while an hysteresis of 5.7% was measured.

However, for $\varphi_{\dot{m}} = 0.025$, the NPR_{trans} was delayed by 15.5% while an hysteresis of 5.4% was measured. These results already indicate that a tradeoff is necessary between the transition delay and the DBN stability should DBNs be used with transverse secondary injection as active flow control.

5.4.3 Reduction of side-loads

By using radial secondary injection in the extension nozzle, the lateral forces generation was considerably reduced (see Fig. 5.16). From $\varphi_{\dot{m}} = 0.015$ and above, the side-loads magnitude generated during the transitions and the retransitions fall within the balance measurement noise (± 0.5 N). In the aforementioned mass flow rate ratio range, the force balance could not measure any side-loads peak. The presence of the cavity was already sufficient to decrease the lateral forces compared to the smooth configuration as the side-loads generated during transitions dropped from 2.4% of the nozzle thrust to 1.1%. Eventually, once secondary injection was used for $\varphi_{\dot{m}} = 0.011$ and above, the side-loads during transition dropped below 1% of the nozzle thrust.

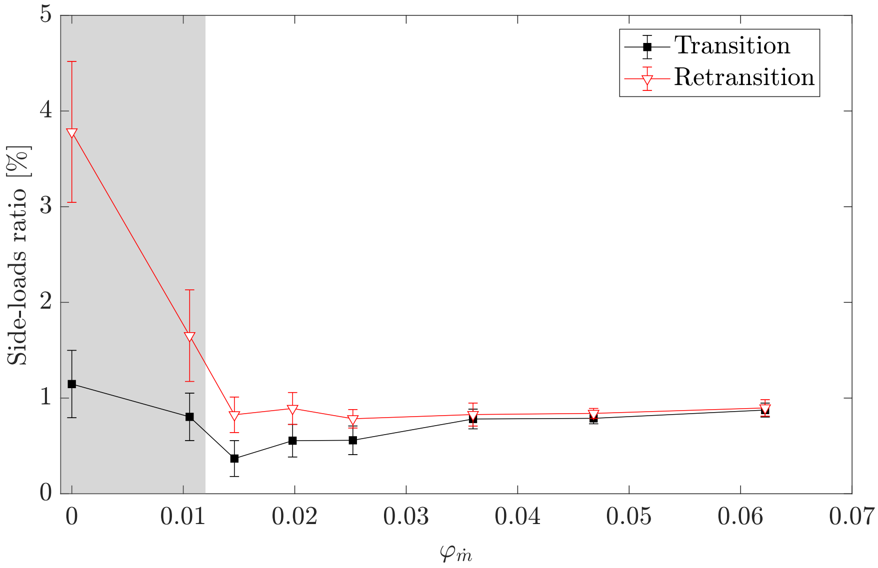

Fig. 5.16 Side-loads ratio vs mass flow rate ratio

Lateral forces generated during the retransition phases have always been greater than during the transition phases in the present DBN. Indeed, the side-loads generated during retransition reached 3.4% of the nozzle thrust in the smooth nozzle configuration. However, secondary injection application brought side-loads during retransition below 1% of the nozzle thrust for $\varphi_{\dot{m}} = 0.015$ and above, providing over three times lower lateral forces magnitude compared to the smooth nozzle configuration. From $\varphi_{\dot{m}} = 0.036$ and above, a slight increase in lateral forces is visible during both, the transition and the retransition phases. This rise in lateral forces also falls within the measurement noise. The overall decrease in side forces generated by the DBN with secondary injection raises questions on the mechanism driving this decrease. Two possible reasons for this decline were identified. The first is based on Schmucker's work [107], which states that the side forces generated in a separated nozzle flow are inversely proportional to the wall pressure gradient in the nozzle. Consequently, in the case of a DBN operating with secondary injection, the adverse wall pressure gradient induced by the presence of the secondary jet may decrease the magnitude of the side forces. As the adverse pressure gradient increases with the secondary mass flow rate ratio, it may be favorable to induce a larger decrease in side-loads generation. The second reason for the decrease in lateral forces is based on an obstacle perspective. In separated nozzle flow, a recent study showed that the side-loads generation process is based on a feedback loop process involving upstream and downstream propagating waves, similar to screech resonance [23]. The paper indicates that 20% of the lateral forces are attributed to the resonant waves, and 80% to the shock motion, itself induced by the resonance. Therefore, the presence of a sonic secondary jet may break the feedback loop necessary for generating side loads. The higher the secondary mass flow rate ratio, the greater the favourable effect on the side-loads generation process.

5.4.4 Reduction of thrust jump

The influence of secondary injection on thrust jump during the transition and the retransition phases is shown in Fig. 5.17. The test series revealed that the secondary mass flow rate did not present any significant impact on the thrust jump magnitude during transition and retransition between $\varphi_{\dot{m}} = 0.015$ to $\varphi_{\dot{m}} = 0.025$ as it stays fairly constant, though much less important than the smooth nozzle configuration. For $\varphi_{\dot{m}} = 0.011$, the jumps magnitude during both, the ascent and the descent, are slightly higher than for the other cases. The latter observation might emanate from the non-sonic secondary injection jet at $\varphi_{\dot{m}} = 0.011$ which can be a source of instability in the flow and a more thorough investigation is necessary to validate this hypothesis. Above $\varphi_{\dot{m}} = 0.025$, an extra decrease in thrust jump is visible as the secondary injection pressure is increased, though the maximum decrease remains fairly close to the values between $\varphi_{\dot{m}} = 0.015$ and $\varphi_{\dot{m}} = 0.025$.

Fig. 5.17 also reveals that no significant differences were measured between the cavity connected to the injection pipes configuration and the different injection cases during the transition. However, when comparing the smooth nozzle case to the injection cases, the presence of the injection jet induced a decrease in thrust jump during transition by a factor of 3.2.

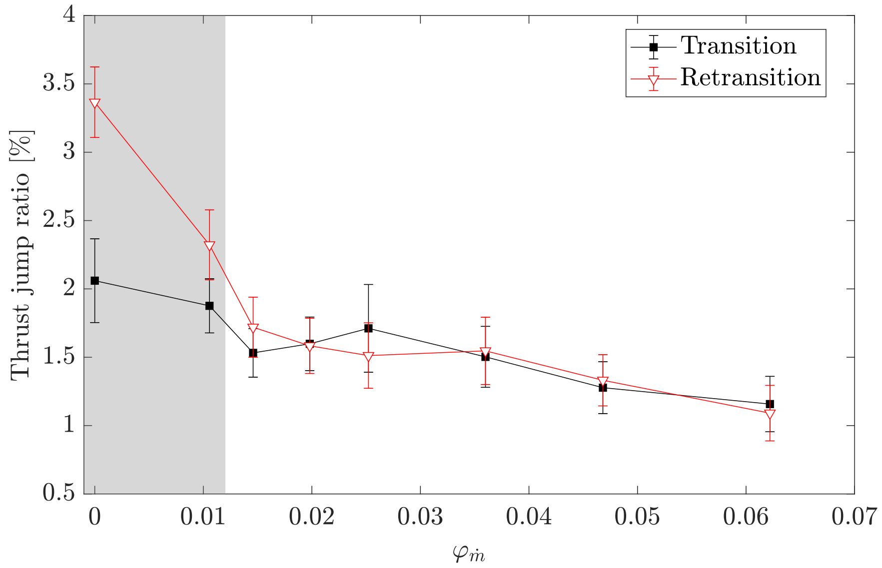

Fig. 5.17 Thrust jump ratio vs mass flow rate ratio

During the retransition phase, the presence of secondary injection reduced the thrust jump up to 2.3 percentage points compared to the cavity with pipes case, and 3.1 percentage points (a factor of 3.8) compared to the smooth nozzle configuration. A particular behaviour was observed in the DBN during the experiments in the high-end of the secondary mass flow rate ratio. As displayed in Fig. 5.18, in the presence of high secondary mass flow rate ratios, the jump in specific impulse curve during the transition and the retransition phases is preceded by a specific impulse plateau and becomes less steep (or spread on larger NPR range).

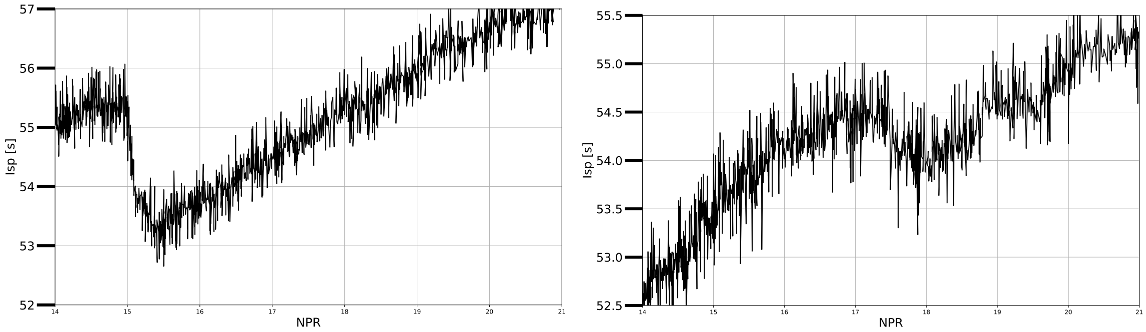

(a) Smooth DBN.

(b) DBN with secondary injection: $\varphi_{\dot{m}} = 0.062$

Fig. 5.18 Specific impulse trajectory in the smooth DBN (left) and the DBN operated with secondary injection (right) during an ascent phase.

In these configurations, the transition and retransition processes seem to take place more continuously, as is the case in a negative pressure gradient extension section. The schlieren videos also support this theory as the shock cell movement from the inflexion point to the nozzle lip takes place during a longer period of time. Unfortunately, a precise measurement of the transition and retransition time to quantify this phenomenon could not be achieved in the current experimental setup. The steady RANS simulations could not further explain the aforementioned observation, which brings an additional unanswered question to the DBNs' behaviour.

5.5 Conclusions

This chapter presented the effects of radial secondary injection through an annular slot in the extension section of the DBN. The experimental data was analysed and compared to the numerical results. Several secondary mass flow rate ratios ranging from 0.011 to 0.062 were considered in the experimental test campaign. The experiments showed that the transition NPR was delayed up to nearly 24% for a mass flow rate ratio of 0.025 compared to the smooth nozzle. The retransition NPR was increased up to 20.1% for a mass flow rate ratio of 0.036 compared to the smooth nozzle. The experiments showed that the transition and the retransition NPR delay were limited, reaching their maximum values in the middle range of secondary mass flow rate ratio used. The numerical simulations suggested that the delay in transition NPR was attributed to the presence of the fluidic obstacle, displacing and forcing the separation location in the vicinity of the inflexion point. The increase in retransition NPR was also attributed to the fluidic obstacle, inducing a recirculation bubble whose length increases with the secondary mass flow rate ratio, triggering early retransition.Furthermore, the simulations indicated that for the highest secondary mass flow rate ratios investigated, the upstream separation bubble extends upstream of the inflexion point, preventing the separation front from interacting with the inflexion point. This phenomenon was identified as a potential cause for the limited effect of secondary injection on the DBN's behaviour, and the decline in NPR_{trans} and $NPR_{retrans}$ for the highest secondary mass flow rate ratios.

The side-loads were reduced below 1% of the nozzle thrust during both: transition, and retransition phases using a secondary mass flow rate ratio of only 0.015. The important adverse pressure gradient induced by the secondary flow and the transverse sonic jet boundary were assumed to be responsible for this significant achievement.

Moreover, secondary injection reduced the thrust-jump-to-thrust ratio during transition up to 2.6 percentage points and during retransition up to 3.1 percentage points for the highest secondary mass flow rate ratio compared to the smooth nozzle case. The influence of the secondary injection mass flow rate ratio on the DBN transition and retransition process duration was brought to light, providing other investigation topics for the complete understanding of

DBNs' behaviour. Nevertheless, the secondary injection, with its capabilities for decreasing lateral forces and sudden change in thrust while improving the nozzle efficiency, could, therefore be seen as a genuine asset for the next generation of reusable launchers.

A further parametrical investigation and, noticeably, the streamwise position of the injection slot will be an interesting aspect of DBNs regime transition control and will be discussed in the next chapter. The results presented constitute a proof of concept of the radial secondary injection on a cold flow subscale DBN model and investigations at industrial Reynolds number must be undertaken to demonstrate the effectiveness of the injection method on a full-scale DBN.

Chapter 6

Dual-bell nozzle optimisation potential

6.1 Introduction

This chapter aims to address two key aspects: first, to examine the interaction between the secondary injection and the inflexion point, and second, to observe the effects of the injectant gas characteristics on the behaviour of the DBN.

The first section of the chapter studies the influence of the secondary injection position by analysing two DBNs of the same profile but different secondary injection slot positions. The secondary injection slot was located 8 mm downstream of the inflexion point in the first DBN (DBNi8), and 16 mm downstream of the inflexion point in the second nozzle (DBNi16). The injection location influence is discussed firstly by comparing the exhaust flow topology for both cases. Then, a quantitative analysis is performed by studying the experimental data. The results are compared together to present the influence of the secondary injection location in a subscale DBN.

The second part of the chapter focuses on the secondary injectant gas nature influence in the DBNi8 test specimen. The study was performed by operating the DBNi8 with helium and the results were compared to the DBNi8 case operating with air. Similarly to the injection position influence study, the effect of helium as a secondary injectant gas is assessed firstly through a qualitative analysis of the exhaust plume flow. A quantitative analysis is then performed where the key DBN's parameters are investigated and the results are opposed to those of the DBNi8 operating with air to stress the impact of a different injectant gas on the DBN's behaviour.

6.2 Influence of the secondary injection location

6.2.1 Preliminary section

This section discusses the influence of the secondary injection position on the DBN's behaviour. To do so, a DBN referred to as DBNi16 was manufactured with the same profile as the DBNi8 test specimen, but with a secondary injection slot located 16 mm downstream of the inflexion point (see Chapter 2). The testing conditions were similar to those of the previous chapters with a stagnation pressure of 350 kPa and a varying ambient pressure to reach nozzle pressure ratio values of NPR $\in$ [12;60]. The stagnation pressure P_i used to feed the secondary jet averagely ranged within $P_i \in [36.6;87.8]$ kPa for the DBNi16 test specimen, corresponding to a mass flow ratio range of $\varphi_{\dot{m}} \in [0.011;0.027]$.
Fig. 6.1 shows the NPR, specific impulse, side-loads ratio, and secondary pressure ratio as a function of time during a customary experiment.

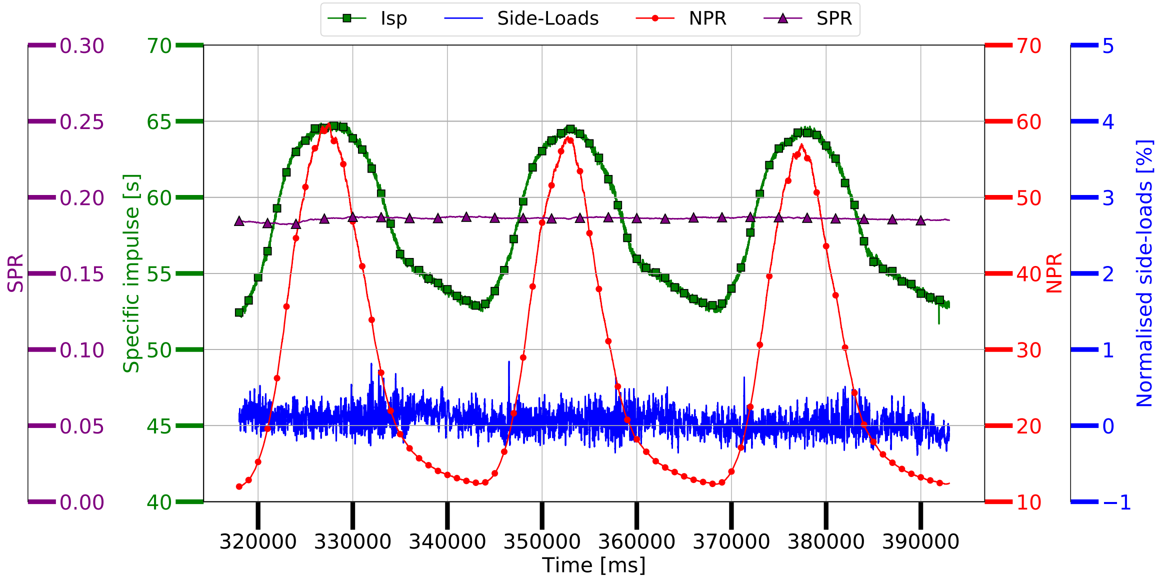

Fig. 6.1 Specific impulse, NPR, SPR, and side-loads ratio as a function of time: DBNi16 operating with $\varphi_{\dot{m}} \approx 0.020$

The pressure decrease in the wind tunnel test section causes the NPR to rise. The rise in NPR causes the DBN's specific impulse to increase until the transition from the low-altitude mode to the high-altitude mode occurs. Here, neither the sudden jump in the specific impulse nor the peak in lateral force are apparent. This surprising and unparalleled observation, not documented in the open literature, will be investigated in a subsequent section. During the descent phase, when the NPR decreases, the DBN eventually retransition from the high-altitude mode to the low-altitude mode. Again, no sudden jump in specific impulse or side load peak is visible. It is worth noting that Fig. 6.1, which highlights some of the DBN's crucial parameters, already illustrates the critical influence of the secondary injection position on the DBN's behaviour when compared to Fig. 5.2.

The next sections provide a qualitative analysis of the DBN exhaust plume topology and a quantitative analysis of the DBN key parameters in the DBNi16, namely the transition NPR, side forces, and thrust jump measured during the transition and the retransition phases. The results are compared to the DBNi8 test specimen to observe the direct effects of the secondary injection position on the DBN's behaviour.

6.2.2 Qualitative analysis

This section compares a series of schlieren images from the experiments performed with the DBNi8 and DBNi16 test specimens. The shock system being similar during the ascent and descent phases, the exhaust flow features are discussed for several NPRs during the transition phase only. Fig. 6.2 shows schlieren images of the DBN exhaust plume for roughly NPR $\in [17.4;50]$ in the DBNi8 and DBNi16 nozzles operating at $\varphi_{\dot{m}} = 0.025$ and $\varphi_{\dot{m}} = 0.027$, respectively.

At NPR ≈ 17.4, the two dual-bell nozzles operate in low-altitude mode. The flow analysis performed in Chapter 5 showed that the DBNi8 flow contains two main shock systems: the shock induced by the secondary injection jet (SI shock) and the shock induced by the high ambient pressure (HAP shock) compressing the core flow. The DBNi16 nozzle exhibits both of these features prominently, as depicted in Figure 6.2b. The secondary jet acts as an obstacle and generates a bow shock wave locally. The adverse pressure gradient induced by the jet causes the boundary layer to separate upstream, inducing an oblique separation shock, the SI shock. The shock reflections on the schlieren image indicate that the angle of the SI shock is of the same magnitude as the HAP shock. The distance between the two shocks' feet makes their distinction possible. However, when the secondary injection slot is moved downstream, this gap diminishes, causing the two shock structures to interact closer together. This proximity makes it more challenging to distinguish between them, especially since the internal flow visualisation is not available. For both test specimens, a series of compression and expansion cells follow these structures until the exhaust plume pressure adapts to the ambient pressure in the wind tunnel test section.

As the NPR increases to 18, the flow expands, and the two principal shock structures move downstream for both DBNs. However, the two shocks remain difficult to tell apart in the DBNi16 configuration.

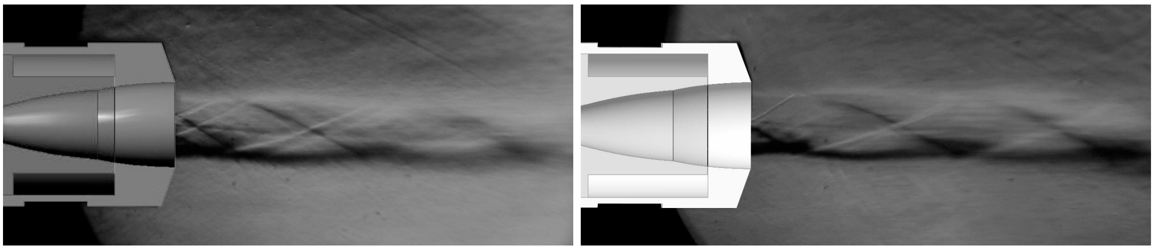

(a) DBNi8 - NPR = 17.47 (b) DBNi16 - NPR = 17.41

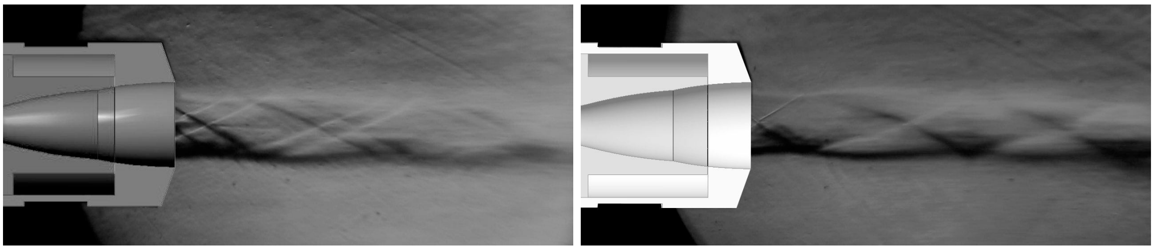

(c) DBNi8 - NPR = 18 (d) DBNi16 - NPR = 18

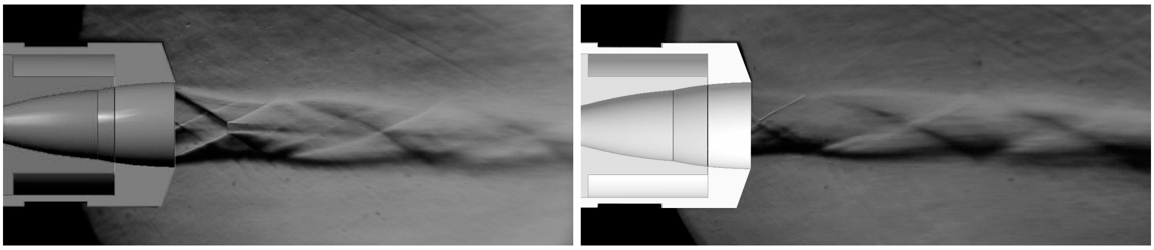

(e) DBNi8 - NPR = 18.48 (f) DBNi16 - NPR = 18.46

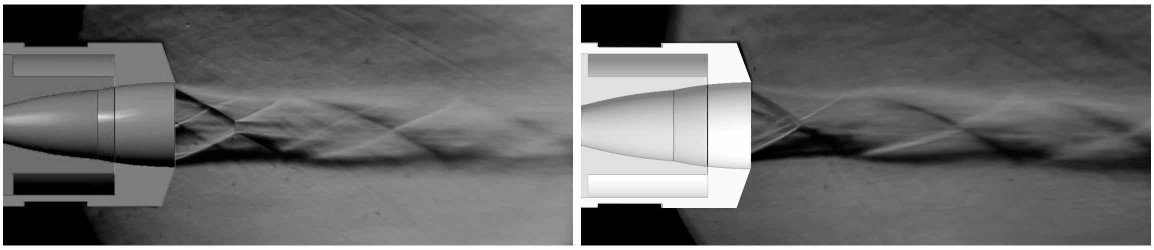

(g) DBNi8 - NPR = 19.77 (h) DBNi16 - NPR = 19.77

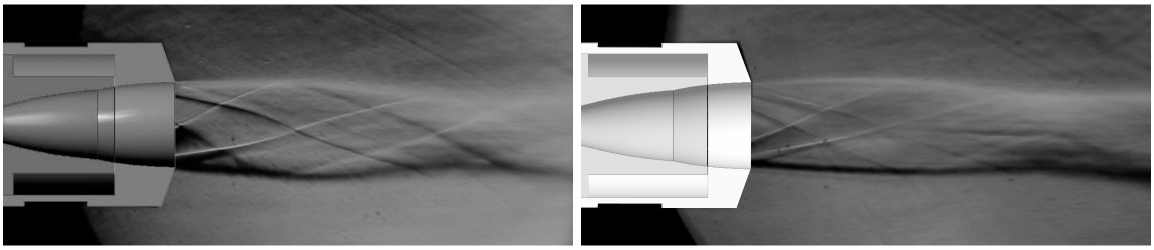

(i) DBNi8 - NPR = 50.09 (j) DBNi16 - NPR = 49.98

Fig. 6.2 Experimental schlieren during a transition phase for the DBNi8 (left) and DBNi16 (right) test specimens operating at $\varphi_{\dot{m}} = 0.025$ and $\varphi_{\dot{m}} = 0.027$, respectively.

At NPR $\approx$ 18.50, the transition from the low-altitude mode to the high-altitude mode occurred almost fully in the DBNi8 test specimen. Here, the flow has reattached to the extension section wall, but the absence of internal recompression shock suggests that the flow is not fully attached to the entirety of the extension wall. Similarly to the low-altitude mode, the higher ambient pressure compresses the jet column and an oblique shock wave (HAP shock) emerges from the nozzle wall. At this NPR, the strong nature of the HAP shock is supported by the singular Mach reflection, where the schlieren depicts a Mach disk, a reflected shock and slip lines at the triple point. Both, the SI shock and the HAP shock induce a series of compression and expansion cells in the exhaust plume downstream. Conversely, the DBNi16 has yet to transition to the high-altitude mode and the shock system is the same as for NPR = 18.

At NPR = 19.77, the transition has taken place in the DBNi16 nozzle. The SI shock, the HAP shock, and the Mach disk become apparent. Similarly to the DBNi8 nozzle at NPR = 18.48, the DBNi16 does not show any internal recompression shock, which suggests that the flow is not fully attached to the entirety of the extension wall. The well-known compression and expansion cells following the primary shock systems are also visible. As for the DBNi8 nozzle, the transition has fully occurred, and an internal recompression shock emerges due to the constant pressure nature of the extension section.

At NPR $\approx$ 50, the two DBNs operate in the high-altitude mode. The oblique HAP shock ceased to exist. Both schlieren images display the SI shock and the internal recompression shock, which extends throughout the exhaust plume. Because the secondary injection slot is displaced in the aft part of the extension section in the DBNi16 nozzle, the reflection of the SI shock is displaced further downstream, as opposed to the DBNi8 test specimen, where the reflection is positioned in the vicinity of the nozzle exit. Nonetheless, both shock topologies exhibit similar patterns.

It is noteworthy to mention that, in the experiments conducted in the DBNi16 with relatively high secondary mass flow rate ratios, the Schlieren videos revealed transition and retransition phases that appeared to unfold more continuously, with less abruptness. The subsequent section explores this observation, offering a qualitative analysis of the DBN's behavior.

6.2.3 Quantitative analysis

One of the main reasons transverse secondary injection is used in DBNs is to delay the early transition NPR during the rocket ascent phase. Delaying the transition from the low-to-high-altitude mode would result in better performances as the transition would occur closer to the optimum transition point. This delay in transition was successfully achieved by performing an annular, transverse secondary injection in the extension section, 8 mm downstream of the inflexion point (see Chapter 5). Fig. 6.3 shows the transition and retransition NPR for several secondary mass flow rate ratios from experiments performed with DBNi8 and DBNi16. The same behaviour is observed in both cases: the transition and the retransition NPRs increase with the secondary mass flow rate ratio. This observation is primarily attributed to the secondary injection jet acting as an obstacle to the upcoming flow. The adverse pressure gradient caused by the presence of the jet induces the boundary layer to thicken and separate upstream of the injection slot. The higher the secondary mass flow rate ratio in the low-altitude mode, the higher the wall pressure in the extension section. The strong wall pressure combined with the pressure gradients and the flow deviation in the vicinity of the injection slot forces the flow to remain separated in the extension section for higher NPR, inducing higher transition NPR. In high-altitude mode, the stronger the secondary mass flow rate, the wider the recirculation bubble spreads in the extension section. Combined with the radial fluid injection deviating the core flow towards the nozzle symmetry axis, the flow is less resistant to the adverse pressure gradient and separates at higher NPR in the descent phase, justifying the increase in retransition NPR.

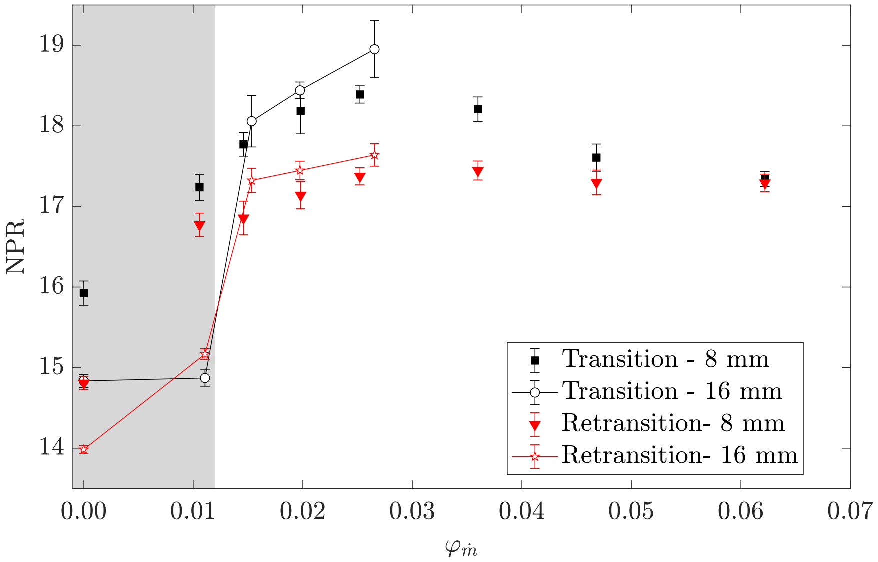

Fig. 6.3 Transition NPR as a function of mass flow rate ratio for different secondary injection positions.

The difference in NPR_{trans} and $NPR_{retrans}$ between the DBNi8 and DBNi16 cases remains marginal for $\varphi_{\dot{m}} > 0.011$. The DBNi16 NPR_{trans} was at most 3.1% higher than in the DBNi8 case when operating with $\varphi_{\dot{m}} = 0.027$ and $\varphi_{\dot{m}} = 0.025$, respectively. During the descent phases, the DBNi16 $NPR_{retrans}$ was at most 2.8% higher than in the DBNi8 case when operating with $\varphi_{\dot{m}} = 0.015$ and $\varphi_{\dot{m}} = 0.015$, respectively. Displacing the injection slot 16 mm downstream of the inflexion point does not have a significant impact on the transition and

retransition NPRs for $\varphi_{\dot{m}} > 0.011$. The lack of data points for $\varphi_{\dot{m}} > 0.027$ in the DBNi16 configuration does not allow to state whether for higher secondary mass flow rate ratio the NPR_{trans} and $NPR_{retrans}$ will decrease, as observed in the DBNi8 case.
However, even though the NPR_{trans} and $NPR_{retrans}$ evolution as a function of $\varphi_{\dot{m}}$ followed a similar trend in the DBNi8 and DBNi16 configurations, the transition process was found to be significantly different. In the DBNi16 case and for $\varphi_{\dot{m}} > 0.011$, the transition process took place less suddenly and sometimes without any sudden jump in specific impulse (see Fig. 6.4).

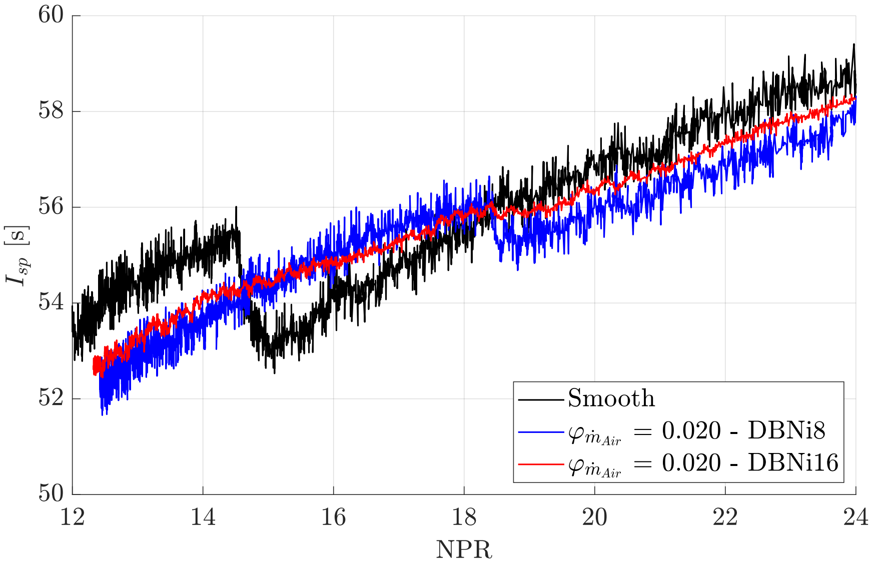

Fig. 6.4 Specific impulse as a function NPR during an ascent phase for the smooth DBN, DBNi8 operating with $\varphi_{\dot{m}} = 0.020$ and DBNi16 operating with $\varphi_{\dot{m}} = 0.020$.

This distinctive characteristic was observed in neither the smooth DBN nor the DBNi8 configurations and the open literature. The higher the secondary mass flow ratio, the more continuous the transition and retransition phases become, with a stronger effect during the transition phases. These effects are shown in Fig. 6.5, which displays the I_{sp} for DBNi16 operating with $\varphi_{\dot{m}} = 0.011$ and $\varphi_{\dot{m}} = 0.015$, and Fig 6.6, which displays the I_{sp} as a function of NPR during an ascent and a descent phase. This observation was also supported by the schlieren videos, which show that the transitions and retransitions occur less abruptly and more continuously.

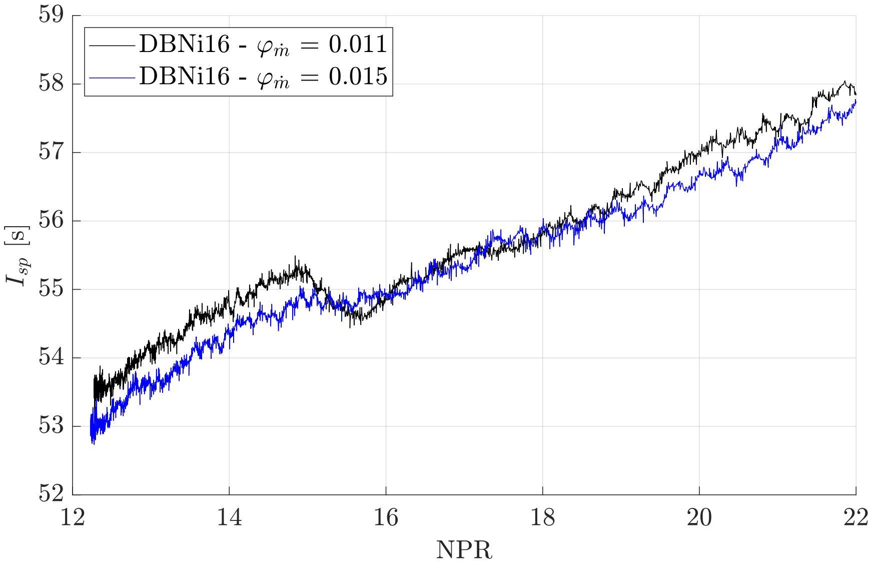

Fig. 6.5 Specific impulse as a function NPR during an ascent phase in the DBNi16 configuration operating with $\varphi_{\dot{m}} = 0.011$ and $\varphi_{\dot{m}} = 0.015$.

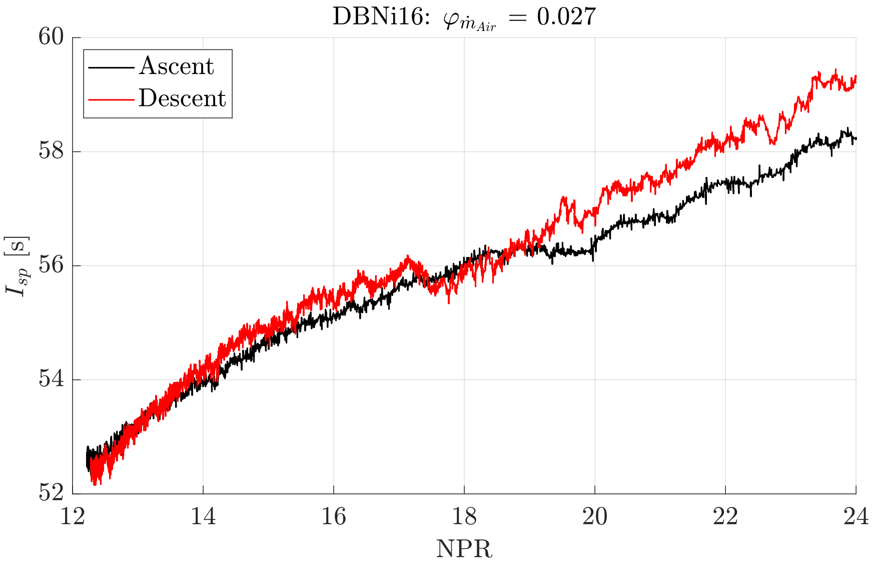

Fig. 6.6 Specific impulse as a function NPR during an ascent and a descent phase in the DBNi16 configuration operating with $\varphi_{\dot{m}} = 0.027$.

Because the transitions and the retransitions occurred smoothly, the NPR_{trans} and $NPR_{retrans}$ detection method was changed. When the I_{sp} versus NPR curve did not show a sudden change in operating mode, the NPR_{trans} (resp. $NPR_{retrans}$) was identified as the NPR at which the slope of the I_{sp} versus NPR curve changes during the ascent (resp. descent) phase.

Often the curves would not result in a simple slope change but rather in a specific impulse plateau (assumed to be the beginning of the transition, when the separation point moves downstream of the inflexion point) followed by a slope change (assumed to be the end of the transition, when the separation front reaches the end of the extension). In the latter case, the NPR_{trans} was taken as the beginning of the I_{sp} plateau. Fig. 6.7 shows the NPR_{trans} by identifying the I_{sp} plateau during an ascent phase. The challenging identification of the change in operating mode justifies the larger error bars for measurements made throughout this test campaign.

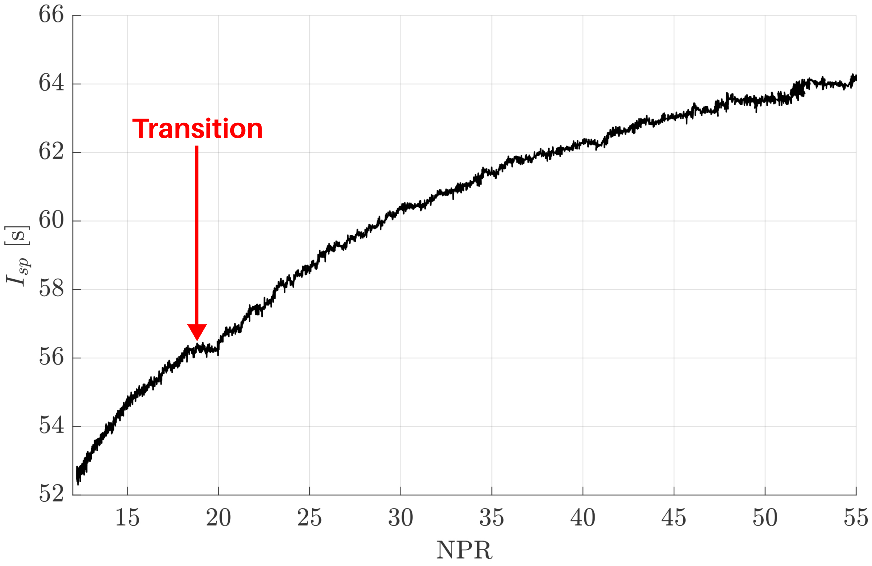

Fig. 6.7 Specific impulse as a function NPR during an ascent phase in the DBNi16 configuration operating with $\varphi_{\dot{m}} = 0.027$. The red arrow indicates the change in slope.

Nonetheless, a substantial difference in NPR_{trans} and $NPR_{retrans}$ exists between DBNi8 and DBNi16 for the lowest secondary mass flow rate ratio case and the cavity with pipes case (no injection). In the latter configuration and as discussed in Chapter 4, the presence of the secondary injection slot in the DBNi16 case mostly affected the $NPR_{retrans}$, as opposed to DBNi8 configuration where it mostly affected the NPR_{trans}. For $\varphi_{\dot{m}} = 0.011$, two key results are observed in the DBNi16 case: 1) the substantially lower NPR_{trans} and $NPR_{retrans}$, and 2) the negative hysteresis. For $\varphi_{\dot{m}} = 0.011$, positioning the secondary injection slot 16 mm downstream of the inflexion point had a limited impact on the transition point as the NPR_{trans} increased by 0.2% compared to the cavity with pipes case or the smooth configuration. In this case, the adverse pressure gradient induced by the secondary injection might be too far downstream to influence the boundary layer in the vicinity of the inflexion point. As a result, the sudden transition occurs at a similar NPR as in a case without any secondary injection slot, namely the smooth configuration. However, the $NPR_{retrans}$ sees a significant increase compared to the cavity with pipes case (+8.5%) and becomes higher than the NPR_{trans}, resulting in what appears as an inverted hysteresis. In fact, the hysteresis is not inverted as such; it is suppressed. Fig. 6.8 shows the specific impulse as a function of NPR during an ascent and a descent phase for DBNi16 operating with $\varphi_{\dot{m}} = 0.011$. It shows that not only does the transition and the retransition take place on a larger NPR range (more continuously) than with the smooth DBN, but also that the hysteresis does not exist anymore. In this case, the specific impulse trajectory almost entirely follows the same path during the transition and the retransition phases. Furthermore, the increasing ambient pressure during the descent induces changes in the shock system and pushes the separation front location inside the extension section. The proximity of the secondary injection to the nozzle exit in the DBNi16 induces unfavourable conditions for the boundary layer in the vicinity of the nozzle exit, which makes it more sensitive to the exhaust jet compression induced by the high ambient pressure. Therefore, the retransition takes place earlier, hence the higher $NPR_{retrans}$.

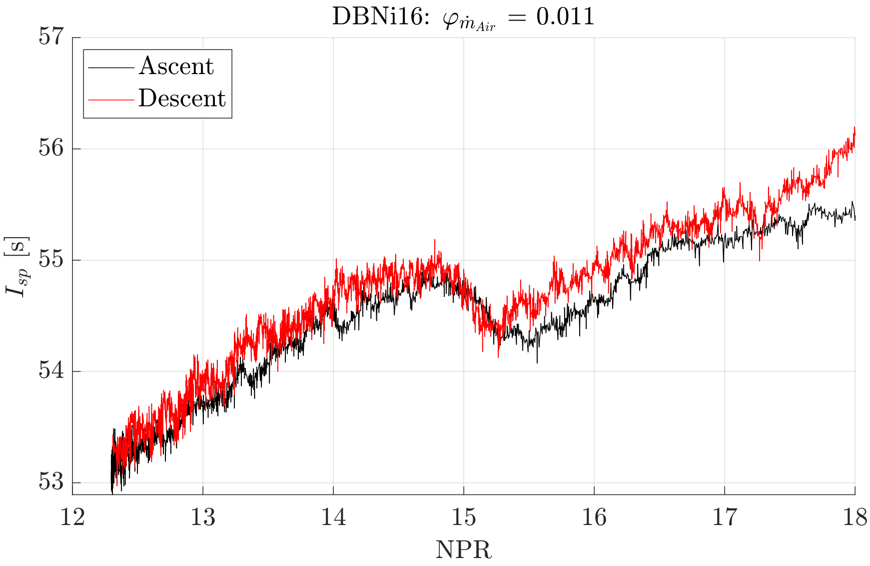

Fig. 6.8 Specific impulse as a function NPR during an ascent and a descent phase in the DBNi16 configuration operating with $\varphi_{\dot{m}} = 0.011$.

Increasing the secondary mass flow rate ratio above 0.011 resulted in the reappearance of the conventional hysteresis effect. Fig. 6.6 shows the specific impulse as a function of NPR during an ascent and a descent phase. It shows that the transition NPR is harder to observe due to the continuous transition while the retransition is still identifiable at NPR = 17.64. The smoothing of the transition and retransition processes observed in the DBNi16 configuration might emanate from the wall pressure distribution in the extension section. In the DBNi8 configuration, the injection slot is located at 22% of the extension length and the conventional, sudden transition and retransition processes are identifiable. In this case, the secondary injection potentially influences the upstream flow on 22% of the extension length. When the injection slot is displaced downstream to 44% of the extension length for DBNi16, the influence of the secondary injection on the upstream flow potentially increases to 44% of the extension section. The adverse pressure gradient caused by the secondary injection jet on the longer extension section proportion may cause the separation line to travel progressively throughout the extension section, justifying the more continuous transition and retransition processes. The previous analysis is based on experimental measurements and observations, numerical simulations performed in the DBNi8 case, and physical sense to provide a first assumption to the phenomena taking place in DBNs operating with transverse secondary injection.

For both configurations, not only did the transition and retransition NPR increase with the secondary mass flow rate ratio, but the side forces were decreased to an extent where the force balance could not measure them as they fell within the force balance measurement noise (± 0.5 N); the side loads were brought to (or below) 1% of the nozzle thrust in all of the cases of the DBNi16 test specimen.

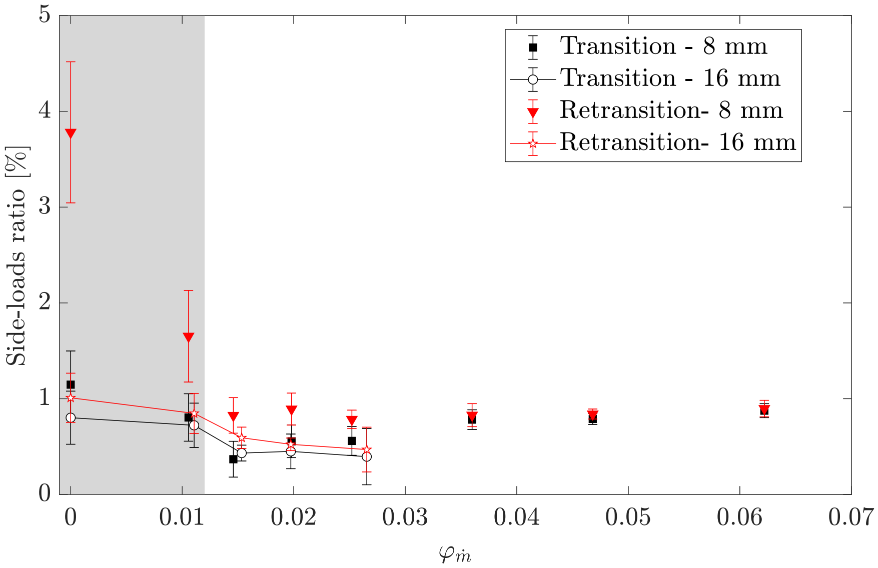

Fig. 6.9 Side force ratio as a function of mass flow rate ratio for different secondary injection positions.

The side-loads decrease in DBNs using secondary injection had already been observed in the DBNi8 configuration, however, the influence of secondary injection was found to be stronger for DBNi16. In the DBNi16 cavity with pipes case, the side-loads generated during retransition were brought to 1% of the nozzle thrust, as opposed to 3.78% for the DBNi8 configuration. Reducing the lateral forces below 1% of the nozzle thrust during the transition and the retransition necessitated a secondary mass flow rate ratio $\varphi_{\dot{m}}$ of 0.011 and 0.015, respectively. The mechanism driving the decrease in side forces in the DBNi16 is assumed to be similar to the DBNi8 configuration. Namely, the adverse pressure gradient caused by the secondary injection jet combined with the pressure gradient induced by the inflexion point, or the breaking of the feedback loop process in the separated flow region which fuels the generation of side-loads in the supersonic separated nozzle flows. Displacing the secondary injection slot downstream could have an enhanced effect on the DBN behaviour and further investigation is needed to comprehend all of the experimental measurements.

Operating secondary injection in the DBNi16 configuration brought the thrust jump ratio below 1% of the nozzle thrust for every mass flow rate ratio configuration. It is worth mentioning that, like the side-loads measurements, a thrust jump of less than 1% of the nozzle thrust falls within the balance measurement noise and cannot be measured. As underlined at the beginning of this section, in the secondary mass flow rate ratio higher-end range of the DBNi16 configuration, the transition took place continuously. The continuous transition induces a lower jump in thrust during the mode switches. The continuous transition and the associated reduction in thrust jump ratio was already observed in the DBNi8 configuration but the effects of the secondary jet were less pronounced, indicating the significant influence of the secondary injection jet location in the extension section.

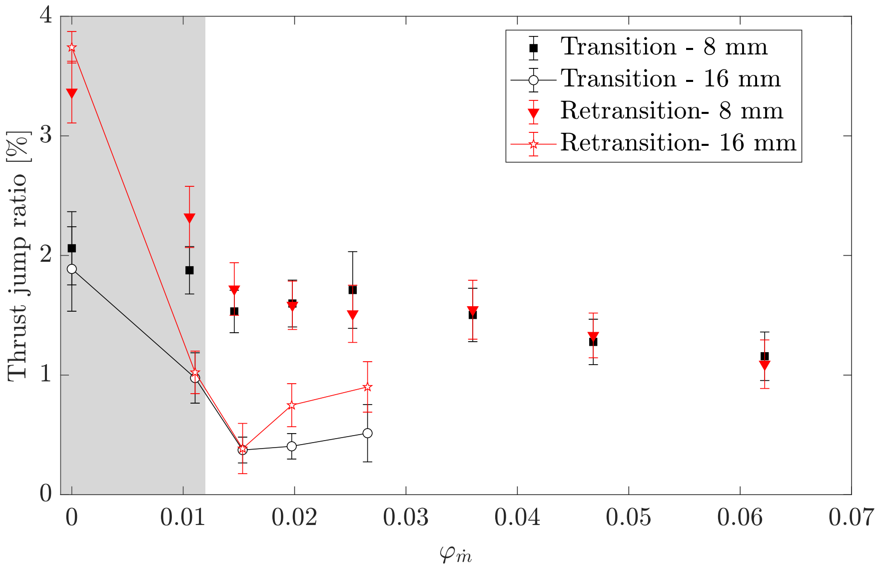

Fig. 6.10 Thrust jump ratio as a function of mass flow rate ratio for different secondary injection positions.

6.3 Influence of the secondary injectant gas

6.3.1 Preliminary section

This section investigates the influence of the secondary injectant gas with different properties on the DBN's behaviour. In a previous study on thrust vector control conducted in [3], it was observed that introducing helium as a secondary injectant gas into a nozzle, which was operating with cold dry air as the mainstream flow, resulted in a larger separation length compared to using a secondary injection of air. This effect was clearly observed, even with a relatively small secondary mass flow rate ratio. Furthermore, helium exhibits potential as a cost-effective option for DBN flow control in rocket launchers, given its common usage in propellant compression. Consequently, the present study aims to explore the impact of helium as a secondary injectant gas on the DBN behaviour. The key flow properties evaluated at the critical conditions and for a stagnation temperature of 298K are given in Table 6.1.

Table 6.1 Isentropically calculated mass flow rates for different species and different SPRs at T_0 = 293K.

Specie	Molar mass [g/mol]	γ c_p/c_v	$\dot{m}_i$ (SPR = 0.11) [g/s]	$\dot{m}_i$ (SPR = 0.15) [g/s]
Air	28.96	1.4	1.98	2.73
He	4	1.659	0.79	1.10

The secondary injection speed, density, and momentum are deduced and presented in Table 6.2. The comparison reveals that for a constant SPR, helium exhibits a considerably lower density but a significantly higher velocity than air. Specifically, at SPR = 0.11, the secondary injection of helium results in an almost 12.4% boost in energy compared to using air. As the SPR increases to 0.15, this enhancement further rises to 13.1%.

Table 6.2 Isentropically calculated secondary injection density, velocity, momentum, and energy for two SPRs.

	SPR = 0.11				SPR = 0.15			
	ρ	u	$\rho U/\rho^* U^*$	$\rho U^2/\rho^* U^{*2}$	ρ	U	$\rho U/\rho^* U^*$	$\rho U^2/\rho^* U^{*2}$
Air	0.28	313	0.105	0.105	0.38	313	0.145	0.145
He	0.04	872	0.042	0.118	0.056	872	0.059	0.164

The DBNi8 test specimen was mounted on the force balance, but the secondary injection was operated with helium. The gas was stored in a helium bottle under 200 bar. The testing conditions were similar to when air was the secondary injectant gas. A stagnation pressure of

350 kPa generated the DBN mainstream flow and the ambient pressure was varied to trigger the transition and retransition phases. For the helium configuration, the nozzle pressure ratio values ranged within NPR $\in$ [12;65], while the stagnation pressure for the secondary jet P_i averagely ranged within $P_i \in$ [24.3;52.4] kPa. This secondary injection pressure range corresponds to a mass flow rate ratio range $\varphi_{\dot{m}} \in$ [0.003;0.006]. The experiments performed with air are referred to as DBNi8-Air and those performed with helium as DBNi8-He.
Fig. 6.11 shows the NPR, specific impulse, side-loads ratio, and secondary pressure ratio as a function of time during an experiment in the DBNi8 test specimen operating with helium as a secondary injectant gas for a mass flow rate ratio equals to 0.003. In this case, the secondary injection jet was not sonic and the secondary pressure ratio varied between 0.061 and 0.087.

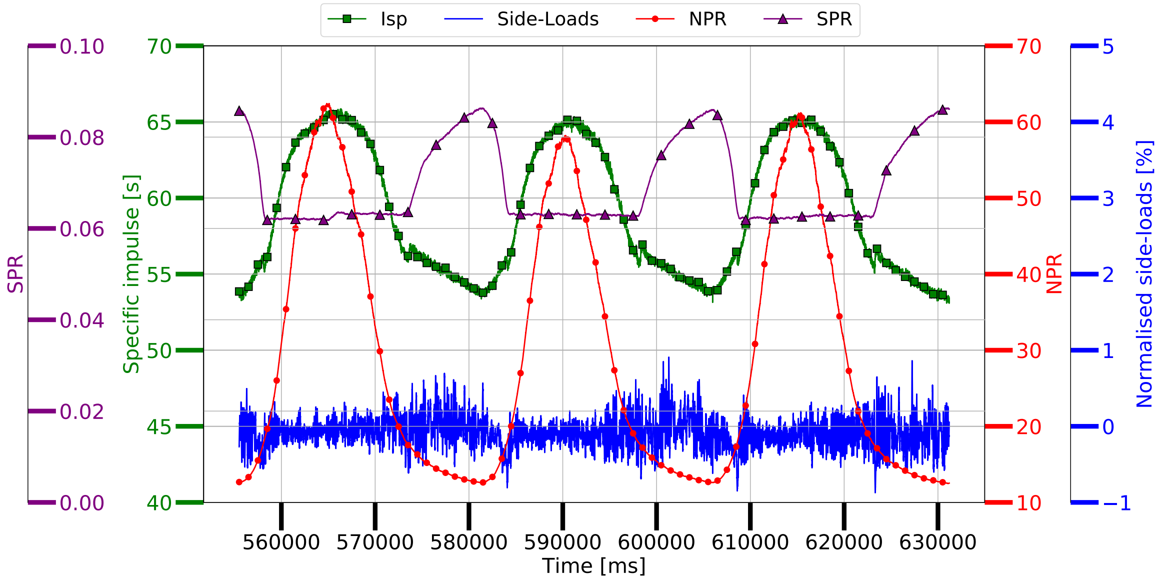

Fig. 6.11 Specific impulse, NPR, and side-loads as a function of time: DBNi8-He operating with $\varphi_{\dot{m}_{He}} \approx 0.003$.

The pressure decrease in the wind tunnel test section causes the NPR to rise. The rise in NPR increases the DBN's specific impulse until the transition from the low-altitude mode to the high-altitude mode occurs. The transition from one mode to another gives rise to a sudden but marginal jump in specific impulse while the side force peaks remain obscurely defined. Similarly to the previous section, these observations are investigated in a subsequent section. During the descent phase, when the NPR decreases, the DBN eventually retransition from the high-altitude mode to the low-altitude mode. Again, no significant sudden jump in specific impulse or side load peak is visible. As in the injection position influence study, Fig. 6.11, which highlights some of the DBN's crucial parameters, illustrates the critical influence of the secondary injectant gas on the DBN's behaviour.

The next sections provide a qualitative analysis of the DBN exhaust plume topology and a quantitative analysis of the DBN key parameters, namely the transition NPR, side forces, and thrust jump. The results are compared to the DBNi8-Air test specimen to observe the direct effects of the secondary injectant gas on the DBN's behaviour.

6.3.2 Qualitative analysis

This section investigates the influence of helium as a secondary injectant gas on the DBN's exhaust flow topology. First, the influence of the helium SPR on the flow structure is presented when the DBN operates in both low-altitude and high-altitude modes. Fig. 6.12 and Fig. 6.13 shows the influence of the SPR on the exhaust plume topology in the low-altitude mode and the high-altitude mode when helium is operated as a secondary injectant gas.

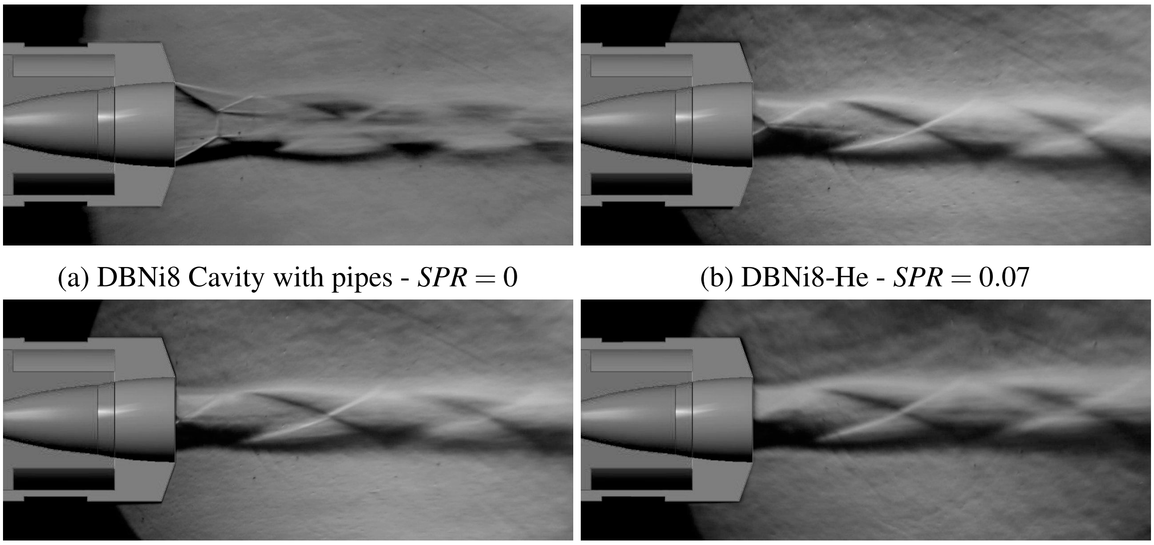
(a) DBNi8 Cavity with pipes - $SPR = 0$

(b) DBNi8-He - $SPR = 0.07$

(c) DBNi8-He - $SPR = 0.11$

(d) DBNi8-He - $SPR = 0.15$

Fig. 6.12 Experimental schlieren of the DBNi8-He operating with different SPR at $NPR \approx 17$ (low-altitude mode).

In the low-altitude mode, the secondary injection of helium delays the transition NPR as the transition has fully occurred in the cavity with pipes configuration (no injection). An increase in helium SPR results in the upstream movement of the shock system, evident from the observed shift in the shock reflection within the DBN. Similarly, in the high-altitude mode, higher SPR increases the SI shock angle relative to the nozzle wall. Despite this difference, the overall flow topology remains consistent across the SPR configurations under investigation.

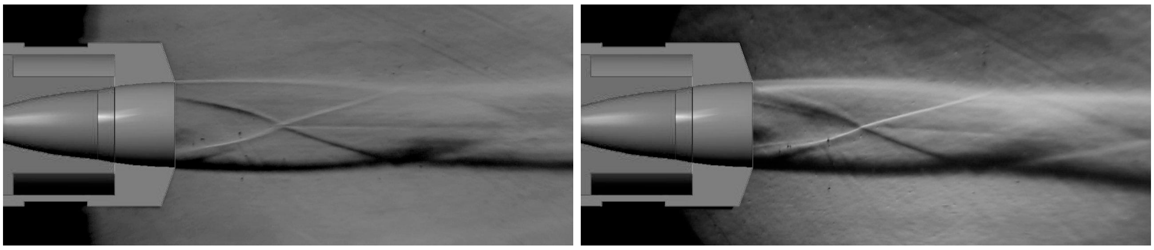

(a) DBNi8 Cavity with pipes - $SPR = 0$ (b) DBNi8-He - $SPR = 0.07$

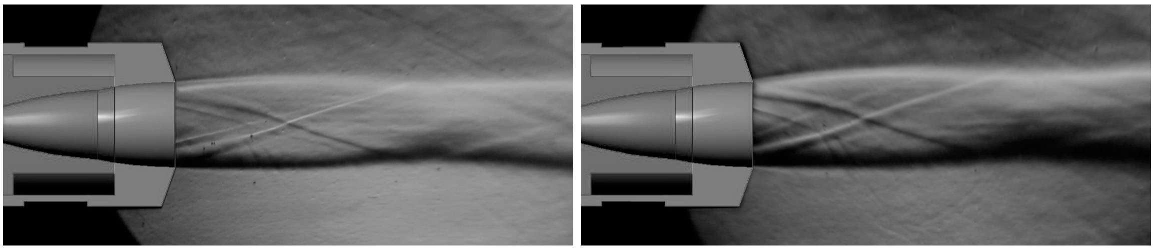

(c) DBNi8-He - $SPR = 0.11$ (d) DBNi8-He - $SPR = 0.15$

Fig. 6.13 Experimental schlieren of the DBNi8-He operating with different SPR at $NPR \approx 50$ (high-altitude mode).

Below, we conduct a comparison of the flow features observed in the DBN when operated with both air and helium. As in the previous section, the exhaust jet flow features are discussed for several NPRs during the transition phase only. Because of the low SPR investigated in the DBNi8-He configuration, a comparison at an equivalent mass flow rate ratio with DBNi-Air cannot be performed. Nevertheless, a comparison at equivalent SPR is possible for SPR $\approx \{0.11; 0.15\}$. Fig. 6.14 shows a series of schlieren images of the DBN exhaust plume for roughly NPR $\in$ [17;50] in both DBNi8-Air and DBNi8-He at SPR = 0.11. At NPR $\approx$ 17, the dual-bell nozzle operates in the low-altitude mode for both cases. The high ambient pressure compresses the jet column and causes the flow to separate in the vicinity of the inflexion point. Downstream of the separation point, an oblique shock emerges and is reflected at the symmetry axis. Both exhaust jets' topologies closely resemble each other, showcasing the aforementionned shock structure, followed by subsequent reflections downstream.

At NPR $\approx$ 18, the transition occurred in the DBNi8-Air configuration. Here, the flow reattached the extension section wall and separates at the nozzle exit. In the vicinity of the nozzle exit, three shock structures are distinctly visible: the HAP shock, the SI shock, and the internal recompression shock. At this NPR, the HAP shock interacts with a Mach disk and a reflected shock at a triple point. Slip lines emerge downstream of the triple point and downstream of the interaction between the internal recompression shock and the HAP shock.

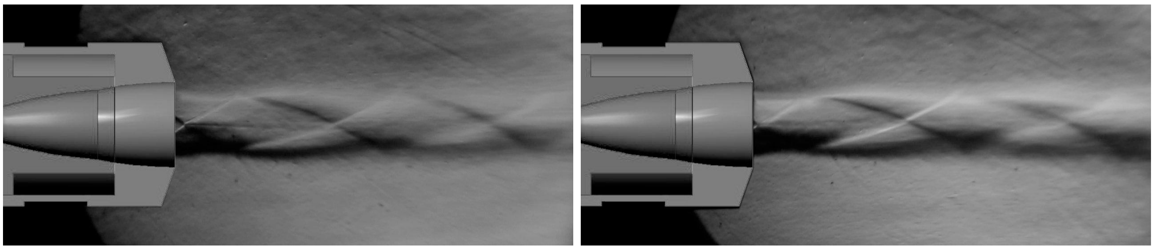

(a) DBNi8-Air - $NPR = 17.01$ (b) DBNi8-He - $NPR = 17.03$

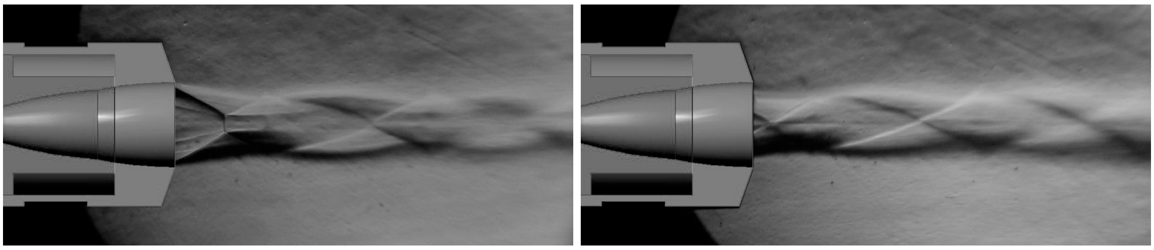

(c) DBNi8-Air - $NPR = 18.03$ (d) DBNi8-He - $NPR = 17.98$

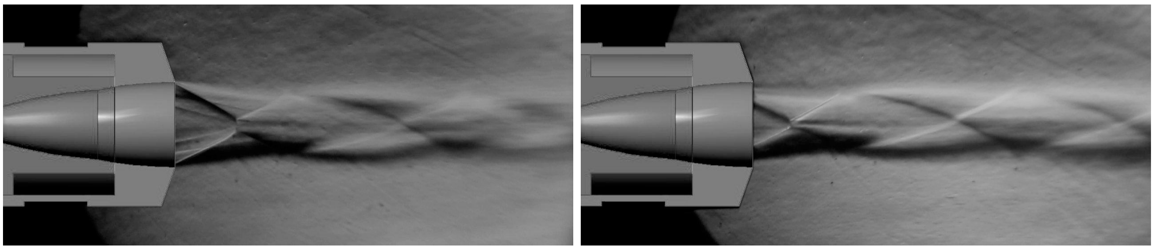

(e) DBNi8-Air - $NPR = 19.99$ (f) DBNi8-He - $NPR = 19.97$

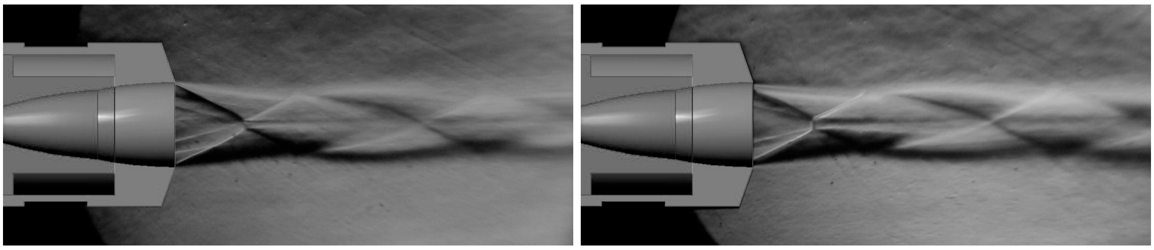

(g) DBNi8-Air - $NPR = 21.97$ (h) DBNi8-He - $NPR = 22.03$

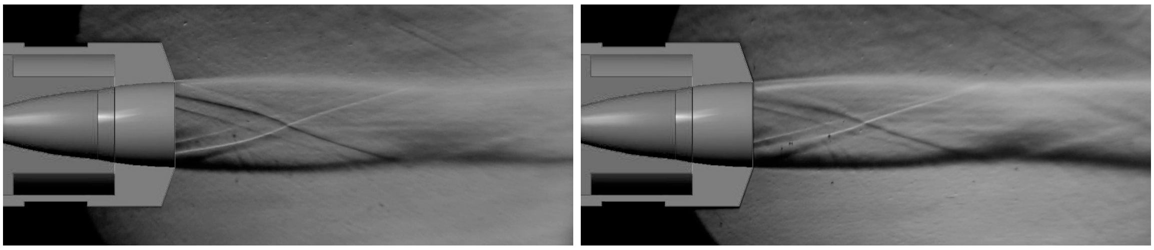

(i) DBNi8-Air - $NPR = 49.89$ (j) DBNi8-He - $NPR = 49.99$

Fig. 6.14 Experimental schlieren during a transition phase for the DBNi8-Air and DBNi8-He configurations, both operating at $SPR = 0.11$.

These shock structures interact together upstream of a series of compression and expansion cells that adapt the exhaust flow to the ambient conditions downstream. In the DBNi-He configuration and at NPR $\approx$ 18, the test specimen operates in the low-altitude mode exhibiting a flow topology akin to NPR $\approx$ 17. Nevertheless, the reduction in ambient pressure leads to a noticeable downstream displacement of the shock pattern, resulting in a shock system clearly visible beyond the DBN exit.

As the NPR increases to ~20, the significant displacement of the shock system when compared to NPR $\approx$ 18 suggests that the transition from the low-altitude mode to the high-altitude mode has started to occur in the DBNi8-He case. A small Mach disk and slip lines are apparent at the interaction point between the HAP shock and the reflected shock. Upon analysing the video footage between these two configurations, it becomes evident that the shifts in operating modes occur more gradually in the DBNi8-He configuration, in contrast to the abrupt transitions observed in the DBNi8-Air configuration. Meanwhile, at this NPR, the DBNi8-Air exhibits a flow topology akin to that described for NPR $\approx$ 18.

At NPR $\approx$ 22, the transition fully occurred in the DBNi8-He configuration. Here, the flow has reattached to the extension section wall, giving rise to the appearance of an internal recompression shock and an oblique shock induced by the secondary jet (SI shock).

Nevertheless, the exhaust plume of DBNi8-He in Fig. 6.14h displays a similar shock pattern as for air at equivalent NPR. A HAP oblique shock wave emerges from the nozzle lip wall and interacts with a Mach disk and a reflected shock at a triple point. The HAP shock induces a series of compression and expansion cells further downstream and slip lines are apparent downstream of the Mach disks.

At NPR $\approx$ 50, both DBNs operate in the high-altitude mode. Schlieren images from both configurations reveal the presence of the SI shock and the internal recompression shock. In the DBNi8-He configuration, a diffused recompression shock is observed in the vicinity of the extension wall downstream of the nozzle exit. Here, the overall flow topology remains relatively consistent between the two configurations.

6.3.3 Quantitative analysis

The secondary jet of helium in the DBNi8 test specimen displays, by and large, a similar trend to the air configuration. Fig. 6.15a and Fig. 6.15b show the transition and retransition NPR as a function of the SPR and $\varphi_{\dot{m}}$ when the DBNi8 test specimen is operated with air and helium. They show that increasing the mass flow rate ratio of helium also causes the rise of NPR_{trans} and $NPR_{retrans}$. Within the range of SPR investigated in the helium configuration, the secondary jet of helium was not sonic as the pressure inside the cavity was influenced by the NPR (see Fig. 6.11). The mass flow rate ratios of helium investigated were not large enough to allow for a direct comparison with air at an equivalent mass flow rate ratio. Nevertheless, some important results can be observed from this experimental campaign. The series of experiments demonstrated the superior effect of helium on the transition and the retransition NPRs. The largest helium mass flow rate ratio configuration, which is smaller than the smallest air secondary mass flow rate ratio, displayed a significantly higher NPR_{trans} and $NPR_{retrans}$ than the ones obtained using air. For SPR = 0.11 and SPR = 0.15, the experiments performed with helium showed NPR_{trans} values above 19.40, whereas the air configuration resulted in NPR_{trans} values of 17.24 and 17.77, respectively. The NPR_{trans} for the helium and air configurations were increased by over 30% and by nearly 24% when compared to the smooth DBN, respectively. The latter values correspond to an increase of 22% and 15.5% when compared to the cavity with pipes case, respectively. When compared to the cavity with pipes configuration and for a helium SPR of 0.11, the retransition NPR increased by 34.6%, reaching 19.93. The same SPR using air as a secondary injectant gas resulted in a 13.3% increase, 21.3 percentage points less than when using helium. The absence of hysteresis in the higher-end range of helium SPR is marked by a $NPR_{retrans}$ larger than NPR_{trans}. The limited range of helium mass flow rate ratio did not allow us to observe whether the latter two decrease at high secondary mass flow rate ratios as observed in the DBNi8 operating with air.

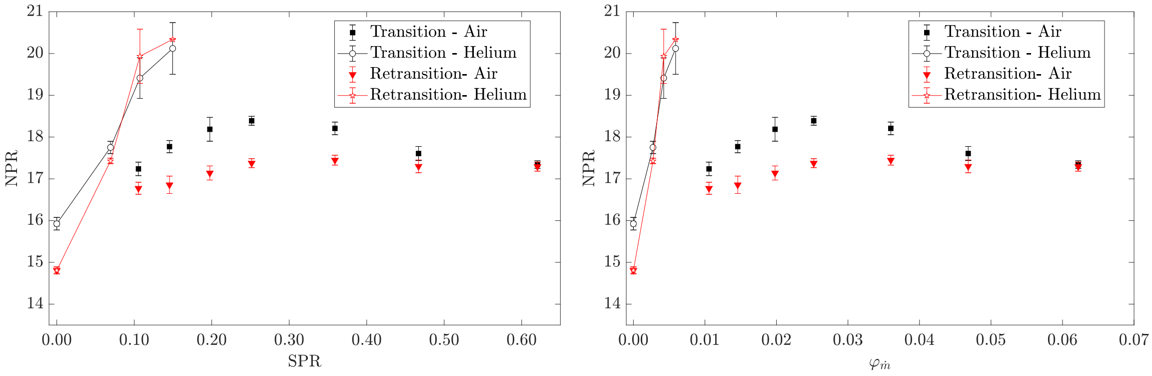

(a) NPR_{trans} and $NPR_{retrans}$ vs SPR. (b) NPR_{trans} and $NPR_{retrans}$ vs $\varphi_{\dot{m}}$.

Fig. 6.15 Transition and retransition NPR as a function of SPR and $\varphi_{\dot{m}}$ for different secondary injectant gas.

The mechanisms governing the transition and retransition NPR are assumed to be of a similar nature to that of the DBNi8 configuration operating with air, where the adverse pressure gradient and increased wall pressure induced by the secondary jet mostly control the transition NPR while the separation bubble size and radial momentum controls the retransition, supposedly.

Fig. 6.16 shows the specific impulse as a function of the NPR for the smooth, DBNi8-Air and DBNi8-He configurations operating at SPR = 0.11. First, it shows that the two secondary injectant gases significantly increase the transition NPR when compared to the smooth DBN. Second, one may notice that the use of helium as a secondary injectant gas suppresses one of the DBN's key features: the sudden transition. Instead, it shows a continuous transition from the low-altitude mode to the high-altitude mode with a mild decrease in I_{sp} in the vicinity of NPR = 19. This smoothening behaviour is also observed during the retransition phases.

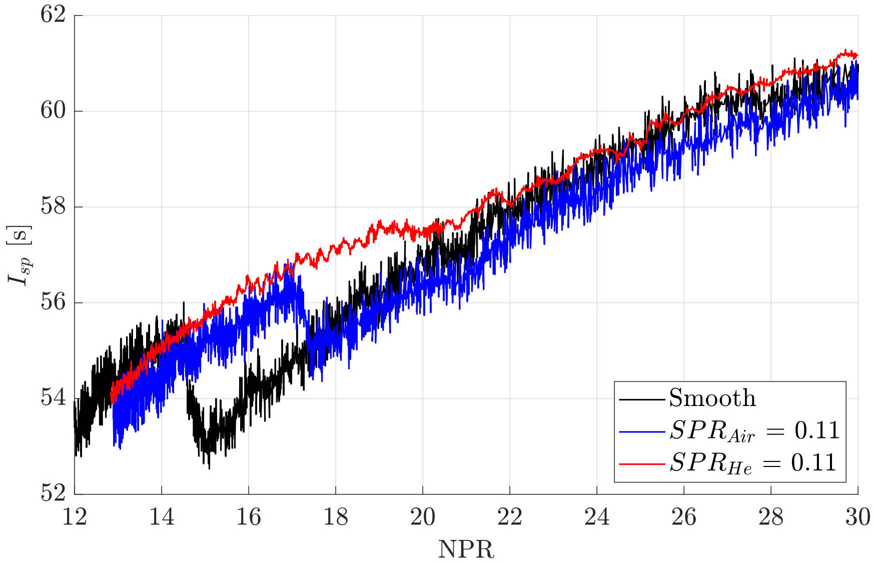

Fig. 6.16 Specific impulse as a function of NPR for different secondary injectant gas at SPR = 0.11.

Fig. 6.17 shows the I_{sp} as a function of the NPR for the lowest and the highest helium mass flow rate ratio during an ascent phase. It reveals that the smoothening effect of the I_{sp} curve increases with an increase in $\varphi_{\dot{m}}$ (or SPR). This phenomenon was already observed in the DBNi16 test specimen and a change in the streamwise wall pressure gradient was designated as a potential cause for this behaviour. In the helium configuration and for SPR = $\{0.11; 0.15\}$, the identification of NPR_{trans} and $NPR_{retrans}$ when the transition occurred continuously had to be changed. The method used was the same as in the DBNi16 test specimen operating with high secondary mass flow rate ratios, which consisted of identifying the I_{sp} plateau and the change in slope of the $I_{sp} = f(NPR)$ curve (see Fig. 6.7). As a result of the difficulty of identifying the switches in working modes, the standard deviation increases for the two highest helium SPR in Fig. 6.15. The smoothening of the specific impulse curve trajectory requires further investigations to fully apprehend this phenomenon.

The small gap between the NPR_{trans} and $NPR_{retrans}$, combined with the large standard deviations, suggest that the DBN could suffer from the flip-flop behaviour should ambient pressure variations be large enough. Yet, no flip-flop behaviour was observed in the experimental test campaign.

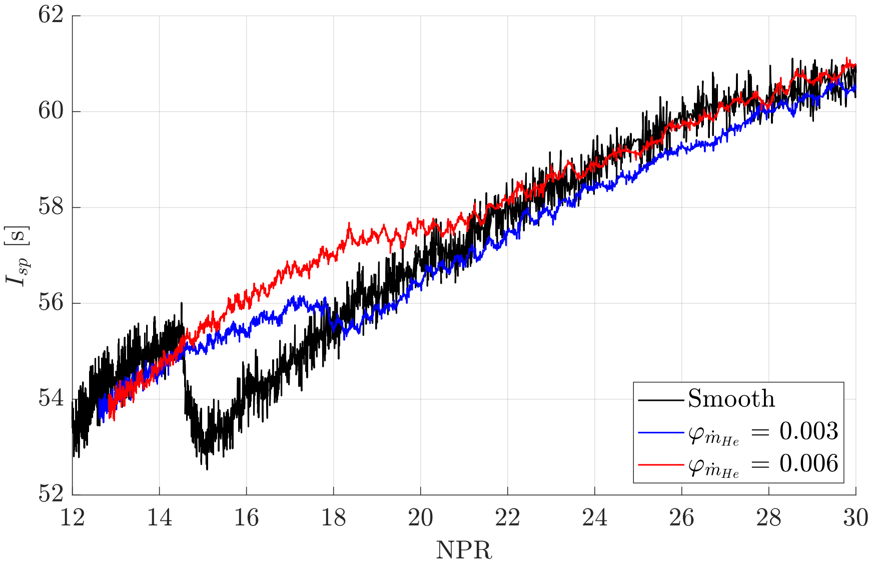

Fig. 6.17 Specific impulse as a function of NPR for different helium secondary mass flow rate ratios.

The increase in NPR_{trans} and $NPR_{retrans}$ and the smoothing effect of the specific impulse trajectory when the DBN is operated with helium come with a decrease in the lateral forces during the working mode changes. Fig. 6.18 shows the side-loads ratio as a function of the secondary mass flow rate ratio. It shows that the side-loads were brought below 1% of the nozzle thrust for all of the helium cases in the DBNi8 test specimen. Here, the lateral force peaks could not be identified as they fell within the balance measurement noise (± 0.5 N). The wall pressure gradient induced by the secondary jet and the presence of the inflexion point may decrease the side-loads magnitude, or the jet may break a feedback loop process between upstream and downstream propagating waves that induce side-loads in overexpanded, separated nozzle flows.

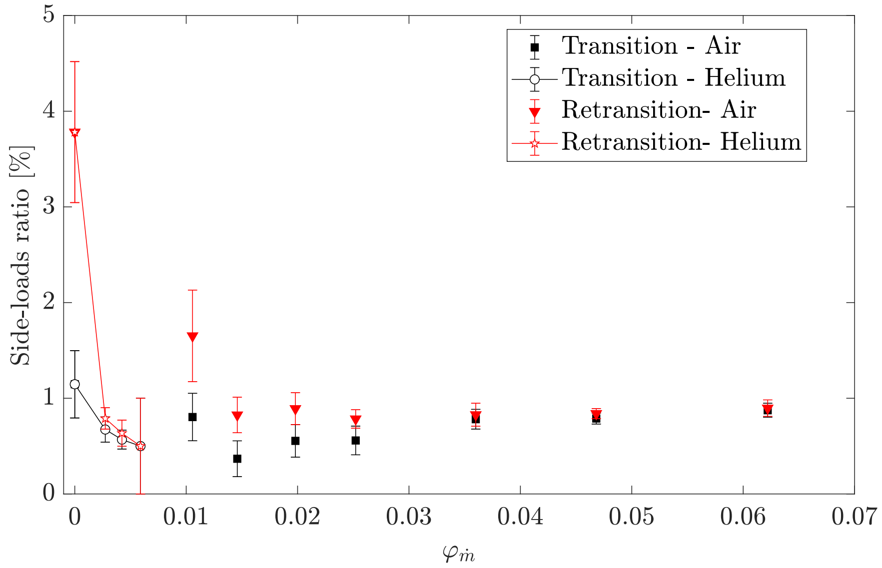

Fig. 6.18 Side force ratio as a function of mass flow rate ratio for different secondary injectant gas.

Fig. 6.19 shows the thrust jump ratio measured during the transition and the retransition phases as a function of the secondary mass flow rate ratio for the DBNi8 test specimen operating with a secondary injection of air or helium. Similarly to the air configuration, the thrust jump ratios measured during the transition and retransition phases decrease with an increase in the secondary mass flow rate ratio.

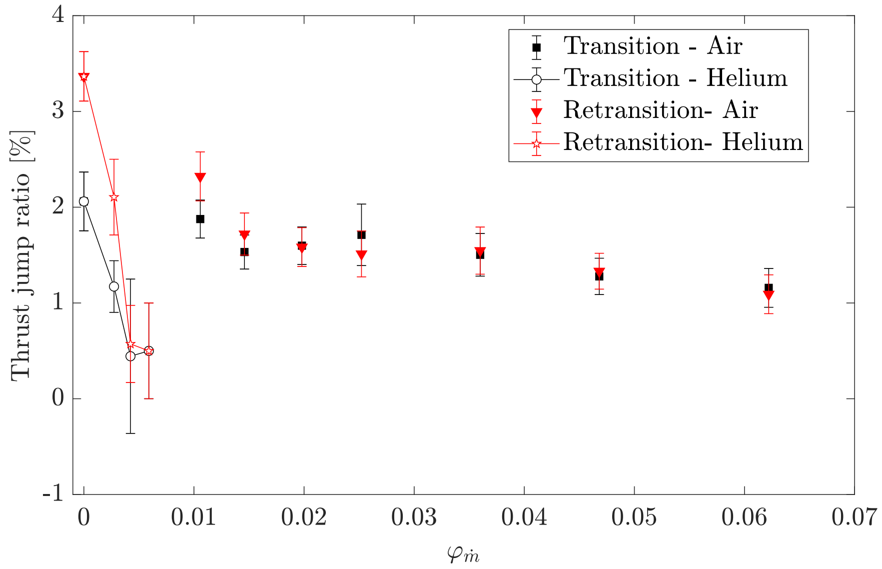

Fig. 6.19 Thrust jump ratio as a function of mass flow rate ratio for different secondary injectant gas.

Due to the continuous transition and retransition phases for $\varphi_{\dot{m}_{He}} \geq 0.004$, the thrust jump ratio decreases to less than 1% of the nozzle thrust and cannot be measured distinctively by the force balance. Meanwhile, the lowest thrust jump measured in the air configuration reached 1.1% (descent phase) and was achieved for $\varphi_{\dot{m}_{Air}} = 0.062$. Nevertheless, the experiments show that the thrust jump may be reduced to less than one percent of the nozzle thrust with a relatively low secondary to primary mass flow rate ratio, which was not achieved with the experiments performed with air.

The previous findings demonstrate that the secondary injectant gas dramatically changes the DBN's behaviour. The main features of this concept remain the same for the smallest secondary mass flow rates investigated, namely the existence of a transition and retransition NPR, the generation of side-loads, or the jump in thrust during the operation mode switches. However, the dynamics are significantly different when the secondary mass flow rate increases, with the observation of continuous transitions and retransitions (only possible in negative pressure gradient extension profiles) and the absence of a jump in thrust. The secondary injection of helium, as was the case for air, demonstrated its capabilities of lowering the lateral forces during the change in operating modes, while delaying the transition process.

6.4 Conclusions

This chapter investigated the influence of two parameters for the performance optimisation of a subscale DBN: 1) the position of the secondary injection, and 2) the secondary injectant gas. The first section of the chapter focused on the influence of the secondary injection position. Two DBNs of the same profile but different secondary injection slot positions were analysed. The secondary injection slot was located 8 mm downstream of the inflexion point in the first test specimen (DBNi8), while the secondary injection slot was located 16 mm downstream of the inflexion point in the second nozzle (DBNi16). The previous chapter showed the capability of delaying the transition and the retransition while decreasing the side-loads to less than 1% of the nozzle thrust. The experiments carried out in this chapter revealed that the transition and retransition can be delayed in the DBNi16 nozzle while reducing the side loads and thrust jump to less than 1% of the nozzle thrust. In the range of secondary mass flow rate ratio studied in the test campaigns, the transition NPR was delayed at most by nearly 28% in the DBNi16 compared to the smooth DBN, as opposed to 24% in the DBNi8 test specimen. The retransition NPR was increased at most by 21.4% and 20.1%, respectively. The DBNi8 showed the capability of reducing the side-loads magnitude to less than 1% of the nozzle thrust for a relatively small mass flow rate ratio $\varphi_{\dot{m}}$, less than 2%, while this result was achieved for $\varphi_{\dot{m}} \leq 1\%$ with the DBNi16. Although the two test specimens exhibited similar behaviours, the DBNi16 showed a smoothening of the specific impulse trajectory during the ascent and the descent phases. Indeed, from $\varphi_{\dot{m}} \geq 0.020$, the sudden jump in specific impulse could not be distinctly identified and the transition occurred continuously. These findings unequivocally point to opportunities for improving the performance of DBNs through the position of the secondary injection.

The second section of this chapter discussed the influence of the secondary injectant gas in a subscale DBN. The study was performed with the DBNi8 test specimen. The DBNi8's performance was evaluated in a test campaign where helium was introduced as the secondary injectant gas. The results are contrasted to those from the initial campaign using air with the identical DBN. The experiments proved that the transition and retransition could be delayed even more should the DBNi8 be operated with helium instead of air. In the range of secondary mass flow rate ratio studied in the test campaigns and compared to the smooth DBN, the transition NPR was delayed by over 30% for the DBNi8 nozzle operating with helium, as opposed to 24% when operated with air. The retransition NPR rose by over 37% when helium was operated as the secondary injectant gas but by 20.1% for the air configuration. Similarly to the DBNi16 configuration, the DBNi8 test specimen operating with helium exhibited continuous transition, with the absence of specific impulse jump during the switch in operating modes. The magnitude of side-loads was brought to less than 1% of the nozzle thrust using a secondary to primary mass flow rate ratio of less than 0.003. The results obtained from the DBNi8 test specimen operating with helium as a secondary injection gas undeniably highlight the room for enhancing DBNs' performance through different secondary injectant gases.

General conclusion and perspectives

This thesis investigated the optimisation potential of DBNs by comprehensively exploring the influence of secondary injection on their transition behaviour in altitude-varying conditions. The first chapter provided contextual elements and addressed issues associated with DBNs. The second chapter introduced the experimental and numerical assets employed within the thesis, while the other chapters presented the results gathered within this study.

The result section begins by revealing the inherent behaviour of a DBN equipped with a TIC base profile and a constant pressure extension profile. Wall pressure measurements in the test specimen confirmed the constant pressure nature of the extension section. The altitude-varying conditions unveiled abrupt transition and retransition phases, measured at an NPR of 14.85 and 14.53, respectively. The flow topology was illustrated through schlieren images at various stages of the DBN's operating mode. Force balance measurements disclosed the presence of side-loads during operating mode changes. The characterisation of these lateral forces indicated a magnitude of 2.4% of the nozzle thrust during the transition phase and 3.4% during the retransition phase. The specific impulse experienced a significant jump during operating mode changes, reaching 3.8% of the nozzle thrust during the transition phase and 4.2% during the retransition phase.
Experiments performed with and without wall pressure measurements suggested that the presence of surface discontinuities may play a major on the flow dynamics and the instabilities inherent to DBN flows. Hysteresis effects, commonly observed in DBNs, were identified and quantified for the specimen under investigation. The experimental results are then compared to initial steady-state two-dimensional simulations at various NPRs using the $k\omega - SST$ (SST) and the Spalart-Allmaras (SA) turbulence models. revealed that the SST model exhibited superior accuracy in predicting the separation point and exhaust jet topology compared to the SA model. Subsequent to this observation, the SST model underwent calibration to better match the flow characteristics of the DBN. This calibration involved fine-tuning the model's structure parameter — a coefficient that restricts shear stress in the boundary layer. The adjusted coefficient significantly enhanced the flow predictions, particularly in cases where

the SST model initially struggled to accurately predict the boundary layer separation location.

The manuscript proceeds by examining the impact of the injection slot's presence and the volume of the secondary settling chamber, referred to as the cavity, on the natural transition behaviour of the DBN. The experimental test campaign revealed that the natural transition in the DBN was significantly influenced by the cavity volume and by the position of the secondary injection slot in the extension section. In the DBNi8 test specimen, a dual-bell nozzle whose secondary injection is located 8 mm downstream of the inflexion point, the study revealed that the cavity's volume mainly impacted the DBN's behaviour during the transition phase, where the transition NPR increased with an increase in the cavity volume. The transition NPR rose by 7.3% at most when compared to the DBN without any secondary injection slot, the smooth DBN. At the same time, the side-loads and thrust jump ratio were reduced to 1.1% and 2.1% of the nozzle thrust, a decrease of 1.3 and 1.7 percentage points when compared to the smooth DBN. The influence of the cavity's volume on these parameters during the retransition phase was not readily observable, suggesting a limited impact on the DBN during the descent phase.

Conversely, a series of experiments in a DBN equipped with a secondary injection slot located 16 mm downstream of the inflexion point (DBNi16) showed a limited effect of the injection slot presence and cavity volume during the transition process. A maximum decrease in transition NPR of 1.7% was measured for the smallest cavity's volume when compared to the smooth DBN. Meanwhile, the presence of the injection slot decreased the retransition NPR by over 5%, whereas the DBNi8 exhibited a maximum change in retransition NPR of less than 2% (observed with the largest cavity volume). The further secondary injection slot showed a decrease in side forces to less than 1% of the nozzle thrust during both, the ascent and the descent phases, as opposed to the DBNi8 case which showed a limited influence of the injection slot on side forces during the descents. The thrust jumps during the transition phase were reduced to the same extent for both DBNs but the effect of the injection slot remained limited during the retransition phase in both cases.

The results presented showed the clear impact of the secondary injection slot position in the DBN's extension section, especially regarding its stronger impact during the retransition phases should it be positioned further downstream. The nature of this phenomenon is presumed to be associated with the proximity of the injection slot to the inflexion point. However, a more comprehensive parametric study and numerical simulations are required to validate these assumptions. This series of experiments further underscores the considerable sensitivity of the DBN's flow to the surface condition and the location of these surface discontinuities.

After examining the natural transition and retransition in the different test specimens, a range of secondary injection pressures was applied in the secondary settling chamber, employing air as the secondary injectant gas in the DBNi8. The experiments showed that both the transition and retransition NPR were increased by over 20% when compared to the smooth DBN. The rise in transition and retransition NPRs was observed to be constrained, with the maximum values attained within the mid-range of the mass flow rate ratio investigated. The numerical simulations suggested that the increase in transition NPR was attributed to the presence of the fluidic obstacle and the higher extension wall pressure, displacing and forcing the separation location in the vicinity of the inflexion point. The increased retransition NPR was also attributed to the fluidic obstacle and the presence of a significant separation bubble spreading within a non-negligible part of the extension section. Furthermore, the simulations indicated that for the highest secondary mass flow rate ratios investigated, the upstream separation bubble extends upstream of the inflexion point, preventing the separation front from interacting with the inflexion point. This phenomenon was identified as a potential cause for the constrained effect of secondary injection on the DBN's behaviour, and the decline in NPR_{trans} and $NPR_{retrans}$ for the highest secondary mass flow rate ratios. The side-loads were reduced below 1% of the nozzle thrust during both: transition, and retransition phases using a secondary mass flow rate ratio of only 0.015. The important adverse pressure gradient induced by the secondary flow and the transverse sonic jet boundary were assumed to be responsible for this significant achievement. The decrease in side-loads was accompanied by a decrease in the thrust-jump-to-thrust ratio during both the transition phase and the retransition phase.

An additional test campaign aimed at exploring the interaction between the secondary jet and the inflexion point was conducted by introducing secondary injection in the DBNi16 test specimen. The results obtained with the DBNi16 closely resembled those of the DBNi8. Specifically, a rise in the secondary mass flow rate ratio led to an increase in transition and retransition NPRs. Interestingly, positioning the secondary jet at a further point resulted in higher transition and retransition NPRs compared to the DBNi8. Additionally, side-loads were reduced to below 1% of the nozzle thrust, highlighting opportunities for enhancing DBN performance through optimising the position of the secondary injection. However, in the DBNi16 test specimen, continuous transition was observed when operated with the higher-end range of secondary mass flow rate. In these configurations, the transition and retransition processes occurred smoothly instead of abruptly. The reasons for these observations remain unclear and require further investigation.

Finally, the impact of helium, a gas with distinct properties, was explored and compared to results obtained with air. A similar trend was noted, wherein transition and retransition NPRs increased with the secondary mass flow rate ratio. However, helium yielded remarkable results, showcasing an increase in transition and retransition NPRs by over 30% and 37%, respectively, compared to the smooth DBN. Additionally, side-loads were reduced to below 1% of the nozzle thrust, and the smoothing effect of the operating mode change was also observed. Notably, no jump in specific impulse was observed for the two highest secondary mass flow rate ratios as the transition and retransition occurred continuously. These observations, unprecedented in the open literature, call for further investigations. Nevertheless, this series of experiments emphasises the evident potential to overcome the scientific challenges inherent to DBNs and to enhance their performance. The secondary injection, with its capabilities for decreasing lateral forces and sudden change in thrust while improving the nozzle efficiency, could therefore be seen as a genuine asset for the next generation of launchers.

Perspectives

The perspectives of this thesis extend beyond the current investigation, offering promising avenues for future research. Scaling up the study to match the scale of engines employed in the launchers of micro and nano satellites holds great potential, providing a bridge between experimental and industrial applications. Expanding our exploration, we aim to delve into more challenging simulations, employing more advanced closure models and incorporating unsteady simulations to further unravel the complex flow dynamics of DBNs. Additionally, the investigation will be complemented by experiments involving an injection slot positioned closer to the inflexion point (4 mm downstream), as well as farther downstream (22 mm), adding a new dimension to our understanding. The investigation of the existing DBN can be further enhanced through studies on thrust vector control and by exploring different configurations of secondary injection slots. This research has garnered attention from governmental organisations following the submission of a startup project by the author focusing on DBN technology. The project received recognition from the French General Secretariat for Investment (SGPI) and BPI France through the i-PhD contest, earning a prize. Subsequently, we have benefited from valuable mentorship to propel this startup project forward, underscoring the commitment of nations to foster the growth of new industries and companies. Consequently, our aim is to develop and seamlessly integrate this innovative concept into an industrial asset, creating a synergy between academia and industry to drive impactful advancements in the space sector.

References

[1] Gerald Hagemann, Manuel Frey, and Wolfgang Koschel. Appearance of restricted shock separation in rocket nozzles. *Journal of Propulsion and Power*, 18:577–584, 2002.

[2] Gerald Hagemann, Hans Immich, Thong Van Nguyen, and Gennady E Dumnov. Advanced rocket nozzles. *Journal of Propulsion and Power*, 14:620–634, 1998.

[3] Vladeta Zmijanovic. *Secondary injection fluidic thrust vectoring of an axisymmetric supersonic nozzle*. PhD thesis, Université d'Orléans,, 2013.

[4] Euroconsult. Satellites to be built & launched. (25th edition), 12 2022.

[5] Ralf Stark, Chloé Génin, Dirk Schneider, and Christian Fromm. Ariane 5 performance optimization using dual-bell nozzle extension. *Journal of Spacecraft and Rockets*, 53:743–750, 2016.

[6] David Migdal and Fred Landis. Characteristics of conical supersonic nozzles. *ARS Journal*, 32:1898–1901, 12 1962.

[7] H. L. G. Sunley and V. N. Ferriman. Jet separation in conical nozzles. *The Journal of the Royal Aeronautical Society*, 68:808–817, 12 1964.

[8] Sherwin Kalt and David L. Badal. Conical rocket nozzle performance under flow-separated conditions. *Journal of Spacecraft and Rockets*, 2:447–449, 1965.

[9] Ruyan Jia, Zhenyu Jiang, Min Xiang, and Weihua Zhang. Three-dimensional numerical study of the conical nozzle side loads during staging. *Journal of Aerospace Engineering*, 29, 9 2016.

[10] Ellis M. Landsbaum. Contour nozzles. *ARS Journal*, 30:244–250, 3 1960.

[11] J. H. Ahlberg, S. Hamilton, D. Migdal, and E. N. Nilson. Truncated perfect nozzles in optimum nozzle design. *ARS Journal*, 31:614–620, 5 1961.

[12] G. V. R. Rao. Exhaust nozzle contour for optimum thrust. *Journal of Jet Propulsion*, 28:377–382, 6 1958.

[13] S. B. Verma and Oskar Haidn. Cold gas testing of thrust-optimized parabolic nozzle in a high-altitude test facility. *Journal of Propulsion and Power*, 27:1238–1246, 2011.

[14] G. V. R. Rao. Approximation of optimum thrust nozzle contour. *ARS Journal*, 30:561, 6 1960.

[15] Sébastien Deck and Philippe Guillen. Numerical simulation of side loads in an ideal truncated nozzle. *Journal of Propulsion and Power*, 18:261–269, 2002.

[16] Sébastien Deck and Anh Thi Nguyen. Unsteady side loads in a thrust-optimized contour nozzle at hysteresis regime. *AIAA Journal*, 42:1878–1888, 2004.

[17] Sébastien Deck. Delayed detached eddy simulation of the end-effect regime and side-loads in an overexpanded nozzle flow. *Shock Waves*, 19:239–249, 7 2009.

[18] Shashi Verma, Manisankar Chidambaranathan, and Abdellah Hadjadj. Analysis of shock unsteadiness in a supersonic over-expanded planar nozzle. *European Journal of Mechanics, B/Fluids*, 68:55–65, 3 2018.

[19] E. Martelli, P. P. Ciottoli, L. Saccoccio, F. Nasuti, M. Valorani, and M. Bernardini. Characterization of unsteadiness in an overexpanded planar nozzle. *AIAA Journal*, 57:239–251, 2019.

[20] Gerald Hagemann and Manuel Frey. Shock pattern in the plume of rocket nozzles: Needs for design consideration. *Shock Waves*, 17:387–395, 5 2008.

[21] Ralf Stark and Bernd Wagner. Experimental study of boundary layer separation in truncated ideal contour nozzles. *Shock Waves*, 19:185–191, 07 2009.

[22] V. Jaunet, S. Arbos, G. Lehnasch, and S. Girard. Wall pressure and external velocity field relation in overexpanded supersonic jets. *AIAA Journal*, 55:4245–4257, 2017.

[23] Florian Bakulu, Guillaume Lehnasch, Vincent Jaunet, Eric Goncalves da Silva, and Steve Girard. Jet resonance in truncated ideally contoured nozzles. *Journal of Fluid Mechanics*, 919:A32, 2021.

[24] Alfred S Valerino, Robert F Zappa, and Kaleel L Abdalla. Effects of external stream on the performance of isentropic plug-type nozzles at mach numbers of 2.0, 1.8, and 1.5, 3 1962.

[25] T Rommel, G Hagemann, C Schley, G Krulle, and D Manski. Plug nozzle flowfield calculations for ssto applications. In *31st AIAA/ASME/SAE/ASEE Joint Propulsion Conference and Exhibit*, 1995.

[26] Kiran Chutkey, B. Vasudevan, and N. Balakrishnan. Flowfield analysis of linear plug nozzle. *Journal of Spacecraft and Rockets*, 49:1109–1119, 2012.

[27] A. Khan, A. S. Bhesania, and R. Kumar. An experimental study on the control of plug nozzle jets. *Shock Waves*, 31:31–47, 1 2021.

[28] C C Lee. Fortran programs for plug nozzle design, 1963.

[29] Milton A Beheim and Aaron S Boksenbom. Variable geometry requirements in inlets and exhaust nozzles for high mach number applications, 1968.

[30] Kiran Chutkey, B. Vasudevan, and N. Balakrishnan. Flow and performance analysis of annular cluster truncated plug nozzle. *Journal of Propulsion and Power*, 32(6):1442–1453, 2016.

[31] Randall Smith-Kent, Hai-Tien Loh, and Pawel Chwalowski. Analytical contouring of pintle nozzle exit cone using computational fluid dynamics. In *31st Joint Propulsion Conference and Exhibit*. American Institute of Aeronautics and Astronautics, 7 1995.

[32] R. Ewen and C. Obrien. Dual throat thruster test results. In *22nd Joint Propulsion Conference*. American Institute of Aeronautics and Astronautics, 6 1986.

[33] T. Nguyen, J. Hyde, and M. Ostrander. Aerodynamic performance analysis of dual-fuel/dual-expander nozzles. In *24th Joint Propulsion Conference*. American Institute of Aeronautics and Astronautics (AIAA), 7 1988.

[34] Detlef Manski, Gerald Hagemann, and Hagen D. Saβnick. Optimization of dual-expander rocket engines in single-stage-to-orbit vehicles. *Acta Astronautica*, 40:151–163, 1 1997.

[35] Gerald Hagemann, Gerd Krülle, and Detlef Manski. Dual-expander engine flowfield simulations. In *31st Joint Propulsion Conference and Exhibit*. American Institute of Aeronautics and Astronautics Inc, AIAA, 1995.

[36] J. Mockenhaupt and R. Drzewiecki. Investigation of the aerodynamic loads induced on an extendible nozzle exit cone during and after deployment in flight. In *13th Propulsion Conference*. American Institute of Aeronautics and Astronautics, 7 1977.

[37] Charles N Scott, Robert W Nordlie, William W Sowa, and George C Marshall. Investigation of extendable nozzle concepts, 1972.

[38] M. Lacoste, A. Lacombe, P. Joyez, R.A. Ellis, J.C. Lee, and F.M. Payne. Carbon/carbon extendible nozzles. *Acta Astronautica*, 50:357–367, 3 2002.

[39] Masaki Sato, Shin-Ichi Moriya, Makoto Tadano, Masahiro Sato, Tadashi Masuoka, and Makoto Yoshida. Experimental study on transitional phenomena of extendible nozzle. In *43rd AIAA/ASME/SAE/ASEE Joint Propulsion Conference & Exhibit*, 2007.

[40] R. C. Parsley and K. J. Van Stelle. Altitude compensating nozzle evaluation. In *AIAA/ASME/SAE/ASEE 28th Joint Propulsion Conference and Exhibit, 1992*. American Institute of Aeronautics and Astronautics Inc, AIAA, 1992.

[41] Norman T Musial and James J Ward. overexpanded performance of conical nozzles with area ratios of 6 and 9 with and without supersonic external flow, 1959.

[42] J. Östlund and B. Muhammad-Klingmann. Supersonic flow separation with application to rocket engine nozzles. *Applied Mechanics Reviews*, 58:143–177, 5 2005.

[43] VN Sreerag, Fazil Mohammad, Vishnu Nandan, Anurag Pramod, KP. Subhajayan, and Samik Jash. Parametric study on a method to control flow separation in rocket nozzles. *Materials Today: Proceedings*, 46:9950–9955, 2021. International Mechanical Engineering Congress 2019.

[44] Mohamed Sellam, Vladeta Zmijanovic, Luc Leger, and Amer Chpoun. Assessment of gas thermodynamic characteristics on fluidic thrust vectoring performance: Analytical, experimental and numerical study. *International Journal of Heat and Fluid Flow*, 53:156–166, 6 2015.

[45] Vladeta Zmijanovic, Luc Leger, Eric Depussay, Mohamed Sellam, and Amer Chpoun. Experimental-numerical parametric investigation of a rocket nozzle secondary injection thrust vectoring. *Journal of Propulsion and Power*, 32:196–213, 2016.

[46] Richard M. Clayton and Lloyd H. Back. Thrust improvement with ablative insert nozzle extension. *Journal of Propulsion and Power*, 2:91–93, 1986.

[47] N S Goncharov, V A Orlov, V S Rachuk, A V Shostak, and R Starke. Reusable launch vehicle propulsion based on the rd-0120 engine. In *31st AIAA/ASME/SAE/ASEE Joint Propulsion Conference and Exhibit*, 1995.

[48] G D Luke and D E Adams. Use of nozzle trip rings to reduce nozzle separation side force during staging. In *AIAA/SAE/ASME/ASEE 28th Joint Propulsion Conference and Exhibit*, 1992.

[49] Robert H. Schmucker. A procedure for calculation of boundary layer trip protuberances in overexpanded rocket nozzles, 1973.

[50] M Horn and S Fisher. Dual-bell altitude compensating nozzles, 1993.

[51] Swan Walter .C. The influence of nozzle design on the flight performance of rocket vehicles, with an analysis of the results of jet separation, 1948.

[52] Alois T. Sutor. Rockwell international corp. assignee, step nozzle, us patent 339,454,9 a,, 1968.

[53] Charles R. Foster and Frederick B. Cowles. Experimental study of gas-flow separation in overexpanded exhaust nozzles for rocket motors, 5 1949.

[54] Hans Immich and Marco Caporicci. Festip technology developments in liquid rocket propulsion for reusable launch vehicles. In *32nd Joint Propulsion Conference and Exhibit*, pages 1–14. American Institute of Aeronautics and Astronautics Inc, AIAA, 1996.

[55] G. Hagemann, M. Frey, and D. Manski. A critical assessment of dual-bell nozzles. In *33rd Joint Propulsion Conference and Exhibit*. American Institute of Aeronautics and Astronautics Inc, AIAA, 1997.

[56] F A Haidinger, J Gorgen', and D Haeseler. Numerical prediction of flow separation for advanced nozzle concepts. In *34th AIAA/ASME/SAE/ASEE*, 1998.

[57] Manuel Frey and Gerald Hagemann. Critical assessment of dual-bell nozzles. *Journal of Propulsion and Power*, 15:137–143, 1999.

[58] Gerald Hagemann, Michael Terhardt, Dietrich Haeseler, and Manuel Frey. Experimental and analytical design verification of the dual-bell concept. *Journal of Propulsion and Power*, 18:116–122, 2002.

[59] A Kumakawa, H Tamura, M Niino, M Nosaka, H Yamada, A Kanmuri, A Konno, and M Atsumi. Propulsion research for rocket sstos at nal/krc. In *35th AIAA/ASME/SAE/ASEE Joint Propulsion Conference and Exhibit*, 1999.

[60] K Kusaka, A Kumakawa, M Niino, A Konno, and M Atsumi. Experimental study on extendible and dual-bell nozzles under high altitude conditions. In *36th AIAA/ASME/SAE/ASEE Joint Propulsion Conference and Exhibit*, 2000.

[61] Masafumi Miyazawa, Susumu Takeuchi, and Miyuki Takahashi. Flight performance of dual-bell nozzles. In *40th AIAA Aerospace Sciences Meeting and Exhibit*, 2002.

[62] G. E. Dumnov, N. B. Ponomaryov, and A. L. Voinov. Dual bell nozzles for rocket engines of launch vehicle upper stages and orbital transfer vehicles. In *33rd Joint Propulsion Conference and Exhibit*. American Institute of Aeronautics and Astronautics Inc, AIAA, 1997.

[63] Andrea Ferrero, Antonietta Conte, Emanuele Martelli, Francesco Nasuti, and Dario Pastrone. Dual-bell nozzle with fluidic control of transition for space launchers. *Acta Astronautica*, 193:130–137, 4 2022.

[64] Francesco Nasuti, Marcello Onofri, and Emanuele Martelli. Role of wall shape on the transition in axisymmetric dual-bell nozzles. *Journal of Propulsion and Power*, 21:243–250, 2005.

[65] T Kimura, K Niu, K Yonezawa, and Y Tsujimoto. Experimental and analytical study for design of dual-bell nozzles. In *45th AIAA/ASME/SAE/ASEE Joint Propulsion Conference & Exhibit*, 2009.

[66] Takeo Tomita, Mamoru Takahashi, and Masaki Sasaki. Investigation on characteristics of conventional-nozzle-based altitude compensating nozzles by cold-flow tests (ii) - side-load characteristics during transition. In *43rd AIAA/ASME/SAE/ASEE Joint Propulsion Conference & Exhibit*. American Institute of Aeronautics and Astronautics, 7 2007.

[67] S. B. Verma, R. Stark, C. Nuerenberger-Genin, and O. Haidn. Cold-gas experiments to study the flow separation characteristics of a dual-bell nozzle during its transition modes. *Shock Waves*, 20:191–203, 2010.

[68] Takeo Tomita, Mamoru Takahashi, Masaki Sasaki, and Hiroshi Tamura. Investigation on characteristics of conventional-nozzle-based altitude compensating nozzles by cold-flow tests. In *42nd AIAA/ASME/SAE/ASEE Joint Propulsion Conference & Exhibit*, 2006.

[69] Robert H Schmucker. Flow processes in overexpanded chemical rocket nozzles. part 1: Flow separation, 1984.

[70] Ralf Stark. Flow separation in rocket nozzles – an overview. In *49th AIAA/ASME/SAE/ASEE Joint Propulsion Conference*, volume 1 PartF, pages 1–10. American Institute of Aeronautics and Astronautics Inc., 2013.

[71] Francesco Nasuti, Marcello Onofri, and Emanuele Martelli. Numerical study of transition between the two operating modes of dual-bell nozzles. In *38th AIAA/ASME/SAE/ASEE*, 2002.

[72] M Frey and G Hagemann. Status of flow separation prediction in rocket nozzles. In *34th AIAA/ASME/SAE/ASEE Joint Propulsion Conference and Exhibit*, 1998.

[73] Chloe Nürnberger-Genin and Ralf Stark. Flow transition in dual bell nozzles. *Shock Waves*, 19:265–270, 7 2009.

[74] Chloé Génin and Ralf H. Stark. Side loads in subscale dual bell nozzles. *Journal of Propulsion and Power*, 27:828–837, 2011.

[75] R. Stark and C. Géniny. Scaling effects on side load generation in subscale rocket nozzles. In *52nd AIAA/SAE/ASEE Joint Propulsion Conference, 2016*. American Institute of Aeronautics and Astronautics Inc, AIAA, 2016.

[76] S. B. Verma, R. Stark, and O. Haidn. Effect of ambient pressure fluctuations on dual-bell transition behavior. *Journal of Propulsion and Power*, 30:1192–1198, 9 2014.

[77] E. Martelli, B. Betti, and F. Nasuti. Flow separation response to unsteady external disturbances in dual bell nozzles. In *50th AIAA/ASME/SAE/ASEE Joint Propulsion Conference 2014*. American Institute of Aeronautics and Astronautics Inc., 2014.

[78] Dzianis Proshchanka, Yonezawa Koichi, Hiroaki Tsukuda, Kasumi Araki, Yoshinobu Tsujimoto, Tatsuya Kimura, and Kazuhiko Yokota. Jet oscillation at low-altitude operation mode in dual-bell nozzle. *Journal of Propulsion and Power*, 28:1071–1080, 2012.

[79] C. Génin, R. Stark, O. Haidn, K. Quering, and M. Frey. Experimental and numerical study of dual bell nozzle flow. In *4th European Conference for Aerospace Sciences*, pages 363–376. EDP Sciences, 6 2013.

[80] Chloé Génin, Andreas Gernoth, and Ralf Stark. Experimental and numerical study of heat flux in dual bell nozzles. *Journal of Propulsion and Power*, 29:21–26, 01 2013.

[81] S. B. Verma, R. Stark, and O. Haidn. Gas density effects on dual-bell transition behavior. *Journal of Propulsion and Power*, 28:1315–1323, 2012.

[82] Vladeta Zmijanovic, Luc Leger, Mohamed Sellam, and Amer Chpoun. Assessment of transition regimes in a dual-bell nozzle and possibility of active fluidic control. *Aerospace Science and Technology*, 82-83:1–8, 11 2018.

[83] Chloé Génin and Ralf Stark. Experimental investigation of the inflection geometry on dual bell nozzle flow behavior. In *47th AIAA/ASME/SAE/ASEE Joint Propulsion Conference & Exhibit*, 2011.

[84] Sven Scharnowski and Christian J. Kähler. Investigation of the base flow of a generic space launcher with dual-bell nozzle. *CEAS Space Journal*, 13:197–216, 4 2020.

[85] Alexander Barklage, Wolfgang Schröder, Simon Loosen, and Rolf Radespiel. Reynolds number influence on the hysteresis behavior of a dual-bell nozzle. In *8th European Conference for Aeronautics and Aerospace Sciences (EUCASS)*, 2019.

[86] Dirk Schneider and Chloé Génin. Numerical investigation of flow transition behavior in cold flow dual-bell rocket nozzles. *Journal of Propulsion and Power*, 32:1212–1219, 2016.

[87] S. B. Verma, R. Stark, and O. Haidn. Reynolds number influence on dual-bell transition phenomena. *Journal of Propulsion and Power*, 29:602–609, 2013.

[88] Emanuele Martelli, Francesco Nasuti, and Marcello Onofri. Numerical parametric analysis of dual-bell nozzle flows. *AIAA Journal*, 45:640–650, 3 2007.

[89] R. Stark and C. Génin. Flow separation in rocket nozzles under high altitude condition. *Shock Waves*, 27:63–68, 1 2017.

[90] Chloe Génin and Ralf Stark. Influence of the test environment on the transition of dual-bell nozzles. *Transactions of the Japan Society for Aeronautical and Space Sciences, Aerospace Technology Japan*, 10(ists28):49–53, 2012.

[91] J. D. Mockenhaupt. Cold flow tests with chamber-bleed gas injection thrust vector control. In *24th Joint Propulsion Conference*, volume 4, pages 14–23, 1988.

[92] Ralf H. Stark and Chloé Génin. Experimental study on rocket nozzle side load reduction. *Journal of Propulsion and Power*, 28:307–311, 2012.

[93] R. Stark and C. Génin. Optimization of a rocket nozzle side load reduction device. *Journal of Propulsion and Power*, 32:1395–1402, 2016.

[94] Emanuele Martelli, Francesco Nasuti, and Marcello Onofri. Numerical analysis of film cooling in advanced rocket nozzles. *AIAA Journal*, 47:2558–2566, 11 2009.

[95] Dirk Schneider, Ralf Stark, Chloé Génin, Michael Oschwald, and Konstantin Kostyrkin. Active control of dual-bell nozzle operation mode transition by film cooling and mixture ratio variation. *Journal of Propulsion and Power*, 36:47–58, 2019.

[96] Dzianis Proshchanka, Koichi Yonezawa, Hidekazu Koga, Yoshinobu Tsujimoto, Tatsuya Kimura, and Kazuhiko Yokota. Control of operation mode transition in dual-bell nozzles with film cooling. *Journal of Propulsion and Power*, 28:517–529, 2012.

[97] Takeo Tomita, Mamoru Takahashi, and Masaki Sasaki. Control of transition between two working modes of a dual-bell nozzle by gas injection. In *45th AIAA/ASME/SAE/ASEE Joint Propulsion Conference & Exhibit*, 2009.

[98] L. Léger, V. Zmijanovic, M. Sellam, and A. Chpoun. Controlled flow regime transition in a dual bell nozzle by secondary radial injection. *Experiments in Fluids*, 61, 12 2020.

[99] L. Léger, V. Zmijanovic, M. Sellam, and A. Chpoun. Experimental investigation of forced flow regime transition in a dual bell nozzle by secondary fluidic injection. *International Journal of Heat and Fluid Flow*, 89, 6 2021.

[100] Chloe Numberger-Genin and Ralf Stark. Experimental study on flow transition in dual bell nozzles. *Journal of Propulsion and Power*, 26(3):497–502, 2010.

[101] Andrew Trettel and Johan Larsson. Mean velocity scaling for compressible wall turbulence with heat transfer. *Physics of Fluids*, 28:026102, 02 2016.

[102] Nicholas DiGregorio, Tomasz Drozda, and Cyrus Madnia. Comparison of boundary layer similarity transformations for high mach number flows. In *AIAA Scitech 2019 Forum*, 01 2019.

[103] Florian Menter, M. Kuntz, and RB Langtry. Ten years of industrial experience with the sst turbulence model. *Heat and Mass Transfer*, 4, 01 2003.

[104] Philippe Spalart and Steven Allmaras. A one-equation turbulence model for aerodynamic flows. *Recherche Aerospatiale*, 94:1–22, 01 1994.

[105] Nicholas Georgiadis and Dennis Yoder. Recalibration of the shear stress transport model to improve calculation of shock separated flows. In *51st AIAA Aerospace Sciences Meeting including the New Horizons Forum and Aerospace Exposition 2013*, 01 2013.

[106] Allamaprabhu Yaravintelimath, Raghunandan Bn, and Jose A. Moriñigo. Numerical prediction of nozzle flow separation: Issue of turbulence modeling. *Aerospace Science and Technology*, 50, 12 2015.

[107] Robert H. Schmucker. Flow processes in overexpanded chemical rocket nozzles. part 2: Side loads due to asymmetric separation., 1984.

Appendix A

Mesh sensitivity analysis

The steady modelling approach was chosen to perform the mesh sensitivity analysis at different nozzle pressure ratios. The $k\omega - SST$ turbulence model with its standard coefficients was used. Generating the meshes with a first cell height of $2.3e^{-6}$ m at the nozzle wall outlet resulted in y^{+} values along the wall near to one for the coarser mesh; the other grids' size was therefore only increased by adding cells in the streamwise direction. The numerical results are compared to the experimental nozzle wall pressure distribution and schlieren images.

A.1 Qualitative analysis

This section discusses a first qualitative flow analysis using the contours of Mach number, density, and eddy viscosity obtained with the simulations. The different DBN flow regimes are presented for the grid D case and a comparison between the different grid sizes is carried on. The numerical schlieren images are then compared to the experimental schlieren at several nozzle pressure ratios.

A.1.1 The dual-bell nozzle working modes

Because the intrinsic mechanisms governing the dual-bell nozzle transition involve small and large time scales, it is extremely difficult to resolve the full flow during an entire transition. Due to the numerous experimental configurations performed during the experimental test campaign, it was decided to focus only on the 2D steady modelling approach at different NPRs. No significant differences were noticeable for the different meshes. Consequently, only numerical data obtained with the grid D case is presented. Fig. A.1 shows the DBN mach number contour at different NPR for the grid D case.

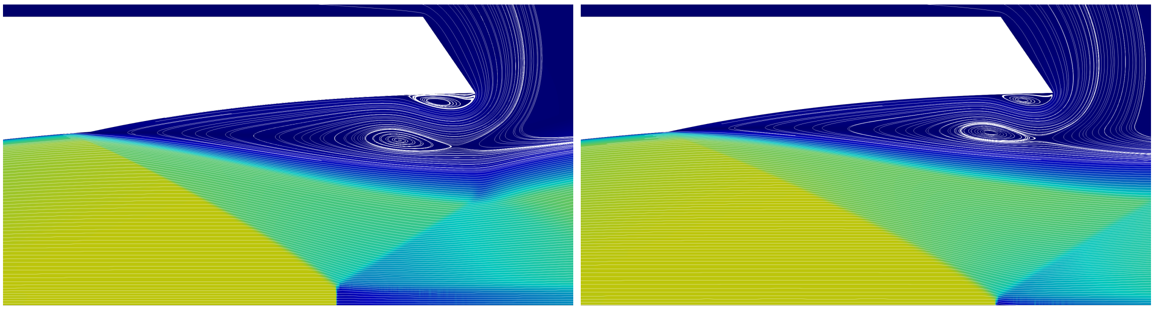

(a) NPR = 11.67

(b) NPR = 14

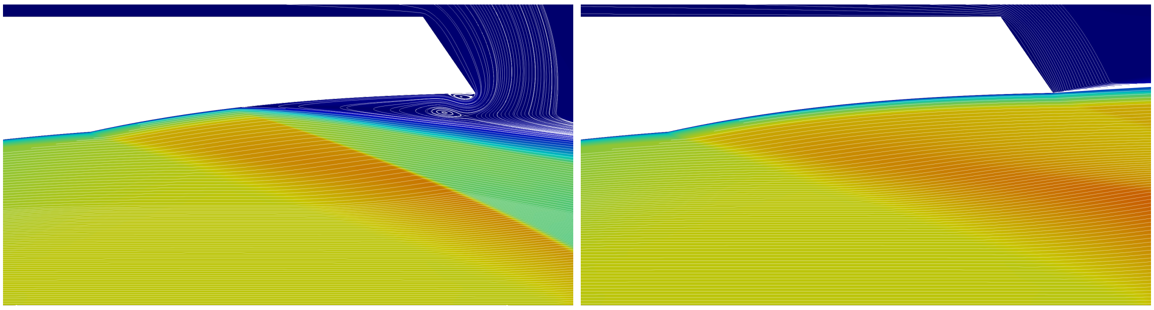

(c) NPR = 17.5

(d) NPR = 50

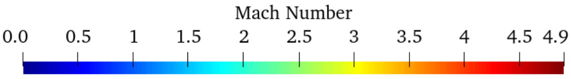

Fig. A.1 Mach number contour and streamlines at several NPR for grid D.

At NPR = 11.67, the DBN is in low-altitude mode (see Fig. A.1a). The jet column is compressed due to the high ambient pressure, causing the boundary layer to separate from the wall upstream of the inflexion point. An oblique shock emerges from the separation point and intersects with the Mach disk close to the nozzle symmetry axis. A series of compression and expansion cells continues further downstream to adapt the exhaust jet to the ambient conditions. A significant recirculation bubble exits downstream of the separation point, inducing lower wall pressures than in the far field. The lower wall pressure on the extension wall induces a decrease in thrust, called aspiration drag, which accounts for less than 3% of the nozzle thrust. Two trapped vortices are visible in the separation bubble: one core vortex in the detached flow area, the other close to the wall at the nozzle exit.

At NPR = 14, the DBN remains in the low-altitude mode. The lower ambient pressure causes the size of the recirculation bubble to decrease, yet the two trapped vortices remain visible. The lower wall static pressure in the extension causes the boundary layer separation point to be displaced downstream, at the inflexion point. A similar shock topology as discussed previously is observed, except that this configuration displays a smaller Mach disk height.

As the ambient pressure is further decreased, the recirculation bubble size is reduced (Fig. A.1c). At NPR = 17.5, the DBN is transitioning from the low-altitude mode to the high-altitude mode. The lower wall pressure inside the separation bubble is such that the separation onset is located inside the extension section. In this configuration, an expansion fan located at the inflexion point accelerates and turns the flow in the extension section. It is worth mentioning that this flow state exists only for a short period of time experimentally. Indeed, the extension section is designed as a CP extension, causing a rapid transition between the low-to-high-altitude mode during the experiments. However, the steady-state simulations force the solutions to converge in these intermediate states.

Fig. A.1d shows the DBN in high-altitude mode, at NPR = 50, where the ambient pressure is low enough to cause the flow to separate at the extension section exit. In this configuration, the flow is fully attached to the DBN wall, and there exists no recirculating region in the core flow. Here, the flow fully expands from the inflexion point, hence the significant Mach number increase in the core flow. A recompression shock arises in the flow downstream of the inflexion point, which is a distinctive feature of DBNs with a CP extension profile during the full-flowing mode.

Along with the Mach number contours discussed above, Fig. A.2 shows the density and the pressure contours in the DBN at several NPR.

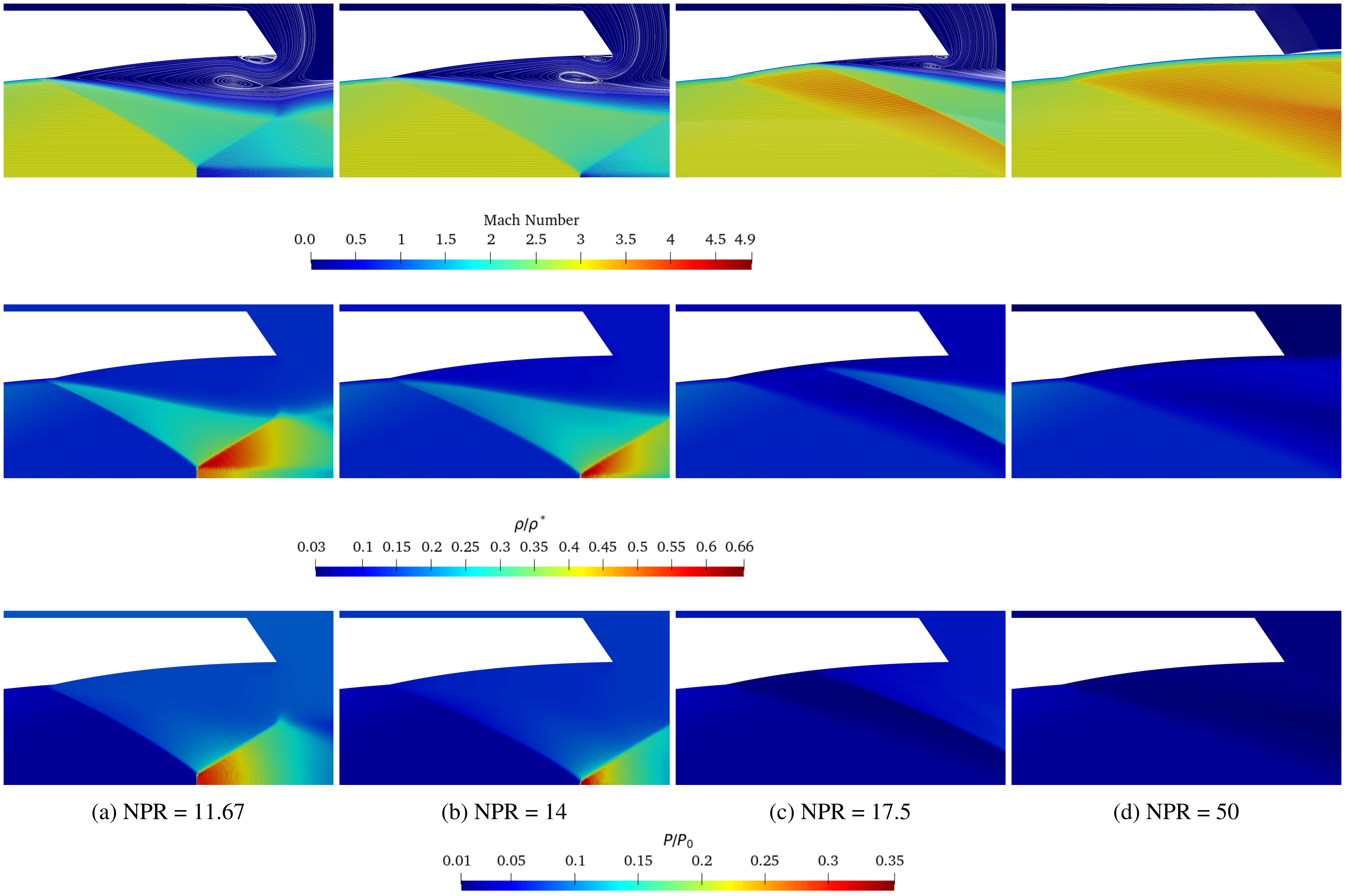

(a) NPR = 11.67

(b) NPR = 14

(c) NPR = 17.5

(d) NPR = 50

Fig. A.2 Mach number (top), density (middle) and pressure (bottom) contours at several NPR (from left to right)

A.1.2 Flow topology analysis

This section exposes the flow topology obtained from using the experimental schlieren imaging technique and the numerical schlieren computed in CFD. In the experiments performed in the EDITH wind tunnel, the schlieren technique revealed itself useful not only for the analysis of the flow topology during post-processing, but also to be able to see on live screen the mode in which the DBN is functioning. Fig. A.3a to Fig. A.3e display the comparison between the experimental and the numerical schlieren images for several nozzle pressure ratios. No significant differences were noticeable for the different meshes. Consequently, only numerical data obtained with the grid D case is presented.

At NPR = 11.67, the DBN is working in low-altitude mode and the flow topology is in good agreement with the experiment. The simulation provides the user with information about the flow features that are not visible in the experiment, especially regarding the flow inside the DBN. In Fig. A.3a, the separation shock at the inflexion point is clearly identified. The separation shock intersects with a Mach disk at the triple point further downstream, where a reflected shock emerges. The reflected shock then intersects with the jet boundary and is turned into an expansion fan. Further downstream, a recompression shock emerge and intersects with another Mach disk near the nozzle symmetry axis. The intersection between the second mach disk with the nozzle symmetry axis is predicted slightly upstream by the simulations compared to the experiments. The slip line downstream the second Mach disk visible numerically is in good agreement with the one observed experimentally. Moreover, a light line is visible after the nozzle exit in the experiment, whose position is relatively symmetric to the slip line downstream of the first Mach disk, indicating that a Mach disk is also present experimentally. This compression/expansion process continues downstream, but one can notice that the exhaust plume is significantly bigger in the experiments than in the simulation, which may be induced by the low diffusivity in the numerical model.

At NPR = 14, the experiment and the simulation are again in good agreement. At this NPR, the DBN is still operating in low-altitude mode, the flow separates at the inflexion point, and the flow topology is similar to the one described above, with the exception that, due to a lower NPR, the shocks intersection with the nozzle symmetry axis are located further downstream. The several shock intersections with the symmetry axis are also well predicted by the simulation. The presence of symmetric slip lines in the experiment and the simulation confirms the existence of a Mach disk inside the DBN in the experimental test specimen.

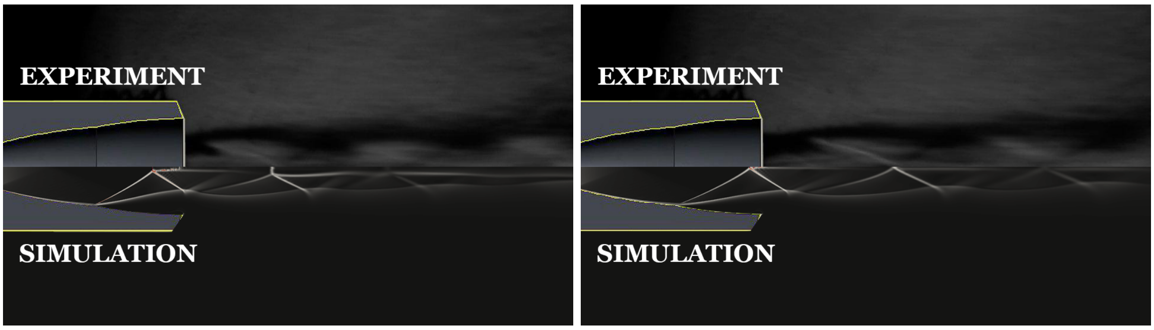

(a) NPR = 11.67 (b) NPR = 14

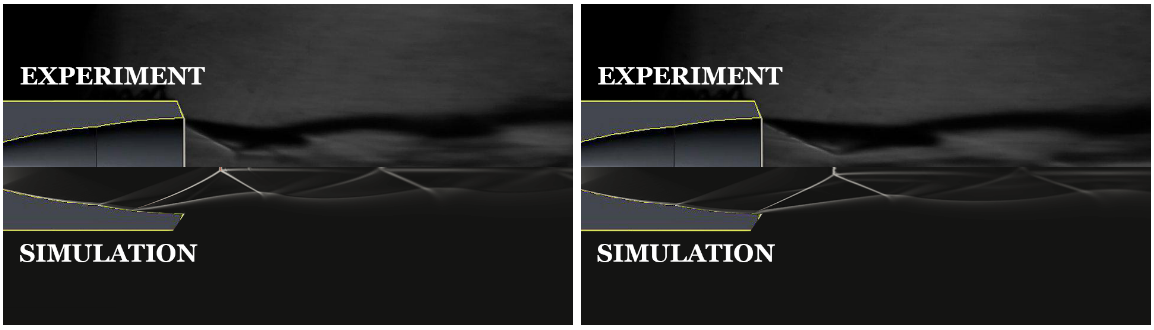

(c) NPR = 17.5 (d) NPR = 23.33

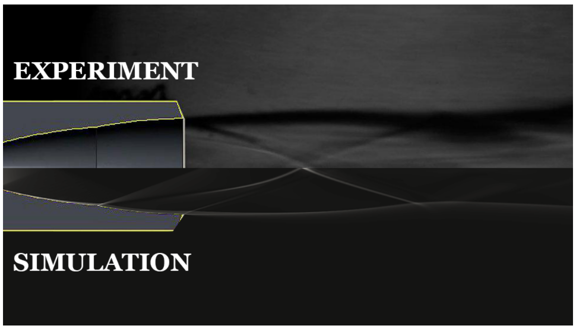

(e) NPR = 50

Fig. A.3 Experimental and numerical schlieren imaging for several NPR.

At NPR = 17.5, the transition has fully taken place experimentally and the flow is attached in the extension profile. However, the simulation performed by the $k\omega$-SST turbulence model has under-predicted the separation location and the flow separates in the extension section. As opposed to the last two previous cases, the flow is accelerated at the inflexion point through an expansion fan. Because separation takes place in the extension profile in the simulation instead of the end of the extension section, the shock topology predicted by the simulation is displaced upstream of the experimental findings. Because the flow did not fully expand compared to the experiment, a smaller Mach disk is observed numerically and the internal recompression shock induced by the CP extension is only visible experimentally.

At NPR = 23.33, the DBN operates in the high-altitude mode and the flow separates at the nozzle exit in the experiment and the simulation. Similar flow topology as described in Fig. A.3a is visible in Fig. A.3d. At this NPR, the simulation and the experiment are in good agreement. The numerical internal recompression shock, the oblique shock at the nozzle exit, the Mach disk, and the oblique shock reflection correspond well with the experimental observations. However, the shock intersection with the nozzle symmetry axis further downstream is predicted ahead of the one observed experimentally. The exhaust plume thickness predicted by the simulation is again smaller than the jet in the experiments, due to the low model diffusivity.

At NPR = 50, the DBN is in high-altitude mode and the simulation is in good agreement with the experiment. The shock topology can be described more easily, as the most prominent feature is the internal recompression shock and its reflections. At this NPR, the flow topology obtained numerically is almost the perfect symmetry of the experiment. Here, the jets' plume thicknesses are fairly close to one another.

A.2 Quantitative analysis

A.2.1 Wall pressure and separation location

Fig. A.4 to Fig. A.9 show the nozzle wall pressure and the nozzle axial wall shear stress distribution at different nozzle pressure ratio for the experiment and the simulations using the different meshes. The wall pressure and the streamwise direction are respectively normalised by the nozzle feeding total pressure P_0 and the nozzle throat radius r_{th}. The skin friction coefficient was computed with the following relation:

$$C_f = \frac{\tau_w}{\rho^* u^{*2}}, \tag{A.1}$$

where τ_w, ρ^* and u^* are, respectively, the axial wall shear stress, the density and velocity at the nozzle throat obtained from the isentropic relations.

At NPR = 11.67, both, the experiments and the simulations predict the separation location upstream of the inflexion point (see Fig. A.4a). The analysis of the skin friction coefficient in Fig. A.4b reveals a numerical separation location at x_{sep}/r_{th} = 5.71 for the grid D that being $0.18 \cdot r_t h$ upstream of the inflexion point. After the separation point, a recirculating flow region forms in the extension part and the pressure increases. The pressure in the separated flow region is lower than the ambient pressure, causing the well-known aspiration drag. The numerical pressure recovery downstream of the separation location is in good agreement with the experiments, which indicates a reasonably well-captured separation bubble size and length. The differences between the meshes were negligible, even though the coarser meshes present discrepancies at the nozzle exit. Here, the skin friction coefficient slightly varies between the different meshes near the separation location and at the nozzle exit (except for grid D and grid E), but these differences had no impact on the separation location prediction.

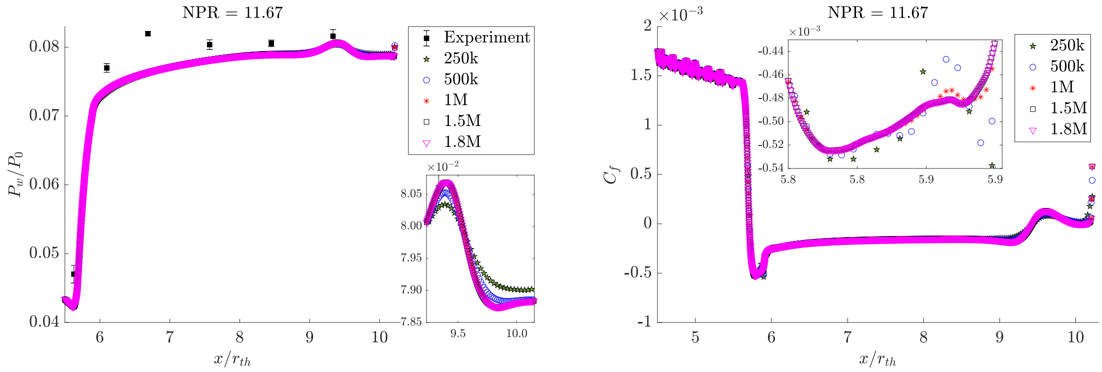

(a) Wall pressure (NPR=11.67)

(b) Skin friction coefficient (NPR=11.67)

Fig. A.4 Streamwise wall pressure and axial skin friction coefficient distribution at NPR=11.67

Fig. A.5a shows the DBN wall pressure distribution at NPR = 14, where the nozzle is still operating in low-altitude mode. Fig. A.5a and Fig. A.5b show that the flow separates at the inflexion point, at x_{sep}/r_{th} = 5.90 for the two finer meshes, where no substantial difference in separation location was observed. For coarser meshes such as with grid C and grid A, the separation location was positioned further downstream, at x_{sep}/r_{th} = 5.91 and x_{sep}/r_{th} = 5.93, respectively. Experimentally, the pressure sensor distribution does not allow to precisely state whether the separation line is ahead, within, or after the inflection point. However, the separation location prediction and the following pressure recovery predicted by the simulations are in good agreement with the experimental data. One may notice that the numerical pressure values in Fig. A.5a downstream of the separation, in the vicinity of x_{sep}/r_{th} = 6.69, does not fully correspond to the experimental data. Indeed, the experiments show a fairly constant wall pressure distribution in the extension part, while the simulations reveal an increasing wall pressure. This numerical discrepancy might emanate from the smaller jet spreading rate and/or wrong recirculation bubble size downstream of the separation line. A closer look at the nozzle exit pressure illustrates once more the difficulty of obtaining reliable results using the coarser grid sizes, as the wall pressures differ in this region for coarser meshes. The skin friction coefficient slightly differs between the different meshes near the separation location and at the nozzle exit (except for grid D and grid E), but these differences only had a limited impact on the separation location prediction (see Fig. A.6).

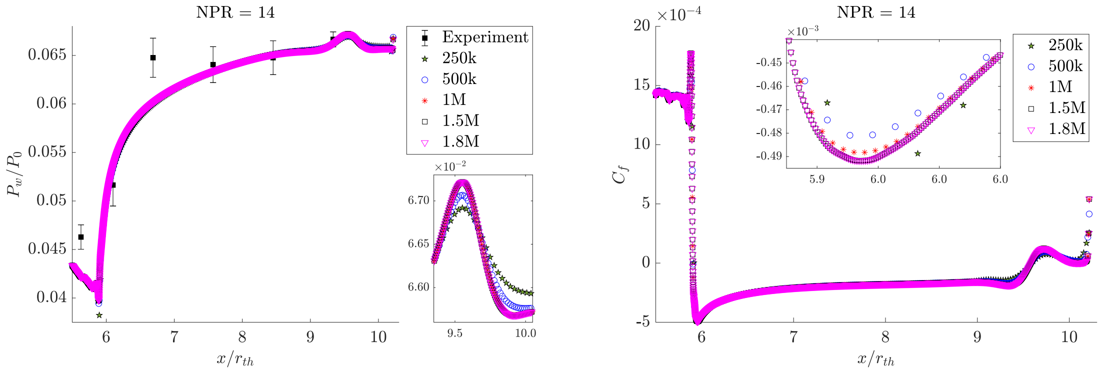

(a) Wall pressure (NPR=14)

(b) Skin friction coefficient (NPR=14)

Fig. A.5 Streamwise wall pressure and axial skin friction coefficient distribution at NPR=14

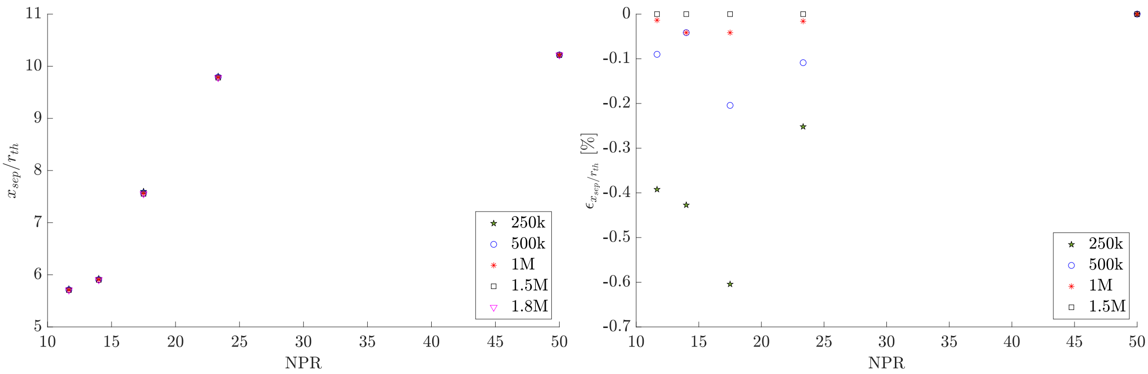

(a) Separation point location.

(b) Separation location relative difference.

Fig. A.6 Separation point location and relative difference at several NPR for the different grid sizes. Relative differences were calculated using the grid E

At NPR = 17.5, the simulations show the DBN during its transition process, where the flow separation takes place in the extension section of the nozzle, while in the experiment, the DBN has transitioned to the high-altitude mode, with a flow completely attached to the extension wall (see Fig. A.7a). This failure of the $k\omega - SST$ turbulence model in predicting the separation location is well known in rocket nozzles with flow separation due to the inexact values of Reynolds shear stress in the eddy-viscosity hypothesis. Meanwhile, the separation location difference between the several meshes was relatively small, reaching a maximum difference of 0.6% between the grid A and the grid E. The skin friction coefficients in Fig. A.7b show the flow separation location at $x_{sep}/r_{th} = 7.55$, after which the pressure recovery is fairly similar for the different meshes. However, a zoom-in at the nozzle exit indicates pressure differences between the coarser grids and the finer ones.

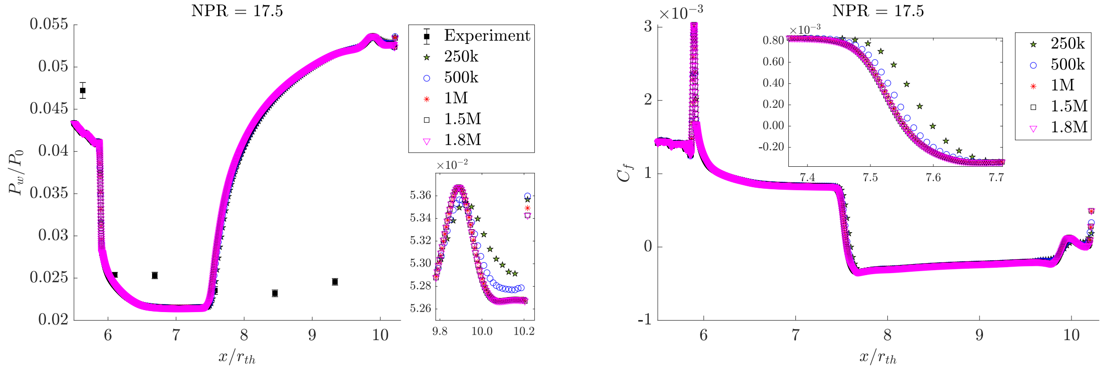

(a) Wall pressure (NPR=17.5)

(b) Skin friction coefficient (NPR=17.5)

Fig. A.7 Streamwise wall pressure and axial skin friction coefficient distribution at NPR=17.5

At NPR = 23.33, the experimental data indicate that the DBN is in high-altitude mode as the pressure sensors show an attached flow in the extension profile (see Fig. A.8a). The wall pressure distributions obtained from the simulations are in good agreement with the experimental values as the flow is attached in most part of the nozzle wall. Slim differences in pressure recovery gradients are noticeable with grid A and grid B compared to the more refined grids. At $x_{sep}/r_{th} = 9.78$, upstream of the nozzle exit, the skin friction becomes negative, and the flow separates from the nozzle wall. The lack of a pressure sensor at the exit of the nozzle does not allow us to state whether the flow has really separated near the nozzle exit at this NPR or if the flow is attached in the entirety of the extension section.

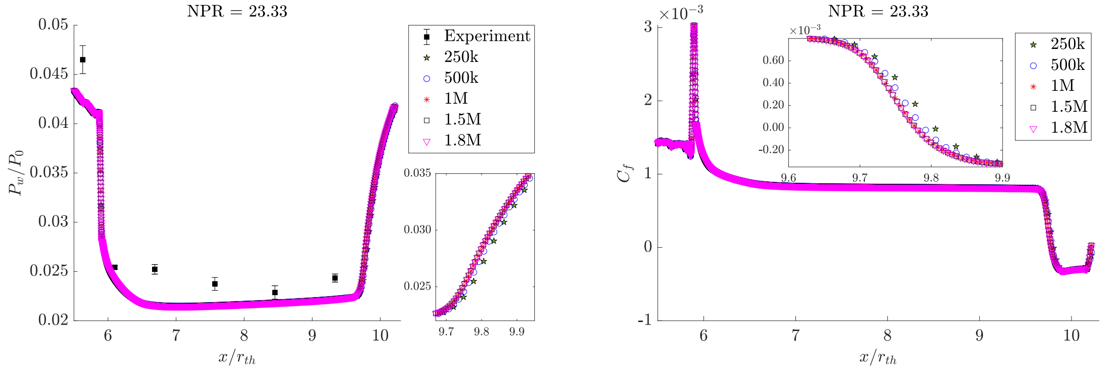

(a) Wall pressure (NPR=23.33)

(b) Skin friction coefficient (NPR=23.33)

Fig. A.8 Streamwise wall pressure and axial skin friction coefficient distribution at NPR=23.33

Finally, at NPR = 50, the wall pressure distributions obtained from the simulations are in good agreement with the experimental values. In the simulations and the experiment, the flow is fully attached to the base and the extension sections. No significant difference between the meshes was noticed, and zoom-in on Fig. A.9a shows the marginal discrepancies observed at the nozzle exit. Here again, the geometrical constraints did not permit the presence of a pressure sensor in the vicinity of the nozzle exit to verify the wall pressure drop obtained numerically at the nozzle exit. The axial skin friction coefficient at NPR = 50 is displayed in Fig. A.9b and it confirms that flow separation does not occur in the DBN.

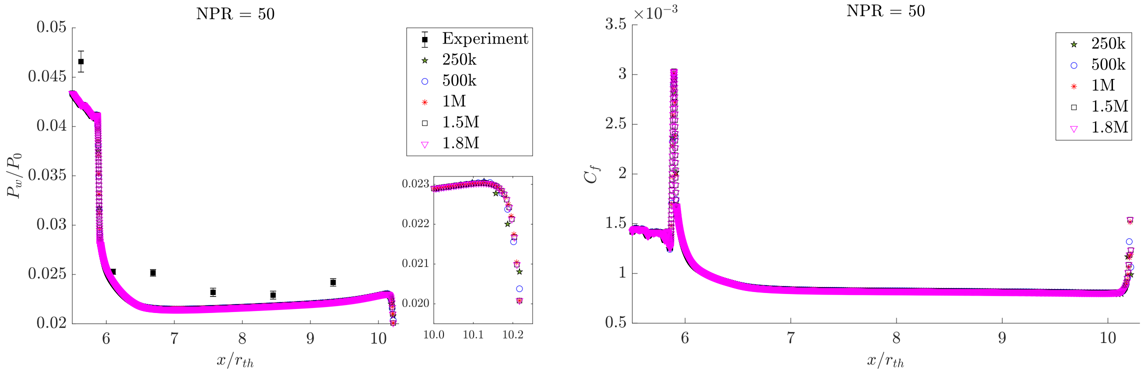

(a) Wall pressure (NPR=50)

(b) Skin friction coefficient (NPR=50)

Fig. A.9 Streamwise wall pressure and axial skin friction coefficient distribution at NPR=50

A.2.2 Thrust and specific impulse validation

Calculating the thrust using the equations above for the different nozzle pressure ratios and the different grid sizes, we can plot the thrust as a function of the nozzle pressure ratio (see Fig. A.10a). The thrust coefficient, visible in Fig. A.10b was calculated using the nozzle thrust, pressure and cross-section area as $C_{fx} = F_x/(P^*A^*)$, where the star superscript indicates the critical values at the nozzle throat. In Fig. A.10, the experimental values have been averaged using a dozen data points during transition phases and retransition phases. The error bars represent the standard deviation around the averaged values. For NPR < 15, the flow is attached to the base nozzle and separates at the inflexion point. Therefore, the DBN performances follow the conventional base nozzle theoretical performances. For NPR > 15, the flow reattaches in the extension profile and the DBN operates in the high-altitude mode, following the performances of a conventional nozzle with the same expansion ratio as the DBN extension nozzle. Fig. A.10 shows one of the main characteristics of DBNs, which is the transition before the optimum transition point. In the smooth DBN, the transition NPR obtained experimentally reached 14.85, against 43.03 for the optimum transition point.

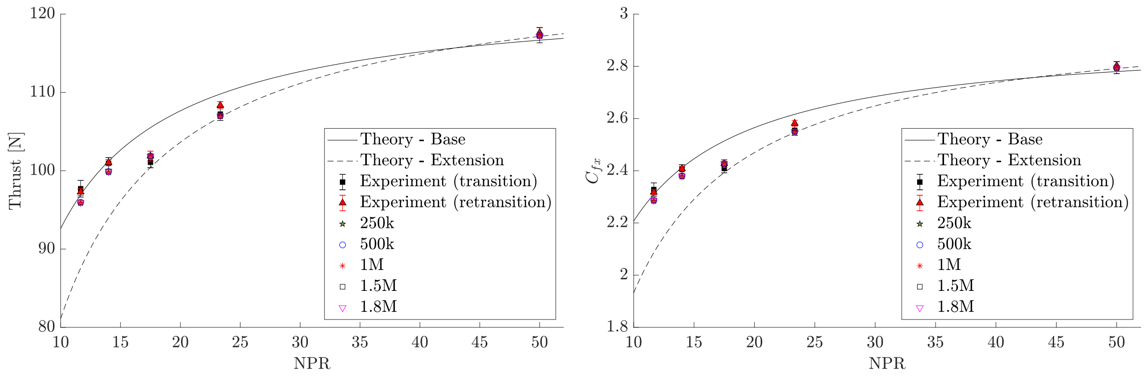

(a) Thrust as function of NPR (b) Thrust coefficient as function of NPR

Fig. A.10 Performance curves for the theory, the experiments, and all mesh grid sizes.

A slight difference is noticeable between the thrust measured during the transition phases and during the retransition phases. This gap emanates from multiple factors, namely the hysteresis effect, feeding total temperature and pressure changes during the experiment, instabilities in the flow during operating modes changes, etc... The relative difference between the thrust measured experimentally and calculated numerically is displayed in Fig. A.11a and Fig. A.11b. Because of the discrepancies existing between the thrust measured in the transition phases and the retransition phases, the relative difference was computed by separating the transition and the retransition phases using the relation:

$$\varepsilon_{C_{fx}}\Big|_{trans/retrans} = \frac{C_{fx_{trans/retrans}} - C_{fx_{CFD}}}{C_{fx_{trans/retrans}}} \tag{A.2}$$

In both cases, the values computed using the numerical simulations are in good agreement with the experiments as the relative difference between the two stays within 2%. No significant differences were found between the different grid sizes, which indicates that even though the recirculation bubble was mildly diverging for the coarser meshes, the impact on a global parameter such as the thrust is negligible.

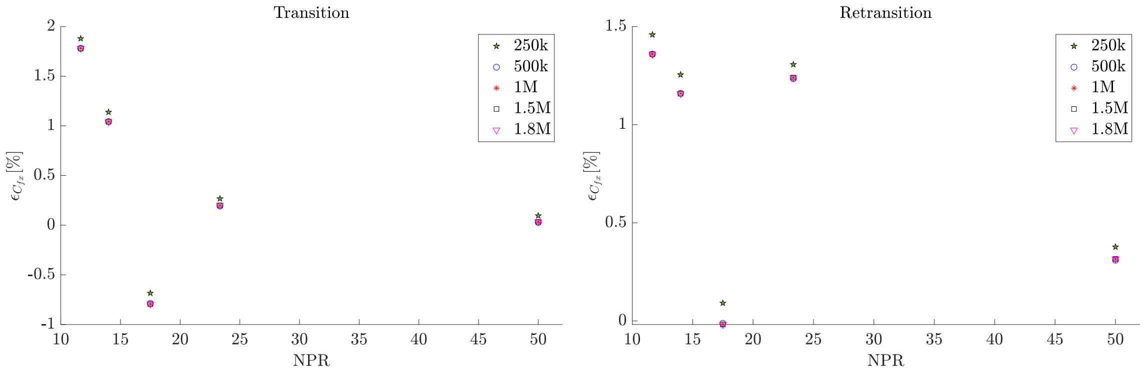

(a) Relative difference during transition phases (b) Relative difference during retransition phases

Fig. A.11 Thrust coefficient relative difference during transition and retransition phases

A.3 Conclusion

In this section, the results obtained from the mesh sensitivity analysis have been presented. Five meshes were considered with a grid density ranging from 250,770 cells to 1,835,300 cells. The wall pressure distribution, the dual-bell nozzle performances, and the flow field were analysed and compared with experimental data so as to quantify the mesh that would provide the most reliable results. The wall pressure data calculated numerically was in good agreement with the experiment, except when the flow separation was underpredicted for NPR = 17.5. The numerical schlieren, which allowed the comparison between the numerical and experimental flow topology matched the experimental findings for the cases where the wall pressure distribution was predicted correctly. The differences between the meshes were slim, but the grid counting 1,544,300 cells (grid D) presented fewer discrepancies when compared to the largest grid size and will be used for the next numerical simulation campaigns.

Appendix B

Technical drawings

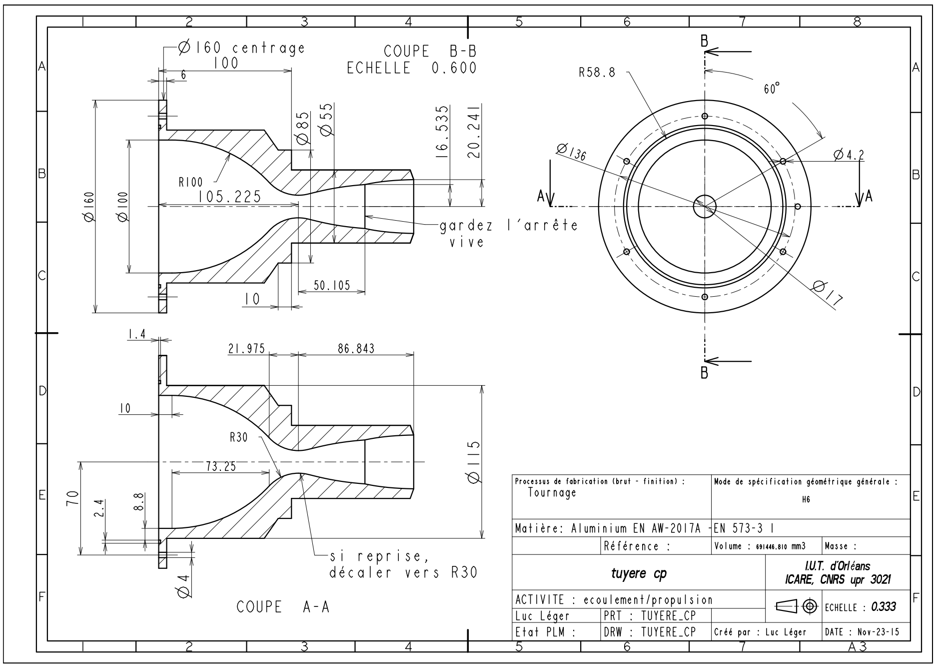

Fig. B.1 Technical drawing of the smooth DBN.

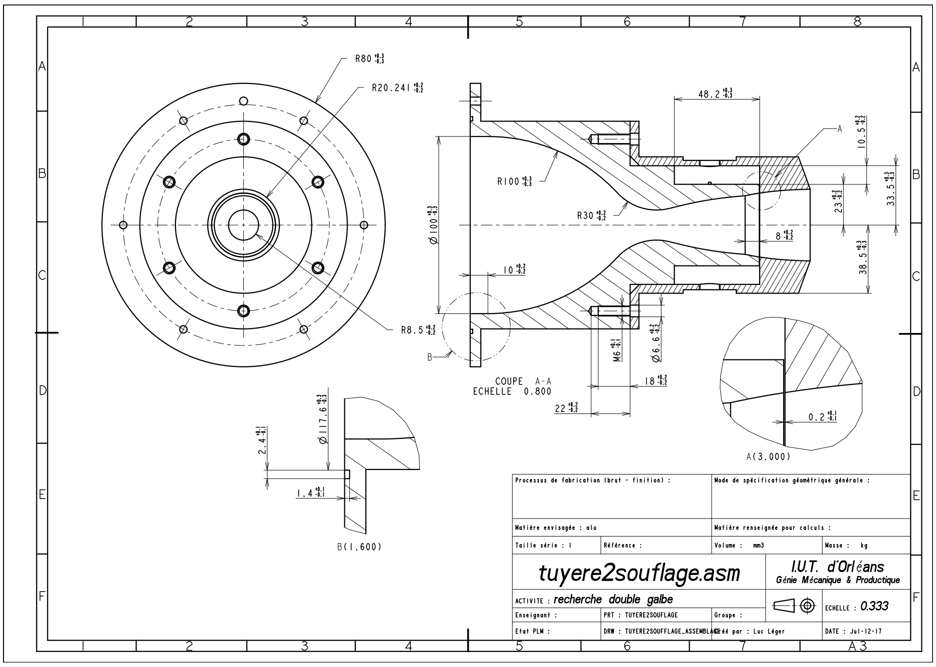

Fig. B.2 Technical drawing of the DBNi8.

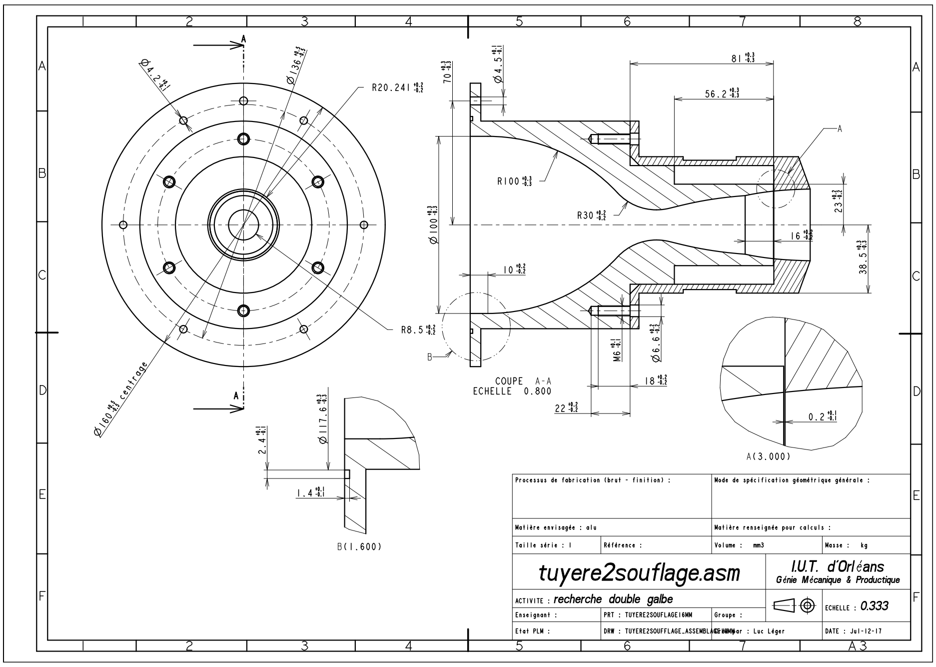

Fig. B.3 Technical drawing of the DBNi16.

Appendix C

Version Française

Introduction Générale

Optimisation de tuyères propulsives

L'industrie du lancement spatial connaît une croissance et une concurrence sans précédent, alimentées par la demande grandissante de déploiements de satellites et de missions d'exploration spatiale. Le marché mondial du lancement spatial connaît une augmentation considérable de l'activité, avec des agences spatiales établies et des entreprises privées cherchant à obtenir une part de la demande. Un rapport d'Euroconsult [4] prédit une augmentation des revenus de lancement de 23%, atteignant 111 milliards de dollars au cours de la prochaine décennie, contre 72 milliards au cours de la décennie précendente. Dans cet environnement en évolution rapide, les entreprises recherchent des moyens de se démarquer par des innovations et par l'utilisation de technologies disruptives. Les tuyères de fusée conventionnelles, bien que fiables, présentent des limites pour s'adapter aux conditions atmosphériques variables pendant l'ascension de la fusée vers l'espace. Le défi réside dans l'optimisation de la tuyère pour des altitudes faibles (au niveau du sol) et élevées (dans le vide), tout en atténuant le risque de charges latérales à basse altitude causées par un écoulement décollé dans la tuyère. Cette limitation entraîne des performances sous-optimales de la tuyère, une capacité de charge utile réduite et des coûts de lancement plus élevés. Les tuyères de fusée innovantes jouent un rôle crucial pour surmonter ces défis en offrant des capacités d'adaptation à l'altitude, un contrôle vectoriel de la poussée et une amélioration globale des performances.

De nombreuses tuyères dotées de capacités d'adaptation à l'altitude ont été étudiées par le passé, et une sélection de celles-ci sera brièvement présentée dans le chapitre suivant. Cependant, parmi la multitude de concepts de tuyères adaptatives, deux solutions ont accumulé un intérêt substantiel ces dernières années : la tuyère à double galbe (DBN) et la tuyère aérospike. Ces deux tuyères présentent des performances supérieures à la fois à basse et haute altitude par rapport à une tuyère propulsive conventionnelle. La tuyère aérospike réalise une adaptation continue de l'écoulement en maintenant le contact entre l'écoulement de sortie et l'air ambiant, tandis que la DBN, caractérisée par deux profils de tuyère en cloche successifs, offre deux modes opérationnels : un mode basse altitude et un mode haute altitude. Dans le contexte de cette thèse, l'accent sera uniquement mis sur l'étude de la DBN.

La polyvalence inhérente à la conception des DBNs, permettant un ajustement sur mesure entre deux profils de cloche distincts, facilite l'optimisation pour deux régimes d'altitude différents. Ce concept permet non seulement un gain global d'impulsion spécifique le long de la trajectoire de vol, mais offre également la possibilité de contrôle vectoriel de la poussée. Ce dernier aspect contribue de manière significative à une manœuvrabilité améliorée et à l'optimisation de la trajectoire, faisant de la DBN un sujet captivant pour une exploration approfondie dans le cadre de cette étude.

Cependant, l'utilisation de la DBN pendant l'ascension d'une fusée présente trois défis critiques : la transition précoce du mode basse altitude au mode haute altitude, la génération de charges latérales substantielles pendant le processus de transition, et un problème de stabilité qui pourrait provoquer des secousses entre les deux modes de fonctionnement, amplifiant le risque de charges latérales. Les études existantes dans la littérature ont mis en lumière l'influence de la géométrie de la DBN et de l'environnement opérationnel sur son comportement à la fois pendant la montée et la descente, dont les détails seront discutés dans le chapitre suivant.

Des recherches récentes, utilisant le contrôle actif de l'écoulement, ont démontré le potentiel de résoudre ces obstacles scientifiques. Ces études ont révélé une transition retardée pendant la phase de montée et une réduction de l'amplitude des charges latérales, montrant ainsi le potentiel du contrôle actif de l'écoulement pour relever ces défis.

Contexte de l'étude

Le gain potentiel de charge utile réalisable avec la DBN pourrait entraîner une amélioration significative de la compétitivité tant pour les entreprises que pour les agences gouvernementales. La présente thèse est menée dans le cadre du Labex CAPRYSSES, dont l'objectif est de favoriser les interactions entre ses domaines d'expertise – cinétique chimique, dynamique des fluides, et plasma – afin de mieux comprendre leur couplage dans la production d'énergie, la propulsion, les explosions chimiques et le contrôle d'écoulement, dans le but d'améliorer l'efficacité de la combustion et les performances aérodynamiques. L'optimisation de la tuyère à double galbe s'aligne parfaitement avec ce cadre, et l'amélioration de ses performances grâce à l'injection secondaire annulaire radiale au sein de son extension a donné des résultats prometteurs, conduisant au dépôt de brevets sur plusieurs continents.

L'objectif de cette thèse est de mettre en avant le potentiel d'optimisation des DBNs en explorant de manière approfondie l'impact de l'injection secondaire sur son comportement dans des conditions d'altitude variable. S'appuyant sur une étude antérieure sur le contrôle vectoriel de la poussée dans une tuyère de fusée conventionnelle [3], la présente étude vise à mettre en lumière le potentiel d'optimisation des performances des DBNs tout en veillant à ce que le rapport de débit massique secondaire sur débit massique primaire reste inférieur à 5%.

Cette étude se concentre principalement sur des essais expérimentaux réalisés dans la soufflerie dépressurisée EDITH à l'Institut ICARE du CNRS. Pour compléter ces expériences, une approche numérique préliminaire est entreprise en utilisant des calculs RANS (Reynolds-Averaged Navier-Stokes) stationnaires sur le cluster CaSciModOT (Calcul Scientifique et Modélisation Orléans Tours). La comparaison entre les résultats expérimentaux et les simulations numériques vise à faire progresser notre compréhension des caractéristiques de l'écoulement dans les DBNs.

Organisation du document

Le premier chapitre donne un aperçu des études liées aux tuyères propulsives de fusée. Les principes de base de fonctionnement des tuyères propulsives sont exposés, et l'accent sur la tuyère à double galbe augmente à mesure que le lecteur progresse dans le chapitre. Les principales caractéristiques des DBNs sont discutées, et les motivations de cette thèse sont présentées.

Le deuxième chapitre décrit le dispositif expérimental et numérique à notre disposition pour les campagnes d'essais. La section sur le dispositif expérimental décrit l'installation de la soufflerie EDITH et les différents moyens de mesure utilisés pour analyser les prototypes de tuyères. Le dispositif numérique utilisé pour les campagnes de simulation est présenté.

Le troisième chapitre analyse expérimentalement le comportement de la DBN lisse, qui n'est pas équipée d'une fente d'injection ; il s'agit d'une DBN conventionnelle. Les résultats expérimentaux sont utilisés pour améliorer la capacité du modèle de turbulence à prédire la position du décollement de la couche limite dans la DBN.

Le quatrième chapitre traite de l'effet de la présence d'une fente d'injection secondaire annulaire sans injection secondaire opérationnelle. L'étude est réalisée pour deux positions distinctes de la fente d'injection : à 8 mm et à 16 mm en aval du point d'inflexion.

Le cinquième chapitre présente une étude paramétrique sur la DBN fonctionnant avec une injection secondaire d'air à 8 mm en aval du point d'inflexion.

Le sixième chapitre étend l'analyse effectuée dans le chapitre cinq en réalisant deux campagnes d'essais, la première pour étudier l'influence de la position de l'injection secondaire dans la section d'extension et la seconde pour l'effet d'un autre gaz secondaire, l'hélium. Une conclusion générale est ensuite donnée, résumant les principaux résultats de cette thèse. Des perspectives pour des travaux futurs et des améliorations potentielles du dispositif expérimental et numérique sont données.

C.1 Chapitre 1

Ce chapitre est dédié au contexte historique de cette étude, au principe de fonctionnement des tuyères propulsives, ainsi qu'à l'état de l'art sur le sujet des tuyères à double galbe. La vague de déploiements de petits satellites a marqué le début d'une nouvelle ère où l'industrie aérospatiale a dû s'adapter rapidement pour répondre à un marché en évolution. La demande de lancements fréquents et économiques est devenue la nouvelle norme, suscitant le besoin de systèmes de propulsion capables de répondre efficacement à un large éventail de profils de mission.

Malheureusement, les performances des tuyères de fusée actuelles sont limitées car elles ne parviennent pas à s'ajuster aux changements d'altitude lors de l'ascension de la fusée dans l'atmosphère. Trois modes de fonctionnement sont possible dans une tuyère: sur-détendu, adapté, ou sous-détendu. Ces différents modes de fonctionnement sont généralement observés à basse, moyenne, et haute altitudes, respectivement. Lorsque la pression en sortie de la tuyère est inférieure à la pression ambiante, l'écoulement est dit sur-détendu, et la pression du jet de sortie doit augmenter pour s'ajuster à la pression ambiante. Cette adaptation se produit à travers un choc à la sortie de la tuyère, diminuant les performances de celle-ci.

Dans le cas où la pression en sortie de la tuyère est égale à la pression ambiante, l'écoulement est dit adapté et sort de la tuyère sous la forme d'un jet cylindrique, séparé de l'air ambiant par une ligne de glissement.

Enfin, si la pression en sortie de la tuyère est supérieure à la pression ambiante, l'écoulement de la tuyère est sous-détendu, et la pression du jet d'échappement doit diminuer pour s'adapter aux conditions ambiantes. Dans cette configuration, l'écoulement se détend à la lèvre de la tuyère à travers un faisceau de détente centré, déviant radialement l'écoulement loin de l'axe de la tuyère. La composante radiale de l'écoulement ne contribue pas à la poussée effective, entraînant des pertes supplémentaires.

Une sur-détente excessive représente une menace car elle entraîne un décollement de la couche limite à l'intérieur de la tuyère. Le décollement étant asymétrique, il génère des charges latérales significatives, présentant un risque pour l'intégrité de la tuyère et pouvant entraîner sa destruction. Pour prévenir le décollement de la couche limite dans la tuyère au niveau de la mer, les lanceurs actuels adoptent un rapport d'expansion de tuyère réduit. Cependant, ce compromis limite considérablement les performances à des altitudes plus élevées, où une détente importante est essentielle pour une efficacité optimale.

Un rapport de section plus élevé ε (où $\varepsilon = A_e/A^*$) promet des performances supérieures dans le vide mais se fait au détriment d'une efficacité limitée au niveau de la mer, caractérisée par un écoulement fortement sur-détendu et un décollement interne produisant des charges latérales. Inversement, un rapport de section plus bas offre de meilleures performances au niveau de la mer avec des risques de charges latérales réduits, mais au prix d'un écoulement fortement sous-détendu à des altitudes plus élevées. Ce défi persiste depuis longtemps, et malgré les efforts importants déployés pour la recherche sur les tuyères dotées de capacités d'adaptation à l'altitude, parmi lesquelles on peut citer la tuyère aérospike, la tuyère déployable, ou encore la tuyère à double galbe.

L'étude présentée dans cette thèse porte sur cette dernière. Caractérisée par son un profil de base et une extension, tous deux reliés par un point d'inflexion, cette tuyère offre un mode de fonctionnement basse altitude et un mode haute altitude.

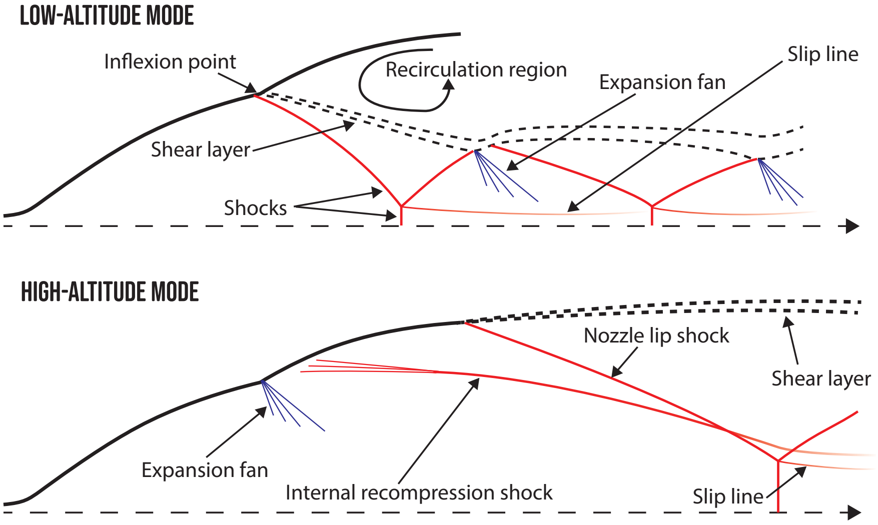

Fig. C.1 Régimes de fonctionnement d'une tuyère à double galbe doté d'une extension à pression constante.

Le changement de régime entre ces deux modes de fonctionnement est appelé la transition pendant la phase de montée et la retransition pendant la phase de descente. Ces phases de transition et de retransition sont définies par la géométrie de la tuyère. Une extension caractérisée par un gradient de pression négatif offrira une transition et une retransition progressives et dépendantes du taux de détente. Ce type de configuration entraîne la génération de charges latérales. Une extension caractérisée par un gradient de pression positif ou nul provoquera une transition abrupte à un NPR défini, limitant le risque de charges latérales. Toutefois, un phénomène d'hystérésis existe au sein de ce type de tuyère, provoquant une différence entre le taux de détente de transition et de retransition. Plus cette différence est faible, plus le risque d'instabilité est élevé, avec la possible apparition d'un phénomène de transition/retransition à répétition appelé flip-flop, augmentant ainsi le risque de charges latérales. On rappelle dans ce chapitre qu'une solution est possible pour pallier aux verrous scientifiques de la DBN :

l’injection secondaire annulaire transverse. Cette solution consistant à injecter un fluide secondaire dans le deuxième galbe de la DBN agit comme un obstacle dans l’écoulement supersonique, forçant le décollement de la couche limite au point d’inflexion pour des taux de détente plus élevés que dans le cadre d’une transition naturelle. Cette méthode permet également de diminuer les charges latérales pendant les changements de régime. La présente étude étend la précédente en étudiant le potentiel d’optimisation de l’injection secondaire annulaire dans le deuxième galbe d’une tuyère à double galbe.

C.2 Chapitre 2

Le deuxième chapitre se divise en deux parties distinctes. La première partie est consacrée à la description du dispositif expérimental et des divers moyens de mesure utilisés dans le cadre de cette étude, tandis que la seconde partie présente le dispositif numérique employé pour mener les campagnes de simulations.

Trois prototypes sont examinés au cours de cette étude : une tuyère sans fente d’injection, également appelée tuyère lisse, une tuyère avec une fente d’injection située à 8 mm en aval du point d’inflexion (DBNi8), et une tuyère avec une fente d’injection localisée à 16 mm en aval du point d’inflexion (DBNi16). À l’exception de la présence de la fente d’injection, les trois prototypes possèdent un profil identique. Ce profil, obtenu à l’aide d’un code basé sur la méthode des caractéristiques, présente un profil de base de type TIC (Truncated Ideal Contoured nozzle), tandis que l’extension est dotée d’un profil à gradient de pression nul à la paroi.

Les campagnes d’essais expérimentaux ont été menées sur la plateforme FAST (Facilities for Aerothermodynamics and Supersonic Technologies) de l’Institut ICARE du CNRS. Les expériences ont été réalisées dans la soufflerie EDITH, une soufflerie Mach 5 à fonctionnement continu initialement conçue pour l’étude des écoulements supersoniques et hypersoniques. EDITH a depuis été adaptée en soufflerie offrant des mesures de test de tuyère dans un environnement dépressurisé. Après avoir été séchée et purifiée par un compresseur Bauer Mini Verticus3, l’air ambiant est comprimé à 30 000 kPa et alimenté à la vanne principale et au régulateur de pression via une conduite de 8 mm de diamètre. Le régulateur de pression ajuste la pression à 600 kPa, et une vanne manuelle en aval régule la pression total du flux principal à 350 kPa avant d’être injectée à travers six conduites distribuées radialement de 10 mm. Ensuite, l’air circule à travers la DBN et sort dans la section d’essai de la soufflerie dépressurisée. La pression à l’intérieur de la section d’essai est contrôlée par une vanne de type papillon en amont d’un groupe de pompage MPR de 345 kW dans le diffuseur de la soufflerie. Les moyens d’analyse qualitative s’appuient sur l’étude de la topologie de chocs à la sortie de la tuyère, effectué à l'aide d'un banc strioscopique de type Schlieren monochromatique en Z. Pour les analyses quantitatives, une balance de force à trois axes mesure à la fois la composante d'effort axial (poussée) et la composante d'effort latérale (charges latérales). Parallèlement, des capteurs de pression et de température enregistrent les conditions génératrices de l'écoulement ainsi que la distribution de pression pariétale dans l'extension de la tuyère. Ces données sont consignées au moyen d'une interface LabView et traitées ultérieurement à l'aide d'un programme Python.

C.3 Chapitre 3

La première section du chapitre est dédiée à l'étude expérimentale de la tuyère lisse dans la soufflerie EDITH. Le comportement natuel (c'est-à-dire sans injection) de la tuyère est analysée pendant les phases de montée et de descente. L'utilisation de la méthode d'imagerie schlieren a permis d'identifier les deux régimes de fonctionnement: basse altitude et haute altitude.

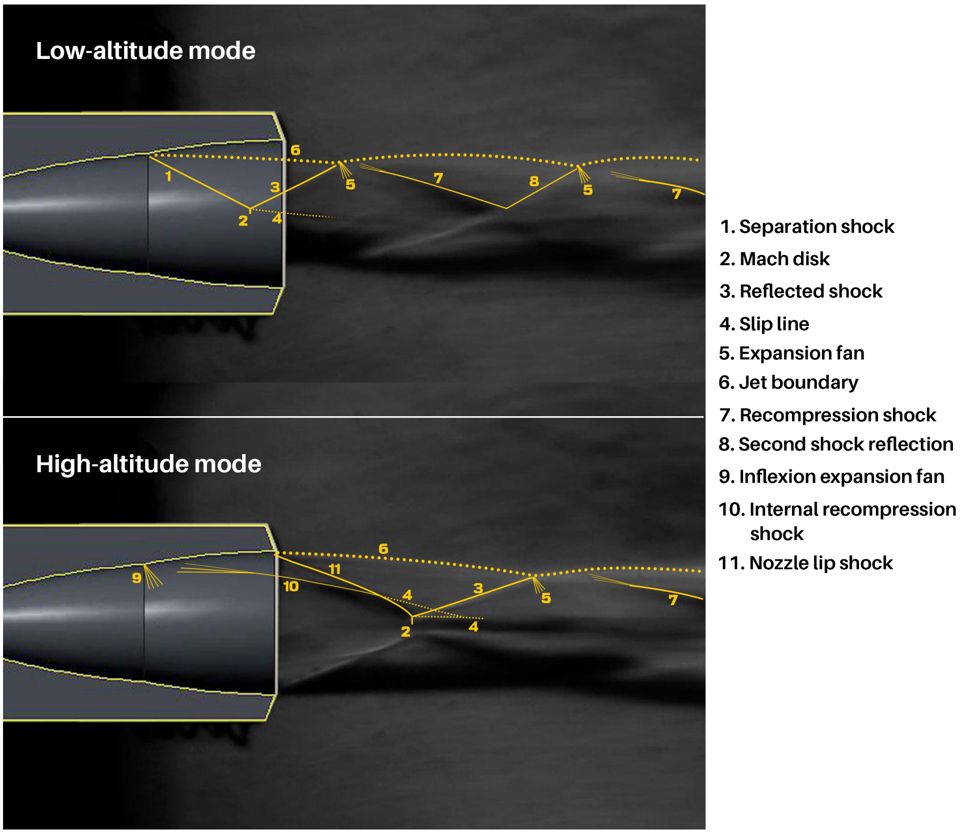

Fig. C.2 Schlieren expérimental de la DBN lisse en mode basse altitude (NPR = 14; figure du haut) et haute altitude (NPR = 30; figure du bas).

L’analyse des images schlieren de l’écoulement permet d’obtenir une description complète de la topologie de l’écoulement pour les deux modes de fonctionnement. Les NPR marquant la transition de la tuyère vers le mode haute altitude et son retour ultérieur au mode basse altitude ont été déterminés comme étant 14,85 and 14,53, respectivement. Des analyses détaillées ont été menées sur la poussée de la tuyère et l’évolution de la de pression pariétale pendant les phases de transition et de retransition. Les résultats expérimentaux ont démontré un accord fort avec les prédictions théoriques.

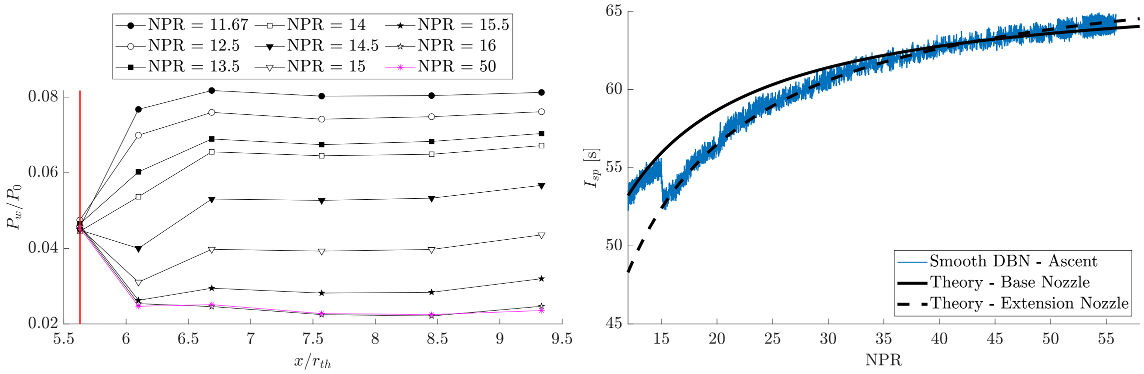

(a) Distribution de la pression pariétale. La ligne rouge indique le point d’inflexion.

(b) Trajectoire d’impulsion spécifique expérimentale et théorique.

Fig. C.3 Distribution de la pression pariétale instantannée (gauche) et trajectoire d’impulsion spécifique en fonction du NPR (droite) pendant une phase ascendante dans la DBN lisse.

La confirmation de l’effet d’hystérésis entre les phases de transition et de retransition a été établie, et sa quantification a révélé une modeste valeur de 2,1%. L’absence du phénomène de flip-flop a été attribuée à l’existence de discontinuités de surface introduites par les trous de capteurs de pression sur la paroi d’extension de la tuyère.

La deuxième section présente une modélisation numérique de l’écoulement à différents NPR au sein de la tuyère, en utilisant une approche RANS stationnaire et le modèle de turbulence standard $k\omega - SST$. Les images schlieren expérimentales et numériques concordent généralement bien pour les différents taux de détente examinés, à l’exception de NPR = 17,5. À ce NPR, des divergences significatives dans la topologie de l’écoulement apparaissent entre la simulation et l’expérience. Ces différences ont été attribuées à la sous-prédiction du point de décollement de la couche limite par le modèle de turbulence. Cela souligne la nécessité d’ajuster le modèle de turbulence, initialement calibré pour des écoulements canoniques, aux spécificités de l’écoulement d’une tuyère à double galbe. L’adaptation du modèle de turbulence a été réalisée en augmentant le taux de cisaillement dans la couche par l’augmentation du paramètre de structure du modèle de turbulence. Ces modifications ont permis d’améliorer la capacité du modèle à prédire plus précisément le point de décollement dans la tuyère sur une large plage de NPR.

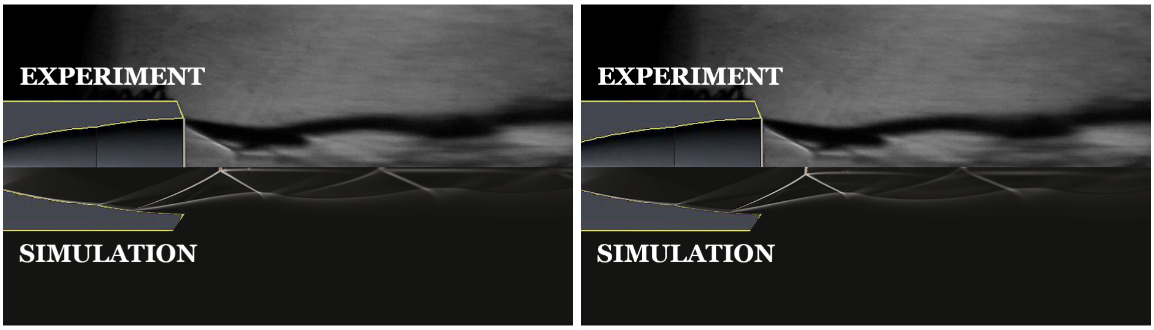

(a) $a_1 = 0,31$ (Modèle SST standard) (b) $a_1 = 0,33$

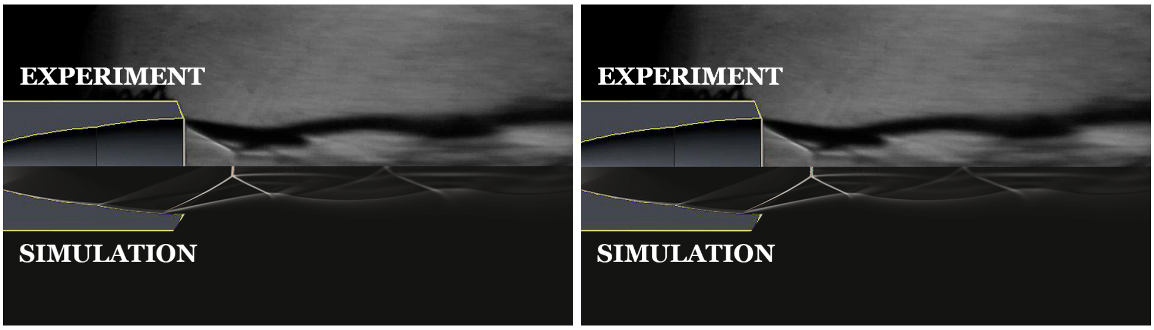

(c) $a_1 = 0,355$ (d) $a_1 = 0,39$

Fig. C.4 Schlieren numérique et expérimental à NPR = 17,5 pour différents paramètres de structure.

Une étude numérique a également été menée en utilisant le modèle de turbulence Spalart-Allmaras, mais celui-ci n’a pas été retenu pour les futures campagnes numériques en raison de ses mauvaises prédictions des points de décollement et de la plus grande disparité de poussée calculée entre ce modèle et l’expérience, comparativement au modèle $k\omega - SST$.

C.4 Chapitre 4

Le chapitre quatre se concentre sur l’effet de la présence d’une fente d’injection dans le deuxième galbe de la tuyère, sans recourir à l’injection secondaire. L’analyse est menée sur deux tuyères équipées d’une fente d’injection secondaire, à savoir la DBNi8 et la DBNi16. Les résultats sont ensuite comparés à ceux obtenus avec la tuyère lisse. L’évaluation de l’impact d’une fente d’injection est complétée par une analyse de l’influence du volume de la cavité d’injection secondaire. En effet, l’injection secondaire nécessite la présence d’une cavité permettant de définir les conditions génératrices de l'écoulement secondaire, dont l'impact du volume n'a jamais été étudié dans la littérature existante.

Cette campagne d'essai a révélé que l'influence de la présence d'une fente d'injection dans l'extension permettait d'agir sur le NPR de transition ou de retransition selon la position de la fente. De plus, il a été montré que le volume de la cavité avait également une influence sur les paramètres importants de la DBN. En effet, l'étude dans la DBNi8 a révélé que le volume de la cavité influençait principalement le comportement de la DBN pendant la phase de transition, où le NPR de transition augmentait avec l'augmentation du volume de la cavité. Le NPR de transition a augmenté de 7,3% au maximum par rapport à la DBN lisse. Dans le même temps, les charges latérales et le saut de poussée ont été réduits à 1,1% et 2,1% de la poussée de la tuyère, une diminution de 1,3 et 1,7 points de pourcentage par rapport à la DBN lisse. L'influence du volume de la cavité sur ces paramètres pendant la phase de retransition n'était pas facilement observable, suggérant un impact limité sur la DBN pendant la phase de descente.

Dans le cas de la DBNi16, le déplacement de la fente d'injection secondaire vers l'aval a eu un effet limité sur le processus de transition, avec une diminution du NPR de transition d'au plus 1,7% pour le plus petit volume de la cavité par rapport à la DBN lisse. Par contre, la présence de la fente d'injection dans le cas DBNi16 a diminué le NPR de retransition de plus de 5%. La présence de la fente d'injection à cette distance a également montré une diminution des forces latérales, mesurées à moins de 1% de la poussée de la tuyère pendant à la fois la montée et la descente, contrairement au cas DBNi8 qui a montré une influence limitée de la fente d'injection sur les forces latérales pendant les descentes. Les sauts de poussée pendant la phase de transition ont été réduits dans la même mesure pour les deux DBN, mais l'effet de la fente d'injection est resté limité pendant la phase de retransition dans les deux cas.

Cette série d'expériences souligne davantage la sensibilité considérable de l'écoulement de la DBN à l'état de surface et à l'emplacement précis de ces discontinuités de surface.

C.5 Chapitre 5

Le chapitre cinq présente les effets de l'injection secondaire radiale à travers une fente annulaire située dans l'extension de la DBNi8. Plusieurs rapports de débit massique secondaires sur débit massique primaire, variant de 0,011 à 0,062, ont été considérés dans la campagne d'essais expérimentaux. Les expériences ont montré que le NPR de transition a augmenté jusqu'à près de 24% pour un rapport de débit massique secondaire de 0,025 par rapport à la tuyère lisse. Le NPR de retransition a augmenté jusqu'à 20,1% pour un rapport de débit massique secondaire de 0,036 par rapport à la tuyère lisse.

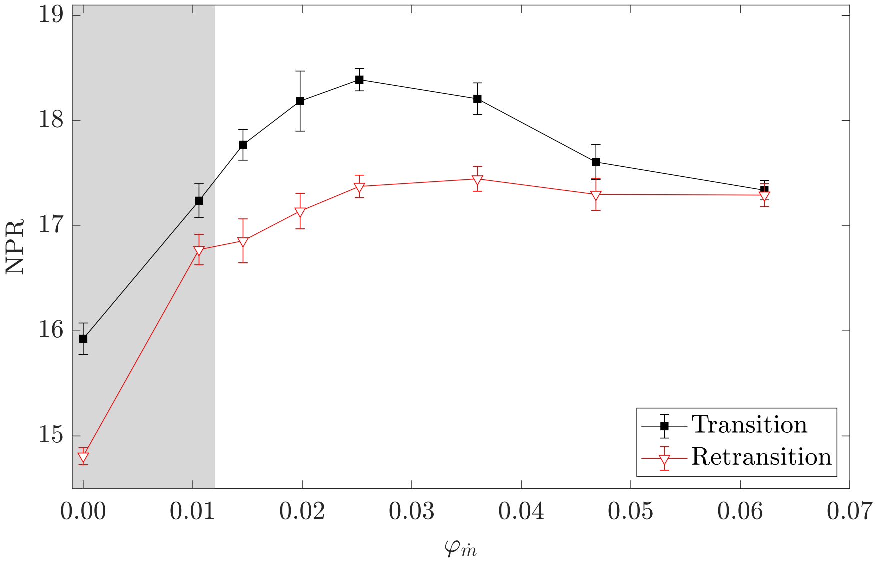

Fig. C.5 NPR de transition et de retransition en fonction du rapport de débit massique secondaire. La partie grisée indique lorsque l'injection secondaire est subsonique. Les barres d'erreur montrent l'écart type calculé pour chaque configuration.

Les expériences ont révélé que cette augmentation du NPR de transition et de retransition était limité, atteignant leurs valeurs maximales dans la plage intermédiaire des rapports de débit massique secondaire utilisées. Cette limitation du NPR de transition et de retransition a été potentiellement identifié comme le manque d'intéraction entre le point de décollement et le point d'inflexion pour les hauts rapports de débit massique (voir Fig. C.6).
L'augmentation du NPR de transition est attribué à la présence de l'obstacle fluidique, déplaçant et forçant le point de décollement à proximité de l'inflexion. L'injection secondaire a également pour effet l'augmentation de la pression le long de la paroi de l'extension, participant au maintien de l'écoulement au niveau du point d'inflexion. La retransition précoce est également attribuée à l'obstacle fluidique qui introduit de la quantité de mouvement radiallement, induisant une bulle de recirculation dont la longueur augmente avec le rapport de débit massique secondaire et entraînant une retransition précoce.

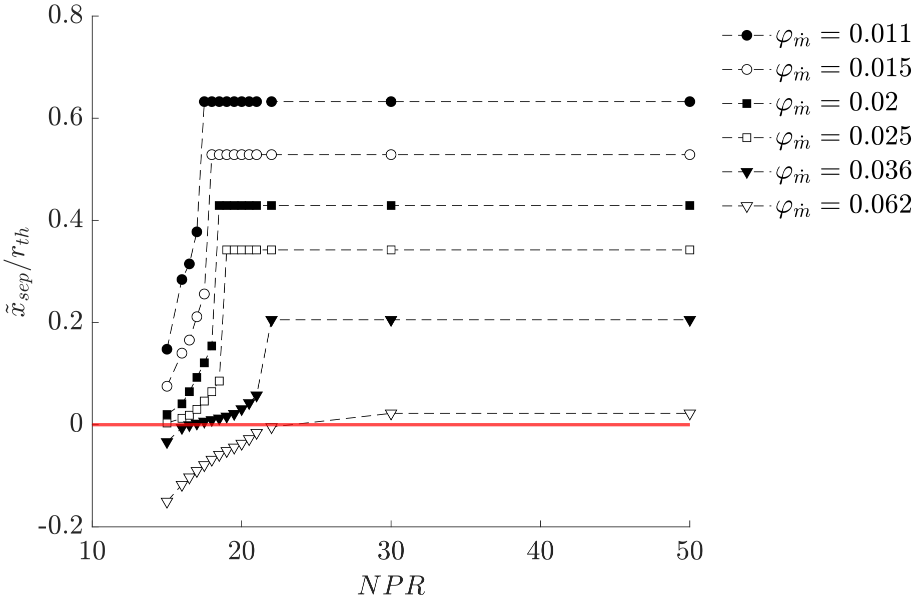

Fig. C.6 Position du décollement depuis le point d'inflexion en fonction du NPR pour tous les rapports de débit massique secondaire (simulations).

Les charges latérales ont été réduites en dessous de 1% de la poussée de la tuyère pendant les phases de transition et de retransition avec un rapport de débit massique secondaire de seulement 0,015. L'important gradient de pression adverse induit par l'écoulement secondaire et la présence du jet sonique transverse agissant comme une barrière aux perturbations remontant l'écoulement sont supposés responsables de cette diminution significative des charges latérales.

Il a été observé que l'injection secondaire réduisait le saut de poussée pendant les changements de régime jusqu'à 2,6 points de pourcentage pendant la transition et jusqu'à 3,1 points de pourcentage pendant la retransition pour le rapport de débit massique secondaire le plus élevé par rapport au cas de la tuyère lisse. L'influence du rapport de débit massique secondaire sur la durée des processus de transition et de retransition a été mise en lumière, fournissant d'autres sujets d'étude pour une compréhension complète du comportement des DBNs. Néanmoins, les résultats montrent des perspectives prometteuses si des tuyères à double galbe dotées d'une injection secondaire venaient à être utilisées dans le futur. L'injection secondaire, avec ses capacités de réduction des charges latérales et des sauts soudain de poussée tout en améliorant l'efficacité de la tuyère, pourrait donc être considérée comme un réel atout pour la prochaine génération de lanceurs.

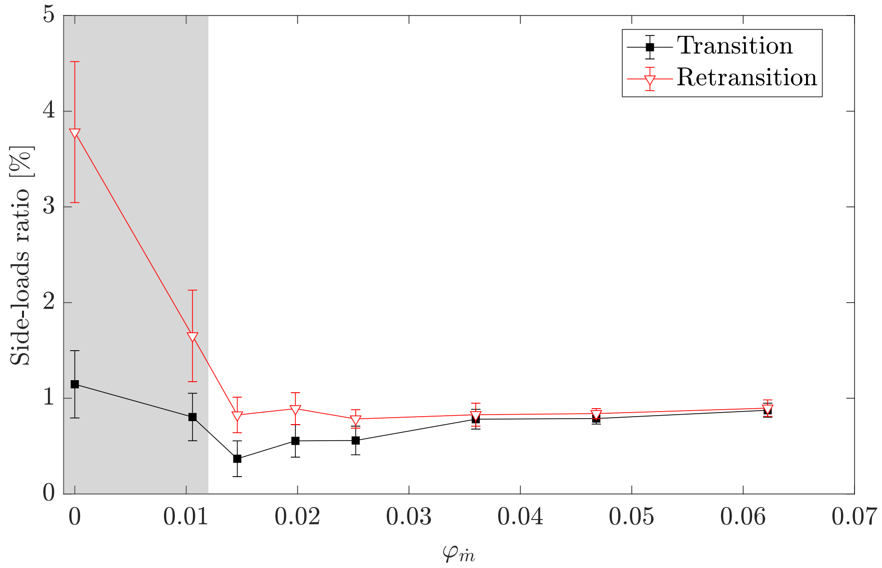

Fig. C.7 Charges latérales rapportées à la poussé en fonction du rapport de débit massique secondaire. La partie grisée indique lorsque l'injection secondaire est subsonique. Les barres d'erreur montrent l'écart type calculé pour chaque configuration.

C.6 Chapitre 6

Le dernier chapitre analyse l'influence de deux paramètres pour l'optimisation des performances d'une tuyère à double galbe : 1) la position de l'injection secondaire et 2) les propriétés du gaz secondaire injecté.

Dans le cadre de l'influence de la position de l'injection secondaire, une campagne d'essai explore l'effet de l'injection secondaire sur le comportement du prototype DBNi16. Les résultats sont comparés à ceux obtenus avec la tuyère DBNi8. Dans la plage de rapport de débit massique secondaire étudiée lors de la campagne d'essais, le NPR de transition a été retardé au maximum de près de 28% dans la DBNi16 par rapport à la tuyère lisse, par opposition à 24% dans la DBNi8. Le NPR de retransition a été augmenté au maximum de 21% et 20%, respectivement. La DBNi8 a montré la capacité de réduire l'amplitude des charges latérales à moins de 1% de la poussée de la tuyère pour un rapport de débit massique $\varphi_{\dot{m}}$ relativement faible, inférieur à 2%, tandis que ce résultat a été atteint pour $\varphi_{\dot{m}} \leq 1\%$ avec la DBNi16. Bien que les deux prototypes aient présenté des comportements similaires, la DBNi16 a montré un lissage de la trajectoire de l'impulsion spécifique pendant les phases de montée et de descente. En effet, à partir de $\varphi_{\dot{m}} \geq 0{,}020$, le saut soudain de l'impulsion spécifique n'a pas pu être clairement identifié et la transition s'est produite de manière continue (see Fig. C.9).

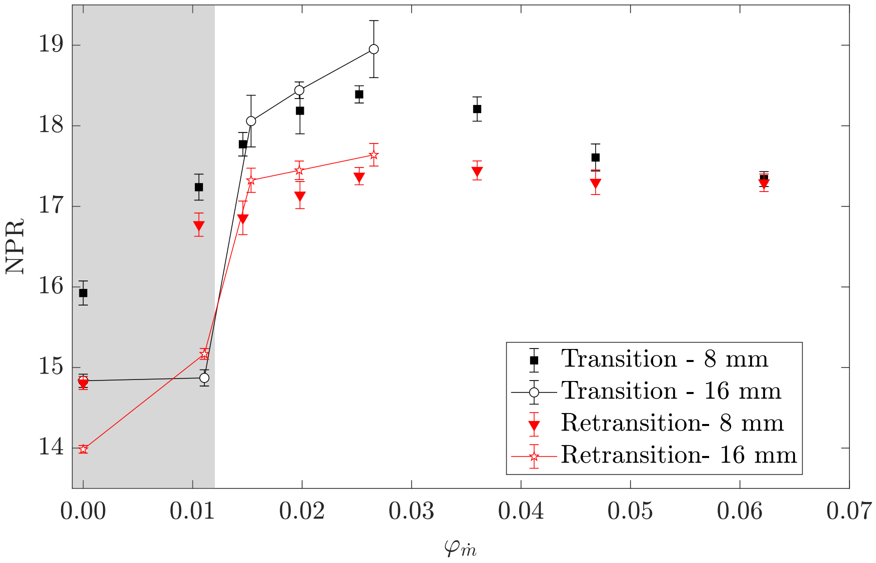

Fig. C.8 NPR de transition et de retransition en fonction du rapport de débit massique secondaire pour différentes positions de l'injection secondaire. La partie grisée indique lorsque l'injection secondaire est subsonique. Les barres d'erreur montrent l'écart type calculé pour chaque configuration.

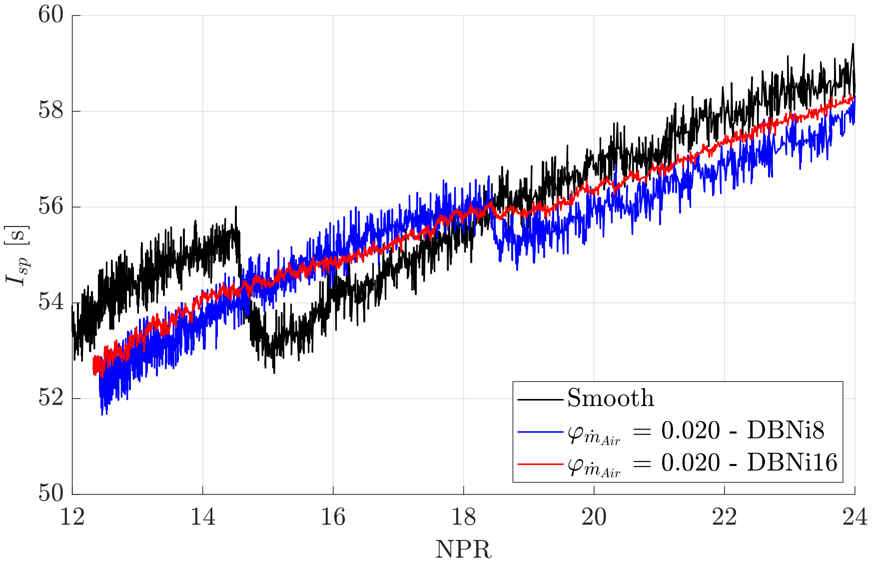

Fig. C.9 Impulsion spécifique en fonction du NPR pendant une phase d'ascension pour la tuyère lisse, la DBNi8 opérant avec $\varphi_{\dot{m}} = 0{,}020$, et la DBNi16 opérant avec $\varphi_{\dot{m}} = 0{,}020$.

La deuxième section de ce chapitre a étudié l'influence des propriétés du gaz secondaire sur le comportement de la DBNi8 et les résultats sont mis en contraste avec ceux de la campagne initiale utilisant de l'air. Les expériences ont prouvé que la transition et la retransition peuvent être retardées encore davantage si la DBNi8 est exploitée avec de l'hélium plutôt qu'avec de l’air.

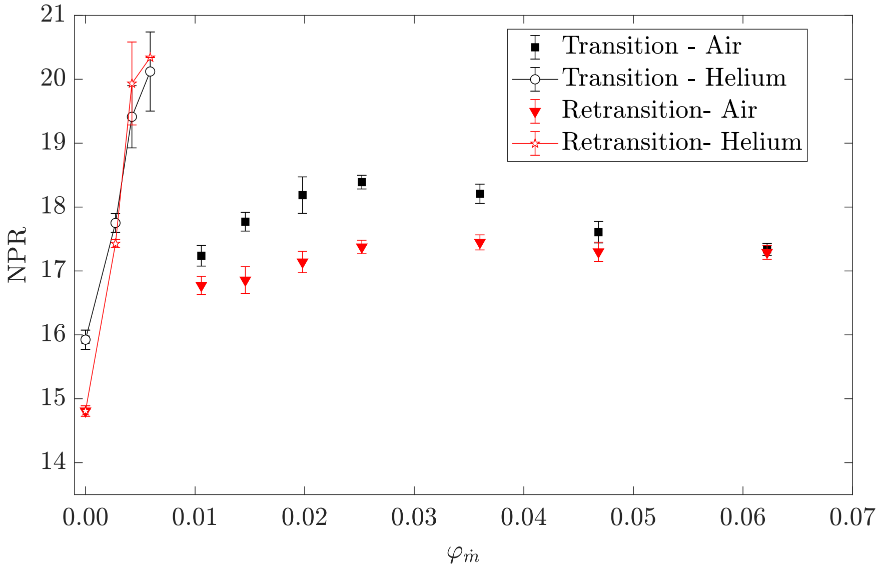

Fig. C.10 NPR de transition et de retransition en fonction du rapport de débit massique secondaire pour différents gaz secondaires. Les barres d’erreur montrent l’écart type calculé pour chaque configuration.

Dans la plage de rapport de débit massique secondaire étudiée lors de cette campagne d’essais et par rapport à la DBN lisse, le NPR de transition a été retardé de plus de 30% pour la DBNi8 fonctionnant à l’hélium, par opposition à 24% lorsqu’elle était exploitée avec de l’air. Le NPR de retransition a augmenté de plus de 37% lorsque l’hélium était utilisé comme gaz secondaire, mais de 20,1% pour la configuration avec de l’air. De manière similaire à la configuration DBNi16, la tuyère DBNi8 fonctionnant à l’hélium a présenté une transition continue, avec l’absence de saut d’impulsion spécifique lors de la transition entre les régimes de fonctionnement (see Fig. C.11). L’amplitude des charges latérales a été réduite à moins de 1% de la poussée de la tuyère pour un rapport de débit massique secondaire inférieur à 0,003.

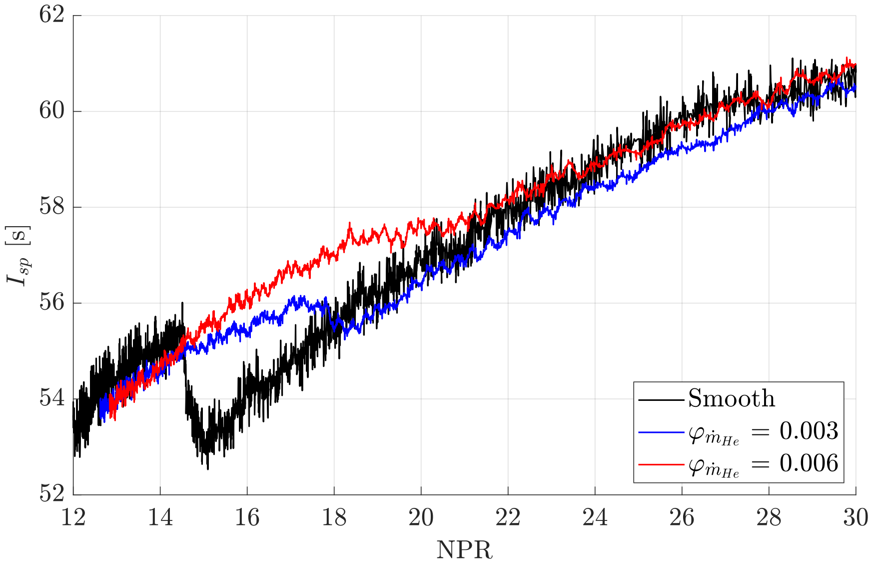

Fig. C.11 Impulsion spécifique en fonction du NPR pendant une phase d'ascension pour différents rapports de débit massique d'injection d'hélium.

Les résultats obtenus avec la DBNi8 fonctionnant à l'hélium comme gaz d'injection secondaire et ceux obtenus avec la DBNi16 exploitée avec de l'air mettent indéniablement en évidence la possibilité d'améliorer les performances des tuyères à double galbe pour la future génération de lanceurs.

Conclusions et perspectives

Conclusions

Cette thèse a étudié le potentiel d'optimisation d'une tuyère à double glabé à échelle réduite en explorant de manière approfondie l'influence de l'injection secondaire sur son comportement pendant les phases de changement de régime dans des conditions d'altitude variables. Le premier chapitre a fourni des éléments contextuels et a abordé les problèmes associés aux DBNs, tandis que le deuxième chapitre a introduit les éléments expérimentaux et numériques utilisés dans la thèse.
Le manuscrit commence par révéler le comportement inhérent d'une DBN équipée d'un profil de base TIC et d'un profil d'extension à pression constante. Les mesures de pression pariétale ont confirmé la nature du profil d'extension : une pression constante. Les conditions d'altitude variable en milieu dépressurisé ont révélé des phases de transition et de retransition abruptes, mesurées à un NPR de 14,85 et 14,53, respectivement. La topologie de l'écoulement a été illustrée à l'aide de l'imagerie schlieren à différents NPRs. Les mesures de la balance des forces ont révélé la présence de charges latérales pendant les changements de régime de fonctionnement. La caractérisation de ces forces latérales a indiqué une amplitude de 2,4% de la poussée pendant la phase de transition et 3,4% pendant la phase de retransition. L'impulsion spécifique a connu un saut significatif pendant les changements de régime de fonctionnement, atteignant 3,8% de la poussée pendant la phase de transition et 4,2% pendant la phase de retransition. Des expériences menées avec et sans mesures de pression sur la paroi ont suggéré que la présence de discontinuités de surface peut jouer un rôle majeur sur la dynamique de l'écoulement et sur les instabilités inhérentes aux DBNs, notamment le phénomène de flip-flop. Des effets d'hystérésis, couramment observés dans les DBNs, ont été identifiés et quantifiés pour la DBN étudiée.

La thèse continue en étudiant l'impact de la présence de la fente d'injection et du volume de la chambre de tranquillisation secondaire, appelée la cavité, sur le comportement naturel de la DBN pendant les changements de régimes. Deux tuyères dotées chacune d'une fente d'injection sont analysées. La premiere, DBNi8, est dotée d'une fente située à 8 mm en aval du point d'inflexion. La seconde, DBNi16, doté d'une fente positionnée à 16 mm en aval du point d'inflexion. La campagne d'essais expérimentaux a révélé que la transition naturelle dans la DBN était significativement influencée par le volume de la cavité et par la position de la fente d'injection secondaire.
Dans la DBNi8, l'étude a révélé que le volume de la cavité impactait principalement le comportement de la tuyère pendant la phase de transition, où le NPR de transition augmentait

avec une augmentation du volume de la cavité. Dans le même temps, les charges latérales et le saut de pousée étaient réduits à 1,1% and 2,1% de la poussée, soit une diminution de 1,3 et 1,7 points de pourcentage par rapport à la tuyère lisse. L'impact du volume de la cavité sur ces paramètres n'était pas clairement observable pendant la phase de retransition, ce qui suggère une influence limitée sur la DBN lors de la phase de descente.

À l'inverse, la série d'expériences réalisée avec la DBNi16 a montré un effet limité de la présence de la fente d'injection et du volume de la cavité pendant la phase de transition. Une diminution maximale du NPR de transition de 1,7% a été mesurée par rapport à la tuyère lisse. Pendant ce temps, la présence de la fente d'injection a diminué le NPR de retransition de plus de 5%, tandis que le DBNi8 a montré un changement maximal du NPR de retransition de moins de 2%. La fente d'injection secondaire plus éloignée a montré une diminution des forces latérales pendant les deux phases de changement de régime, avec une amplitude de moins de 1% de la poussée de la tuyère, contrairement à la DBNi8 qui a montré une influence limitée de la fente d'injection sur les forces latérales pendant les descentes. Les sauts de poussée pendant la phase de transition ont été réduits dans la même mesure pour les deux DBN, mais l'effet de la fente d'injection est resté limité pendant la phase de retransition dans les deux cas.

Après avoir étudié la transition et la retransition naturelle dans les différentes tuyères, une série de pressions d'injection secondaire a été appliquée dans la cavité de la DBNi8 en utilisant de l'air comme gaz. Les expériences ont montré que les NPRs de transition et de retransition étaient augmentés de plus de 20% par rapport à la tuyère lisse. L'augmentation des NPR de transition et de retransition s'est montrée limitée, tandis que les charges latérales ont été réduites à moins de 1% de la poussée pendant les deux types de changement de régime et pour une rapport de débit massique secondaire de seulement 0,015. On note également que la diminution des charges latérales s'accompagne d'une réduction du saut de poussée pendant les phases de transition et de retransition. L'important gradient de pression adverse et l'effet d'obstacle introduit par le jet secondaire a été identifié comme la cause de ce changement radical de comportement.

Une autre campagne d'essais visant à explorer la nature de l'interaction entre le jet secondaire et le point d'inflexion a été menée en étudiant la DBNi16 avec l'utilisation d'une injection secondaire. Les résultats obtenus ressemblaient étroitement à ceux de la DBNi8. En effet, une augmentation du rapport de débit massique secondaire a entraîné une augmentation des NPR de transition et de retransition. Aussi, éloigner le jet secondaire du point d'inflexion a conduit à des NPR de transition et de retransition plus élevés que ceux mesurés au sein de la DBNi8. De plus, les charges latérales ont été réduites à moins de 1% de la poussée de la tuyère, soulignant des opportunités pour améliorer les performances de la tuyère en optimisant la position de l'injection secondaire. Toutefois, l'utilisation de la DBNi16 avec un rapport de débit massique secondaire élevé a laissé apparaître une différence pendant les changements de régime. Dans certaines configurations, les processus de transition et de retransition se sont déroulés de manière continue plutôt que brusque. Les raisons de ces observations restent floues et nécessitent des études plus approfondies.

Enfin, l'impact de l'hélium, un gaz aux propriétés différentes, a été exploré et comparé aux résultats obtenus avec de l'air. Une tendance similaire a été notée, où les NPR de transition et de retransition augmentaient avec le rapport de débit massique secondaire. Cependant, l'hélium a produit des résultats remarquables, montrant une augmentation des NPR de transition et de retransition respectivement de plus de 30% et 37%, par rapport à la tuyère lisse. De plus, les charges latérales ont été réduites à moins de 1% de la poussée de la tuyère, et l'effet de lissage du changement de mode de fonctionnement a également été observé.

Il est à noter qu'aucun saut d'impulsion spécifique n'a été observé pour les deux rapports de débit massique secondaire les plus élevés, car la transition et la retransition se sont produites de manière continue. Ces observations, sans précédent dans la littérature scientifique, appellent à des études plus approfondies. Néanmoins, cette série d'expériences souligne le potentiel évident de surmonter les défis scientifiques inhérents aux tuyères à double galbe et d'améliorer leurs performances.

L'injection secondaire, avec sa capacité à réduire les charges latérales et les changements soudains de poussée tout en améliorant l'efficacité de la tuyère, pourrait donc être considérée comme une véritable solution technologique afin de faire des tuyères à double galbe un atout pour la prochaine génération de lanceurs.

Perspectives

Les perspectives de cette thèse vont au-delà de l'étude actuelle, offrant des pistes prometteuses pour des futures recherches. Elargir l'étude pour correspondre à l'échelle des moteurs utilisés sur les lanceurs de micro et nano-satellites est une étape clé, faisant ainsi un lien entre les essais en laboratoire et les essais industriels.

Pour étendre notre analyse, nous avons l'intention de nous plonger dans des simulations plus complexes, en utilisant des modèles de fermeture plus avancés et en incorporant des simulations instationnaires pour mieux comprendre la dynamique complexe de l'écoulement des tuyères à double galbe.

De plus, l'analyse sera complétée par des expériences impliquant une fente d'injection positionnée plus près du point d'inflexion (4 mm en aval), mais également plus loin en aval (22 mm), ajoutant une nouvelle dimension à notre compréhension.

L'analyse de la tuyère existante peut être renforcée grâce à des études sur le contrôle vectoriel de la poussée et en explorant différentes configurations de fentes d'injection secondaire, de profils de tuyère.

Cette recherche a attiré l'attention d'organisations gouvernementales suite à la soumission d'un projet de startup par l'auteur axé sur la technologie des tuyères à double galbe. Le projet a été reconnu par le Secrétariat Général pour l'Investissement (SGPI) et BPI France dans le cadre du concours i-PhD, remportant ainsi un prix.
Par la suite, nous avons bénéficié d'un mentorat précieux pour faire avancer ce projet de startup, soulignant l'engagement des nations à favoriser la croissance de nouvelles industries et entreprises. Par conséquent, notre objectif est d'intégrer harmonieusement ce concept novateur dans l'industrie, stimulant des avancées significatives dans le secteur spatial.

Brian LEGROS

Contrôle d'écoulement dans les tuyères à double galbe : optimisation du changement de régime par l'injection radiale de fluide secondaire

Résumé :

Le contrôle du changement de régime dans une tuyère à double galbe est étudié par le biais d'une injection fluidique annulaire radiale positionnée en aval du point d'inflexion, dans le profil d'extension de la tuyère. L'objectif de cette étude est d'améliorer les performances de la tuyère et montrer qu'elle peut être une alternative aux tuyères conventionnelles peu efficientes. L'étude s'appuie sur une approche expérimentale et numérique. Elle comprend une étude paramétrique portant sur l'impact de la présence d'une fente d'injection, la position de cette injection dans l'extension de la tuyère, et l'utilisation d'un gaz secondaire aux propriétés différentes de l'air.

L'analyse des résultats révèle la sensibilité de la tuyère à l'état de surface du divergent, où la présence d'une discontinuité modifie le taux de détente (NPR) de changement de régime et diminue les charges latérales. L'injection secondaire démontre la capacité à augmenter significativement les NPR de changement de régime tout en réduisant les charges latérales. L'étude de la position de l'injection confirme le potentiel d'optimisation de la tuyère à double galbe pour améliorer ses performances. Les essais avec un gaz secondaire différent montrent des améliorations plus significatives qu'avec de l'air, levant ainsi les verrous scientifiques associés à cette technologie.

Mots clés : Tuyère à double galbe, Contrôle actif d'écoulement, Ecoulement supersonique, Onde de choc

Flow control in dual-bell nozzles: optimisation of operating mode transition using radial secondary fluidic injection

Summary:

The control of the operating mode switch in a dual-bell nozzle is studied through radial annular secondary fluidic injection positioned downstream of the inflexion point in the nozzle's extension profile. The objective of this study is to enhance the performance of the nozzle and demonstrate its potential as an alternative to conventional nozzles with sub-optimal efficiency. The study employs experimental and numerical approaches, including a parametric investigation into the impact of the presence of an injection slot, the position of the injection in the nozzle's extension, and the use of a secondary gas with properties different from air.

Analysis of the results reveals the nozzle's sensitivity to the surface condition of the divergent, where the presence of a discontinuity alters the nozzle pressure ratio (NPR) at which the switch in operating mode occurs and reduces lateral loads. Secondary injection demonstrates the ability to significantly increase the NPR at which these changes in operating modes occur while reducing lateral loads. The study of the injection position confirms the optimisation potential of the dual-bell nozzle to enhance its performance. Experiments with a different secondary gas show more significant improvements than with air, thereby overcoming scientific challenges associated with this technology.

Keywords: Dual-bell nozzle, Active flow control, Supersonic flow, Shock wave

Institut ICARE
1C, avenue de la Recherche Scientifique
45071 Orléans Cedex 2

Laboratoire PRISME
8 Rue Léonard de Vinci
45072 Orléans